

Chemical Approaches to Organometallic Chemical Vapor Deposition of Wide Band-Gap II-VI Layers and Nanocrystal Composites

by

Michal Danek

B.S. Inorganic Chemistry, Charles University, Prague (1987)

M.S. Inorganic Chemistry, Charles University, Prague (1987)

Submitted to the Department of Chemistry in Partial Fulfillment of the Requirements for the Degree of

Doctor of Philosophy

at the

Massachusetts Institute of Technology

February 1995

© 1995 Massachusetts Institute of Technology

All rights reserved

Signature of Author

Department of Chemistry
January 17, 1995

Certified by

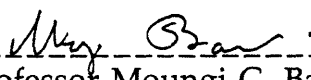
Klavs F. Jensen
Professor, Department of Chemical Engineering and Materials Science
Thesis Supervisor

Accepted by

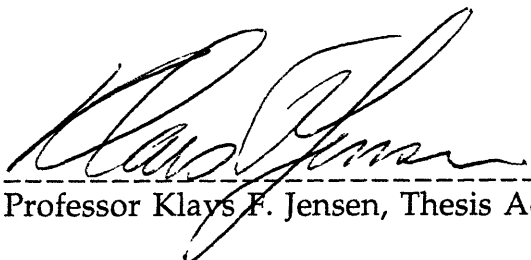
Dietmar Seyferth
Professor of Chemistry
Chair, Departmental Committee on Graduate Students
Science

MAR 1 1995


This doctoral thesis has been examined by a Committee of the Department of Chemistry as follows:



Professor Mouni G. Bawendi, Chairman



Professor Klavs F. Jensen, Thesis Advisor



Professor Dietmar Seyferth, Thesis Co-advisor

Chemical Approaches to Organometallic Chemical Vapor Deposition of Wide Band-Gap II-VI Layers and Nanocrystal Composites

by

Michal Danek

Submitted to the Department of Chemistry on January 17, 1995 in partial fulfillment of the requirements for the degree of Doctor of Philosophy in Inorganic Chemistry

Abstract

Organometallic chemical vapor deposition (OMCVD) of ZnTe was explored with *tert*-butyl(trifluoromethyl)tellurium, a novel precursor with a high vapor pressure and low decomposition temperature. Contamination of ZnTe films with ZnF₂ crystallites was observed at growth temperatures below 400 °C, while almost pure ZnTe films were grown above 400 °C. Growth from bis(trifluoromethyl)tellurium yielded ZnTe films with low fluorine concentrations. The contamination mechanism was probed by molecular beam mass spectroscopy under OMCVD growth conditions.

OMCVD of epitaxial ZnSe was explored with new organometallic selenium precursors. Particular emphasis was placed on the development of precursor chemistry for low temperature growth and p-type doping of ZnSe. Growth experiments with *tert*-butyl(allyl)selenium, in combination with (CH₃)₂ZnN(C₂H₅)₃, yielded films with good surface morphologies and negligible carbon contamination (<5×10¹⁷ atoms/cm³). Low temperature photoluminescence spectroscopy and double crystal x-ray diffraction were used to assess the crystallinity and optical quality of the layers. Gas-phase pyrolysis of *tert*-butyl(allyl)selenium was investigated by molecular beam mass spectrometry and a pyrolysis mechanism of the precursor under OMCVD conditions was proposed. Tripropylphosphine selenide, in combination with dimethylzinc and a helium carrier gas, allowed growth of epitaxial ZnSe at 375-450 °C. The films possessed good photoluminescence spectra and smooth surface morphologies. Secondary ion mass spectrometry (SIMS) confirmed negligible carbon and phosphorus incorporation (<2×10¹⁷ atoms/cm³ and <10¹⁷ atoms/cm³, respectively). The hydrogen content in the layers was low, comparable to the detection limit of SIMS (~10¹⁸ atoms /cm³). The possibility to increase the volatility of phosphine selenide precursors was explored with dimethyl(alkyl)phosphine selenides. Growth experiments with

dimethyl(butyl)phosphine selenide yielded ZnSe films of high quality, comparable to the layers synthesized from tripropylphosphine selenide.

Novel CdSe/ZnSe quantum dot composites for light emitting devices were synthesized by a new technique combining electrospray and OMCVD. In this technique, size selected CdSe nanocrystals are transferred into an OMCVD reactor by electrospray and co-deposited with a ZnSe matrix synthesized from hydrogen selenide and diethylzinc. The microstructure of the composites was probed by high resolution transmission electron microscopy, scanning transmission electron microscopy, Auger electron spectroscopy and x-ray diffraction. The composite films showed room temperature photoluminescence characteristic of the incorporated nanocrystals.

To enhance luminescence properties of CdSe/ZnSe composites, the surface of CdSe nanocrystals was electronically passivated by an overlayer of ZnSe. The ZnSe overlayer was synthesized prior to the electrospray OMCVD synthesis *via* an organometallic solution route. CdSe/ZnSe particles were characterized by high resolution electron transmission microscopy, optical absorption and photoluminescence spectroscopies, x-ray fluorescence, Auger electron spectroscopy analysis, and x-ray diffraction. A dramatic enhancement of photoluminescence yield (by two orders of magnitude) and improved thermal stability of the composites were obtained with the passivated nanocrystals.

Thesis Supervisor : Professor Klavs F. Jensen

Title : Professor of Chemical Engineering and Materials Science

Contents

List of figures	7
List of schemes and tables	15
1. Introduction	16
1.1. The scope of the thesis and research goals	20
1.2. Literature review	21
1.2.1. OMCVD of Wide Band Gap II-VI Semiconductors	21
1.2.2. OMCVD Precursors for ZnSe and ZnTe	23
1.2.3. Semiconductor Quantum Dot Composites	28
1.2.4. Electronic passivation of Quantum Dots with a Wide Band Gap Overlayer	30
1.3. Thesis Outline	32
2. <i>tert</i>-Butyl(trifluoromethyl)tellurium - a novel OMCVD source for ZnTe	39
2.1. Introduction	39
2.2. Experimental	41
2.3. Results and discussion	45
2.3.1. Growth and materials characterization	45
2.3.2. Gas-phase pyrolysis study of tBTcCF ₃	53
2.4. Conclusion	62
3. OMCVD growth and pyrolysis study with <i>tert</i>- butyl(allyl)selenium	64
3.1. Introduction	64
3.2. Experimental	65
3.3. Results and discussion	69
3.3.1. Growth and characterization of ZnSe	69
3.3.2. Gas-phase pyrolysis study of tBAsE	75
3.4 Conclusion	94

4. OMCVD of ZnSe with tripropylphosphine selenides	97
4.1. Introduction	97
4.2. Experimental	100
4.3. Results and discussion	102
4.3.1. OMCVD with tripropylphosphine selenide (TPPSe)	102
4.3.2. OMCVD with dimethyl(butyl)phosphine selenide (DMBPSe)	116
4.4. Conclusion	123
5. Electrospray OMCVD synthesis of CdSe/ZnSe quantum dot composites	127
5.1. Introduction	127
5.2. Experimental	128
5.3. Results and discussion	132
5.4. Conclusion	146
6. Synthesis and Characterization of CdSe/ZnSe Composites with Passivated CdSe Nanocrystals	149
6.1. Introduction	149
6.2. Experimental	150
6.3 Results and discussion	
6.3.1. Synthesis and characterization of CdSe/ZnSe nanoparticles	154
6.3.2. Synthesis of CdSe/ZnSe composites with passivated nanocrystals	165
6.4. Conclusion	177
7. Conclusions and Future Work	180
Acknowledgments	183
List of publications	184

List of Figures

- Figure 1.1** A schematic of a full color thin film electroluminescent display (TFED) [3] and cold cathode field emission display (FED) [2a]. 18
- Figure 1.2** A schematic of a blue LD [8]. 19
- Figure 2.1.** Schematic of the microbalance system. 42
- Figure 2.2.** Schematic of the molecular beam mass spectrometer (MBMS) system. 44
- Figure 2.3.** SEM micrographs of films grown from $t\text{BTeCF}_3$ at various substrate temperatures at $[\text{Te}/\text{Zn}] = 1.0$. (a) 400°C , (b) 350°C and (c) 300°C . 46
- Figure 2.4.** SEM micrographs of films grown from $t\text{BTeCF}_3$ at various $[\text{Te}/\text{Zn}]$ ratios at 350°C . (a) 2.5 and (b) 0.25. 47
- Figure 2.5.** Auger electron spectra of films grown at $[\text{Te}/\text{Zn}]=1.0$. (a) film from $t\text{BTeCF}_3$ at 400°C (surface sputtered), (b) film with crystallites from $t\text{BTeCF}_3$ at 350°C , (c) crystallite on film from $t\text{BTeCF}_3$ at 300°C , (d) film between crystallites from $t\text{BTeCF}_3$ at 300°C , and (e) film from $(\text{CF}_3)_2\text{Te}$ at 500°C (surface sputtered). 48
- Figure 2.6.** SIMS fluorine map of a film grown from $t\text{BTeCF}_3$ at 400°C . Black color indicates an elevated fluorine content. 49
- Figure 2.7.** X-ray diffraction of films grown at $[\text{Te}/\text{Zn}] = 1.0$. (a) film from $t\text{BTeCF}_3$ at 400°C , (b) film from $t\text{BTeCF}_3$ at 350°C , (c) film from $t\text{BTeCF}_3$ at 300°C , (d) film from $(\text{CF}_3)_2\text{Te}$ at 500°C . 51
- Figure 2.8.** Arrhenius plot for growth from $t\text{BTeCF}_3$ at $[\text{Te}/\text{Zn}]$ equals to 2.0 (l), 1.0 (n) and 0.5 (s). The flux of $t\text{BTeCF}_3$ was varied. 52
- Figure 2.9.** Growth rate of ZnTe at 440°C at various $[\text{Te}/\text{Zn}]$ ratios. The flux of $t\text{BTeCF}_3$ was varied. 54
- Figure 2.10.** MBMS spectra of $t\text{BTeCF}_3$ pyrolysed in hydrogen at 412°C (a), in helium at 398°C (b). The peak denoted by (*) corresponds

to SiF_3^+ . It is observed only above the decomposition temperature of the source and may have its origin in the reaction of HF with the quartz insulating plate of the MBMS heater. 56

Figure 2.11. Normalized MBMS intensities of the gas-phase species for pyrolysis of tBTeCF_3 in H_2 at 30 Torr. The following symbols are used: \blacktriangle parent, \square 2-methylpropene ($m/z=56$), \circ 2-methylpropane ($m/z=43$), \bullet hydrogen fluoride ($m/z=20$), Δ tetrafluoroethene ($m/z=100$), \blacksquare 1,1-difluoro-2,2-dimethylcyclopropane ($m/z=91$). 57

Figure 2.12. Effect of 2-methylpropene addition on the ratio of ion signals at $m/z=100$ (tetrafluoroethene) and $m/z=91$ (1,1-difluoro-2,2-dimethylcyclopropane) during pyrolysis of tBTeCF_3 . (a) tBTeCF_3 (20 $\mu\text{mol}/\text{min}$) in hydrogen, (b) tBTeCF_3 (20 $\mu\text{mol}/\text{min}$) and 2-methylpropene (170 $\mu\text{mol}/\text{min}$) in hydrogen. 60

Figure 2.13. Ratio of 2-methylpropene vs. 2-methylpropane partial pressures as a function of heater temperatures during pyrolysis of tBTeCF_3 . 61

Figure 3.1. Schematic of the OMCVD reactor. 67

Figure 3.2. Growth rate of ZnSe for MASE (\blacksquare), DASE (\blacklozenge) and tBAsE (\bullet) as a function of substrates temperatures. The growth rate data for DASE and MASE are from ref. [4]. 70

Figure 3.3. SEM images of the surface morphology of ZnSe films deposited from tBAsE (40 $\mu\text{mol}/\text{min}$) and DMZnNEt_3 (20 $\mu\text{mol}/\text{min}$) in hydrogen at various growth temperatures: (a) 325°C (b) 350°C (c) 400°C. 71

Figure 3.4. Low temperature (10 K) photoluminescence spectra of ZnSe grown from tBAsE (40 $\mu\text{mol}/\text{min}$) and DMZnNEt_3 (20 $\mu\text{mol}/\text{min}$) in hydrogen at 350°C. 73

Figure 3.5. Dependence of carbon concentration on the [VI/II] ratio for ZnSe films grown from MASE (\blacksquare) [growth at 520 °C], DASE (\blacklozenge) [growth at 400 °C] and tBAsE (\bullet) [growth at 350°C]. The samples from MASE and DASE were prepared previously [4]. 74

- Figure 3.6.** Molecular beam mass spectra of the gas-phase recorded during pyrolysis of tBAsE in hydrogen at 100 °C (a), 240 °C (b), and 440 °C (c). The spectra are corrected for the temperature dependence of the sampling flux. 76
- Figure 3.7.** Partial pressures of tBAsE and the hydrocarbon products in the gas-phase during pyrolysis of tBAsE in hydrogen at various temperatures; ● tBAsE, ■ propene, □ 2-methylpropene, Δ 2-methylpropane, and ○ 1,5-hexadiene. 77
- Figure 3.8.** Partial pressure ratios of propene vs. 1,5-hexadiene (●) and 2-methylpropene vs. 2-methylpropane (□) for the pyrolysis of tBAsE in hydrogen. 79
- Figure 3.9.** Relative MBMS intensities of tBAsE and DAsE for pyrolysis of tBAsE in hydrogen. ● tBAsE ($m/z=178$ amu) and ◇ DAsE ($m/z=162$ amu). 80
- Figure 3.10.** The hydrocarbon region of the molecular beam mass spectra recorded during pyrolysis of tBAsE in deuterium and hydrogen: (a) 100 °C in deuterium, (b) 100 °C in hydrogen, (c) 250°C in deuterium, (d) 240 °C in hydrogen, (e) at 450 °C in deuterium, and (f) 440 °C in hydrogen. 81
- Figure 3.11.** Molecular beam mass spectra of the gas-phase for co-pyrolysis of an equimolar mixture of tBAsE and DMZn in hydrogen at 100 °C (a), 320°C (b), and 450 °C (c). The spectra are corrected for the temperature dependence of the sampling flux. 87
- Figure 3.12.** Partial pressures of tBAsE, DMZn and the hydrocarbon products for co-pyrolysis of tBAsE and DMZn in hydrogen at various temperatures; ● tBAsE, × DMZn, ◆ methane, ▲ ethane, ■ propene, □ 2-methylpropene, Δ 2-methylpropane, and ○ 1,5-hexadiene. 88
- Figure 3.13.** The partial pressure ratios of propene vs. 1,5-hexadiene (●) and 2-methylpropene vs. 2-methylpropane (□) for co-pyrolysis of tBAsE and DMZn in hydrogen. 90
- Figure 3.14.** Relative MBMS intensities of tBAsE, DAsE, MAsE and DMSe for pyrolysis of tBAsE in hydrogen at various temperatures; ● tBAsE ($m/z=178$ amu), ◇ DAsE ($m/z=162$ amu), + MAsE ($m/z=136$), and ▼ DMSe ($m/z=110$ amu). 91

- Figure 4.1.** Schematic of the OMCVD reactor and gas-handling system used for growth experiments with the phosphine selenides. 101
- Figure 4.2.** Temperature dependence of ZnSe growth rate. The ZnSe film was deposited from TPPSe (5 μ mol/min) and DMZn (5 μ mol/min) in helium at 300Torr. 103
- Figure 4.3.** SEM images of surface morphology of ZnSe films grown from TPPSe (5 μ mol/min) and DMZn (5 μ mol/min) in He at 375 °C (a), 400 °C (b), 425 °C (c), and 450 °C (d). The layer thicknesses were ~0.5 μ m (a,b) and ~1.0 μ m (c,d). 105
- Figure 4.4.** SIMS concentration profiles for hydrogen (a), phosphorus (b), and carbon (c) in films grown from TPPSe (5 μ mol/min) and DMZn (5 μ mol/min) in He at 400 °C (solid curve), and tBASE (40 μ mol/min) and DMZnNEt₃ (20 μ mol/min) in H₂ at 350 °C (dashed curve). 106
- Figure 4.5.** SEM image of a ZnSe film grown from TPPSe (5 μ mol/min) and DMZn (5 μ mol/min) in H₂ at 400 °C. The layer thickness was ~0.5 μ m. The white particles were identified by Auger electron spectroscopy as ZnSe. 108
- Figure 4.6.** SIMS concentration profiles for hydrogen, phosphorus, and carbon in a films grown from TPPSe (5 μ mol/min) and DMZn (5 μ mol/min) in H₂ at 425 °C. 109
- Figure 4.7.** 10 K PL spectra of ZnSe grown from TPPSe (5 μ mol/min) and DMZn in He at 425 °C at the [VI/II] ratio equals to 0.5 (a), 1 (b) and 2 (c). The film thicknesses were ~1 μ m. 110
- Figure 4.8.** 1.9 K near band-edge PL of ZnSe. The films were grown from TPPSe (5 μ mol/min) and DMZn in He at 425 °C at the [VI/II] ratio equals to 0.5 (a), 1 (b) and 2 (c). The film thicknesses were ~1 μ m. 111
- Figure 4.9.** 10 K PL spectra of ZnSe grown from TPPSe (5 μ mol/min) andDMZn (5 μ mol/min) in He at various substrate temperatures: 375 °C (a), 400 °C (b), 425°C (c), and 450 °C (d). 114
- Figure 4.10.** 1.9 K near band-edge PL of ZnSe. The films were grown from TPPSe (5 μ mol/min) andDMZn (5 μ mol/min) in He at

- various substrate temperatures: 375 °C (a), 400 °C (b), 425°C (c), and 450 °C (d). 115
- Figure 4.11.** 10 K PL spectrum of a ZnSe film grown from TPPSe (5 μ mol/min) and DMZn (5 μ mol/min) in H₂ at 400 °C. The inset shows the band-edge emission. 117
- Figure 4.12.** Vapor pressure for DMBPSe (●) and TPPSe (□) at various temperatures. 118
- Figure 4.13.** SEM image of a ZnSe film grown from DMBPSe (5 μ mol/min) and DMZn (5 μ mol/min) in He at 425 °C. The layer thickness was ~1 μ m. 119
- Figure 4.14.** SIMS concentration profiles for hydrogen, phosphorus, and carbon in a films grown from DMBPSe (5 μ mol/min) and DMZn (5 μ mol/min) in He at 425 °C. 120
- Figure 4.15.** 10 K PL spectrum of a ZnSe film grown from DMBPSe (5 μ mol/min) and DMZn (5 μ mol/min) in He at 425 °C. The layer thickness was 0.5 μ m. The insert shows the band-edge emission. 122
- Figure 5.1.** Schematic of the Electrospray OMCVD reactor. 130
- Figure 5.2.** X-ray diffraction patterns of CdSe/ZnSe composites deposited by ES-OMCVD at 150 °C (a), 200 °C (b), and 250 °C (c). The size of the CdSe nanocrystals was ~5.0 nm. The zinc blende and wurtzite diffractions of ZnSe are labeled with ◆ and ○, respectively. 134
- Figure 5.3.** SEM images of CdSe/ZnSe composites deposited by ES-OMCVD at 150 °C (a), 200 °C (b), and 250 °C (c). 135
- Figure 5.4.** AES depth profiles of Zn (n) and Cd (m) concentrations in a CdSe/ZnSe composite with ~3.5 nm CdSe nanocrystals. The film was deposited at 240°C. 136
- Figure 5.5.** Optical absorption (dashed line) and PL (solid line) spectra of a CdSe/ZnSe composite incorporating ~3.5 nm CdSe nanocrystals. The excitation wavelength for the PL spectrum was 470 nm. 138

- Figure 5.6.** Room temperature PL (a,b) and PL excitation (c,d) spectra of CdSe/ZnSe quantum dot composites with ~3.5 nm nanocrystals (a,c) and ~5.0 nm nanocrystals (b,d), respectively. The films were deposited at 150°C. The excitation wavelength for the PL spectra was 470 nm. The detection wavelengths for the PL excitation spectra were 570 nm (c) and 616 nm (d), respectively. 139
- Figure 5.7.** Room temperature PL of CdSe/ZnSe quantum dot composites deposited at various substrate temperatures. The size of the imbedded nanocrystals was ~5.0 nm. The excitation wavelength was 470 nm. 141
- Figure 5.8.** Bright field TEM images of a CdSe/ZnSe quantum dot composite film with ~ 5.0 nm nanocrystals deposited on a C/Ni TEM grid at 250°C. The view shows individual CdSe nanocrystals surrounded by grains of a ZnSe matrix. The (002) wurtzite planes of the nanocrystals are resolved ($d_{002}=0.35$ nm). 142
- Figure 5.9.** STEM image of a CdSe/ZnSe quantum dot composite film with ~5.0 nm nanocrystals deposited on a C/Ni TEM grid at 250°C (a), and the corresponding Zn, Se and Cd elemental maps (white color represents regions of high concentration levels, black color shows areas with low concentrations). 144
- Figure 5.10.** HRTEM image of an agglomerate of ~5.0 nm CdSe nanocrystals formed in electrospray. The agglomerate was collected on a C/Ni TEM. 145
- Figure 6.1.** Evolution of the UV/Vis absorption spectra of the reaction mixture during overgrowth of ~4.0 nm CdSe nanocrystals with ZnSe. The inset shows the corresponding particle sizes as determined with HRTEM. 155
- Figure 6.2.** Low magnification TEM image of CdSe/ZnSe particles with [ZnSe/CdSe]=2.5. The initial size of the CdSe nanocrystals was ~4.0 nm. 157
- Figure 6.3.** HRTEM image of CdSe/ZnSe particles with [ZnSe/CdSe]=2.5. The initial size of the CdSe nanocrystals was ~4.0 nm. 159

- Figure 6.4.** X-ray diffraction spectra of ~6.8 nm CdSe/ZnSe particles (a), ~4.0 nm CdSe nanocrystals (b), and powder diffraction lines of wurtzite ZnSe (c) and wurtzite CdSe (d). The [ZnSe/CdSe] ratio for the overcoated particles was ~2.5. 160
- Figure 6.5.** Optical absorption spectra of a film of CdSe/ZnSe particles with [ZnSe/CdSe]=2.5 before (a) and after (b) annealing in hydrogen at ~450 °C. The calculated band-gap energy for Zn_{0.7}Cd_{0.3}Se bulk is shown. 161
- Figure 6.6.** Optical absorption and PL spectra of CdSe (a) and CdSe/ZnSe particles with various [ZnSe/CdSe] ratios: 3.6 (b), 4.3 (c) and 4.8 (d). The samples were dispersed in pyridine. The excitation wavelength for the PL was 480 nm. 163
- Figure 6.7.** PL excitation spectra of CdSe (●) and CdSe/ZnSe particles with [ZnSe/CdSe] ratio of 3.6 (◆), 4.3 (Δ) and 4.8 (□). The samples were dispersed in pyridine. The PL was detected at 570 nm and the spectra were normalized to the PL intensity at 550 nm. 166
- Figure 6.8.** 300K PL spectra of CdSe/ZnSe composite films with bare CdSe nanocrystals (~3.5 nm). The films were synthesized by ES-OMCVD at substrate temperatures of 150 °C (a), 200 °C (b) and 250 °C (c). The excitation wavelength was 480 nm. 167
- Figure 6.9.** 10K PL spectra of CdSe/ZnSe composite films with bare CdSe nanocrystals (~3.5 nm). The films were synthesized by ES-OMCVD at substrate temperatures of 150 °C (a), 200 °C (b) and 250 °C (c). The excitation wavelength was 480 nm. 169
- Figure 6.10.** 300 K and 10K PL excitation spectra of CdSe/ZnSe composite films with bare CdSe nanocrystals (~3.5nm) synthesized by ES-OMCVD at 200 °C. The 300 K PL was detected at 554 nm (●), the 10 K PL detection wavelengths were 546 nm (□) and 710 nm (◇). The band-gap energies of zinc blende ZnSe at 300 K and 10K are shown with the arrows. 170
- Figure 6.11.** 300 K PL spectra of CdSe/ZnSe composite films with overcoated CdSe nanocrystals. The size of the initial CdSe dots was ~3.7nm; [ZnSe/CdSe]=4.0. The films were synthesized by ES-OMCVD at substrate temperatures of 150 °C

(a), 200 °C (b) and 270 °C (c). The excitation wavelength was 480 nm. 172

Figure 6.12. 10 K PL spectra of CdSe/ZnSe composite films with overcoated CdSe nanocrystals. The size of the initial CdSe dots was ~3.7nm; [ZnSe/CdSe]=4.0. The films were synthesized at substrate temperatures of 150 °C (a), 200 °C (b) and 270 °C (c). The excitation wavelength was 480 nm. 173

Figure 6.13. 300 K and 10K PL excitation spectra of a CdSe/ZnSe composite film with overcoated CdSe nanocrystals. The film was synthesized by ES-OMCVD at 200 °C. The size of the initial CdSe dots was ~3.7nm; [ZnSe/CdSe]=4.0. The 300 K PL was detected at 576 nm (●), the 10 K PL was monitored at 570 nm (□). The band-gaps of zinc blende ZnSe at 300 K and 10K are shown with the arrows. 174

Figure 6.14. Relative band-edge PL yields for CdSe/ZnSe composite films with bare and passivated CdSe dots. The samples were synthesized by ES-OMCVD at substrate temperatures of 200°C (●) and 260 °C (□). The number of ZnSe monolayers in the passivating layer was estimated from the know size of the initial CdSe nanocrystals and [ZnSe/CdSe] stoichiometry of the composite particles assuming a symmetrical core-shell structure. The excitation wavelength was 500 nm. 76

List of Schemes and Tables

- Scheme 2.1.** Proposed gas-phase decomposition mechanism of $t\text{BTeCF}_3$. 58
- Scheme 3.1.** Pyrolysis mechanism of $t\text{BAsSe}$ under reduced pressure OMCVD conditions. The major low temperature reactions are shown with bold arrows. The symbol $[\text{H}^\bullet]$ represents hydrogen radical donors. 83
- Scheme 3.2.** Mechanism of formation of the selenium containing by-products for co-pyrolysis of $t\text{BAsSe}$ and DMZn . The major low temperature reactions are shown with bold arrows. The symbols $[\text{H}^\bullet]$ and $[\text{CH}_3^\bullet]$ stand for hydrogen radical and methyl radical donors; $[\text{Zn}]$ represents zinc bearing species, such as $(\text{CH}_3)_2\text{Zn}$, $\text{CH}_3\text{Zn}^\bullet$, and elemental zinc. 93
- Table 1.1.** Fundamental properties of wide band gap semiconductors [1] 16
- Table 2.1.** Vapor pressure of tellurium OMCVD sources at 20 °C. 40

1. Introduction

Wide band gap II-VI semiconductors, including the binary compounds ZnS, ZnSe, ZnTe, CdS and CdSe, and their alloys, are materials with zinc blende (ZB) or wurtzite (W) structure and a large direct band gap [1]. The band gap energies of the most stable binary phases and corresponding lattice parameters and effective masses are listed in Tab. 1.1. The band gap energies for the alloys follow in many cases a linear dependence on the composition (*e.g.*, $\text{ZnS}_x\text{Se}_{1-x}$ or $\text{Zn}_x\text{Cd}_{1-x}\text{Se}$), while a highly non-linear relationship is observed for other systems (*e.g.*, $\text{ZnS}_x\text{Te}_{1-x}$) [1]. The bonding in wide band gap II-VI semiconductors has a high degree of ionic character and the fundamental electronic properties of the materials, therefore, differ significantly from those for Si, Ge and III-V semiconductors.

Table 1.1. Fundamental properties of wide band gap semiconductors [1]

Compound	E_g [eV]	a_{ZB} [nm]	a_{W} [nm]	c_{W} [nm]	m_n/m_0	m_p/m_0
ZnS	3.70	5.4102	-	-	0.28 [2]	0.49 [2]
ZnSe	2.70	5.6676	-	-	0.16	0.75
ZnTe	2.35	6.1037	-	-	0.11	0.6
CdS	2.49	-	4.1367	6.7161	0.17	0.7 ($\perp c$)
CdSe	1.75	-	4.2999	7.0109	0.11	0.45 ($\perp c$)

Wide band gap II-VI semiconductors are attractive materials for optoelectronics, specifically for light emitting devices. Traditionally, polycrystalline ZnS or $\text{Zn}_x\text{Cd}_{1-x}\text{S}$ doped with Mn, Cu, Ag, Cl and rare earth elements are used as efficient phosphors in cathode ray tubes (CRTs) and high field electroluminescent devices (EDs) [2]. The conventional II-VI phosphors may also become important in full color flat panel displays. Examples of promising display technologies utilizing phosphor are thin film electroluminescence displays (TFEDs) and cold cathode field emission

displays (FEDs) (Fig. 1.1) [3]. However, further improvements in the luminance and stability of phosphor materials are necessary to realize the potential of these technologies. A new approach to high luminance phosphors relies on layered structures incorporating thin films of doped materials, *e.g.*, ZnS:Mn or ZnS:Tm, between undoped layers, *e.g.*, ZnS or SrS [4]. The undoped films function as electron acceleration or carrier confinement layers, while the doped films emit light. One of the future prospects is construction of quantum well and superlattice phosphor structures [4]. Development of high luminance blue phosphors for both TFEDs and FEDs remains one of the most challenging problems in the field and new combinations of host lattices and dopants are being explored [3].

Light emitting carrier injection devices, *e.g.*, light emitting diodes (LEDs) and laser diodes (LDs), operating in the blue-green spectral region represent another important area for application of wide band gap II-VI semiconductors [5]. These devices are demanded in many areas of technology, including optical telecommunication, optical data recording, printing, displays and sensors. Epitaxial films of ZnSe and its alloys, such as $\text{ZnS}_x\text{Se}_{1-x}$, $\text{Zn}_x\text{Cd}_{1-x}\text{Se}$ and $\text{Zn}_x\text{Mg}_{1-x}\text{S}_y\text{Se}_{1-y}$, are the most promising materials for construction of II-VI LEDs and LDs because of the large band gap energies and close lattice match with GaAs substrates [6]. Construction of these devices demands growth of epitaxial layers with precisely controlled thickness and stoichiometry. Layers with a low density of structural defects, such as misfit dislocations, are required for low threshold operation and stability of the devices [7]. Such materials can be obtained by growing perfectly lattice matched alloys or strained quantum wells accommodating the lattice mismatch without defect formation. A schematic of the state of the art LD structure is shown in Fig. 1.2 to illustrate the materials complexity of the current II-VI injection devices. Such complexity imposes strict requirements on the growth and doping process [8]. In principle, II-VI semiconductors other than ZnSe can be also used for realization of injection devices. For example, the combination of ZnS (naturally n-type) and ZnTe (naturally p-type) allowed construction of blue LEDs operating at room temperature [9]. However, difficulties in finding a good substrate material makes these alternatives less practical.

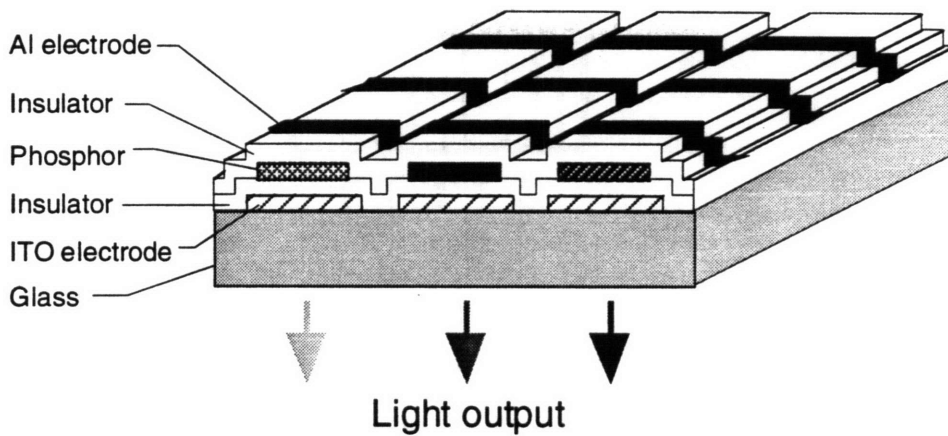


Figure 1.1a. A schematic of a full color TFED [3]. The display consists of a matrix of row and column of electrodes and a stack of insulator layers and patterned phosphors emitting red, green and blue light. The luminescence is generated by a pulse of a high electric field and matrix addressing is used to excite individual pixels. The display is viewed through the glass substrate.

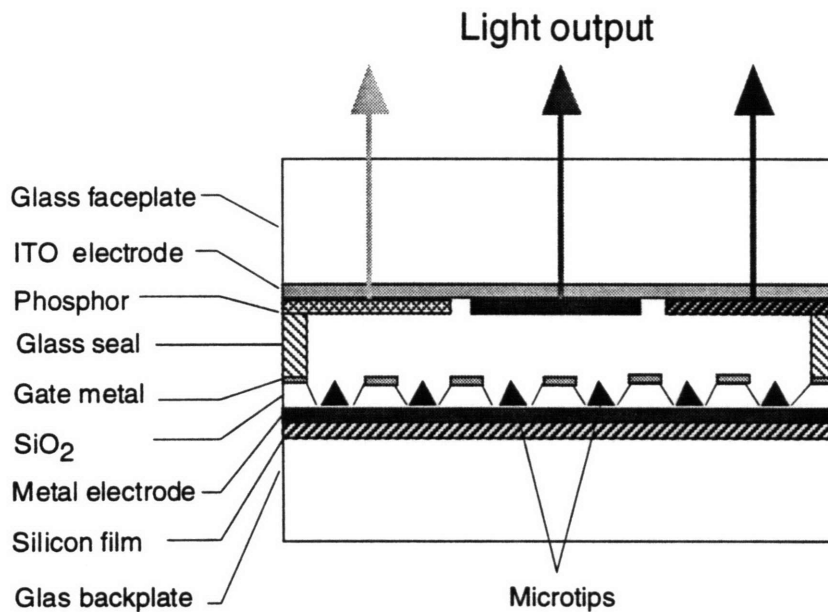


Figure 1.1b. A schematic of a full color FED [2a]. The electrons emitted from the microtips excite the patterned phosphors.

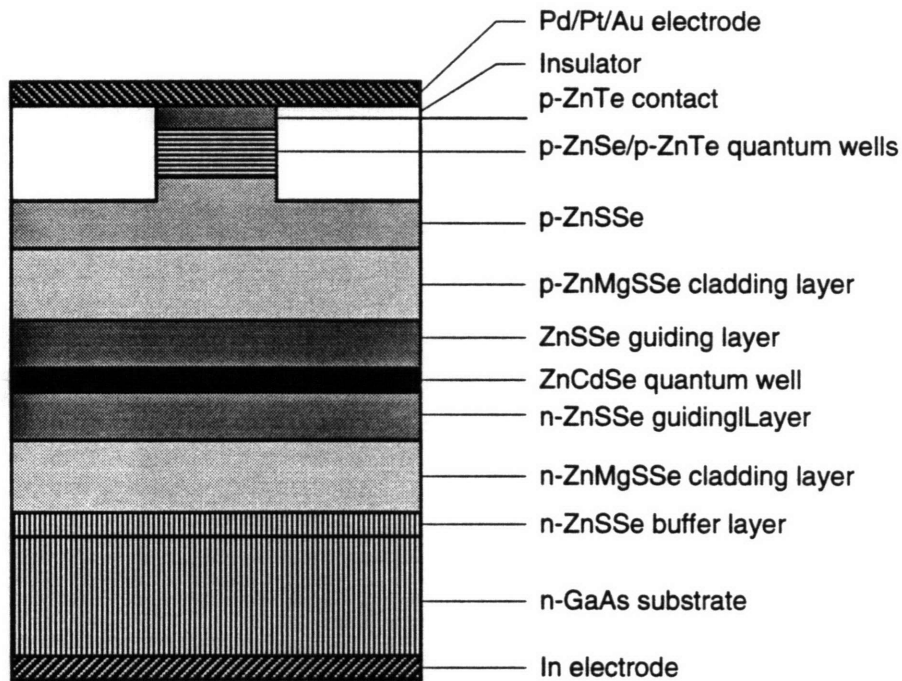


Figure 1.2. A schematic of a blue LD [8]. The LD structure was grown on (100) n-GaAs substrate by molecular beam epitaxy (MBE). The p-n junction is formed by p-ZnSse layer, ZnCdSe quantum well (5 nm thick) and n-ZnSse layer. The Cd content in the ZnCdSe alloy was sufficiently high to keep the injected carriers confined in the quantum well even at room temperature. The doped ZnSse layers surrounded by ZnMgSse cladding layers form the laser waveguide. In order to provide for a low resistance ohmic contact to the p-type side of the device, a graded p-ZnTe/p-ZnSe quantum well structure is grown on the p-type cladding layer. The laser cavity is defined by cleaved facets covered with high reflectivity coatings. Because of low density of structural defects, the LD emits blue light in both continuous wave (CW) and pulse modes at room temperature.

1.1. The Scope of the Thesis and Research Goals

The purpose of the thesis research is to contribute to the development of organometallic chemical vapor deposition (OMCVD) of wide band gap II-VI semiconductors, specifically ZnSe and ZnTe. The emphasis is placed on the following areas:

(1) OMCVD of ZnTe with novel (trifluoromethyl)tellurium precursors. These precursors, *e.g.* *tert*-butyl(trifluoromethyl)tellurium (tBCF₃), were recently proposed as an alternative to the low vapor pressure dialkyltellurium sources currently used for low temperature deposition of group IIb tellurides and their alloys [10]. OMCVD with fluorinated tellurium reagents is essentially unexplored. The goal of this project is to probe the deposition chemistry of tBT₃CF₃ in OMCVD and gas-phase pyrolysis experiments, and assess the feasibility of the (trifluoromethyl)tellurium precursors for synthesis of ZnTe.

(2) Low temperature OMCVD of ZnSe with allylselenium compounds. Growth of epitaxial ZnSe films was explored with *tert*-butyl(allyl)selenium (tBAs₃) in combination with dimethylzinc triethylamine adduct (DMZnNEt₃). The research objective is to test the potential of the selenium precursor for low temperature synthesis of epitaxial ZnSe free of carbon contamination. Gas-phase pyrolysis experiments under OMCVD growth conditions were conducted to elucidate the decomposition mechanism of the precursor and identify the critical deposition parameters.

(3) Development of precursor chemistry for OMCVD of ZnSe with a low hydrogen content. New precursor chemistry combining trialkylphosphine selenides, dimethylzinc (DMZn) and a helium carrier gas, is proposed to circumvent hydrogen incorporation into ZnSe films which is a limiting factor in synthesis of p-ZnSe:N. The precursor chemistry was tested in OMCVD growth experiments with

tripropylphosphine selenide (TPPSe) and dimethyl(butyl)phosphine selenide (DMBPSe).

(4) Synthesis of CdSe/ZnSe quantum dot composites. New luminescent composites incorporating CdSe nanocrystals (quantum dots) in a ZnSe matrix are proposed. These composites should possess pronounced luminescence properties characteristic of the imbedded quantum dots. The objective of the research is to develop an OMCVD related technique for synthesis of thin composite films and explore their structure and photoluminescence properties.

(5) Synthesis of CdSe/ZnSe composites with passivated CdSe quantum dots. Electronic and chemical passivation of the CdSe surface is necessary for preserving the pronounced luminescence of quantum dots upon incorporation into ZnSe matrices. The goal of the research is to develop a solution procedure for passivation of CdSe nanocrystals with a thin overlayer of ZnSe and use the passivated particles for synthesis of CdSe/ZnSe composite films.

1.2. Literature Review

The purpose of this section is to provide a concise overview of the current development in the areas of the thesis research. The emphasis is placed mainly on new studies not yet reviewed in the literature. Recent reviews are referred to for more general information.

1.2.1. OMCVD of Wide Band Gap II-VI Semiconductors

Organometallic chemical vapor deposition (OMCVD), sometimes also called organometallic vapor phase epitaxy (OMVPE), is a fundamental thin film deposition technique relying on synthesis of materials by chemical conversion of organometallic precursors on a heated substrate in a flow system (OMCVD reactor) [11]. Atomic layer epitaxy (ALE), a variant of

OMCVD using modulated fluxes of precursors, is the major method for fabrication of thin phosphor films for TFEDs [12]. OMCVD has been recognized for long time as promising technique for deposition of II-VI diode structures due to its potential for low temperature growth, high throughput and excellent control of films thickness and uniformity. However, the progress in OMCVD synthesis of epitaxial II-VI materials is much slower than the progress in synthesis by molecular beam epitaxy (MBE). For example, while MBE allows construction of blue ZnSe LDs emitting at room temperature, OMCVD has not produced high conductivity p-type layers of ZnSe and its alloys. This slow progress of OMCVD technology is caused by several factors:

(a) OMCVD involves both gas-phase and surface reactions of organometallic precursors in a carrier gas ambient. Thus, the deposition chemistry is much more complex in OMCVD than in MBE where the synthesis is carried out under ultra high vacuum using elemental sources. The reactions of organometallic precursors may affect the film quality by impurity incorporation, resulting in unwanted doping, dopant compensation or deterioration of film crystallinity. The gas-phase reactions of group IIb and VIa precursors under growth conditions have only been explored to a limited extend and mechanistic details of the surface reactions remain largely unknown.

(b) OMCVD of II-VI semiconductors is complicated by gas-phase pre-reactions between the organometallic sources, deteriorating surface morphology and film thickness uniformity. These pre-reactions have to be eliminated to grow device quality materials. One solution to the problem is deposition under very low pressure where only surface reactions contribute to the precursor conversion. However, the low pressure conditions lead to low growth rates and, consequently, reduce reactor throughput.

(c) The presence of organometallic precursors and their decomposition products in the gas-phase complicates doping. For example, nitrogen doping with RF plasma, the technique used in MBE synthesis of p-ZnSe:N [13], results in cracking of the precursors and contamination of the films with carbon and hydrogen [14]. In addition, the lifetime of the plasma generated nitrogen atoms is significantly reduced by these unwanted reactions.

Separation of the doping and growth processes have been proposed to circumvent these difficulties [15]. However, the feasibility of this approach has yet to be demonstrated.

(d) The purity of the organometallic precursors is still much lower than the purity of the elemental sources used in MBE. The contaminants in the precursors used in exploratory experiments are usually unidentified, often obscuring interpretation of the growth results. However, a fast progress in development of purification schemes for organometallic precursors is being made and commercial sources with impurity levels below 1 ppm are available [16].

(e) Synthesis of ternary and quaternary alloys, *e.g.*, ZnS_xSe_{1-x} , $Zn_xCd_{1-x}Se$, $Zn_xMg_{1-y}S_xSe_{1-y}$, which are required for the current device structures, is more difficult in OMCVD than in MBE. The variations in reactivity of different organometallic precursors under growth conditions typically result in highly non-linear relationships between the vapor-phase composition and film stoichiometry [17].

(f) OMCVD suffers from a lack of simple *in-situ* diagnostic techniques which would provide for monitoring of the growth on an atomic scale. By contrast, the environment of MBE allows *in-situ* monitoring of the growth by well established ultrahigh vacuum techniques, such as reflection high energy electron diffraction (RHEED) and Auger electron spectroscopy (AES).

1.2.2. OMCVD Precursors for ZnSe and ZnTe

Control of the OMCVD process requires a detailed understanding of the chemical reactions underlying growth and doping. The mechanistic insight has to involve not only the major conversion reactions of the precursors but also the side-reactions as these often contribute to impurity incorporation. It is important to keep in mind that the deposition and doping reactions are inherently coupled with the transport processes in the reactor [11]. A remarkable progress in understanding of OMCVD reaction mechanisms has been made recently [16,18]. On the basis of these results it is possible to design new precursors which allow synthesis of II-VI materials with better electronic

and optical properties. The following paragraphs review some of these accomplishments and point to areas where additional progress is needed.

Zinc Precursors

Dialkylzinc compounds, *e.g.*, dimethylzinc (DMZn) [19] and diethylzinc (DEZn) [20] are traditionally used for OMCVD of ZnSe and $\text{ZnS}_x\text{Se}_{1-x}$. The combination of DMZn and H_2Se allows growth of ZnSe layers with good electrical and optical properties; however, severe gas-phase pre-reaction between the precursors results in poor surface morphology and film uniformity [21]. Wright *et al.* found that addition of a Lewis base, such as pyridine and trialkylamines, to the precursors at the reactor inlet can effectively inhibit the parasitic reaction [22].

A significant improvement in control of the deposition process was obtained using the adduct DMZnNEt_3 as the zinc precursor [23]. Reproducible growth of ZnSe with high carrier mobility and excellent optical properties was reported. Similar results were obtained using adduct of DMZn with 1,3,5-trimethylhexahydro-1,3,5-triazine (tri), DMZn(tri)_2 for growth of ZnS, ZnSe and ZnS/ZnSe quantum wells. Recently Huh *et al.* found that the use of DMZnNEt_3 is particularly effective at low growth temperatures ($<300\text{ }^\circ\text{C}$) and low reactor pressures ($<30\text{ Torr}$) [24]. This result suggests a large contribution of surface reactions in the growth mechanism.

The mechanism of the gas-phase pre-reaction and its inhibition with Lewis bases are not fully understood. Originally it was believed that the reactivity of dialkyl zinc precursors is reduced by formation of stable adducts with bases [23]. However, a recent spectroscopic study revealed that the adducts, such as DMZnNEt_3 , are almost completely dissociated in the gas-phase already at room temperature [25]. Wright *et al.* proposed an alternative mechanism in which Lewis base stabilizes electrophilic radicals, such as RZn^\bullet , formed by reaction of H_2S or H_2Se with the dialkylzinc precursors [26].

This stabilization is expected to inhibit the radical chain reactions between the reagents.

O'Brien pointed that such radical mechanism cannot account for the fast pre-reaction between the sources at room temperature [18]. He proposed that the parasitic reaction may be attributed to Lewis base-acid reaction between H_2Se and DMZn , followed by elimination of methane and subsequent oligomerization of the intermediate to ZnSe clusters. The presence of Lewis base with a high affinity to the coordination unsaturated Zn atoms should stabilize such intermediates and prevent particle growth. Such a mechanism would be consistent with inhibition of the growth of II-VI semiconductor nuclei in solution in the presence of Lewis bases, such as pyridine derivatives, trialkylphosphine and trialkylphosphine oxides [27]. Mechanistic details of the precursor conversion, however, remain obscured.

Interestingly, the adduct approach was also tested with R_2ZnSeR_2 ($\text{R}=\text{methyl}$ or ethyl) [28]. However growth experiments showed that the selenium bases are not capable of effective inhibition of the pre-reaction of the zinc precursors with H_2Se . This result was explained by a lower affinity of selenium dialkyls (soft bases) to R_2Zn compounds (hard acids).

Alternative Selenium Precursors

Although H_2Se , in combination with DMZn [21] or DMZnNEt_3 [23,24], allows synthesis of ZnSe layers with good electrical and optical properties there are several limitations of this source:

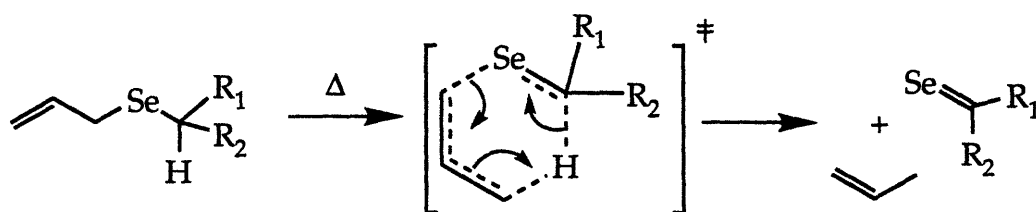
(a) Severe pre-reactions between the sources. The use of the adduct precursor or addition of nitrogen bases directly into the reactor do not entirely eliminate the pre-reaction of the precursors and the surface of the films is still too rough for construction of LED and LD structures. The pre-reaction also results in wall deposits and particle formation, which complicates process reproducibility and reactor maintenance

(b) High toxicity in combination with high vapor pressure. The lethal dose of H₂Se is extremely low (LD₅₀ = 50 ppb), comparable to the lethal doses of phosphine, arsine or phosgene.

(c) Possibility of hydrogen incorporation. Formation of N-H complexes was recently identified as the passivation mechanism for p-type doping of ZnSe in OMCVD [29]. Therefore, growth systems without chemical species containing active hydrogen are desired for development of the OMCVD process for p-ZnSe:N.

Selenium dialkyls, such as Me₂Se [30], Et₂Se [31] and selenophene [33], were tested in OMCVD as the replacement for H₂Se. Even though the gas-phase pre-reaction with zinc dialkyls could be eliminated and the films displayed good surface morphologies, the application of these precursors required high deposition temperatures, typically above 450-550 °C. The layers deposited at such high temperatures are usually highly resistive due to impurity incorporation and formation of structural defects [31b].

Allylselenium compounds, specifically methyl(allyl)selenium (MASE) and diallylselenium (DASE), attracted much attention as promising precursors for low temperature OMCVD of ZnSe [33]. This expectation was based on the low enthalpy of the Se-C(allyl) bond due to the formation of resonance stabilized allyl radical upon homolysis. Even though the allylselenium precursors allowed deposition of ZnSe at low temperatures (below 450 °C), the films were heavily contaminated with carbon (10²⁰-10²¹ atoms/cm³). A gas-phase pyrolysis study [34] revealed that allylselenium compounds decompose not only by the radical mechanism but also intramolecular retro-ene rearrangement reaction:



The intermediate selenoaldehydes are the suspected carbon contaminated species. However, we showed that epitaxial ZnSe films with a negligible carbon contamination can be grown from 2-methylpropaneselenal at low temperatures (350°C) [35]. Thus, the molecular structure of the selenoaldehyde and growth conditions may determine the composition and properties of the layers.

Compounds with *tert*-butylselenium moiety represent another class of selenium precursors for low temperature OMCVD. The temperature decomposition of these compounds is facilitated by both homolysis of the weak Se-C(*tert*-butyl) bond and β -hydrogen elimination. Promising growth results were obtained with di-*tert*-butylselenium (DtBSe) in combination with DEZn [36]. The precursor allowed growth of high optoelectronic quality ZnSe at temperatures as low as 315 °C. The decomposition mechanism of the precursor under the growth conditions is not known, although preliminary mass spectroscopy experiments suggested a significant contribution of β -hydrogen elimination to the overall conversion of the precursor [36c]. Recent reports showed that *tert*-butylselenol (tBSeH) allows growth of high quality ZnSe and ZnS_xSe_{1-x} layers at 280-350 °C without any severe pre-reactions with dialkylzinc precursors [37]. However, the stability of selenols is very low, which complicates their manipulation and storage.

Tellurium Precursors for ZnTe

Several dialkyltellurium precursors have been explored for OMCVD synthesis of ZnTe. OMCVD with dimethyltellurium (DMTe) and diethyltellurium (DETe) required relatively high substrate temperatures (typically above 450 °C) [38]. Much lower deposition temperatures (<300°C) were reported for OMCVD with di-*iso*-propyltellurium (DiPTe) in combination with DEZn [39] or DMZnNEt₃ [40]. Other dialkyltellurium precursors with potential for low temperature deposition of ZnTe are available, including di-*tert*-butyltellurium (DtBTe), methyl(allyl)tellurium (MATE) and diallyltellurium (DATE). These compounds have been explored

mainly for low temperature deposition of narrow band gap II-VI materials, such as CdTe, HgTe and $\text{Cd}_x\text{Hg}_{1-x}\text{Te}$ [41]. However, some of these precursors suffer from low volatility (DtBTe and DATe) and uncompleted conversion due to the formation of stable tellurium by-products (MATE) [42].

The decreasing thermal stability of the compounds $\text{DMTe} > \text{DETe} > \text{DiPte} > \text{DtBTe}$ is consistent with decomposition *via* homolysis of Te-C bonds or β -hydrogen elimination [43]. Gas-phase pyrolysis study of symmetrical and unsymmetrical dialkyltellurium compounds pointed to homolysis as the major decomposition pathway, although compounds with reactive β -hydrogen atoms (*e.g.*, DtBTe) also decompose by β -hydrogen elimination [44]. A detailed pyrolysis study with deuterium-labeled DiPte provided unequivocal evidence that the precursor decomposes under the growth conditions entirely by homolysis of the Te-C bond [45]. However, the distribution of the reaction products as well as their labeling pattern indicate that the formed radicals are surface bound. Pyrolysis studies on allyltellurium compounds also provided strong evidence for homolysis of the Te-C(allyl) bond followed by radical recombination reactions [42]. The retro-ene decomposition pathway is negligible for MATE and DATe.

1.2.3. Semiconductor Quantum Dot Composites

Semiconductor nanocrystals (quantum dots) display unusual optical and electronic properties due to three dimensional confinement of the carriers [46]. The electronic band structure of these particles composes of nearly discrete, molecular-like states with the HOMO-LUMO separation larger than the corresponding band-gap of the bulk. Nanocrystals with electronically passivated surface show intense band-edge luminescence at room temperature.

The pronounced photoluminescence properties of nanocrystals are of interest for light emitting applications. In principle, new highly efficient phosphor materials with adjustable emission wavelength could be prepared

from nanocrystals of selected size. Whether the band-edge luminescence can be efficiently excited by the effect of electric field or by electron impact has yet to be demonstrated. A novel route to high efficient phosphors might be doping of nanocrystals with transition metals or rare earth elements. For example, ZnS nanocrystals doped Mn display a dramatic dependence of photoluminescence quantum yield on the particle size, increasing from <1% for 7.0 nm nanocrystals to ~ 20% for 3.5 nm particles [47]. At the same time the emission lifetime becomes very short (<300 ps), indicating an effective energy transfer from the excited states of the nanocrystals to the d-electron center.

Materials incorporating semiconductor quantum dots in epitaxial semiconductor matrices have attracted much attention due to the potential to construct new quantum effect devices [48]. A variety of techniques, including ultra-high resolution photolithography in combination with ion etching [48a] and selective area OMCVD growth [49], is being explored for fabrication of quantum dot structures. Composites incorporating semiconductor nanocrystals in wide band-gap polycrystalline or amorphous semiconductor matrices are an attractive alternative to the epitaxial quantum dot materials. These materials can be used applications where the epitaxial structure is not required, specifically, as phosphors in light emitting devices.

In principle semiconductor quantum dot composites can be prepared by co-deposition of nanocrystals and matrix using the CVD or OMCVD process. Techniques for gas-phase formation of semiconductor nanoparticles are available, including gas-phase pyrolysis [50], laser ablation [51] and exploding wire method [52]. Liu *et al.* reported on plasma enhanced chemical vapor deposition (PECVD) synthesis of composite films incorporating Si nanocrystals in an amorphous Si matrix (a-Si:H) [53]. The technique relied on formation of Si nanocrystals in a highly diluted SiH₄/H₂ mixture under PECVD conditions. In an alternative approach semiconductor quantum dot composites can be prepared by three dimensional nucleation of the dot material on an appropriate substrate under OMCVD or MBE conditions. So far this technique has been explored only with III-V compound

semiconductors, such as InAs or InGaAs (dot material) and GaAs (substrate) [54].

The techniques for *in situ* formation of nanoparticles, however, suffer from several limitations:

(a) Broad distribution of particles. The growth of particles is often diffusion controlled, resulting in broad distributions of sizes and shapes. Agglomeration and coalescence of the particles further contribute to this broadening.

(b) Poor crystallinity and stoichiometry. The particles formed under the highly non-equilibrium conditions show a large number of structural defect. The control of stoichiometry of compound semiconductor particles is difficult.

(c) These effects lead to a severe heterogeneous broadening of spectral bandwidths and poor luminescence of the materials.

1.2.4. Electronic passivation of Quantum Dots with a Wide Band Gap Overlayer

Electronic passivation of the nanocrystal surface is essential for preparation of materials with band edge emission and a high luminescence quantum yield [46]. The purpose of the passivation is to remove the deep electronic traps associated with the dangling bonds on the particle surface. Electronic passivation of II-VI semiconductor nanocrystals can be easily obtained in solution by coordination of ligands on the nanocrystal surface [27]. Theoretically, effective passivation of the surface states can be also accomplished by capping semiconductor nanocrystals with an overlayer of wide band gap material. In such a system (with large band off-sets) the first excited state should be localized in the core of the passivated particle and the luminescence should be characteristic of the initial quantum dot.

Spanhel *et al.* showed that a layer of $\text{Cd}(\text{OH})_2$ precipitated on CdS nanocrystals can provide for electronic passivation [55]. These "activated"

nanocrystals displayed a strong near band edge luminescence. Even though the quantum yield for room temperature photoluminescence of these "activated" particles was very high (~50 %), it deteriorated at pH<9, indicating a low stability of the passivating layer. More recently Kortan *et al.* described a solution procedure for passivation of CdSe nanocrystals with an overlayer of ZnS [56]. This surface derivatization dramatically enhanced band edge emission of the CdSe core despite the poor crystallinity of the ZnS shell as concluded on the basis of x-ray diffraction and transmission electron microscopy (TEM) studies. The same solution technique was used for re-growth of ZnSe on CdSe nanocrystals and the core-shell structure of the particles was demonstrated by x-ray photoelectron and Auger spectroscopies. Unfortunately no luminescence properties of these layered particles were reported to confirm the passivation effect.

Recently, Hasselbarth *et al.* attempted to passivate β -HgS nanoparticles with CdS [57]. Although they observed an enhancement of the photoluminescence from the core of the overcoated particles, the emission spectrum remained broad, probably due to a wide size distribution of the initial HgS nanocrystals. The core-shell structure of the composite particles was probed by TEM and photoluminescence quenching experiments with methylviologene.

A rather different approach to electronic passivation of semiconductor nanocrystals was described for Si [58]. Silicon nanocrystals, prepared by gas-phase pyrolysis of disilane in helium, were oxidized in gas-phase to form a 1.2 nm SiO₂ shell. The shell provided an effective electronic passivation of the Si surface and the particles display an intense room temperature photoluminescence (quantum yield of 5%).

Previous studies suggest that the concept of electronic passivation of nanocrystals with wide band gap semiconductor or insulator is feasible provided a high quality interface between the materials can be formed. In the case of crystalline interface, a close lattice match between the phases is desired.

1.3. Thesis Outline

The results of the thesis research are described in the following chapters. Chapter 2 presents results of MOCVD growth experiments with *tert*-butyl(trifluoromethyl)tellurium (tBTeCF₃) and bis(trifluoromethyl)tellurium [(CF₃)₂Te] in combination with dimethylzinc (DMZn). A microbalance OMCVD system was used to explore rates of ZnTe growth at various operation conditions, including substrate temperature and the molar ratio of the precursors. Contamination of ZnTe films with ZnF₂ crystallites was observed with tBTeCF₃ at low deposition temperatures (<400 °C). Gas-phase pyrolysis of tBTeCF₃ was probed under the growth conditions using molecular beam mass spectrometric system to gain an insight into the mechanism of the fluorine contamination.

Chapter 3 describes OMCVD growth of ZnSe using *tert*-butyl(allyl)selenium (tBASE). The growth results confirm feasibility of the precursor for low temperature growth of good optoelectronic quality ZnSe. A gas-phase pyrolysis study with tBASE revealed formation of selenium by-products, such as diallylselenium (DASE) and methylallylselenium (MASE), under the growth conditions. A mechanism of the gas-phase decomposition of the precursor is proposed.

Chapter 4 is devoted to OMCVD synthesis of ZnSe from tripropylphosphine selenide (TPPSe) and dimethyl(butyl)phosphine selenide (DMBPSe) in combination with DMZn. Growth experiments and materials characterization, using SIMS and photoluminescence spectroscopy, indicate that this new precursor chemistry is feasible for growth of hydrogen free ZnSe layers.

Chapter 5 describes electrospray OMCVD, a novel technique for synthesis of quantum dot composites incorporating CdSe nanocrystals in ZnSe matrices. In this technique, nearly monodisperse CdSe nanocrystals prepared by a solution method are dispersed in organic solvents and atomized at the inlet of an OMCVD reactor using electrospray. The nanocrystals are

transferred into the gas-phase and co-deposited with a matrix synthesized by OMCVD. The properties of the new composite films were probed by transmission electron microscopy (TEM), Auger electron spectroscopy (AES) and photoluminescence spectroscopy.

Chapter 6 is focused on electronic passivation of CdSe nanocrystals with an overlayer of ZnSe. A new solution procedure utilizing trioctylphosphine selenide and diethylzinc (DEZn) as the ZnSe precursors is described. Results of structural and optical characterization of the overcoated CdSe/ZnSe particles are presented. The passivated particles were used for synthesis of CdSe/ZnSe composites using electrospray OMCVD. The composite films with the passivated nanocrystals displayed a remarkable enhancement of the photoluminescence yield. The conclusions from the thesis research are summarized in Chapter 7.

References:

- [1] Landolt-Börnstein. *Numerical Data and Functional Relationships in Science and Technology* (K.-H. Hellwege, Ed.) Group III, Vol. 17. Springer, 1982.
- [2] (a) Castellano, J. A. *Handbook of Display Technology* Academic Press, Inc., 1992. (b) Sherr, S. *Electronic Displays*, John Wiley&Sons, Inc., 1993.
- [3] Mach, R. *Thin Film Electroluminescence Devices*. in *Solid State Luminescence - Theory, Materials and Devices* (A. H. Kitai, Ed.) Chapman&Hall, 1993.pp. 229-262.
- [4] Kobayashi, H. Proc. 6th Int. Workshop on Electroluminescence, El Paso, 1992, pp. 179.
- [5] (a) Ishibashi, A.; Yoshifumi, M. *J. Cryst. Growth* **1994**, *138*, 677. (b) Ren, J.; Lansari, Y.; Yu, Z.; Cook, J. W.; Schetzina, J. F. *J. Electron. Mater.* **1993**, *22*, 973. (c) Ren, J.; Eason, D. B.; Churchill, L. E.; Yu, Z.; Boney, C.; Cook, Jr.; J. W.; Schetzina, J. F.; El-Masry, N. A. *J. Cryst. Growth* **1994**, *138*, 455. (d) Matsuoka, T.; Ohki, A.; Ohno, T.; Kawaguchi, Y. *J. Cryst. Growth* **1994**, *138*, 727.
- [6] (a) Okuyama, H.; Miyajima, T.; Morinaga, Y.; Hiei, F.; Ozawa, M.; Akimoto, K. *J. Electron. Lett.* **1992**, *28*, 19. (b) Grillo, D. C.; Fan, Y.; Han.; He, L. Gunshor, R. L.; Salokatve, A.; Hagerott, M.; Jeon, H.; Nurmikko, A. V.; Hua, G. C.; Otsuka, N. *Appl. Phys. Lett.* **1993**, *63*, 2723.
- [7] (a) Guha, S.; DePuydt, J. M.; Qiu, J.; Hofler, G. E.; Haase, M. A.; Wu, B. J.; Cheng, H. *Appl. Phys. Lett.* **1993**, *63*, 3023. (b) Guha, S.; DePuydt, J. M.; Haase, M. A.; Qiu, J.; Cheng, H. *Appl. Phys. Lett.* **1993**, *63*, 3107. (c) Guha, S.; Cheng, H.; Haase, M. A.; DePuydt, J. M.; Qiu, J.; Wu, B. J.; Hofler, G. E. *Appl. Phys. Lett.* **1994**, *65*, 801.
- [8] Nakayama, N.; Itoh, S.; Okuyama, H.; Ozawa, M.; Ohata, T.; Nakano, K.; Ikeda, M.; Ishibashi, A.; Mori, Y. *Electron. Lett.* , **1993**, *29*, 2194.
- [9] Yokogawa, T.; Narusawa, T. *Appl. Phys. Lett.* **1992**, *61*, 291.
- [10] Gordon, D. C.; Kirss, R. U.; Brown, D. W. *Organometallics* **1992**, *11*, 2947.
- [11] (a) Kuech, T. F.; Jensen, K. F. *OMVPE of Compound Semiconductors*. in *Thin Film Processes II*, (J. L. Vossen and W. Kern, Eds.) Ch. III-2.

- Academic Press, Inc., 1991. pp. 369-442. (b) Stringfellow, G. B. *Organometallic Vapor Phase Epitaxy*. Academic Press, Inc., 1989.
- [12] Sanders, B. W.; *Atomic Layer Epitaxy of Phosphor Thin Films*, in *Solid State Luminescence - Theory, Materials and Devices*. (A. H. Kitai, Ed.) Chapman&Hall, 1993. pp. 293-312.
- [13] Park, R. M.; Troffer, M. B.; Rouleau, C. M.; DePuydt, J. M.; Haase, M. A. *Appl. Phys. Lett.* **1990**, *57*, 2127.
- [14] Taudt, W.; Schneider, A.; Heuken, M.; Fricke, Ch.; Hoffman, A. J. *Cryst. Growth* **1994**, *138*, 418.
- [15] Heuken, M. J. *Cryst. Growth* - in press.
- [16] Jones, A. C. *J. Cryst. Growth* **1993**, *129*, 728.
- [17] (a) Yamaga, S.; Yoshikawa, A.; Kasai, H. *J. Cryst. Growth* **1990**, *99*, 432. (b) Wright, P. J.; Cockayne, B. *J. Cryst. Growth* **1982**, *59*, 148.
- [18] O'Brien, P. *Chemtronics*, **1991**, *5*, 61.
- [19] Wright, P. J.; Cockayne, B. *J. Cryst. Growth* **1982**, *59*, 148.
- [20] Blanconnier, P.; Cerdet, M.; Henoc, P.; Jean-Louis, A. M. *Thin Solid Films* **1978**, *55*, 375.
- [21] Giapis, K. P.; Lu, D. C.; Jensen, K. F. *Appl. Phys. Lett.* **1989**, *54*, 353.
- [22] Wright, P. J.; Parbrook, P. J.; Cockayne, B.; Jones, A. C.; Orrell, E. D.; O'Donnell, K. P.; Henderson, B. *J. Cryst. Growth* **1989**, *94*, 441.
- [23] (a) Wright, P. J.; Cockayne, B.; Parbrook, P. J.; Jones, A. C.; O'Brien, P.; Walsh, J. *J. Cryst. Growth* **1990**, *104*, 601. (b) Jones, A. C.; Wright, P. J.; Cockayne, B. *J. Cryst. Growth* **1991**, *107*, 297.
- [24] Huh, J.-S.; Parnaik, S.; Jensen, K. F. *J. Electron. Mater.* **1993**, *22*, 509.
- [25] Khan, O. F. Z.; O'Brien, P.; Hamilton, P. A.; Walsh, J. R.; Jones, A. C. *Chemtronics* **1989**, *4*, 224.
- [26] Wright, P. J.; Cockayne, B.; Parbrook, P. J.; Oliver, P. E.; Jones, A. C. *J. Cryst. Growth* **1991**, *108*, 525.
- [27] Murray, C. B.; Norris, D. J.; Bawendi, M. G. *J. Amer. Chem. Soc.* **1993**, *115*, 8706.
- [28] Mitsuhashi, H.; Mitsuishi, I.; Kukimoto, H. *J. Cryst. Growth* **1986**, *77*, 219.
- [29] (a) Wolk, J. A.; Ager III, J. W.; Duxstad, K. J.; Haller, E. E.; Taskar, N. R.; Dorman, D. R.; Olego, D. J. *Appl. Phys. Lett.* **1993**, *63*, 2756. (b) Kamata, A.; Mitsuhashi, H.; Fujita, H. *Appl. Phys. Lett.*, **1993**, *63*, 3353.

- [30] Mitsuhashi, H.; Mitsuishi, I, Kukimoto, H. *Jpn. J. Appl. Phys.* **1985**, *24*, 1864.
- [31] (a) Srithoran S.; Jones, K. *J. Cryst. Growth* **1984**, *66*, 231. (b) Giapis, K. P.; Jensen, K. F. *J. Cryst. Growth* **1990**, *101*, 111.
- [32] Wright, P. J.; Griffiths, R. J. M.; Cockayne, B. *J. Cryst. Growth* **1984**, *66*, 26.
- [33] (a) Giapis, K. P.; Jensen, K. F.; Potts, J. E.; Pachuta, S. J. *J. Electron. Mater.* **1990**, *19*, 453. (b) Patnaik, S.; Jensen, K. F.; Giapis, K. P. *J. Cryst. Growth* **1991**, *107*, 390.
- [34] Patnaik, S.; Ho, K-L.; Jensen, K. F.; Gordon, D. C.; Kirss, R. U.; Brown, D. W. *Chem. Mater.* **1993**, *5*, 305.
- [35] Danek, M.; Huh, J.-S.; Jensen, K. F.; Gordon, D. C.; Kosar, W. P. *Mat. Res. Soc. Symp. Proc. Vol. 334*. **1994**, 231.
- [36] (a) Kuhn, W.; Naumov, A.; Stanzl, H.; Bauer, S.; Wolf, K.; Wagner, H. P.; Gebhardt, W.; Pohl, U. W.; Krost, A.; Richter, W.; Dumichen, U.; Thiele, K. H. *J. Cryst. Growth* **1992**, *123*, 605. (b) Stanzl, H.; Wolf, K.; Bauer, S.; Kuhn, W. Naumov, A. *J. Electron. Mater.* **1993**, *22*, 501. (c) Kuhn, W.; Driad, R.; Stanzl, H.; Lussion, A.; Wolf, K.; Qu'Hen, B.; Sahin, H.; Svob, L.; Grattepain, C.; Quesada, X.; Gebhardt, W.; Gorochoy, O. *J. Cryst. Growth* **1994**, *138*, 448.
- [37] (a) Nishimura, K.; Nagao, Y.; Sakai, K. *Jpn. J. Appl. Phys.* **1993**, *32*, L428. (b) Nishimura, K.; Nagao, Y.; Sakai, K. *J. Cryst. Growth* **1993**, *134*, 293.
- [38] (a) Wilson, B. A.; Bonner, C. E.; Feldman, R. D.; Austin, R. F.; Kisker, D. W.; Krajewski, J.; Bridenbaugh, J. *J. Appl. Phys.* **1988**, *64*, 3210. (b) Ogawa, H.; Nishio, M.; *J. Appl. Phys.* **1988**, *64*, 6750. (c) Ekawa, M.; Kawakami, Y.; Taguchi, T.; Hiraki, A. *J. Cryst. Growth* **1988**, *93*, 115.
- [39] (a) Mullins, J. T.; Clifton, P. A.; Brown, P. D.; Brinkman, A. W.; Woods, J. *J. Cryst. Growth* **1990**, *101*, 100. (b) Wagner, H. P.; Kuhn, W.; Gebhardt, W. *J. Cryst. Growth* **1990**, *101*, 199. (c) Kuhn, W.; Wagner, H. P.; Stanzl, H.; Wolf, K.; Worle, K.; Lankes, S.; Betz, J.; Wortz, M.; Lichtenberger, D.; Leiderer, H.; Gebhardt, W. *Semicond. Sci. Technol.* **1991**, *6 A*, 105.
- [40] Cloitre, T.; Briot, N.; Briot, O.; Gil, B.; Aulombard, R. L. *J. Cryst. Growth*, **1993**, *133*, 101.

- [41] (a) Korenstein, R.; Hoke, W. E.; Lemonias, P. J.; Higa, K. T. Harris, D. C. J. *Appl. Phys.* **1987**, *62*, 4929. (b) Lichtman, L. S.; Parsons, J. D.; Cirlin, E. H. J. *Cryst. Growth* **1988**, *86*, 25. (c) McCalister, T. J. *Cryst. Growth* **1989**, *96*, 552.
- [42] (a) Patnaik, S.; Ho, K-L.; Jensen, K. F.; Gordon, D. C.; Kirss, R. U.; Brown, D. W. *Chem. Mater.* **1993**, *5*, 305. (b) Hails, J. E.; Cle-Hamilton, D. J.; Bell, W. J. *Cryst. Growth* - in print
- [43] Irvine, S. J. C.; Mullin, J. B.; Giess, J.; Gough, J. S.; Royle, A.; Crimes, G. J. *Cryst. Growth* **1988**, *93*, 732.
- [44] Kirss, R. U.; Brown, D. W.; Higa, K. T.; Gedridge, Jr., R. W. *Organometallics* **1991**, *10*, 3589.
- [45] Bell, W.; Stevenson, J.; Cole-Hamilton, D. J.; Hails, J. E. *Polyhedron* **1994**, *13*, 1253.
- [46] (a) Brus, L. E. *Appl. Phys. A* **1991**, *53*, 465. (b) Wang, Y.; Herron, N. J. *Phys. Chem.* **1991**, *95*, 525. (c) Bawendi, M. G.; Steigerwald, M. L.; Brus, L. E. *Annu. Rev. Phys. Chem.* **1990**, *41*, 477. (d) Weller, H. *Angew. Chem. Int. Ed. Engl.* **1993**, *32*, 41. (e) Brus, L. E. *J. Phys. Chem.* **1994**, *98*, 3577.
- [47] Bhargava, R. N.; Gallagher, D.; Hong, X.; Nurmikko, A. *Phys. Review Lett.* **1994**, *72*, 416.
- [48] (a) Mertz, J. L.; Petroff, P. M. *Mater. Sci. Eng.* **1991**, *B9*, 275. (b) Nagamune, Y.; Sakaki, H.; Kouwenhoven, L. P.; Mur, L. C.; Harmans, J. P. M.; Motohisa, J.; Noge, H. *Appl. Phys. Lett.* **1994**, *64*, 2379.
- [49] Nagamune, Y.; Tsukamoto, S.; Nishioka, M.; Arakawa, Y. *J. Cryst. Growth* **1993**, *126*, 707.
- [50] Sercel, P. C.; Saunders, W. A.; Atwater, H. A.; Vahala, K. J.; Flagan, R. C. *Appl. Phys. Lett.*, **1992**, *61*, 696.
- [51] Werwa, E.; Seraphin, A. A.; Chiu, L. A.; Zhou, C.; Kolenbrander, K. D. *Appl. Phys. Lett.* **1994**, *64*, 1821.
- [52] Saunders, W. A.; Sercel, P. C.; Atwater, H. A.; Flagan, R. C. *Appl. Phys. Lett.* **1992**, *60*, 950.
- [53] Liu, X.; Wu, X.; Bao, X.; He, Y. *Appl. Phys. Lett.* **1994**, *64*, 220.
- [54] (a) Moison, J. M.; Houzay, F.; Barthe, F.; Leprince, L. Andre, E.; Vatel, O. *Appl. Phys. Lett.* **1994**, *64*, 196. (b) Oshinowo, J. Nishioka, M.; Ishida, S.; Arakawa, Y. *Appl. Phys. Lett.* **1994**, *65*, 1421.

- [55] Spanhel, L.; Haase, M.; Weller, H.; Henglein, A. *J. Amer. Chem. Soc.* **1987**, *109*, 5649.
- [56] Kortan, A. R.; Hull, R.; Opila, R. L.; Bawendi, M. G.; Steigerwald, M. L.; Carroll, P. J.; Brus, L. E. *J. Amer. Chem. Soc.* **1990**, *112*, 1327.
- [57] Hässelbarth, A.; Eychmüller, A.; Eichberger, R.; Giersig, M.; Mews, A.; Weller, H. *J. Phys. Chem.* **1993**, *97*, 5333.
- [58] (a) Littau, K. A.; Szajowski, P. J.; Muller, A. J.; Kortan, A. R.; Brus, L. E. *J. Phys. Chem.* **1993**, *97*, 1224. (b) Wilson, W. L.; Szajowski, P. J.; Brus, L. E. *Science* **1993**, *262*, 1242.

Chapter 2

tert-Butyl(trifluoromethyl)tellurium - a Novel OMCVD source for ZnTe

2.1. Introduction

The combination of a direct band gap of 2.35 eV (at room temperature) and anaturally p-type character make ZnTe a promising material for optoelectronic devices operating in the short wavelength region of the visible spectrum [1]. In order to reduce the density of intrinsic defects, control stoichiometry, and minimize dopant diffusion across heterojunctions, a low deposition temperature of ZnTe films is necessary. ZnTe films have previously been grown by organometallic chemical vapor deposition (OMCVD) using either dimethyl- or diethylzinc and various tellurium organometallic sources [2-5]. The thermal stability and, consequently, the growth temperature obtained with these sources correlate with the stability of the corresponding radicals generated by homolysis of the Te-alkyl bond, and the accessibility of other decomposition pathways such as β -hydrogen elimination. Tellurium-alkyl bond dissociation enthalpy decreases in the order methyl > primary alkyl > secondary alkyl > tertiary alkyl > allyl. Thus, dimethyltellurium (DMTe) and diethyltellurium (DETe) decompose at high temperatures; OMCVD growth of ZnTe films with these sources has been carried out at temperatures typically above 450°C and 410°C, respectively [2]. Diisopropyltellurium (DIPTe) has been used for ZnTe growth at 350°C [3]. Diallyltellurium (DATE), di-*tert*-butyltellurium (DtBTe) and methylallyltellurium (MATE) have made growth of CdTe and Hg_{1-x}Cd_xTe (MCT) possible below 300°C [4]. However, the low decomposition temperature is accompanied by low vapor pressures which reduce the delivery rate of the sources and growth rate of the films [5].

Unsymmetrical alkyl(trifluoromethyl)tellurium compounds, RTeCF₃ (R = *tert*-butyl or benzyl), were recently proposed as new OMCVD precursors [6]. These

sources were designed to achieve a low decomposition temperature, optimal vapor pressure, and to maintain good stability at room temperature. The trifluoromethyl group reduces intermolecular interactions, resulting in a significant increase in the vapor pressure of the sources compared to the other reagents (Table 2.1). Since *tert*-butyl or benzyl groups form stable free radicals, the sources were expected to decompose at a low temperature by Te-R bond homolysis. However, pyrolysis studies in a hot tube showed that the decomposition of the *tert*-butyl derivative was complete at 335°C, while the benzyl derivative required 450°C [6]. This behavior was explained in terms of β -hydrogen elimination as an alternative decomposition pathway for the *tert*-butyl compound.

Table 2.1. Vapor pressure of tellurium OMCVD sources at 20 °C.

source	vapor pressure at 20°C, [Torr]
dimethyltellurium [4]	40.7
diethyltellurium [4]	7.1
diisopropyltellurium [5]	2.6
di- <i>tert</i> -butyltellurium [5]	1.6
diallyltellurium [5]	1.1
methylallyltellurium [5]	4.5
<i>tert</i> -butyl(trifluoromethyl)tellurium	17.8
bis(trifluoromethyl)tellurium	531

Here we present an OMCVD growth study of ZnTe with *tert*-butyl-(trifluoromethyl)tellurium (tBT₃CF₃). Since the composition of films grown with the *tert*-butyl compound suggests a complex reaction mechanism involving C-F bond activation, we also discuss investigations of the pyrolysis of tBT₃CF₃ at growth conditions in a molecular beam mass spectrometer (MBMS) system. In addition, results from growth with bis(trifluoromethyl)tellurium, (CF₃)₂Te,

another high vapor pressure compound (Table I), is included to provide insight into the role of the Te-CF₃ moiety in fluorine contamination of ZnTe.

2.2. Experimental

Materials. *tert*-Butyl(trifluoromethyl)tellurium and bis(trifluoromethyl)tellurium were prepared at Advanced Technology Materials by previously described procedures [6]. Dimethylzinc and ultrahigh purity argon were supplied by Air Products, ultrahigh purity hydrogen and high purity helium by Matheson. 2-methylpropane and 2-methylpropene were obtained from Aldrich and used as received. Zinc doped (100) GaAs wafers were supplied from Crystal Specialties. All the reagents used for wafer preparation were electronic grade.

OMCVD growth. The growth experiments were conducted in a hot wall tubular reactor equipped with a Cahn 2000 microbalance system for monitoring the growth rate *in situ* (Fig. 2.1). (100) GaAs wafers were degreased in boiling 1,1,2-trichloroethylene and acetone. Then the wafers were etched in HCl and in a mixture of sulfuric acid, hydrogen peroxide (30%) and de-ionized water in a volume ratio of 5:1:1. A controlled oxide layer was grown in de-ionized water and etched in HCl. Finally, the wafers were thoroughly rinsed with isopropyl alcohol and immediately loaded into the reactor. Before growth, the wafers were baked in hydrogen flow at 160-170°C for several hours. The delivery rate of (CH₃)₂Zn (DMZn) was 20 μmol/min, while the delivery rate of tBTeCF₃ was varied from 5 to 50 μmol/min. In the growth experiments with (CF₃)₂Te, the delivery rate of the tellurium source was kept at 20 μmol/min. The reactor pressure was maintained at 10 Torr by a Vacuum General pressure regulator (Model 80-2) and the total carrier gas flow rate was 25 standard cubic centimeters per minute (sccm). Several growth rate measurements at varying temperatures and [Te/Zn] ratios were carried out on one sample. The growth rate at one reference point was monitored during every run to detect deterioration of the sample quality. Because of the composition changes in the films at temperatures below 420°C, the high temperature portion of the growth curves was measured first on each sample.

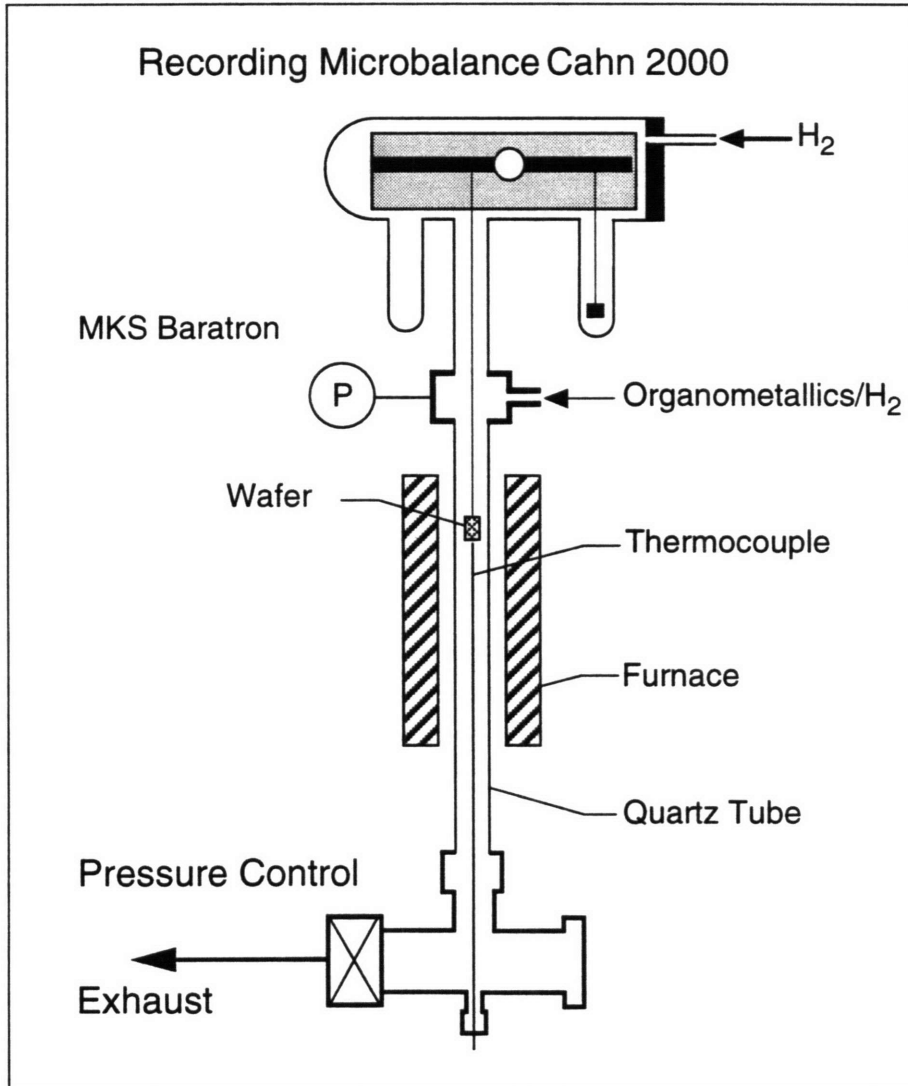


Figure 2.1. Schematic of the microbalance system.

Film characterization. Several samples with film thicknesses ranging from 2 to 20 μm were prepared for characterization. The crystallinity of the films was inspected by x-ray diffraction on a rotating anode Rigaku 300 diffractometer using monochromatized $\text{CuK}\alpha$ radiation. A Perkin-Elmer Auger Scanning Microprobe (Model 660) was used for analysis of the film composition. Surface morphology was observed using a Cambridge scanning electron microscope (Model 250 Mk 3). A secondary ion mass spectrometer (VG Ionex, Ltd., Cs^+ primary beam) was used for estimating the fluorine content in the films grown from *tert*-Bu(CF₃)Te and (CF₃)₂Te.

Pyrolysis of tBT₂CF₃ in the molecular beam mass spectrometer (MBMS) System. The MBMS system is schematically shown in Fig. 2.2 and has been described in detail elsewhere [7]. The tellurium source was pyrolyzed in a hydrogen or helium carrier gas in a stagnant point flow reactor stage. The gas phase in the vicinity of the graphite resistance heater was sampled through a 100 μm orifice in a 25 μm stainless steel foil into a high vacuum stage pumped by a Leybold-Heraeus 450 turbomolecular pump. The expanded molecular beam was extracted by a skimmer into the second stage, differentially pumped with a Leybold-Heraeus 360 turbomolecular pump, and analyzed with a Balzers 311 quadrupole mass spectrometer. In a typical experiment, 20 $\mu\text{mol}/\text{min}$ of tBT₂CF₃ were carried in 25 sccm of hydrogen or helium into the reactor. Reactor pressure was maintained at 30 Torr. In order to correct the spectra for sampling flux at various heater temperatures, 0.4 sccm of argon was flowed with the carrier gas into the reactor. The mass spectra were scaled based upon the Ar^+ signal; the contribution from the fragmentation pattern of the parent was subtracted from the corrected data. In trapping experiments, an approximately tenfold excess of 2-methylpropene was flowed together with tBT₂CF₃ into the MBMS system. The partial pressures for 2-methylpropane and 2-methylpropene were determined from the MBMS intensities at m/z values of 43 and 56, respectively, using authentic compounds.

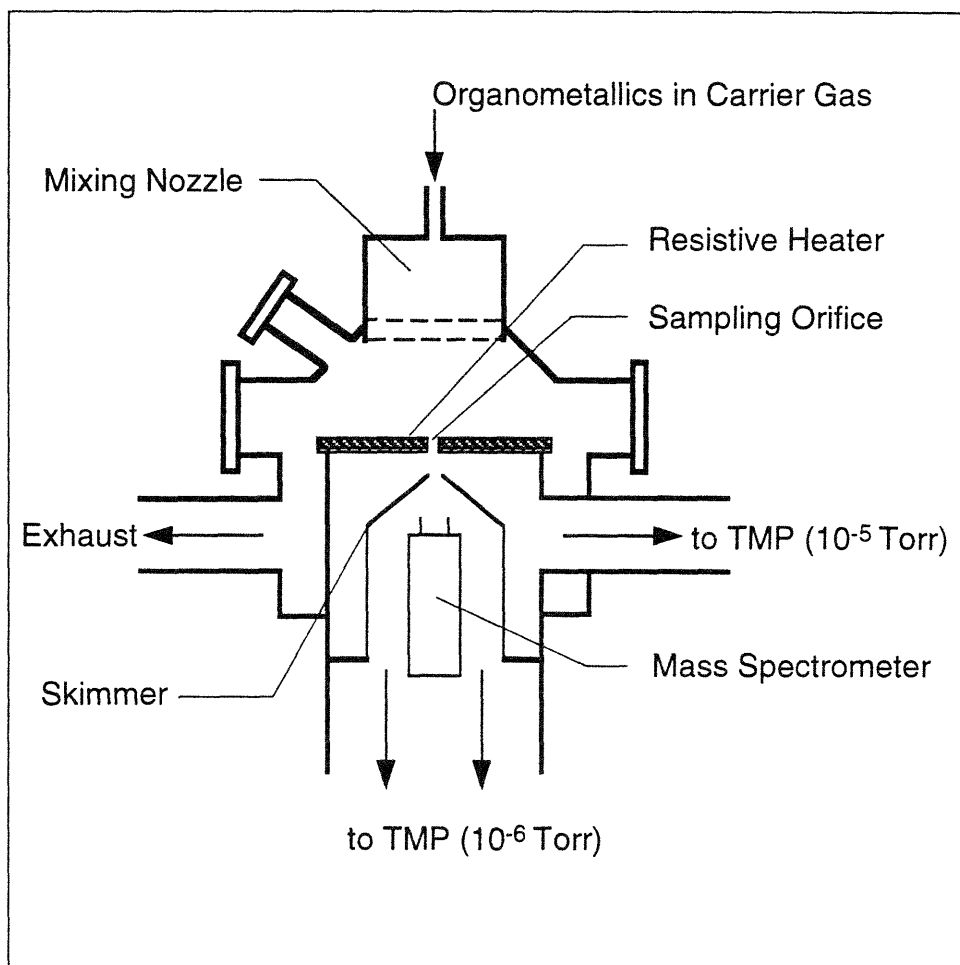


Figure 2.2. Schematic of the molecular beam mass spectrometer (MBMS) system.

2.3. Results and Discussion

2.3.1. Growth and Materials Characterization

OMCVD growth experiments showed that the morphology and composition of the films had a strong dependence on the growth temperature and [Te/Zn] ratio. The SEM micrographs in Fig. 2.3 illustrate the effect of growth temperature. At temperatures above 400°C, the grown layers were relatively smooth with characteristic ridges (Fig. 2.3a). In contrast, the films deposited at 350°C contained surface defects caused by the incorporation of a large number of submicron crystallites (Fig. 2.3b). When the growth temperature was reduced, the crystallites became larger and more scattered (Fig. 2.3c). At constant growth temperature, the crystallite dimensions decreased and the density of the coverage increased with increasing [Te/Zn] ratio. This effect is shown in Fig. 2.4 for growth temperature of 350°C. At high [Te/Zn] ratio, the crystallite size was typically below 1 μm and the coverage was very dense (Fig. 2.4a), while at a ratio of 0.25, the size exceeded 10 μm and the crystallites were scarce (Fig. 2.4b). The layer below the large crystallites (Figs. 2.3c and 2.4b) was smooth and almost featureless.

The Auger electron spectrum of the film grown at 400°C (Fig. 2.5a) contained peaks corresponding to zinc, tellurium, oxygen and carbon. The latter two signals disappeared after short sputtering by Ar^+ , which indicates post-growth contamination when the samples were exposed to air. The content of fluorine in the film was below the detection level of the Auger electron spectrometer (approximately 0.1-0.2 atom. %). Additional analysis of the film grown at 400 °C by SIMS revealed a fluorine content in the range of $\sim 10^{18} - 10^{20}$ atoms/ cm^3 . The fluorine contamination was segregated into islands several micrometers large with a fluorine concentration by one to two orders of magnitude higher than the surrounding film (Fig. 2.6). The tellurium concentration across the film remained nearly constant (not shown).

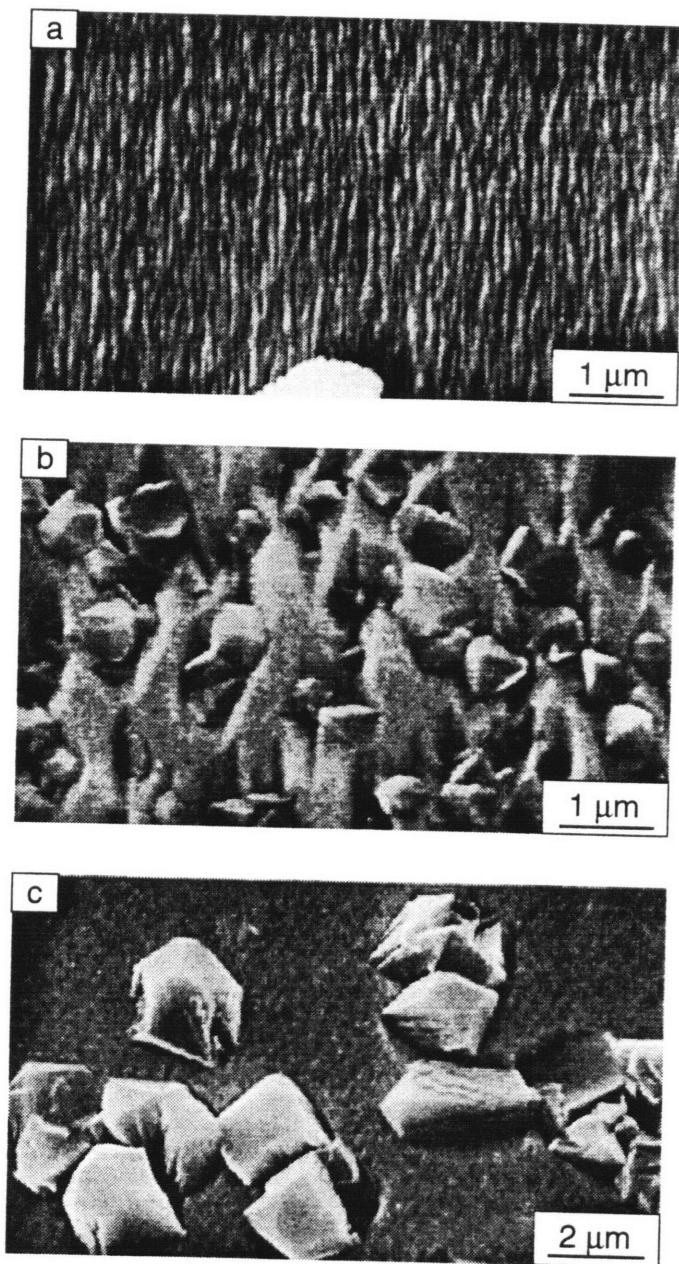


Figure 2.3. SEM micrographs of films grown from $tBTeCF_3$ at various substrate temperatures at $[Te/Zn] = 1.0$. (a) 400°C, (b) 350°C and (c) 300°C.

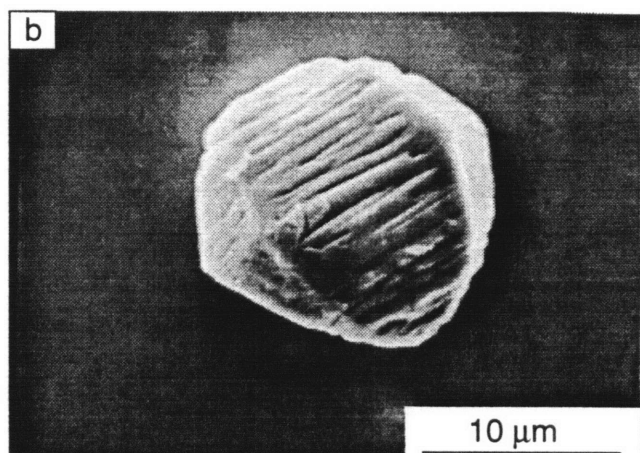
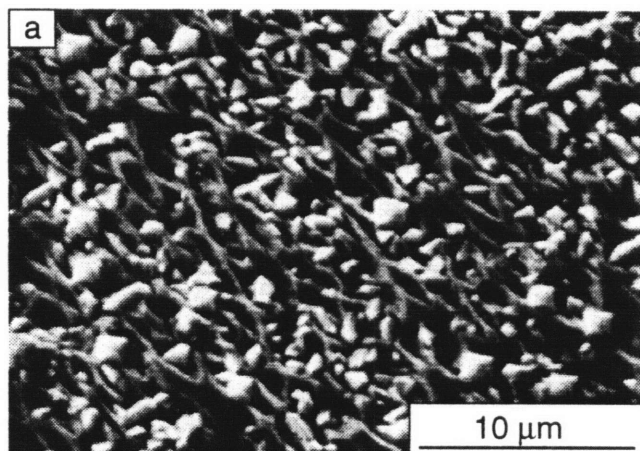


Figure 2.4. SEM micrographs of films grown from $t\text{BTeCF}_3$ at various $[\text{Te}/\text{Zn}]$ ratios at 350°C . (a) 2.5 and (b) 0.25.

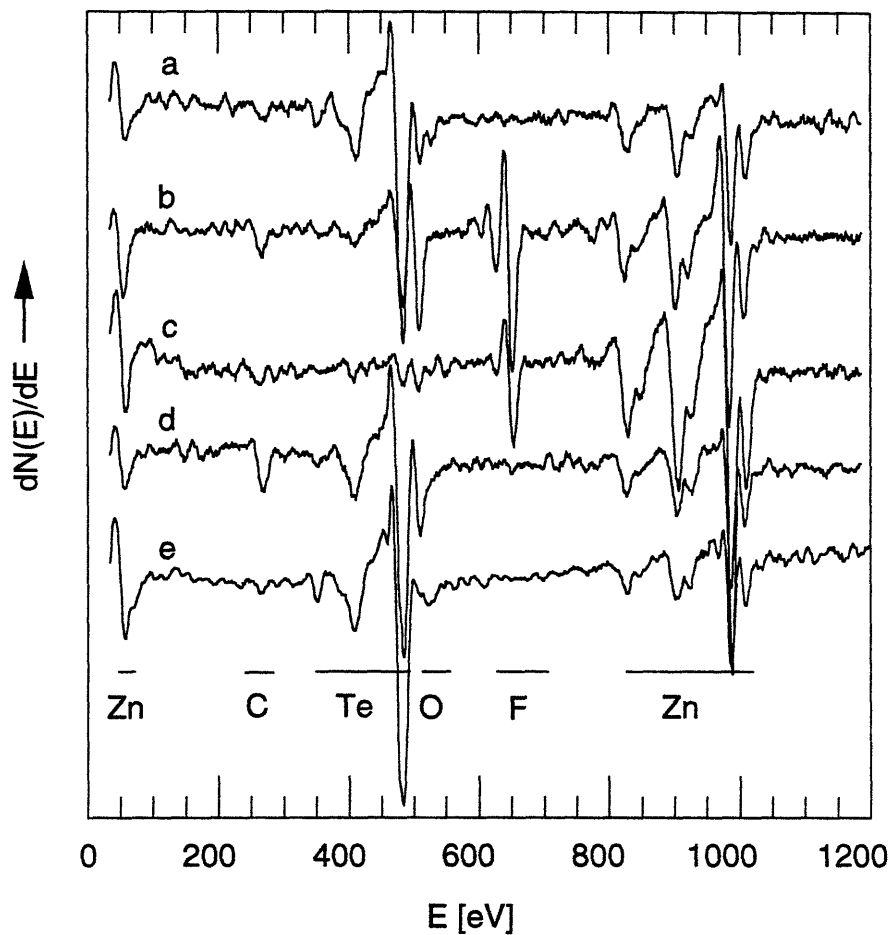


Figure 2.5. Auger electron spectra of films grown at $[\text{Te}/\text{Zn}]=1.0$. (a) film from tBTeCF_3 at 400°C (surface sputtered), (b) film with crystallites from tBTeCF_3 at 350°C , (c) crystallite on film from tBTeCF_3 at 300°C , (d) film between crystallites from tBTeCF_3 at 300°C , and (e) film from $(\text{CF}_3)_2\text{Te}$ at 500°C (surface sputtered).

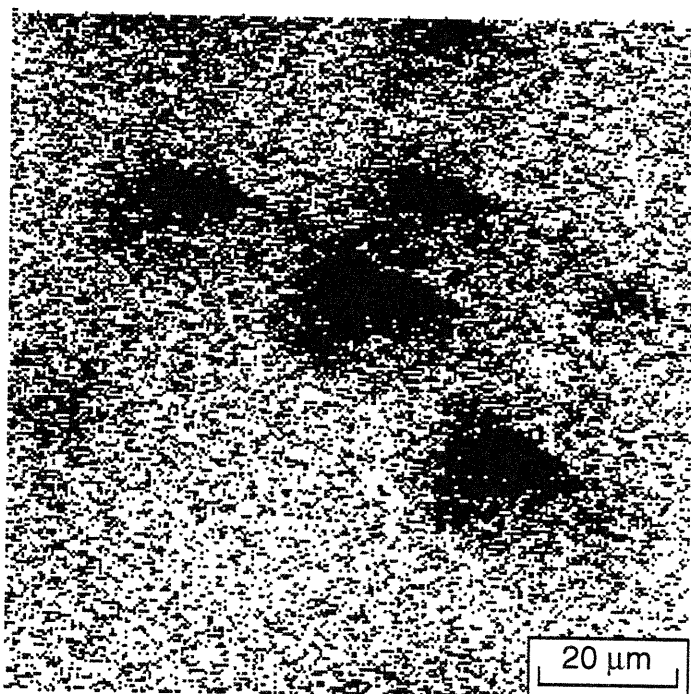


Figure 2.6. SIMS fluorine map of a film grown from $tBTeCF_3$ at $400^\circ C$. Black color indicates an elevated fluorine content.

The film grown at 350°C with a high coverage of crystallites contained zinc, tellurium, and fluorine (Fig. 2.5b). The Auger spectra showed that the dominant constituents of the large crystallites in the films grown below 400°C and at low [Te/Zn] ratio are zinc and fluorine (Fig. 2.5c). The underlying smooth layer consisted of zinc and tellurium without any detectable contamination of fluorine (Fig. 2.5d).

The diffraction patterns from the films grown in the temperature range from 300°C to 400°C at a [Te/Zn] ratio of 1.0 are shown in Fig. 2.7. All of the grown ZnTe layers were highly oriented in the <100> direction. The position of the (400) diffraction corresponds to the bulk lattice parameter indicating that the films have already relaxed [8]. The appearance of the (111) diffraction in the patterns suggests the presence of domains grown in the <111> direction that may have their origin in the large lattice mismatch with the GaAs substrate (7.6% at room temperature) and film contamination. The diffraction pattern of the films grown at 300°C and 350°C (Fig. 2.7b and 2.7c) contained very weak diffraction lines from ZnF₂. The relative intensity of these lines indicates a preferred orientation of the crystallites in the <001> direction.

Corresponding to the film composition, there were two distinct regions in the temperature dependence of the growth rate as is shown in Fig. 2.8. The low temperature region, where the films were contaminated with ZnF₂ crystallites, is characterized by an apparent activation energy of 23 kcal/mol. The growth rate increased with the increase of the [Te/Zn] ratio. The low temperature region ends with a sharp drop of the growth rate in the temperature range 375-420°C, depending upon [Te/Zn] ratio. Above this transition temperature, the growth rate varied only slightly with substrate temperature and the films were not contaminated with ZnF₂ crystallites. The mechanism of the transition is not clear, but the character of the contamination indicates that the nucleation of ZnF₂ on a growing ZnTe film played an important role. At a high ZnTe growth rate, the nucleation of ZnF₂ may be too slow for the formation of the crystallites. Also, the absence of a ZnF₂ phase at high temperatures possibly could be attributed to the equilibrium

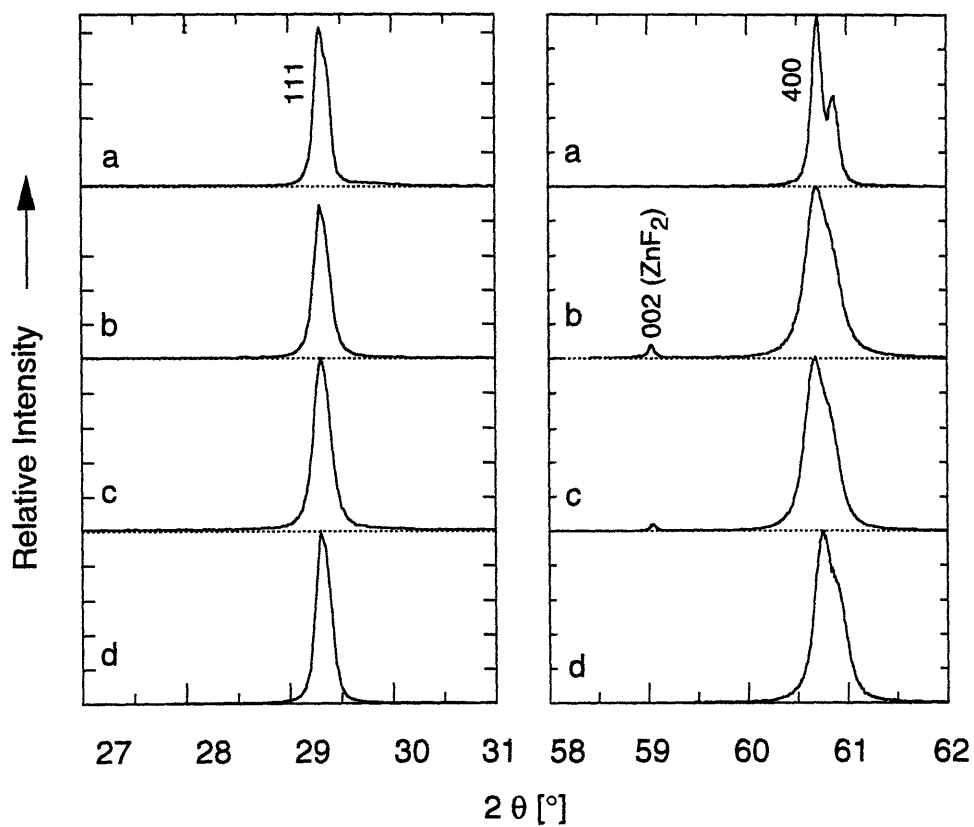


Figure 2.7. X-ray diffraction of films grown at $[\text{Te}/\text{Zn}] = 1.0$. (a) film from tBTeCF_3 at 400°C , (b) film from tBTeCF_3 at 350°C , (c) film from tBTeCF_3 at 300°C , (d) film from $(\text{CF}_3)_2\text{Te}$ at 500°C .

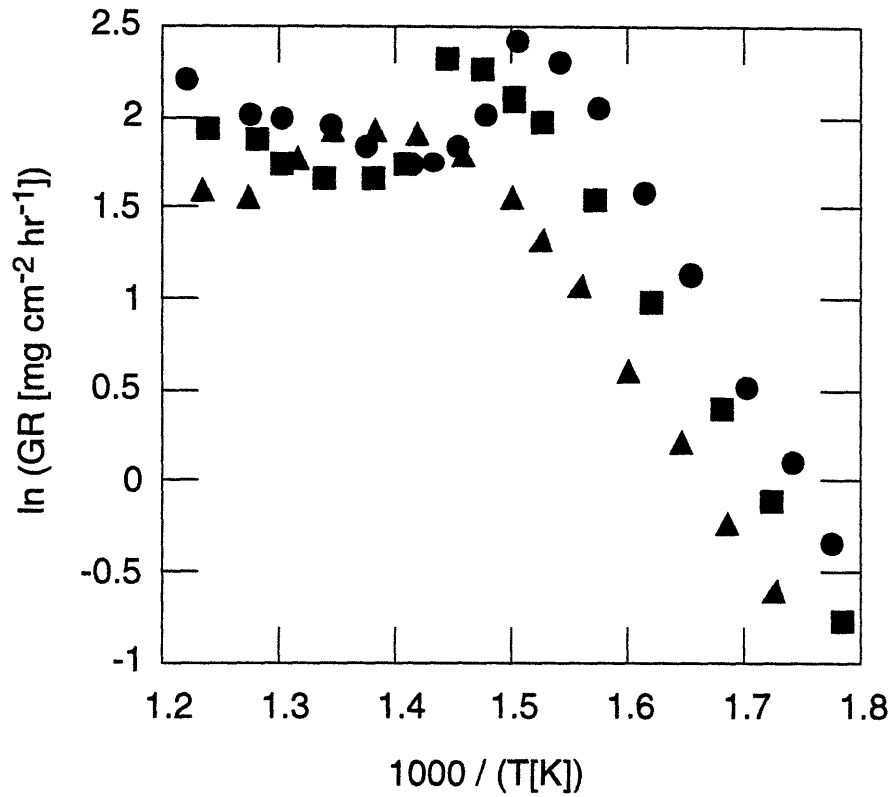
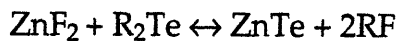


Figure 2.8. Arrhenius plot for growth from $t\text{BTeCF}_3$ at $[\text{Te}/\text{Zn}]$ equals to 2.0 (●), 1.0 (■) and 0.5 (▲). The flux of $t\text{BTeCF}_3$ was varied.



being shifted to the right-hand side at high temperatures. However, the conversion of ZnF_2 to ZnTe is thermodynamically unfavorable even at 400-500°C. This conclusion is relatively insensitive to errors in estimates of the thermodynamic data for R_2Te .

The growth rate in the high temperature region also depended upon the [Te/Zn] ratio and this behavior is illustrated in Fig. 2.9 for a growth temperature of 440°C. For ratios below ~0.5, the tellurium source was rate limiting. The growth rate reached a maximum at [Te/Zn] of 0.6, and was followed by a decrease at higher [Te/Zn] ratios. This phenomenon could be rationalized by the presence of a parasitic reaction depleting DMZn . Estimates of the mass transfer rate based upon the reactor and sample geometry indicated that the measured growth rate was well below the diffusion limit.

Since the growth experiments with tBTeCF_3 pointed towards an unexpected decomposition mechanism involving C-F bond activation and ZnF_2 incorporation, OMCVD growth with another (fluoroalkyl)tellurium compound, $(\text{CF}_3)_2\text{Te}$, was explored even though a high decomposition temperature and a high growth temperature were expected based upon a previous study [6]. Indeed, the growth rate was low, approximately 1 $\mu\text{m/hr}$, even at 500°C. The film surface was featureless and the main constituents are zinc and tellurium (Fig. 2.5e). Surprisingly, fluorine was uniformly incorporated into the film at concentrations below 10^{18} - 10^{19} atoms/ cm^3 . The diffraction pattern of a film grown at 500°C (Fig. 2.7d) is comparable to that for the films grown from tBTeCF_3 under similar conditions.

2.3.2. Gas-phase pyrolysis study of tBTeCF_3

In order to probe the mechanism of ZnF_2 formation, a pyrolysis study of tBTeCF_3 was performed in a molecular beam mass spectrometric system. Mass spectra of the reagent pyrolyzed in hydrogen and helium carrier gases at 412°C

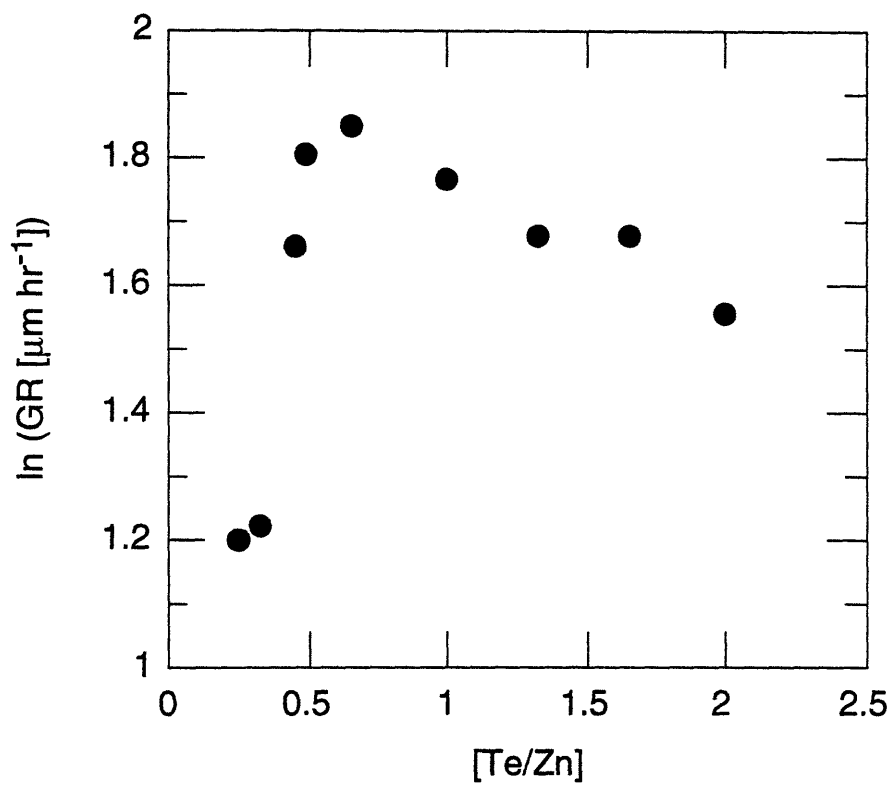


Figure 2.9. Growth rate of ZnTe at 440°C at various [Te/Zn] ratios. The flux of tBTeCF₃ was varied.

and 398°C, respectively, are shown in Fig. 2.10. The difference between the pyrolysis in hydrogen and in helium appears to be marginal. The parent molecule decomposes with an apparent activation energy of 32 kcal/mol, and the pyrolysis yields the following dominant products: 2-methylpropane, 2-methylpropene, hydrogen fluoride, tetrafluoroethene and 1,1-difluoro-2,2-dimethylcyclopropane. The normalized intensities of mass spectral signals corresponding to the parent and the products are shown in Fig. 2.11 as a function of heater temperature. Starting at low temperature, the first volatile product is 2-methylpropene generated with the onset of the source decomposition at 230°C. The generation of 2-methylpropene is followed by the formation of hydrogen fluoride and tetrafluoroethene. 2-methylpropane and 1,1-difluoro-2,2-dimethylcyclopropane are formed above 300°C. The appearance of 1,1-difluoro-2,2-dimethylcyclopropane is accompanied by a drop in tetrafluoroethene concentration indicating the presence of two competing reaction channels. The decomposition of the parent is complete by 400°C, but the expected product, $(\text{CF}_3)_2\text{Te}$, is not observed despite its high thermal stability [6]. The same trend in the distribution of the pyrolysis products was found in helium.

Based upon MBMS data and results from the previous pyrolysis study [6], we propose three possible pathways for the decomposition of tBTcCF_3 (Scheme 2.1). The first channel is homolytic cleavage of the *tert*-Bu-Te bond, yielding trifluoromethyl tellurium and *tert*-butyl radicals (pathway a). The $\text{CF}_3\text{Te}^\bullet$ radicals are expected to undergo recombination, leading initially to $(\text{CF}_3)_2\text{Te}_2$ and eventually to tellurium metal and thermally stable $(\text{CF}_3)_2\text{Te}$ [6]. The absence of $(\text{CF}_3)_2\text{Te}$ in the gas-phase indicates that the contribution of this mechanism to the overall decomposition of tBTcCF_3 is marginal. *tert*-Butyl radicals should disproportionate in the gas phase to 2-methylpropane and 2-methylpropene [6]. In the absence of another hydrogen donor, a 1:1 ratio of these products is expected.

The second decomposition pathway (b) is β -hydrogen elimination leading to (trifluoromethyl)tellurol, CF_3TeH and 2-methylpropene. (Trifluoromethyl)tellurol can either undergo bimolecular condensation yielding $(\text{CF}_3)_2\text{Te}_2$ and H_2 or, more probably at the reduced pressure conditions, monomolecular

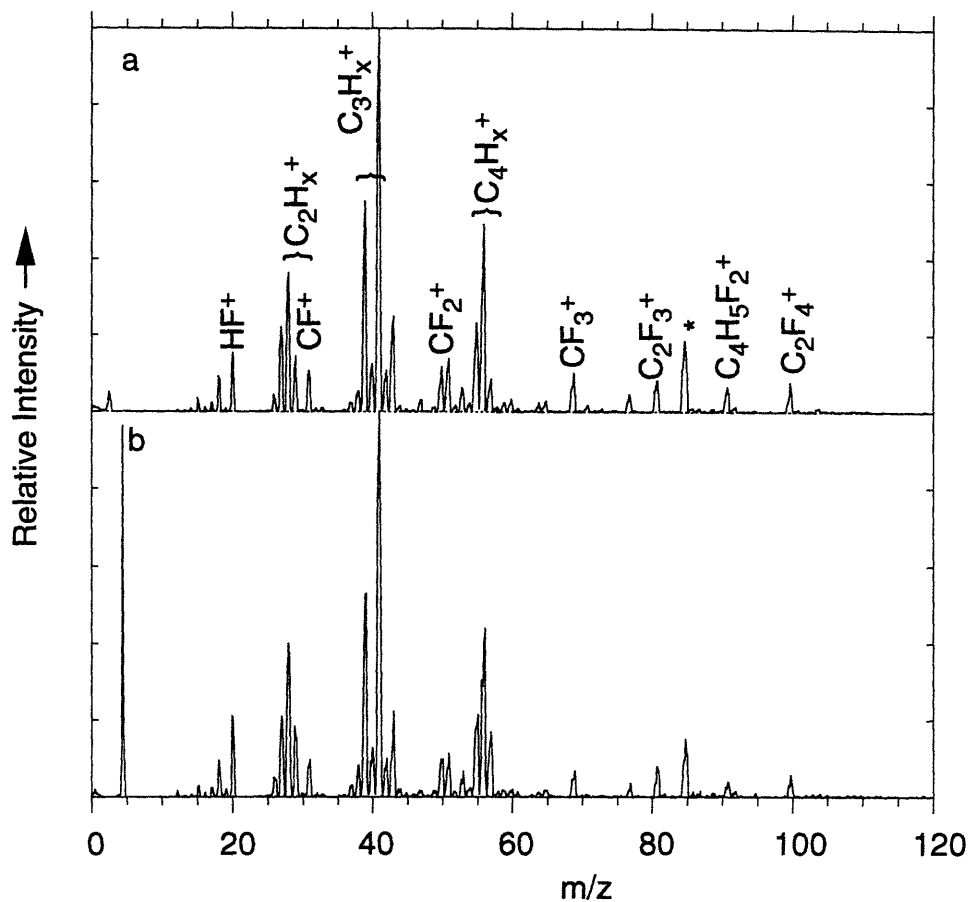


Figure 2.10. MBMS spectra of tBTeCF₃ pyrolysed in hydrogen at 412°C (a), in helium at 398°C (b). The peak denoted by (*) corresponds to SiF₃⁺. It is observed only above the decomposition temperature of the source and may have its origin in the reaction of HF with the quartz insulating plate of the MBMS heater.

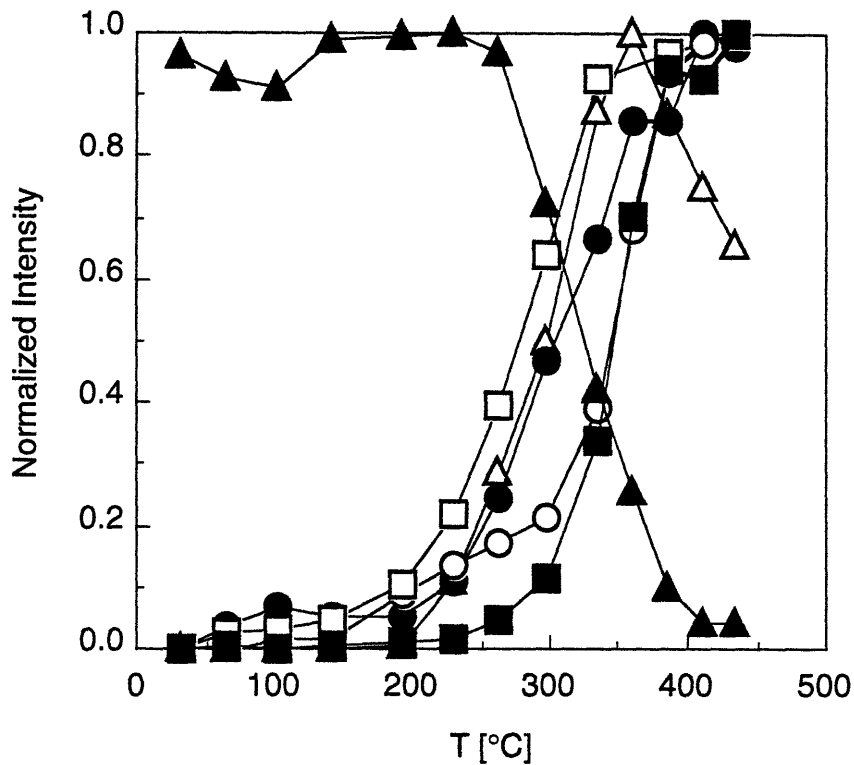
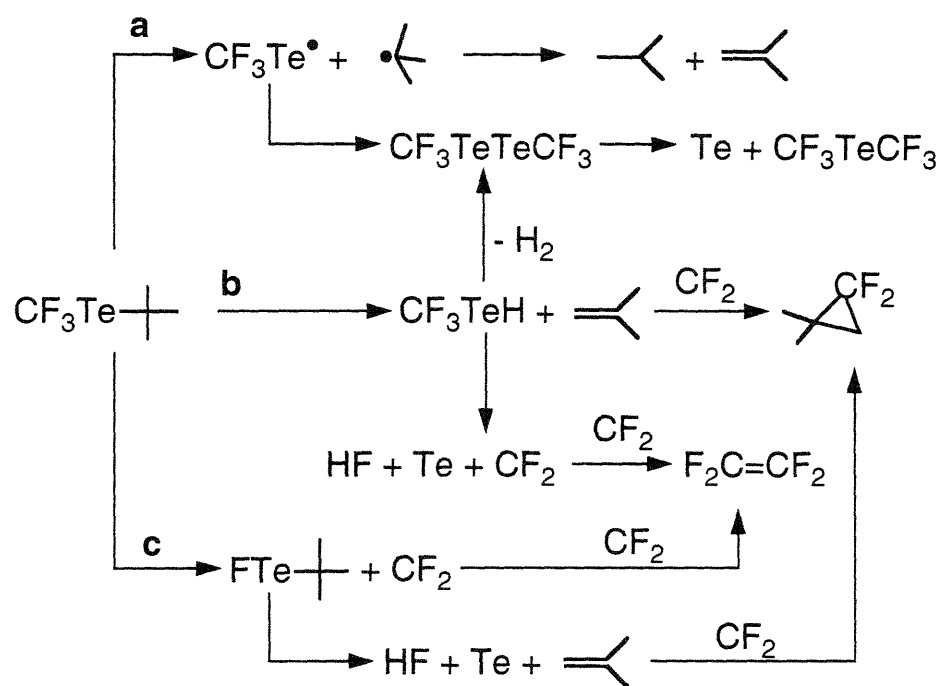


Figure 2.11. Normalized MBMS intensities of the gas-phase species for pyrolysis of $t\text{BTeCF}_3$ in H_2 at 30 Torr. The following symbols are used: ▲ parent, □ 2-methylpropene ($m/z=56$), ○ 2-methylpropane ($m/z=43$), ● hydrogen fluoride ($m/z=20$), △ tetrafluoroethene ($m/z=100$), ■ 1,1-difluoro-2,2-dimethylcyclopropane ($m/z=91$).



Scheme 2.1. Proposed gas-phase decomposition mechanism of tBTeCF_3 .

decomposition *via* difluorocarbene extrusion accompanied by formation of HF and elemental tellurium. Difluorocarbene dimerization and addition to 2-methylpropene account for the formation of tetrafluoroethene and 1,1-difluoro-2,2-dimethylcyclopropane. In agreement with this proposal, a trapping experiment in which excess 2-methylpropene was added showed that the ratio of these products was shifted away from tetrafluoroethene and toward 1,1-difluoro-2,2-dimethylcyclopropane (Fig. 2.12).

The third decomposition pathway (c), which should also be considered [9], starts with difluorocarbene extrusion yielding *tert*-butyltellurium fluoride, (tBTeF). If this tellurium intermediate underwent subsequent β -hydrogen elimination, the same pyrolysis products as in the second decomposition pathway would be expected. Direct observation of tBTeF, the primary product of difluorocarbene extrusion, would support such a mechanism. However, the high decomposition temperatures of analogous benzyl(trifluoromethyl)tellurium [6] and (CF₃)₂Te suggests that difluorocarbene extrusion from RTeCF₃ does not occur readily at temperatures below 400°C.

Theoretically, the relative contributions of β -hydrogen elimination and homolysis should be reflected in the 2-methylpropene/2-methylpropane ratio, since the former produces only 2-methylpropene, whereas the latter produces a 1:1 ratio of 2-methylpropene to 2-methylpropane. (The reaction of *tert*-butyl radical with hydrogen should be too slow in the studied temperature range to contribute significantly to the concentration of 2-methylpropane [10].) The ratio of the corresponding partial pressures *vs.* decomposition temperature is shown in Fig. 2. 13. The ratio has a maximum value at 300°C and then decreases with increasing temperature; however, its value remains large (>15) at all the temperatures. Therefore, though the relative importance of the competing decomposition pathways may change with temperature, the data clearly suggest that β -hydrogen elimination is the predominant decomposition pathway for tBTeCF₃ in the temperature range of 250-450°C. A significant contribution of β -hydrogen elimination to the overall pyrolysis mechanism was reported for related tellurium dialkyls, specifically for di-*tert*butyl tellurium and *tert*-butyl (methyl)tellurium [11].

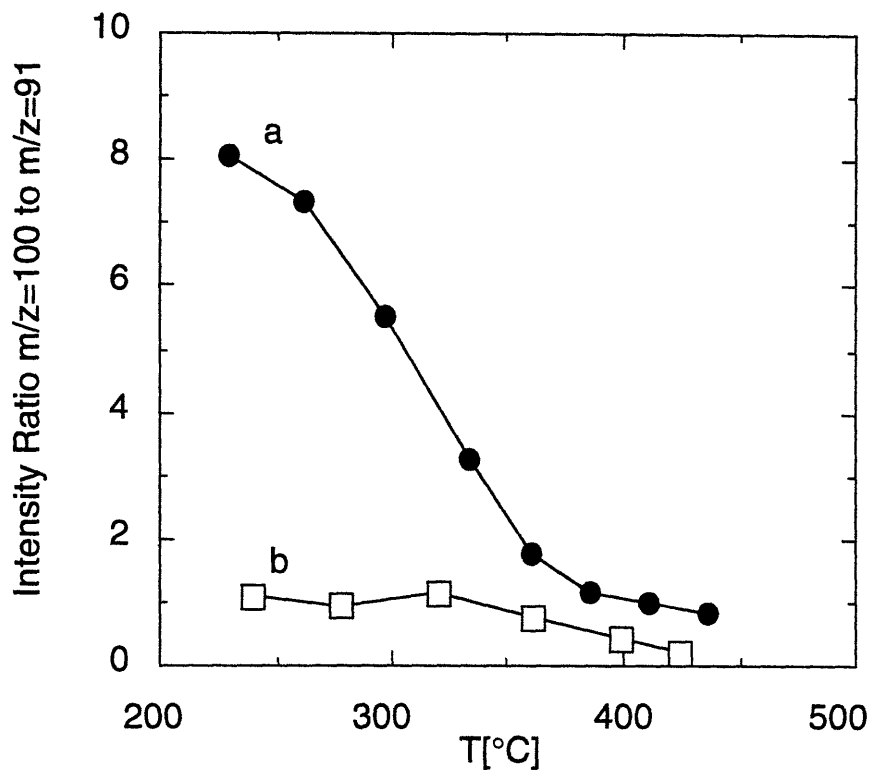


Figure 2.12. Effect of 2-methylpropene addition on the ratio of ion signals at $m/z=100$ (tetrafluoroethene) and $m/z=91$ (1,1-difluoro-2,2-dimethylcyclopropane) during pyrolysis of $t\text{BTeCF}_3$. (a) $t\text{BTeCF}_3$ (20 $\mu\text{mol}/\text{min}$) in hydrogen, (b) $t\text{BTeCF}_3$ (20 $\mu\text{mol}/\text{min}$) and 2-methylpropene (170 $\mu\text{mol}/\text{min}$) in hydrogen.

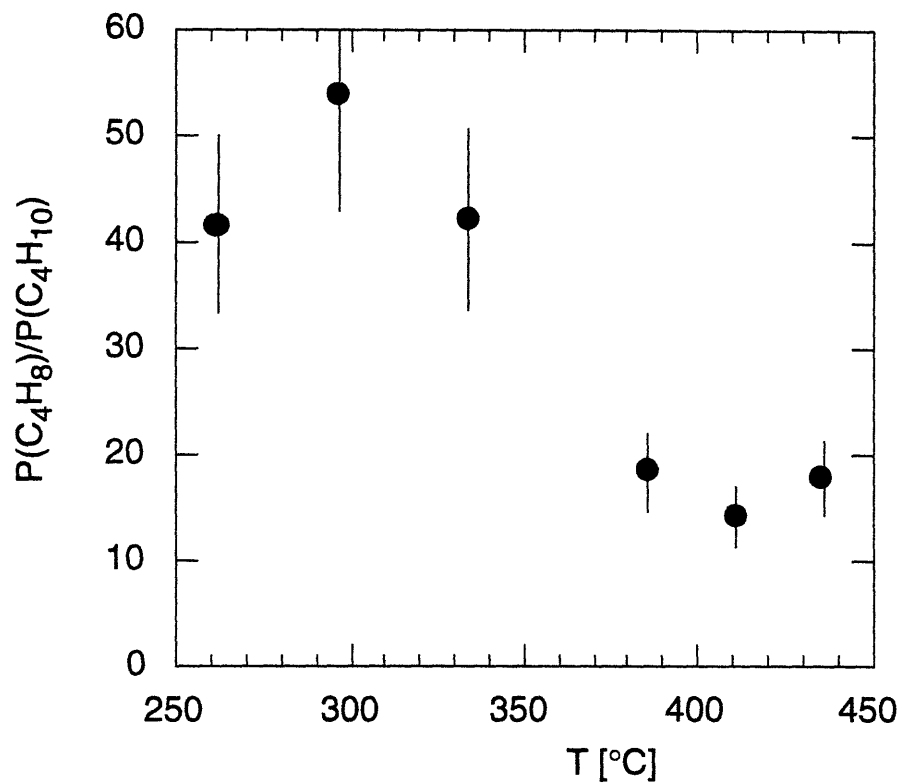


Figure 2.13. Ratio of 2-methylpropene *vs.* 2-methylpropane partial pressures as a function of heater temperatures during pyrolysis of tBTeCF_3 .

Hydrogen fluoride is one of the primary pyrolysis products of $t\text{BTeCF}_3$ and originates presumably from unstable CF_3TeH , the primary intermediate of β -hydrogen elimination. Under the OMCVD conditions, HF undergoes a rapid gas-phase reaction with DMZn to form ZnF_2 , which is observed to contaminate the films at temperatures below 400 °C. Preliminary MBMS studies of the reaction of $t\text{BTeCF}_3$ with DMZn at the growth conditions showed that formation of free HF was dramatically reduced. In addition, the temperature at which decomposition began was significantly reduced for both sources, suggesting that gas-phase adduct formation may also play a role in the growth mechanism. An alternative explanation for ZnF_2 formation is alkyl redistribution between $t\text{BTeCF}_3$ and DMZn to form $(\text{CF}_3)_2\text{Zn}$ which might decompose to CF_2 and ZnF_2 . An analogous reaction was observed to occur when $(\text{CF}_3)_2\text{Te}$ was allowed to react with $(\text{CH}_3)_2\text{Cd}$ [12]. The MBMS spectra show no indication of formation of $\text{CH}_3(\text{CF}_3)\text{Te}$ or $(\text{CH}_3)_2\text{Te}$, the products of alkyl redistribution reactions. Since these products are relatively stable at the temperatures studied and should be detected easily, their absence is a strong indication that alkyl redistribution is not important in the ZnF_2 formation. A second observation supporting this assertion is the absence of ZnF_2 in films grown from $(\text{CF}_3)_2\text{Te}$ and DMZn.

2.4. Conclusion

OMCVD experiments show that ZnTe can be grown from $t\text{BTeCF}_3$ at temperatures above 300 °C. Growth in the range of 300-400 °C yielded films contaminated with ZnF_2 crystallites, but above 400 °C the films consisted of relatively pure ZnTe. Films grown from $(\text{CF}_3)_2\text{Te}$ showed no fluorine incorporation, but required high growth temperatures. Under reduced pressure OMCVD conditions, $t\text{BTeCF}_3$ begins to decompose at 230 °C. The major decomposition pathway at low temperatures is β -hydrogen elimination. The contribution of radical reactions, following homolysis of the *tert*-BuTe moiety, increases with increasing pyrolysis temperatures. ZnF_2 contamination is likely to originate from the gas-phase reactions of DMZn with HF formed from the intermediates of β -hydrogen elimination.

References:

- [1] (a) Kobayashi, M.; Dosho, S.; Imai, A.; Konagai, M.; Takahashi, K. *Appl. Phys. Lett.* **1987**, *51*, 1602. (b) Jackson, M.K.; Miles, R.H.; McGill, T. C.; Faurie, J. P. *Appl. Phys. Lett.* **1989**, *55*, 786. (c) Tarasawa, T.; Ohkawa, K.; Mitsuyu, T. *Appl. Phys. Lett.* **1989**, *54*, 117. (d) Kumazaki, K.; Iida, F.; Ohno, K.; Hatano, K.; Imai, K. *J. Cryst. Growth* **1992**, *117*, 285. (e) Lee, D.; Johnson, A. M.; Zucker, J. E.; Burrus, C. A.; Feldman, R. D.; Austin, R. F. *Appl. Phys. Lett.* **1992**, *60*, 739.
- [2] (a) Wilson, B. A.; Bonner, C. E.; Feldman, R. D.; Austin, R. F.; Kisker, D. W.; Krajewski, J. J.; Bridenbaugh, P. M. *J. Appl. Phys.* **1988**, *64*, 3210. (b) Ogawa, H.; Mitsuhiro, N. *J. Appl. Phys.* **1988**, *64*, 6750. (c) Mitsuhiro, N.; Ogawa, H. *Jpn. J. Appl. Phys.* **1990**, *29*, 145. Yokogawa, T.; Narusawa, T. *Appl. Phys. Lett.* **1992**, *61*, 291.
- [3] (a) Wagner, H. P.; Kuhn, W.; Gebhardt, W. *J. Cryst. Growth* **1990**, *101*, 199. (b) Mullins, J. T.; Clifton, P. A.; Brown, P. D.; Brinkman, A. W.; Woods, J. J. *J. Cryst. Growth* **1990**, *101*, 100.
- [4] Pain, G. N.; Christiansz, G. I.; Dickson, R. S.; Deacon, G. B.; West, B. O.; McGregor, K.; Rowe, R. S. *Polyhedron* **1990**, *9*, 921 and refs therein.
- [5] Hails, J. E.; Irvine, S. J. C.; Mullin, J. B. *Mat. Res. Soc. Symp. Proc.* **1990**, *161*, 343.
- [6] Gordon, D. C.; Kirss, R. U.; Brown, D. W. *Organometallics* **1992**, *11*, 2947.
- [7] (a) Lee, P. W.; Omstead, T. R.; McKenna, D. R.; Jensen, K. F. *J. Cryst. Growth* **1987**, *85*, 165. (b) Lee, P. W.; Omstead, T. R.; McKenna, D. R.; Jensen, K. F. *J. Cryst. Growth* **1988**, *93*, 29.
- [8] Kudlek, G.; Presser, N.; Gutowski, J.; Hingerl, K.; Abramof, E.; Pesek, A.; Pauli, H.; Sitter, H. *J. Cryst. Growth* **1992**, *117*, 290.
- [9] Seyferth, D. In *Carbenes II*; Moss, R. A., Ed; Wiley: New York, 1975; pp 101.
- [10] Kondratiev, V. N. In *Rate Constants of Gas Phase Reactions*; Fristrom, R. M., Ed. NSRDS: 1972.
- [11] (a) McAllister, T. *J. Cryst. Growth* **1989**, *96*, 552. (b) Kirss, R. U.; Brown, D. W.; Higa, K. T.; Gedrich, Jr., R. W. *Organometallics* **1991**, *10*, 3589.
- [12] Naumann, D.; Lange, H. *J. Fluorine Chem.*; **1985**, *27*, 299.

Chapter 3

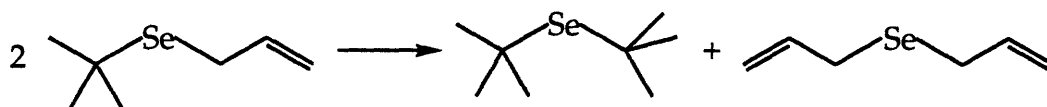
OMCVD Growth and Pyrolysis Study with *tert*-Butyl(allyl)selenium

3. 1. Introduction

Epitaxial films of ZnSe and related alloys are important materials for short-wavelength optoelectronic devices, *e. g.* green-blue light emitting diodes and diode lasers [1]. High quality ZnSe films can be grown on GaAs substrates by OMCVD from hydrogen selenide and dimethylzinc (DMZn) or its triethylamine adduct (DMZnNEt₃) [2]. However, a parasitic gas-phase reaction between the precursors results in poor surface morphology and thickness uniformity. In addition, the extreme toxicity of H₂Se (LD=50ppb), in combination with its high vapor pressure (approximately 9100 Torr at 31 °C), raises serious safety problems. Hence, a variety of dialkylselenium compounds has been tested in the OMCVD process to replace H₂Se [3]. Although low molecular weight selenium dialkyls, such as dimethylselenium (DMSe) and diethylselenium allow deposition of films with improved morphology, relatively high growth temperatures, typically above 450-500 °C, are necessary to achieve acceptable growth rates. Such high temperatures are detrimental to the quality of the ZnSe films. Therefore, particular attention has been paid to the synthesis of organoselenium precursors which would facilitate low temperature OMCVD of epitaxial ZnSe. Dialkylselenium compounds with allyl and *tert*-butyl substituents, groups yielding resonance stabilized free radicals upon decomposition, are promising reagents for low temperature growth. Methyl(allyl)selenium (MASE) and diallylselenium (DASE) were used for growth of epitaxial ZnSe at 400-450°C [4]. Unfortunately, the films were heavily contaminated with carbon, exceeding concentration levels of 10²⁰-10²¹ atoms/cm³. A gas-phase pyrolysis study under OMCVD growth conditions pointed to selenoaldehyde intermediates formed by the retro-ene reaction of the allylselenium compounds as the source of the carbon incorporation [5]. Kuhn *et*

al. used di-*tert*-butylselenium (DtBSe) for low temperature growth of epitaxial ZnSe under atmospheric pressure OMCVD conditions [6]. The films showed excellent crystallinity and sharp near band edge photoluminescence. Nishimura *et al.* reported successful growth experiments using *tert*-butylselenol (tBSeH) despite the high reactivity and difficult purifying the compound [7]

tert-Butyl(allyl)selenium (tBAsE) is a new selenium precursor designed to facilitate low temperature growth of epitaxial ZnSe while minimizing gas-phase pre-reactions. In contrast with MAsE and DAsE, the retro-ene decomposition channel is not accessible for tBAsE due to the presence of the *tert*-butyl group. As a result, low carbon contamination of the films can be expected. However, the presence of two different substituents complicates the pyrolysis reactions of the source. Even though the precursor is stable to the alkyl redistribution:



reactions under the growth conditions, *i.e.* in the presence of DMZn or DMZnNEt₃, may result in the formation of MAsE and DAsE. The formation of these compounds is undesirable from the stand point of material purity and process reliability.

3. 2. Experimental

General procedures. Synthesis and compound manipulations were carried out under an atmosphere of purified nitrogen using standard Schlenk techniques, vacuum lines, and a Vacuum Atmospheres glovebox. ¹H, ¹³C and ⁷⁷Se NMR spectra were recorded at room temperature in d₆-benzene on a WP 200SY NMR spectrometer equipped with a VSP200 broad band probe. ⁷⁷Se spectra were proton decoupled and referenced to Ph₂Se at 402 ppm. ¹H and ¹³C spectra were referenced to solvent peaks. The vapor pressure of tBAsE was measured in a high vacuum system equipped with a MKS Baratron over the

range of 19-45°C. Before the measurement, the precursor was purged with hydrogen to remove traces of high vapor pressure contaminants and degassed by several thaw-freeze-pump cycles.

Synthesis of *tert*-butyl(allyl)selenium. To a solution of diallylselenium (Advanced Technology Materials, Inc.) (50.3g, 0.312 moles) in THF (450 ml) cooled to -77°C was added *tert*-butyllithium (1.6 M in pentane, 0.376 mol) over 30 minutes. The reaction mixture was allowed to stir for one hour at -77 °C then quenched by cautious additions of degassed water. After warming to room temperature the solution was filtered through silica and solvent was removed by distillation at atmospheric pressure. Vacuum distillation of the product gave a colorless liquid. Yield 36g, 0.203 moles, 65%. NMR(C₆D₆) ¹H: δ (ppm) 1.30 (s, 9H), 3.09 (d, 2H, 7 Hz), 4.83 (d, 1H, 10 Hz), 4.98 (d, 1H, 17 Hz), 5.90 (m, 1H); ¹³C: δ (ppm) 25.0, 32.8, 115.9, 136.7; ⁷⁷Se: δ (ppm) 359. Vapor pressure : log (P[Torr]) = 7.846 - 2164 / T[K].

OMCVD growth. Growth experiments were carried out in a vertical downflow OMCVD reactor equipped with a laser interferometer for *in-situ* monitoring of growth rate [2b,4]. A schematic of the OMCVD reactor and gas-handling system is shown in Fig. 3.1. *tert*-Butyl(allyl)selenium and DMZnEt₃ (Epichem) were delivered into the reactor in a hydrogen carrier gas (UHP, Matheson) of total flow rate ~1000 sccm. The substrates were semi-insulating (100) GaAs, misoriented 2° towards <110>. A standard procedure was used to prepare the substrates prior to the deposition [8]. The remaining native oxide was removed at ~600 °C (10 min) in 400 sccm hydrogen flow carrying 150 μmol/min of H₂Se (electronic grade, Solkatrionic) to passivate the substrate surface. The films were grown at a reactor pressure of 300 Torr.

MBMS pyrolysis. Gas-phase pyrolysis was carried out at 30 Torr under steady state flow conditions in a custom-made molecular beam mass spectrometric system (MBMS) described in more detail elsewhere [9]. The MBMS system emulates the flow characteristics of the stagnant point OMCVD reactor used for the growth experiments with tBAsE, and the other allylselenium precursors [4]. In the MBMS system, the gas-phase from the vicinity of a

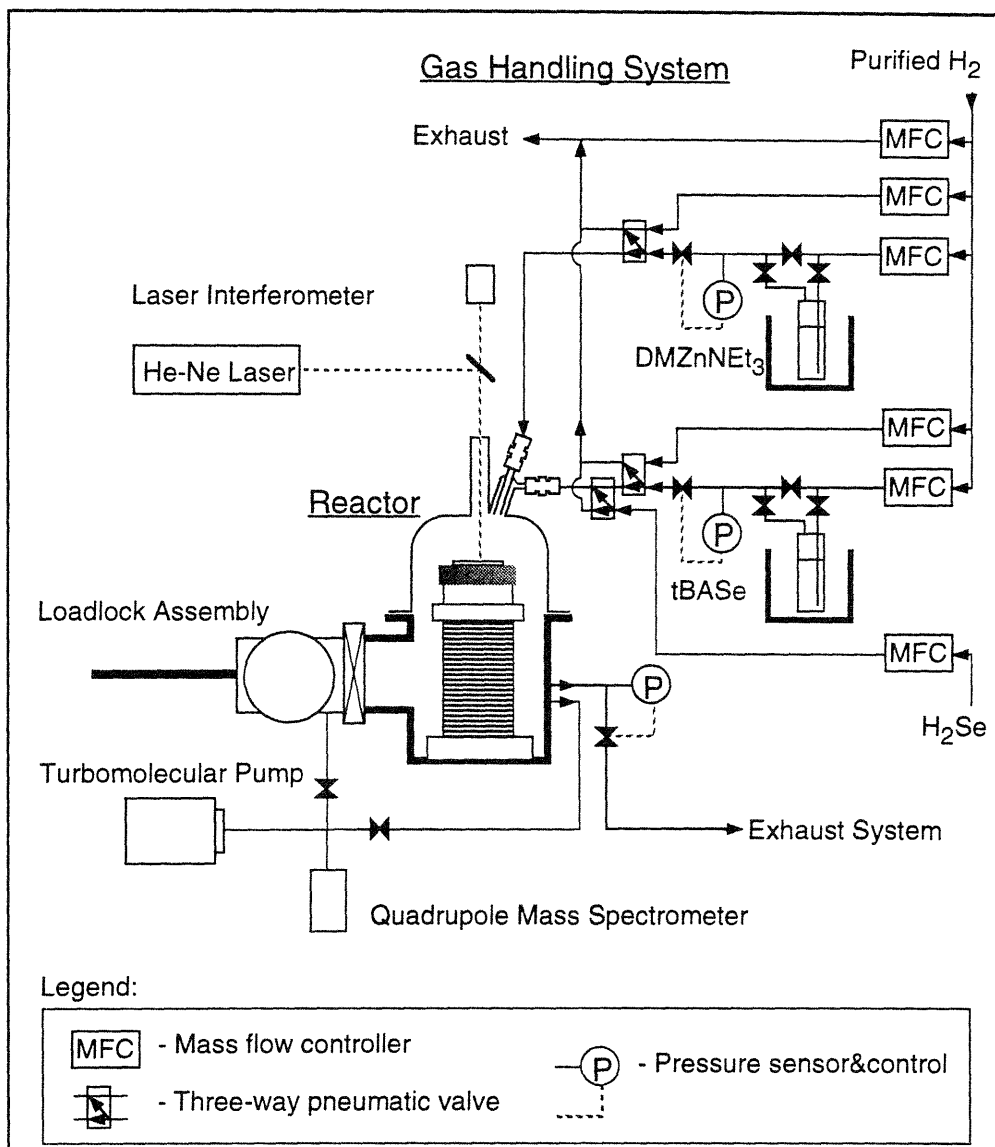


Figure 3.1. Schematic of the OMCVD reactor.

resistively heated graphite susceptor was sampled through a 100 μm pinhole into a high vacuum expansion chamber and collimated with a skimmer into a differentially pumped chamber towards a Baltzers 311 quadrupole mass analyzer. The molecular beam sampling allows monitoring of the composition of the gas-phase without the interference of post-sampling reactions. Delivery rates of the organometallics were maintained at 20 $\mu\text{mol}/\text{min}$ using a hydrogen (UHP, Matheson) or deuterium (99.9%, Matheson) carrier gas with a total flow rate of 25 standard cm^3/min (sccm). Prior to the pyrolysis experiments the inner surfaces of the reactor were exposed to the organometallics at a heater temperature $\sim 500^\circ\text{C}$. The molecular beam mass spectra were recorded at various susceptor temperatures and corrected for the temperature dependence of the sampling flux. The partial pressures of the gas-phase species were determined from the MBMS intensities at the characteristic m/z values: methane - 16, ethane - 30, propene - 42, 2-methylpropane - 43, 2-methylpropene - 56, 1,5-hexadiene - 67, DMZn - 64 and tBAsE -178. The spectrometer sensitivity factors were obtained in a separate experiment with the authentic compounds. The contribution of the fragmentation pattern of tBAsE and DMZn to the characteristic signals of the decomposition products was subtracted from the partial pressure data.

The surface morphology was examined by scanning electron microscopy. The lattice parameters of the ZnSe epilayers were measured by a double crystal diffractometer (model 300, BEDE Scientific, Inc) with $\text{CuK}\alpha$ radiation from a rotating anode X-ray generator (Model RU-200, Rigaku). Measurement of the carbon impurity levels in ZnSe was performed by secondary ion mass spectrometry (SIMS) with a detection limit for ^{12}C around 5×10^{17} atoms/ cm^3 . Undoped ZnSe films grown from $\text{H}_2\text{Se}/\text{DMZnNEt}_3$ showing no detectable carbon impurities were implanted with ^{12}C to provide an internal standard for SIMS measurement of the carbon concentration in ZnSe films. The implants had peak ^{12}C concentrations of 1×10^{19} atoms/ cm^3 . The SIMS measurements of carbon were carried out with a Cameca IMS-4f spectrometer using a Cs^+ primary ion beam.

3.3. Results and Discussion

3.3.1. Growth and Characterization of ZnSe

The temperature dependence of ZnSe growth rate for tBAsE is shown in Figure 3.2. The apparent activation energy of kinetically limited growth was approximately 21 kcal/mol. The transition to mass transport limited growth was at $\sim 400^\circ\text{C}$. This value is significantly lower in comparison with the transition temperatures for DAsE (440°C) and MAsE (480°C) obtained under identical experimental conditions [4]. Deposition experiments with different [VI/II] ratios indicated that the selenium source is the rate-limiting reactant. The growth characteristics of tBAsE are comparable to those reported for DtBSe [6], although a lower temperature for mass transport limited growth ($\sim 315^\circ\text{C}$) was reported for the latter source. This reduction is consistent with a lower thermal stability of DtBSe. Even lower deposition temperatures ($>280^\circ\text{C}$) were obtained with tBSeH [7].

The surface morphology varied with growth temperature (Fig. 3.3), but showed no significant change with the [VI/II] ratio. At low temperatures (325°C) the films were smooth although some contamination with ZnSe particles of submicron size appeared (Fig. 3.3a). The layers grown at intermediate temperatures (350°C) showed smooth surfaces interspersed with small gaps (Fig. 3.3b). At high temperatures (400°C), the films showed a rough surface with a large number of grainy features (Figure 3.3c). Similar surface morphologies were observed on layers grown from DtBSe [6] and tBSeH [7]. Although the surfaces of the films grown from tBAsE were still somewhat rough, the morphology was significantly improved in comparison with the films grown from hydrogen selenide [2].

Double crystal x-ray rocking curves for the (004) diffraction showed FWHM ranging from 220-400 arc/sec, indicating a low density of structural defects in the films [10]. These values are comparable to those reported for the best films grown from DtBSe [6] and tBSeH [7].

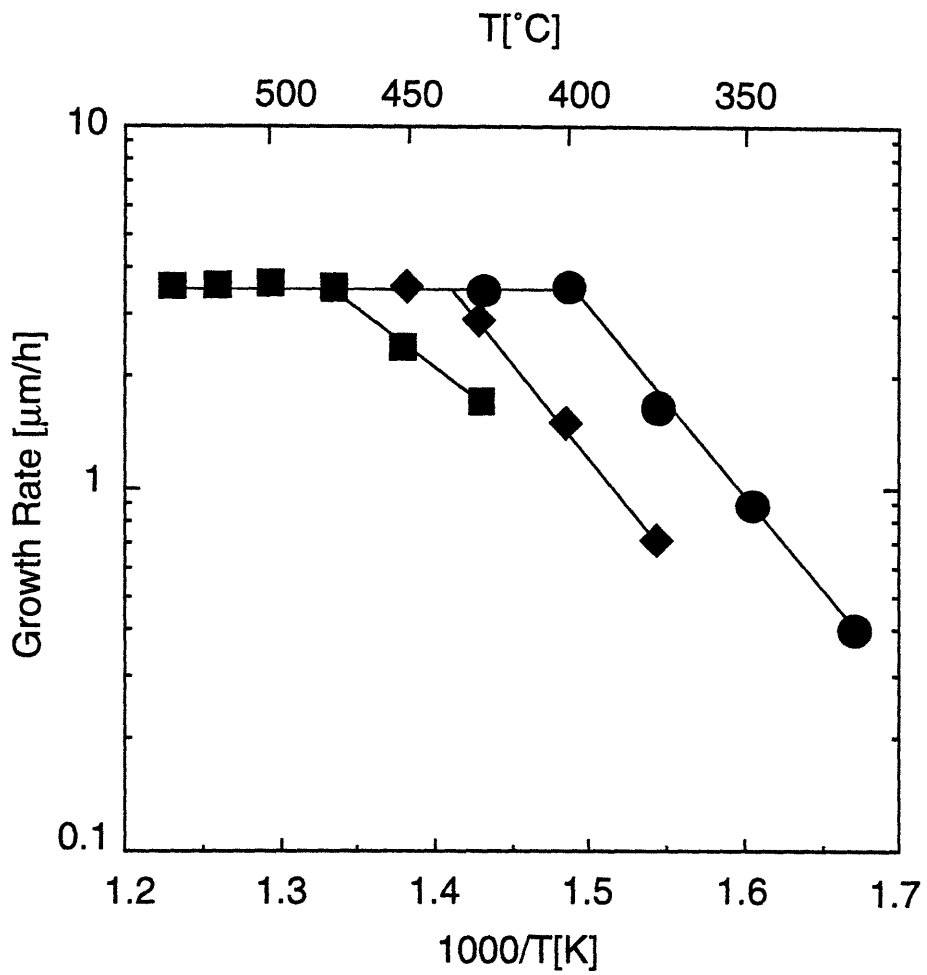


Figure 3.2. Growth rate of ZnSe for MASE (■), DASE (◆) and tBASE (●) as a function of substrates temperatures. The growth rate data for DASE and MASE are from ref. [4].

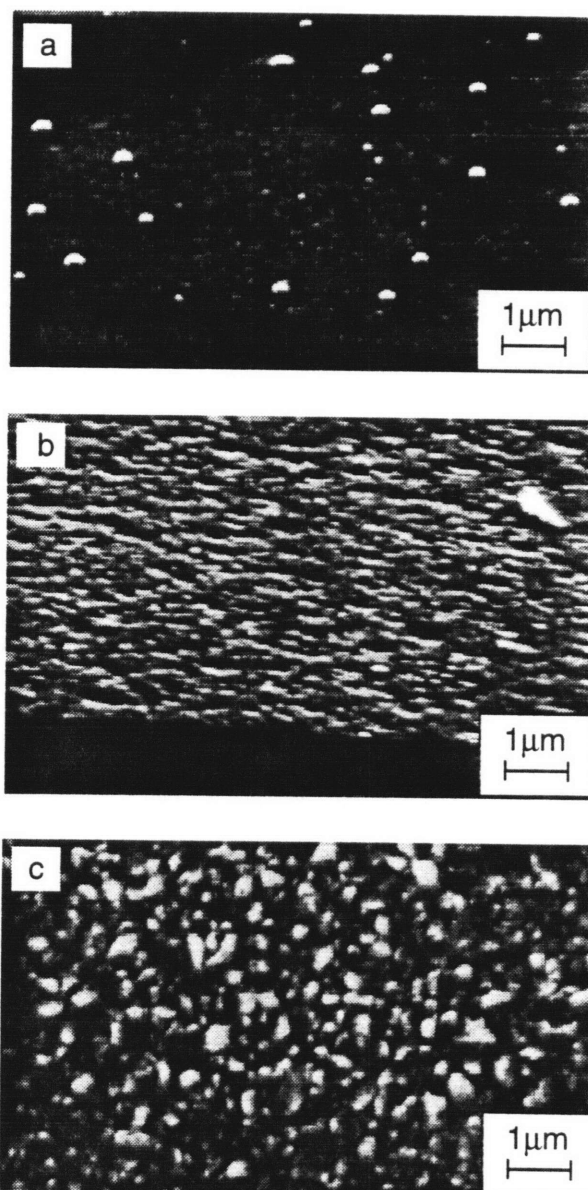


Figure 3.3. SEM images of the surface morphology of ZnSe films deposited from tBAs₂ (40 μmol/min) and DMZnNEt₃ (20 μmol/min) in hydrogen at various growth temperatures: (a) 325°C (b) 350°C (c) 400°C.

The low temperature photoluminescence spectrum of a film grown at 350 °C is shown in Figure 3.4. The near band-edge emission is composed of strong lines of donor-bound excitons at 2.795 eV (I_2^{lh}) and 2.797 eV (I_2^{hh}) and free excitons at 2.800 eV (E_x^{lh}) and ~2.803 eV (E_x^{hh}). Very weak and broad deep-level emission appeared around 2.3 eV. This emission is likely associated with residual impurities in the tBAsSe precursor. The predominance of the donor-bound exciton suggests incorporation of electron donating impurities either from the selenium precursor or from the growth system. Similar I_2 lines, observed on films grown from H_2Se and DMZn or DMZnNEt₃, were attributed to chlorine impurity [2]. The films grown from DtBSe [6] and tBSeH [7] also displayed a strong donor-bound emission, while deep-level emission was weak provided the impurity levels in the precursors were controlled.

Figure 3.5 compares ¹²C SIMS depth profiles for ZnSe films grown from tBAsSe and the other allylselenium sources. The ¹²C concentrations in the films synthesized from DAsSe were very high ($>10^{20}$ atoms/cm³) regardless of the precursor stoichiometry in the gas-phase ([VI/II] ratio). The films from MAsSe contained relatively low carbon concentrations (10^{18} - 10^{19} atoms/cm³) at [VI/II]<3, while a sharp increase of carbon contamination ($\sim 10^{21}$ atoms/cm³) was observed at [VI/II]>3. In contrast, the ZnSe films from tBAsSe showed no significant carbon incorporation even at a high [VI/II] ratio of 6 (the detection limit of the SIMS analysis was $\sim 5 \times 10^{17}$ atoms/cm³). This dramatic difference in the carbon content suggests that the carbon incorporation mechanism present for DAsSe and MAsSe [5] is hindered by the *tert*-butyl group in tBAsSe. Although carbon is not an optically active impurity in ZnSe [11], its level has to be controlled to obtain epitaxial material with a low density of structural defects. For example, all the films with high carbon levels ($>10^{19}$ atoms/cm³) were polycrystalline [4].

The layers grown from tBAsSe above 325 °C were highly resistive. Hall effect measurement on the samples grown at 325 °C revealed n-type character with an electron mobility of 105 cm² V⁻¹ s⁻¹ [10]. This result is consistent with the predominance of the donor-bound exciton emission in the PL spectra. A similar transition from conductive to highly resistive material was also observed with

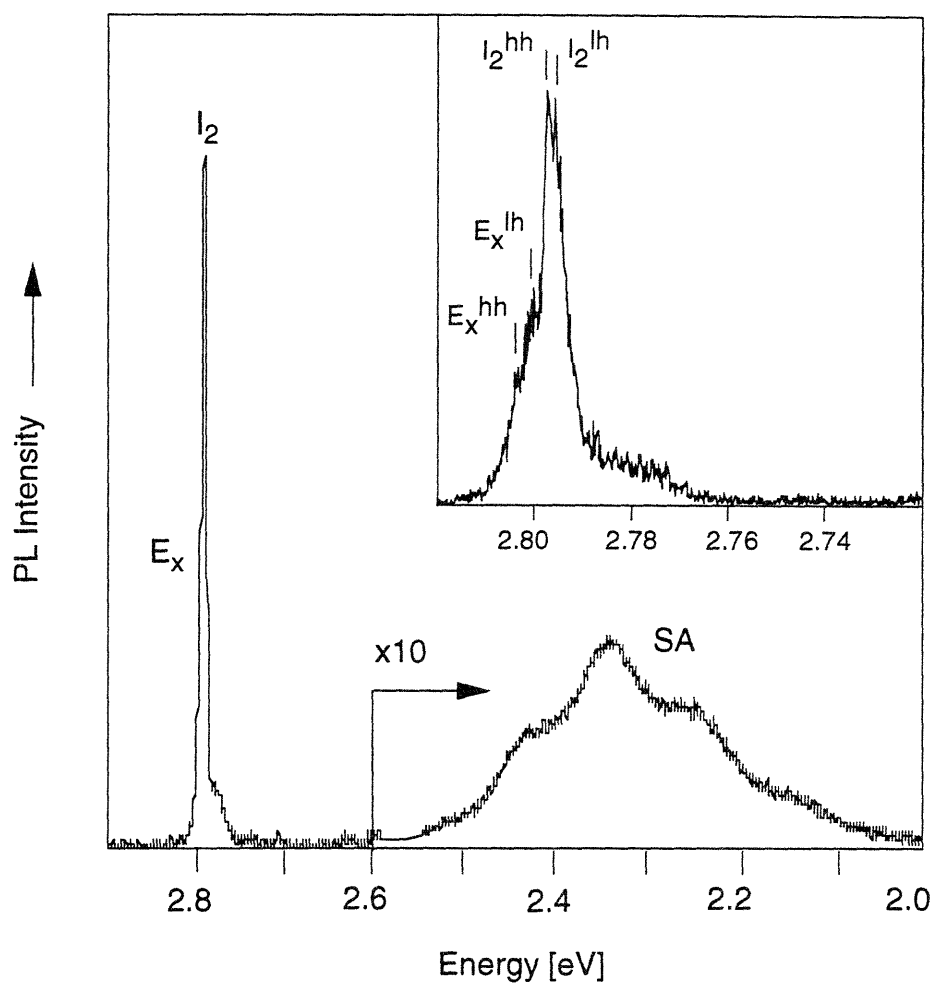


Figure 3.4 Low temperature (10 K) photoluminescence spectra of ZnSe grown from tBAsSe (40 $\mu\text{mol}/\text{min}$) and DMZnNEt₃ (20 $\mu\text{mol}/\text{min}$) in hydrogen at 350°C.

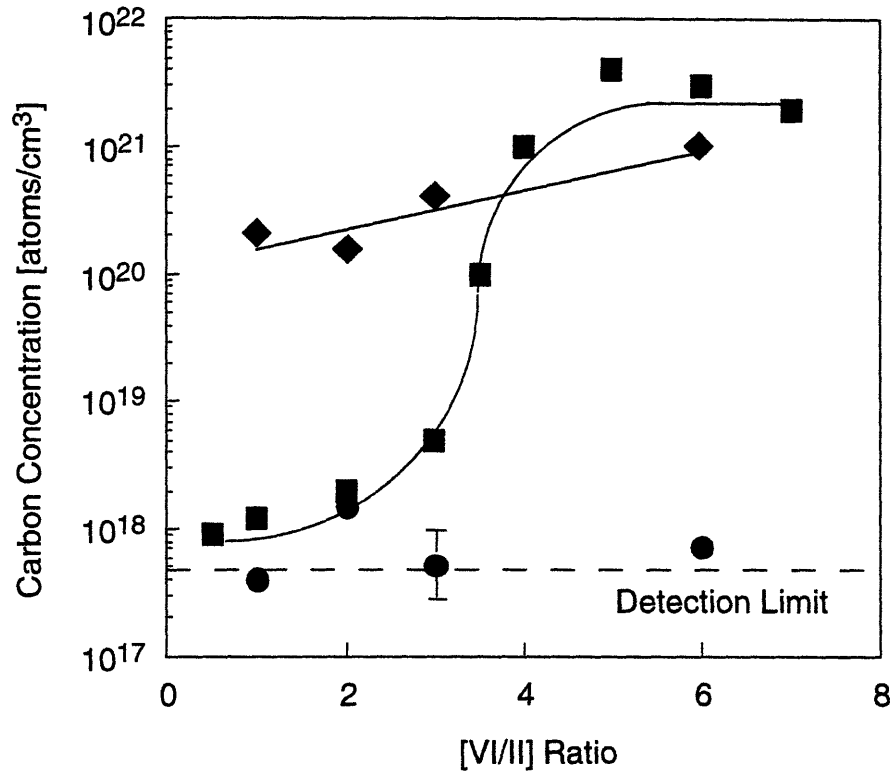


Figure 3.5. Dependence of carbon concentration on the [VI/II] ratio for ZnSe films grown from MASE (■) [growth at 520 °C], DASE (◆) [growth at 400 °C] and tBAsE (●) [growth at 350°C]. The samples from MASE and DASE were prepared previously [4].

the layers grown from H₂Se and DMZn and DMZnNEt₃ [2,12]. The mechanism of this transition is unclear, although formation of structural defects and self-compensation centers becomes more likely at high growth temperatures.

3.3.2 Gas-phase Pyrolysis Study of tBAsE

MBMS pyrolysis of tBAsE in hydrogen. The mass spectra of the gas-phase during pyrolysis of tBAsE in a hydrogen carrier gas are shown in Fig. 3.6 for three susceptor temperatures. The spectrum at 100 °C corresponds to tBAsE without any decomposition products (Fig. 3.6a). There is also no indication of alkyl redistribution reaction resulting in formation of DtBSe and DAsE at this temperature. At 240 °C the precursor is partially pyrolyzed and the gas-phase contains propene, 2-methylpropene, 2-methylpropane, 1,5-hexadiene, and hydrogen selenide (Fig. 3.6b). In addition, a weak signal of DAsE, a by-product of the pyrolysis, can be detected at this intermediate temperature. At 440 °C tBAsE is completely decomposed and the spectrum shows the hydrocarbon products, hydrogen selenide and elemental selenium (Fig. 3.6c).

The decay of tBAsE and the evolution of the hydrocarbon products are shown in Fig. 3.7 as a function of the pyrolysis temperatures. The precursor starts to decompose in a hydrogen carrier gas above ~180 °C and the pyrolysis is completed by ~340 °C. The apparent activation of the pyrolysis, calculated with a well stirred reactor model, is ~25 kcal/mol. This value is almost identical to the apparent activation energy of OMCVD growth, although the temperature required for complete conversion of tBAsE is rather low compared to the transient temperature of ~400 °C for the transport limited growth. The discrepancy is most likely caused by a difference in the residence times for the pyrolysis experiments and the OMCVD growth. The residence time in the MBMS system was ~300 seconds while the residence time in the OMCVD reactor was ~10 seconds. Thus, the longer exposure of the precursor in the hot zone of the MBMS system results in a higher conversion of the precursor than in the OMCVD reactor.

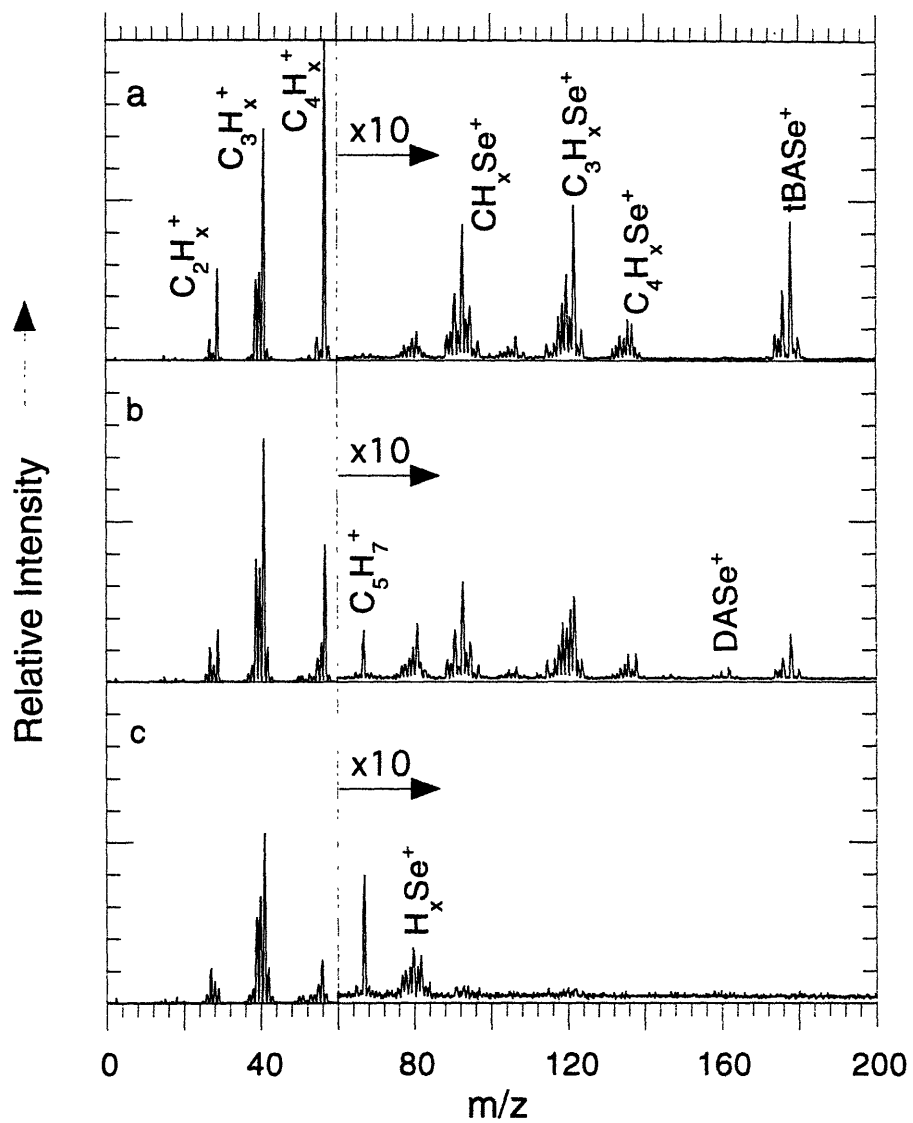


Figure 3.6. Molecular beam mass spectra of the gas-phase recorded during pyrolysis of tBAsE in hydrogen at 100 °C (a), 240 °C (b), and 440 °C (c). The spectra are corrected for the temperature dependence of the sampling flux.

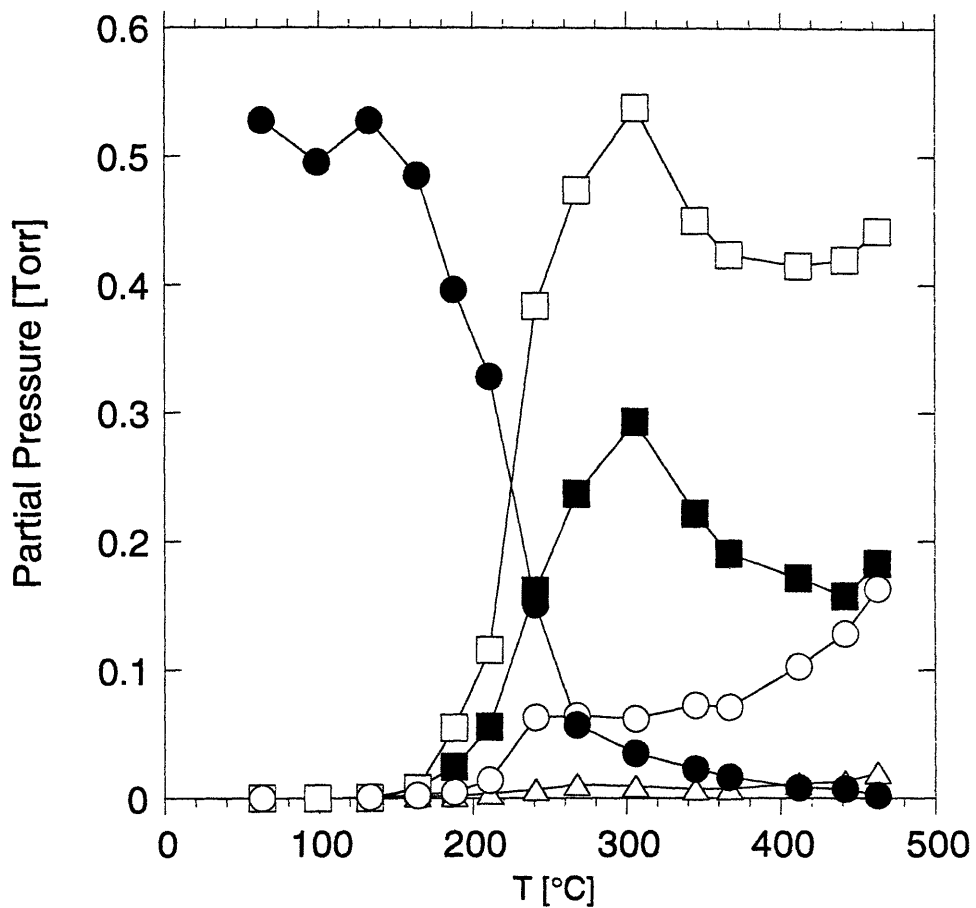


Figure 3.7. Partial pressures of tBAsE and the hydrocarbon products in the gas-phase during pyrolysis of tBAsE in hydrogen at various temperatures; ● tBAsE, ■ propene, □ 2-methylpropene, Δ 2-methylpropane, and ○ 1,5-hexadiene.

Propene, 2-methylpropene and 1,5-hexadiene are the major hydrocarbon pyrolysis products (Fig. 3.7). The partial pressures of propene and 2-methylpropene increase sharply with the onset of the tBAsE decomposition and reach a maximum at ~300 °C. The ratios of propene *vs.* 1,5-hexadiene partial pressures and 2-methylpropene *vs.* 2-methylpropane partial pressures are shown in Fig. 3.8 for various pyrolysis temperatures. Propene and 1,5-hexadiene originate from the allyl group of tBAsE while 2-methylpropene and 2-methylpropane are formed from the *tert*-butyl group of the precursor. The ratios of these hydrocarbons indicate that formation of 1,5-hexadiene and 2-methylpropane is more favorable at increasing pyrolysis temperature, although the latter hydrocarbon remains a minor product even at ~450 °C. The signal of DAsE can be detected in the range of 180-350°C with a peak intensity at 240°C (Fig. 3.9). The decay of the signal from DAsE above ~250 °C is consistent with thermal decomposition of the by-product [5]. The conversion of tBAsE to DAsE was approximately 10% as estimated from the relative intensities of the parent signals. A reliable quantification of the hydrogen selenide and selenium MBMS signals is difficult since the both species are present in the fragmentation patterns of tBAsE and DAsE. However, these species can be clearly identified at high temperatures when the selenium dialkyls are completely decomposed. The MBMS spectra did not show any evidence for the formation of DtBSe.

The role of the carrier gas in the OMCVD of II-VI semiconductors is often a subject of controversy. We probed the effect of a hydrogen carrier gas on the decomposition mechanism of tBAsE by conducting the pyrolysis in deuterium. Theoretically, any mechanism activating the carrier gas, either in the gas-phase or on the surfaces of the reactor, should result in the formation of deuterated hydrocarbons and an increase of the HD partial pressure. Figure 3.10 shows the hydrocarbon region of the mass spectra acquired in deuterium and hydrogen carrier gases at three pyrolysis temperatures. We observed only a slightly lower decomposition temperature in comparison with the pyrolysis in hydrogen, presumably due to a lower purity of the deuterium gas (99.9%). However, the spectra show no evidence of deuterated hydrocarbons at all pyrolysis temperatures up to 450 °C. Consistently, no indication of isotope exchange in the HD region was observed (not shown).

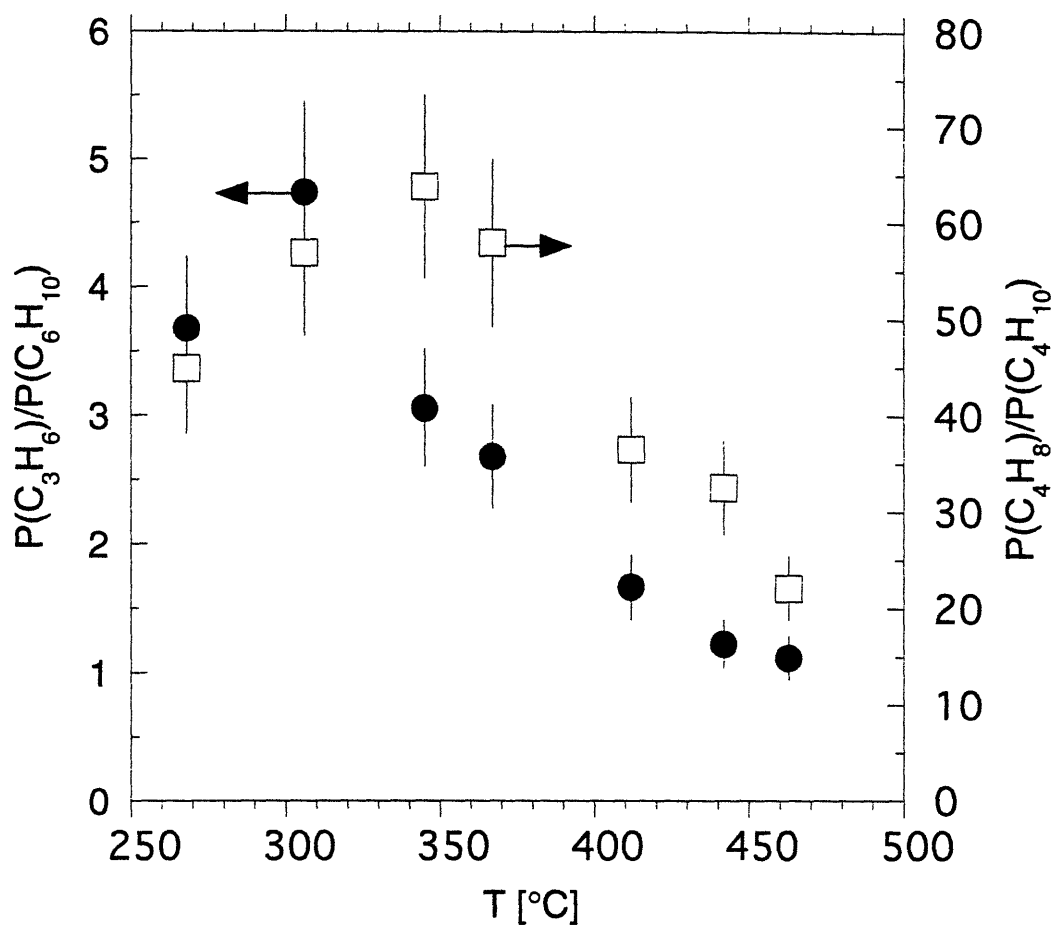


Figure 3.8. Partial pressure ratios of propene *vs.* 1,5-hexadiene (●) and 2-methylpropene *vs.* 2-methylpropane (□) for the pyrolysis of tBAsE in hydrogen.

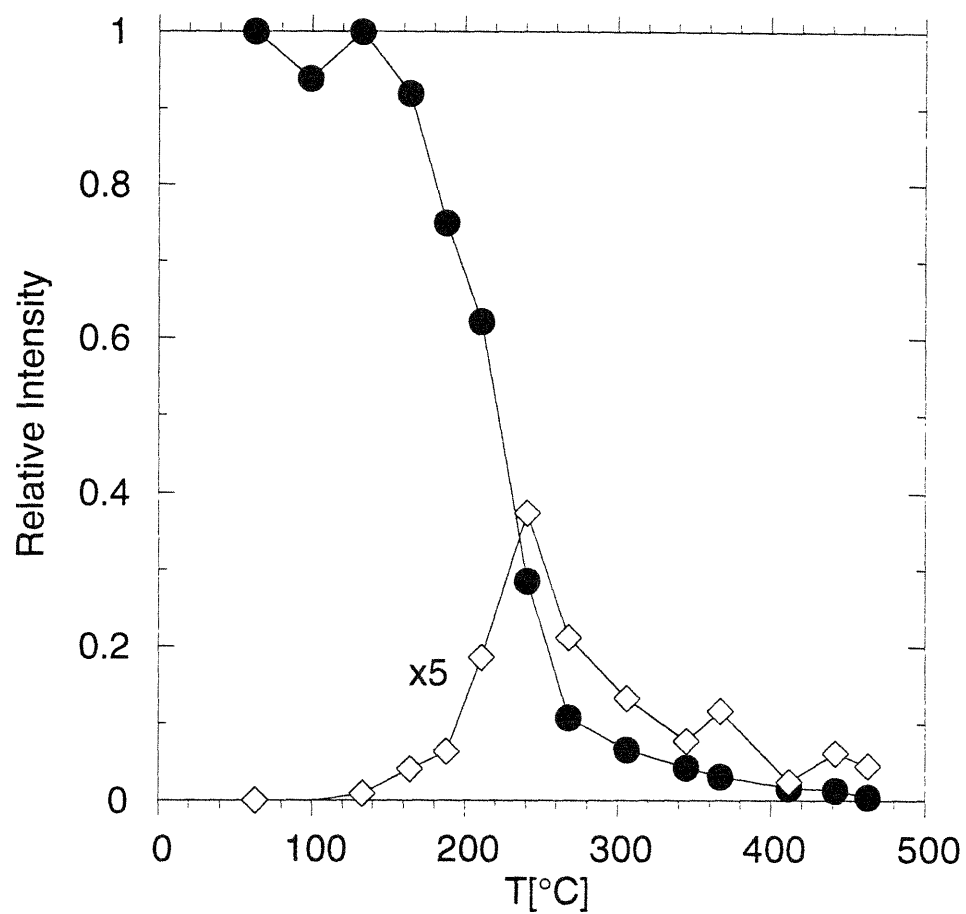


Figure 3.9. Relative MBMS intensities of tBAsE and DAsE for pyrolysis of tBAsE in hydrogen. ● tBAsE ($m/z=178$ amu) and ◇ DAsE ($m/z=162$ amu).

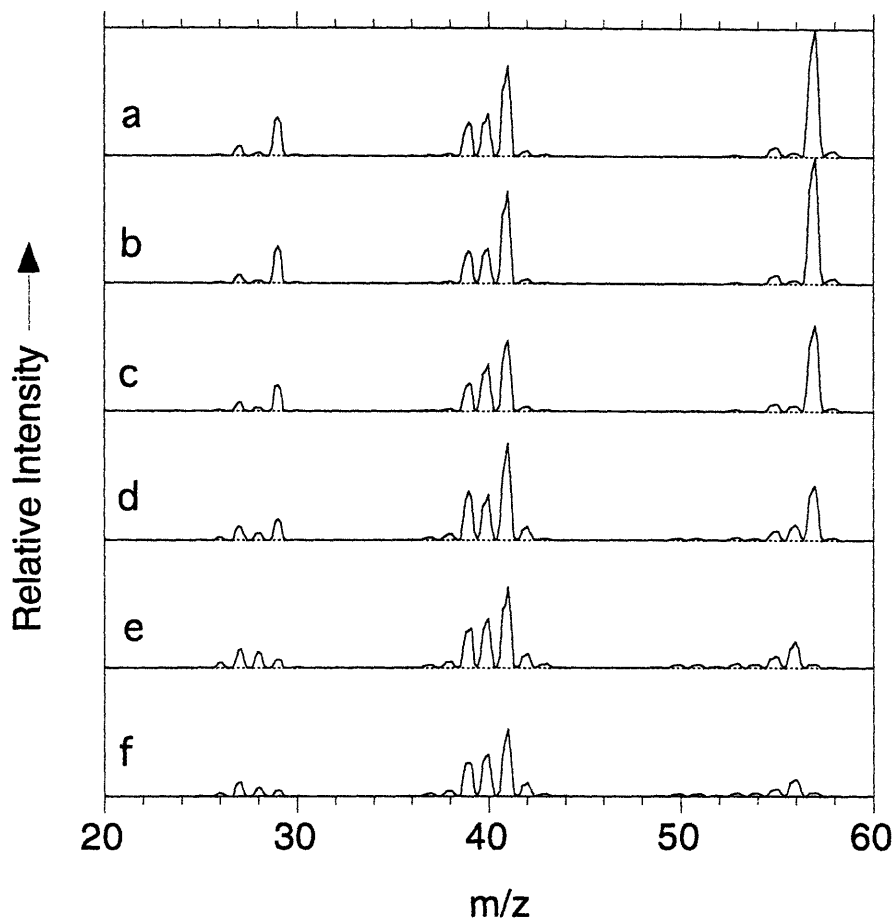
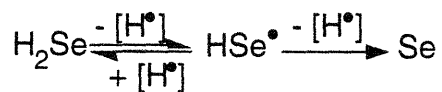
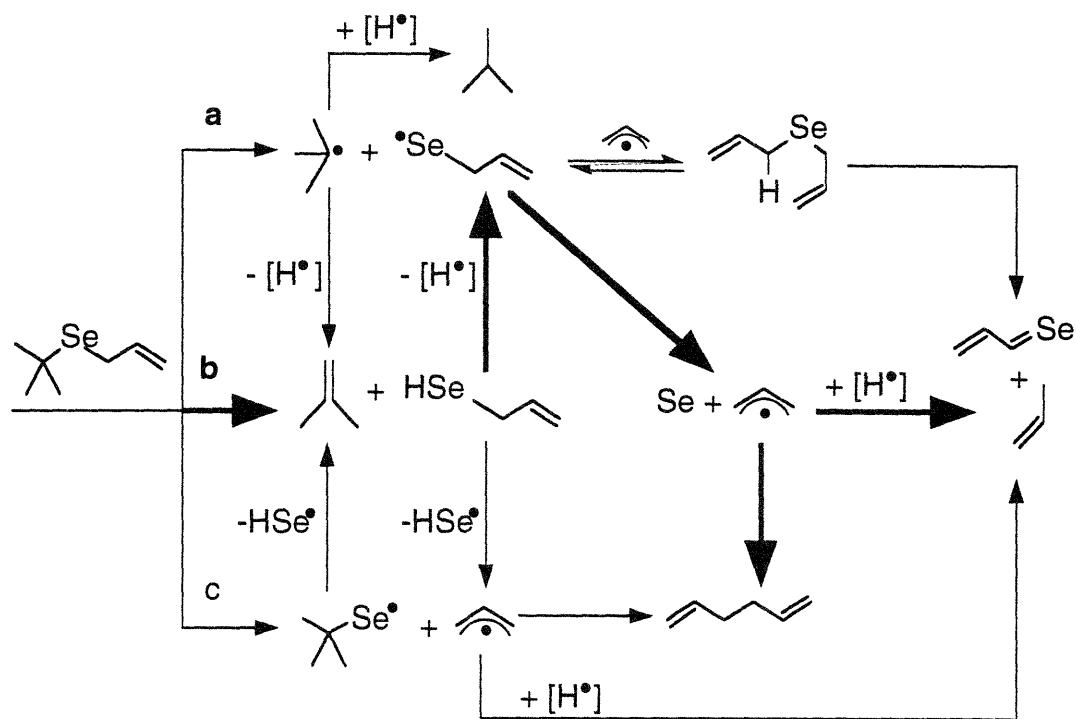


Figure 3.10. The hydrocarbon region of the molecular beam mass spectra recorded during pyrolysis of tBAsE in deuterium and hydrogen: (a) 100 °C in deuterium, (b) 100 °C in hydrogen, (c) 250 °C in deuterium, (d) 240 °C in hydrogen, (e) at 450 °C in deuterium, and (f) 440 °C in hydrogen.

Pyrolysis of tBAsE can be described by a mechanism involving homolytic scission of the Se-C bonds and β -hydrogen elimination as the primary decomposition steps (Scheme 3.1). The *tert*-butyl group facilitates both homolysis of the Se-C bond (path a) and β -hydrogen elimination (path b). The low decomposition temperature of DtBSe, as verified in OMCVD experiments [6], suggests that at least one of these pathways should be feasible at 300-350 °C. The third decomposition step, homolysis of the Se-C(allyl) bond, yielding *tert*-butylselenium radical and resonance stabilized allyl radical (path c) is characteristic of alkylselenium compounds and can be also accessible below ~350°C [5]. The decomposition temperature of tBAsE (~230 °C, determined at 50% conversion) is, however, significantly reduced in comparison with the temperatures for DAsE (~330 °C) and MAsE (~410 °C) observed in the MBMS under identical experimental conditions [5]. This higher reactivity of tBAsE, in comparison with DAsE and MAsE, also mirrors the OMCVD characteristics of the allylselenium precursors. For example, the transition to transport limited growth for tBAsE was observed at ~ 400 °C, in comparison with ~440 °C for DAsE and ~470 °C for MAsE. Thus, the comparison of the relative thermal stability of tBAsE, DAsE and MAsE under OMCVD conditions suggests that the low temperature decomposition path of tBAsE originates from the reactivity of the *tert*-butyl-Se moiety.

The presence of 2-methylpropene and 2-methylpropane is consistent with gas-phase disproportionation of the *tert*-butyl radicals formed by homolysis of Se-C(*tert*-butyl) bond (path a). If path a were the only decomposition reaction, a nearly equimolar 2-methylpropene *vs.* 2-methylpropane ratio could be expected due to the tendency of free *tert*-butyl radicals to disproportionate [13,14]. However, the observed ratio ranges from 20 to 70 (Fig. 3.8), indicating only a minor contribution of path a to the overall conversion of tBAsE. In contrast to these large values, a ratio of ~2 was found for gas-phase pyrolysis of *tert*-butyl(allyl)tellurium [14]. For the tellurium compound, path a is more favorable due to the lower strength of Te-C bond, resulting in increased abundance of 2-methylpropane in the pyrolysis products.

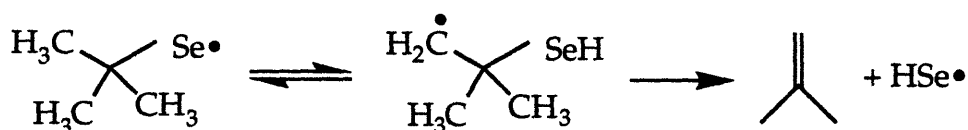


Scheme 3.1. Pyrolysis mechanism of tBAsSe under reduced pressure OMCVD conditions. The major low temperature reactions are shown with bold arrows. The symbol [H[•]] represents hydrogen radical donors.

The large ratios of 2-methylpropene *vs.* 2-methylpropane partial pressures (Fig. 3.8) are consistent with a significant contribution of β -hydrogen elimination (path **b**) to the overall decomposition mechanism of tBAsSe. Direct observation of the intermediate allylselenol would further support this conclusion. However, the compound is expected to be unstable under the pyrolysis conditions and the observation of allylselenol is further complicated by interference from the fragmentation pattern of the other allylselenium species present in the gas-phase. Recent gas-phase pyrolysis studies showed a predominance of β -hydrogen elimination in the overall decomposition mechanism of related *tert*-butylsulphur [15] and *tert*-butyltellurium compounds [14,16]. Kuhn *et al.* suggested β -hydrogen elimination as the major decomposition path for DtBSe [6b].

Provided path **b** dominates the decomposition of tBAsSe, understanding of the pyrolysis chemistry of allylselenol seems to be essential for a mechanistic insight into the OMCVD chemistry of the precursor. Foster *et al.* showed that the main gas-phase pyrolysis pathway of aliphatic selenols is scission of the Se-H bond [17]. Reductive elimination of alkanes and scission of the Se-C bond were found to be only minor pyrolysis channels. On the basis of these results we assume that scission of the Se-H bond is the major decomposition path of allylselenol. Allylselenium radical, formed by this reaction, will likely undergo a consecutive scission of the Se-C bond yielding elemental selenium and allyl radicals [17]. Alternatively, allylselenium radicals will recombine with free allyl radicals to form the observed DAsSe.

Theoretically, 2-methylpropene may be also formed along the radical path **c**. The *tert*-butylselenium radical could undergo tautomerization involving hydrogen atom transfer from one of the methyl groups to the selenium atom, and subsequent decomposition to a hydrogenselenium radical and 2-methylpropene:



Benson pointed out the significance of such a mechanism for the pyrolysis of *tert*-butylsulfur compounds [18]. However, the identical mechanism seems to be less likely for the pyrolysis of *tert*-butylselenium compounds where scission of the C-H bond and formation of the weak Se-H bond [19] is less favorable on a thermodynamic basis. Alternatively, 2-methylpropene and hydrogen selenium radical might be formed from *tert*-butylselenium radical by a concerted reaction involving β -hydrogen transfer. In either case, the rate of the elimination reaction had to be faster than the homolysis of the Se-C(*tert*-butyl) bond since the pyrolysis data argue for a negligible amount of *tert*-butyl radicals being present in the gas-phase.

The allyl radicals formed by scission of Se-C(allyl) bonds may undergo either hydrogen abstraction reactions or radical recombinations. The former reactions account for the formation of propene while the latter mechanism explains the presence of 1,5-hexadiene. It is important to note that propene is also a product of a reductive elimination reaction of allylselenol, and retro-ene re-arrangement of DAsE. However, the contribution of these two mechanisms to the overall formation of propene is marginal due to the low probability of the reductive elimination pathway of selenols [17], and a low conversion of tBAsE to DAsE. Thus, the major reaction yielding propene is hydrogen abstraction, and selenium species containing the weak Se-H bonds, such as allylselenol, are most likely to be the hydrogen donor. Radical recombination, the alternative reaction of free allyl radicals, becomes the dominant reaction channel at high temperatures (Fig. 3.8). This temperature effect is consistent with the increasing probability of a radical decomposition mechanism, specifically with an increasing contribution from path c.

Hydrogen selenium radicals formed from allylselenol or from *tert*-butyl selenium radicals will undergo hydrogen abstraction reactions. These reactions would account for the presence of hydrogen selenide, however, their contribution to the overall pyrolysis mechanism is probably marginal. Nevertheless, the presence of good hydrogen donors in the gas-phase, such as hydrogen selenide and allylselenol, may be critical for OMCVD growth of p-type

ZnSe. Recent studies showed that incorporation of hydrogen into the layers and formation of N-H complexes results in compensation of p-type conductivity [20].

MBMS pyrolysis of tBAsE and DMZn in hydrogen. Addition of DMZn into the flux of tBAsE does not result in any significant decay of the intensity of the tBAsE parent signal up to ~100 °C. This observation is consistent with a negligible gas-phase pre-reaction between the precursors after mixing. Such behavior of the precursors mixture is desirable for uniform growth and smooth surface morphology. Mass spectra of the gas-phase species from the pyrolysis of an equimolar mixture of tBAsE and DMZn in a hydrogen carrier gas at three different temperatures are shown in Fig. 3.11. The spectrum at 100 °C corresponds to superposition of the precursors spectra (Fig. 3.11a). At 317 °C the gas-phase contains small quantities of tBAsE and DMZn along with methane, propene, 2-methylpropene, and 1,5-hexadiene as the major decomposition products (Fig. 3.11b). Traces of ethane, 2-methylpropane, DMSe, MAsE, and DAsE can be detected at this temperature. At 450 °C both precursors are pyrolysed and the gas-phase contains the hydrocarbon products with traces of elemental selenium (Fig. 3.11c). The signals of DAsE and MAsE almost disappeared, while the signal of DMSe increased. The MBMS spectra did not show any evidence for the formation of DtBSe or methyl(*tert*-butyl)selenium.

Figure 3.12 displays the partial pressures of tBAsE, DMZn and the hydrocarbon products at various pyrolysis temperatures. The onset of tBAsE decomposition remains almost unaffected by the presence of DMZn. However, the apparent activation energy of the decomposition of tBAsE in the presence of DMZn is slightly reduced in comparison to the pyrolysis of tBAsE. The decomposition of DMZn follows the decay of tBAsE and both precursors are pyrolysed completely by ~380°C.

The partial pressures of the hydrocarbon pyrolysis products increase with the conversion of the precursors (Fig. 3.12). 2-methylpropene remains the most abundant hydrocarbon in the pyrolysis of tBAsE. The partial pressure data for 2-methylpropene might contain some contribution of 1-butene, the expected product of recombination of methyl radicals from DMZn with allyl radicals. The

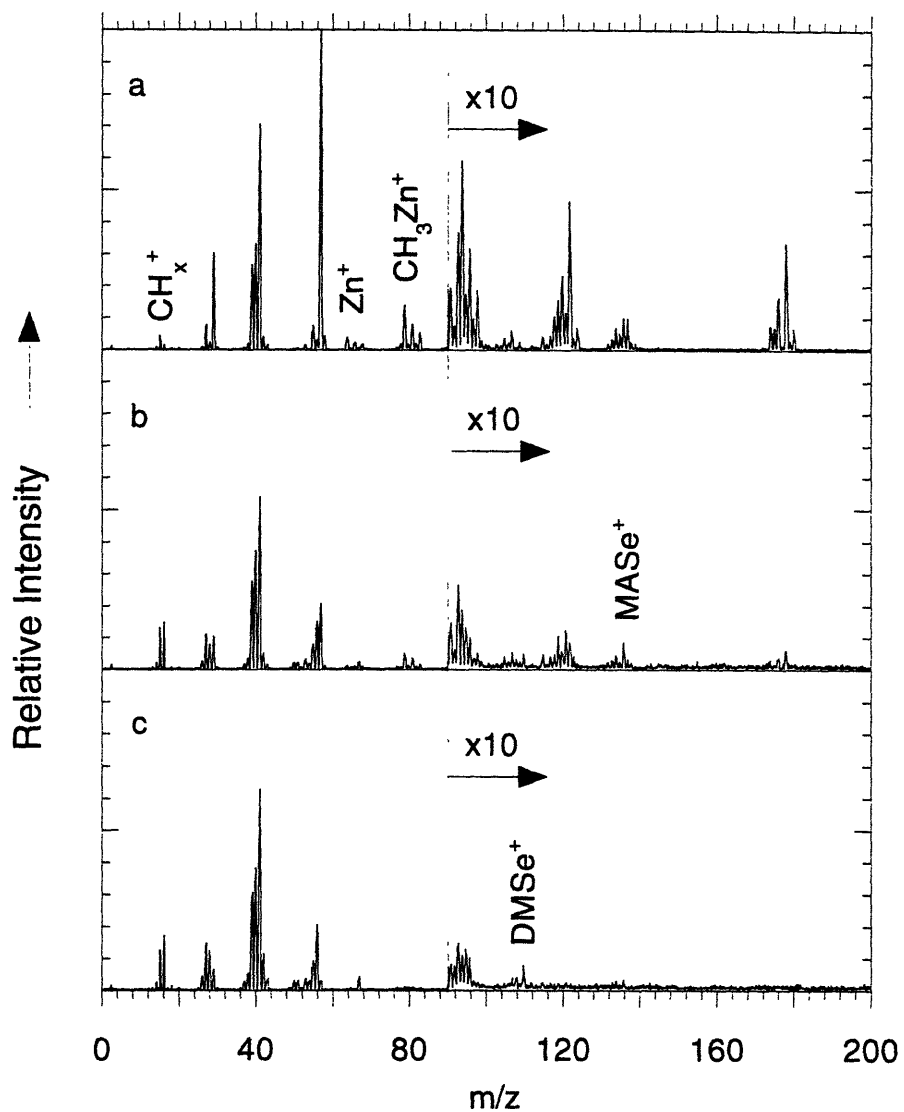


Figure 3.11. Molecular beam mass spectra of the gas-phase for co-pyrolysis of an equimolar mixture of tBAsE and DMZn in hydrogen at 100 °C (a), 320 °C (b), and 450 °C (c). The spectra are corrected for the temperature dependence of the sampling flux.

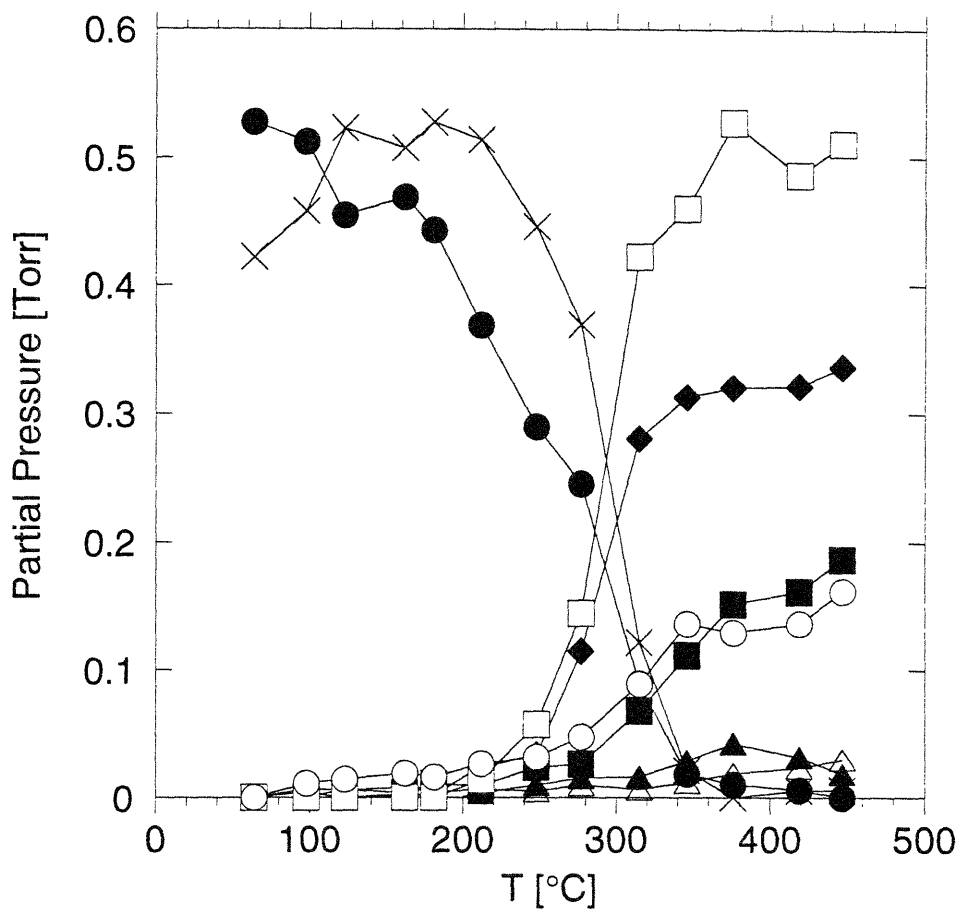


Figure 3.12. Partial pressures of tBAsE, DMZn and the hydrocarbon products for co-pyrolysis of tBAsE and DMZn in hydrogen at various temperatures; ● tBAsE, × DMZn, ◆ methane, ▲ ethane, ■ propene, □ 2-methylpropene, Δ 2-methylpropane, and ○ 1,5-hexadiene.

difficulty in differentiating between 2-methylpropene and 1-butene in the MBMS stems from almost identical fragmentation patterns of the isomers. However, the mass balance of the C₃, C₄ and C₆ hydrocarbons for pyrolysis temperatures above 400 °C indicates that the amount of 1-butene would not exceed ~10 % of the overall signal at $m/z=56$. The gas-phase contains only traces of 2-methylpropane and the ratios of 2-methylpropene *vs.* 2-methylpropane decrease with the pyrolysis temperature in a similar way as for pyrolysis of tBAs_e (Fig. 3.13). The presence of DMZn reduces the formation of propene at intermediate temperatures (250-400 °C) in favor of 1,5-hexadiene as compared to the pyrolysis of tBAs_e (Fig. 3.13). However, at high temperatures (above 400 °C) the ratio of propene *vs.* 1,5-hexadiene converges to the values found for tBAs_e. The partial pressure of methane increases with the pyrolysis temperature, while the formation of ethane slightly decreases above ~380 °C (Fig. 3.12). The partial pressures of methane and ethane account for only ~50% of the DMZn flux. It is expected that the methyl groups in the fluxes of MAs_e, DMs_e and 1-butene represent the remaining 50 %.

The relative intensities of the parent signals of tBAs_e, DAs_e, MAs_e and DMs_e formed during co-pyrolysis of tBAs_e and DMZn are shown in Fig. 3.14. In comparison to the pyrolysis of tBAs_e (Fig. 3.9), the quantity of DAs_e is reduced by a factor of ~4. The intensity of the MAs_e signal starts to increase with the onset of tBAs_e decomposition, reaching a maximum at ~300 °C. Above this temperature the signal starts to decay due to thermal decomposition of the compound [5]. Conversely, the signal of DMs_e keeps increasing with the pyrolysis temperature. Assuming the same sensitivity factors for the parent signals, the conversion of tBAs_e into the selenium side products is roughly 30%. Even though the presence of DMZn results in an increase of overall conversion of tBAs_e into selenium by-products, the partial pressure of DAs_e, a species significantly contributing to the carbon level in the layers, is negligible (conversion less than 3%).

The mechanism of the co-pyrolysis of tBAs_e and DMZn is complex and the MBMS allow only observation of volatile species. Thus, mechanistic details about the reactions between the precursors resulting in formation of non-volatile

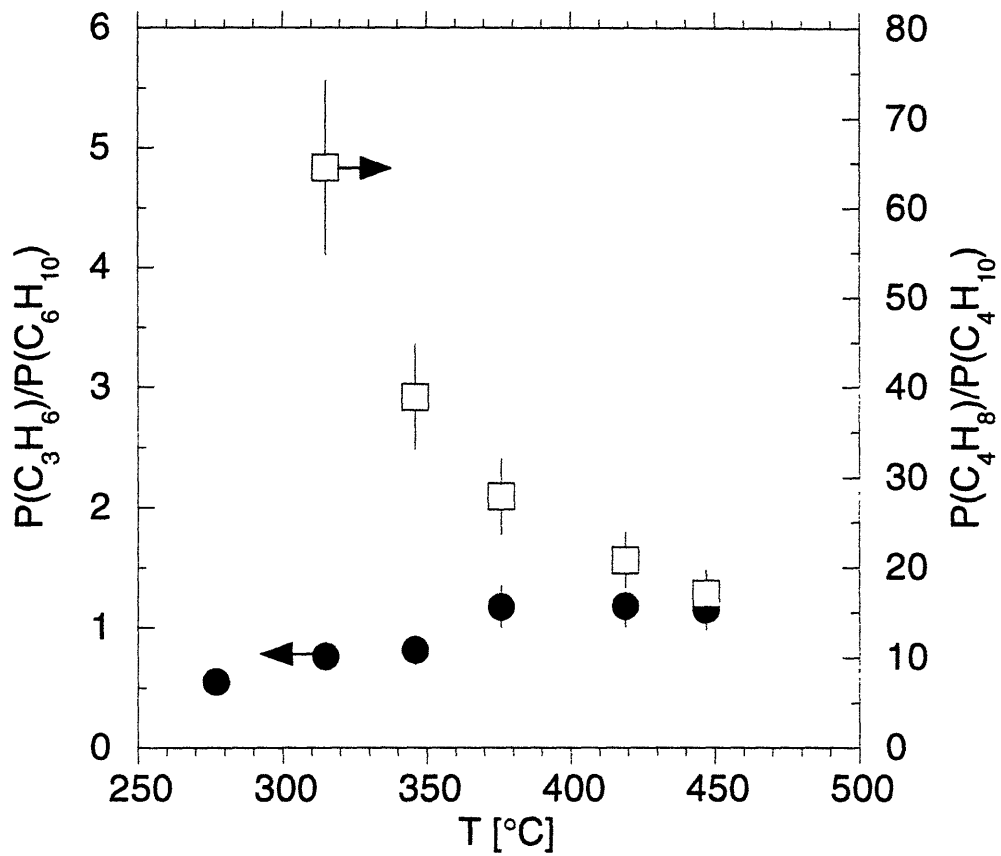


Figure 3.13. The partial pressure ratios of propene vs. 1,5-hexadiene (●) and 2-methylpropene vs. 2-methylpropane (□) for co-pyrolysis of tBAs and DMZn in hydrogen.

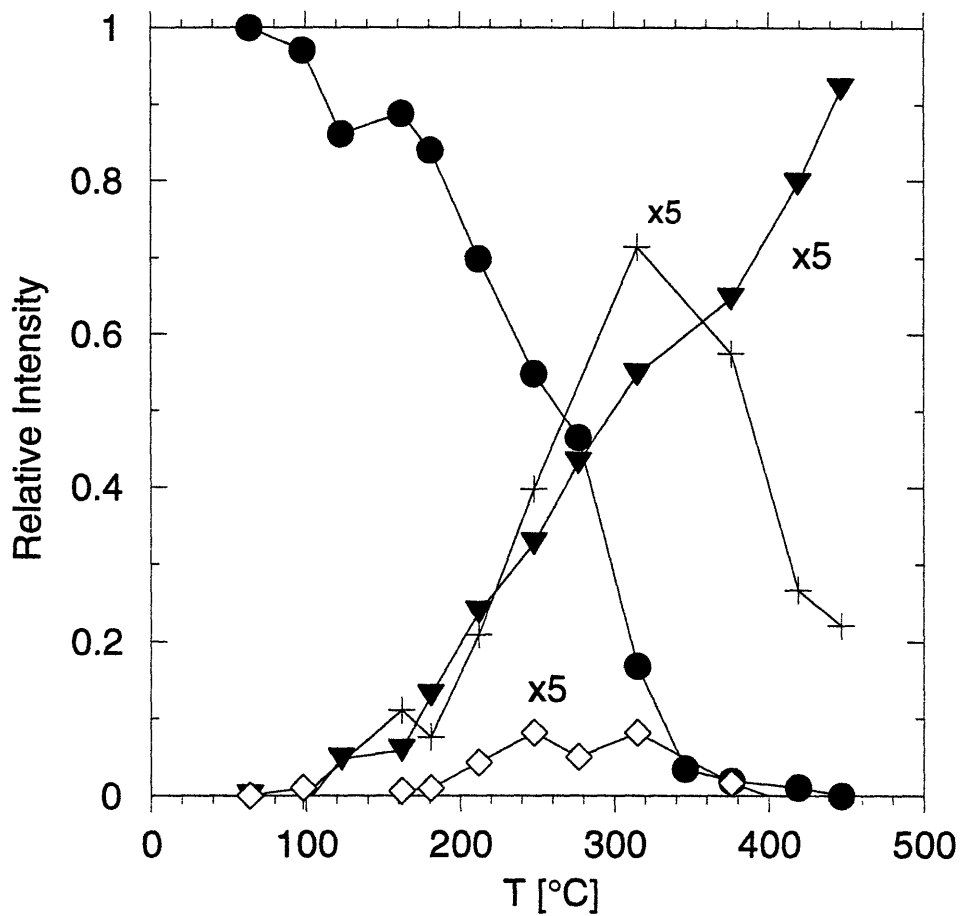


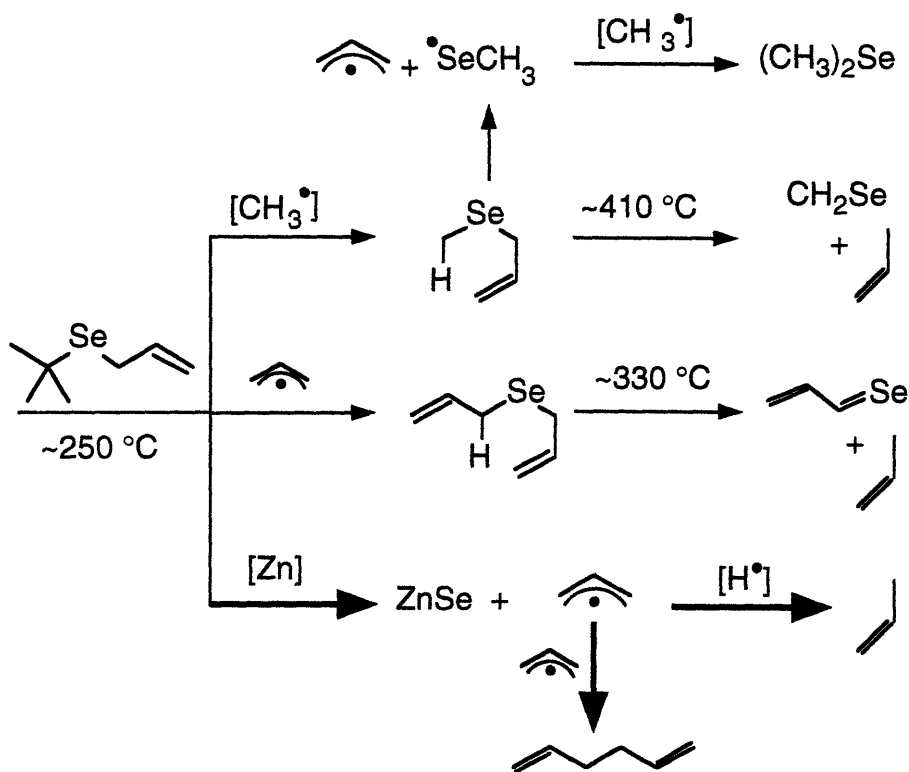
Figure 3.14. Relative MBMS intensities of tBAsE, DAsE, MAsE and DMsE for pyrolysis of tBAsE in hydrogen at various temperatures; ● tBAsE ($m/z=178$ amu), ◇ DAsE ($m/z=162$ amu), + MAsE ($m/z=136$), and ▼ DMsE ($m/z=110$ amu).

products remain obscured. However, some conclusions relevant for the mechanism of the growth can be derived from the MBMS data. The mass spectra of the tBAsE/DMZn mixture showed a negligible gas-phase pre-reaction between the precursors at room temperature. Such stability of the reagents is important for uniform growth and good surface morphology of the layers. Indeed, the layers grown from tBAsE showed a significant improvement in thickness uniformity and surface roughness in comparison with the films grown from hydrogen selenide under similar conditions. The pyrolysis study showed that DMZn in the presence of tBAsE decomposes at significantly lower temperatures than pure DMZn in hydrogen gas^{*)}. On the other hand, the decomposition of tBAsE seems to be affected only slightly by the presence of DMZn. Thus, the decomposition of the co-dosed DMZn is likely initiated by the reactive intermediates formed by pyrolysis of tBAsE. This result is consistent with the OMCVD experiments where tBAsE was found to be the growth limiting reagent in the kinetically controlled growth regime.

A gas-phase mechanism accounting for the formation of the selenium by-products is shown in Scheme 3.2. Allylselenium radicals, formed by pyrolysis of tBAsE, can recombine with allyl radicals to form DAsE or with methyl radicals to yield MAsE. At temperatures above ~400 °C MAsE decomposes to methylselenium radical [5] which may recombine with another methyl radical to yield the observed DMSe. The pathways leading to the allylselenium by-products compete for allylselenium radicals with DMZn or methyl zinc radicals. This reaction channel results in deposition of ZnSe and liberation of allyl radicals. Recombination reactions of allyl radicals account for the presence of 1,5-hexadiene, while hydrogen abstraction explain the formation of propene.

In order to grow ZnSe with a low carbon level, the side-reactions of allylselenium radicals leading to DAsE and MAsE have to be reduced. Low partial pressures of the precursors and a short reactor residence time are important growth parameters which can be used to control these unwanted side-reactions. The most undesirable by-product is DAsE since even low

^{*)} Under identical experimental conditions DMZn started to decompose above 250 °C; 50 % conversion was observed at ~350 °C. - Patnaik, S.; Jensen, K. F. unpublished results.



Scheme 3.2. Mechanism of formation of the selenium containing by-products for co-pyrolysis of tBAsE and DMZn. The major low temperature reactions are shown with bold arrows. The symbols $[\text{H}^\bullet]$ and $[\text{CH}_3^\bullet]$ stand for hydrogen radical and methyl radical donors; $[\text{Zn}]$ represents zinc bearing species, such as $(\text{CH}_3)_2\text{Zn}$, $\text{CH}_3\text{Zn}^\bullet$, and elemental zinc.

concentrations of this species in the gas-phase may result in extensive carbon incorporation. Fortunately, the formation of DAsE is significantly reduced in the presence of DMZn due to competing reactions resulting in the formation of MAsE and ZnSe deposition. Thus, low [VI/II] ratios in the gas-phase can be used to control the concentration of DAsE. Deposition temperature is also an important operating parameter which may provide control of the carbon level in the films. This is due to the fact that tBAsE decomposes at significantly lower temperatures than DAsE and MAsE and this higher reactivity of tBAsE is reflected in higher growth rates. Therefore, if the films are grown at low temperatures (below ~400 °C), the contribution of the allylselenium by-products to the growth should be marginal.

3.4. Conclusion

OMCVD experiments in combination with the MBMS pyrolysis study showed that tBAsE a successfully designed precursor for low temperature growth of ZnSe. The retro-ene pyrolysis pathway, characteristic of MAsE and DAsE, is not available for tBAsE and the films show a negligible carbon contamination, typically below the detection limit of SIMS ($\sim 5 \times 10^{17}$ atoms/cm³). The ZnSe films display smooth surface morphology, good crystalline quality, and photoluminescence spectra with sharp near band-edge emission. A complex pyrolysis mechanism of the heteroleptic precursor complicates the growth chemistry due to the formation of DAsE and MAsE by-products. In order to reduce the extent of the side-reactions potentially affecting the quality of the layers, OMCVD growth has to be carried out at a low temperature, low partial pressures of the precursors, low [VI/II] ratios and a short reactor residence time. Such growth conditions are also desirable for synthesis of uniform layers with a low density of structural defects.

References:

- [1] (a) Park, R.M.; Troffer, M.B.; Rouleau, C.M.; Depuydt, J.M.; Haase, M.A. *Appl. Phys. Lett.*, **1990**, *57*, 2127. (b) Haase, M.A.; Qiu, J.; Depuydt, J.M.; Cheng, H. *Appl. Phys. Lett.* **1991**, *59*, 1272. (c) Xie, W.; Grillo, D.C.; Gunshor, R.L.; Kobayashi, M.; Hua, G.C.; Otsuka, N.; Jeon, H.; Ding, J.; Nurmikko, D.V. *Appl. Phys. Lett.*, **1992**, *60*, 463. (d) Jeon, H.; Ding, J.; Patterson, W.; Nurmikko, D.V.; Xie, W.; Grillo, D.C.; Kobayashi, M.; Gunshor, R.L. *Appl. Phys. Lett.*, **1991**, *59*, 3619. (e) Haase, M. A.; P. F. Baude; Hagedorn, M. S.; Qui, J.; DePuydt, J. M.; Cheng, H.; Guha, S. Hofler, G. E.; Wu, B. J. *Appl. Phys. Lett.*, **1993**, *63*, 2315. (f) Grillo, D. C.; Fan, Y.; Han, J.; He, L.; Gunshor, R. I.; Salokatve, A.; Hagerott, M.; Jeon, H.; Nurmikko, A. V.; Hua, G. C.; Otsuka, N. *Appl. Phys. Lett.* **1993**, *63*, 2723. (g) Grillo, D. C.; Fan, Y.; Han, J.; He, L.; Gunshor, R. I.; Salokatve, A.; Hagerott, M.; Jeon, H.; Nurmikko, A. V.; Hua, G. C.; Otsuka, N. *Appl. Phys. Lett.* **1993**, *63*, 2723. (g) Petruzzello, J.; Drenten, R.; Gaines, J. M. *J. Cryst. Growth* **1994**, *138*, 686.
- [2] (a) Giapis, K. P.; Lu, D. C.; Jensen, K. F., *Appl. Phys. Lett.* **1989**, *54*, 353. (b) J.-S. Huh, Patnaik, S.; Jensen, K. F. *J. Electron. Mater.* **1993**, *22*, 509.
- [3] for a recent reviews see (a) Jones, A. C.; Wright, P. J.; Cockayne, B. J. *Cryst. Growth* **1991**, *107*, 297. (b) O'Brien, P. *Chemtronics* **1991**, *5*, 61. (c) Jones, A. C. *J. Cryst. Growth* **1993**, *129*, 728.
- [4] (a) Giapis, K. P.; Jensen, K. F.; Potts, J. E.; Pachuta, S. J. *Electron. Mater.* **1990**, *19*, 453. (b) Patnaik, S.; Jensen, K. F.; Giapis, K. P. *J. Cryst. Growth* **1991**, *107*, 390.
- [5] Patnaik, S.; Ho, K-L.; Jensen, K. F.; Gordon, D. C.; Kirss, R. U.; Brown, D. W. *Chem. Mater.* **1993**, *5*, 305.
- [6] (a) Kuhn, W.; Naumov, A.; Stanzl, H.; Bauer, S.; Wolf, K.; Wagner, H. P.; Gebhardt, W.; Pohl, U. W.; Krost, A.; Richter, W.; Dumichen, U.; Thiele, K. *J. Cryst. Growth* **1992**, *123*, 605. (b) Stanzl, H.; Wolf, K.; Bauer, S.; Kuhn, W. Naumov, A. *J. Electron. Mater.* **1993**, *22*, 501. (c) Kuhn, W.; Driad, R.; Stanzl, H.; Lusson, A.; Wolf, K.; Qu'Hen, B.; Sahin, H.; Svob, L.; Grattepain, C.; Quesada, X.; Gebhardt, W.; Gorochoy, O. *J. Cryst. Growth* **1994**, *138*, 448.
- [7] (a) Nishimura, K.; Nagao, Y.; Sakai, K. *Jpn. J. Appl. Phys.* **1993**, *32*, L428. (b) Nishimura, K.; Nagao, Y.; Sakai, K. *J. Cryst. Growth* **1993**, *134*, 293.

- [8] (a) Stutius, W. *Appl. Phys. Lett.*, **1981**, *38*, 352. (b) Stutius, W. *J. Electron. Mater.*, **1981**, *10*, 95.
- [9] Lee, P. W.; Omstead, T. R.; McKenna, D. R.; Jensen, K. F. *J. Cryst. Growth* **1987**, *85*, 165.
- [10] (a) Danek, M.; Huh, J-S.; Jensen, K. F. Gordon, D. C.; Kosar, W. P. *Mat. Res. Soc. Symp. Proc. Vol. 334*, **1994**, 231. (b) Huh, J-S. Ph.D. Thesis. MIT. **1994**.
- [11] Skromme, B. J.; Liu, W.; Jensen, K. F.; Giapis, K. P. *J. Cryst Growth* **1994**, *138*, 338.
- [12] Giapis, K.P.; Lu, D.-C. Fotiadis; D.I.; Jensen, K.F. *J. Cryst. Growth*, **1990**, *104*, 629.
- [13] (a) Blackham, A. U.; Eatough, N. L. *J. Amer. Chem. Soc.* **19962**, *84*, 2922. (b) V. N. Kondratiev, Rate Constant of Gas Phase Reactions, NSRDS, National Bureau of Standarads, U. S. Dept. Commerce, Washington, DC, 1972, pp 176-177.
- [14] Kirss, R. U.; Brown, D. W.; Higa, K. T.; Gedridge, Jr.,R. W. *Organometallics* **1991**, *10*, 3589.
- [15] (a) G. Martin, N. Barroeta, *Int. J. Chem. Kinet.* **12**, 699 (1980), (b) G. Martin, H. Martinez, J. Ascanio, *Int. J. Chem. Kinet.* **21**, 193 (1989), (c) G. Martin, J. Ascanio, *React. Kinet. Catal. Lett.* **43**, 13 (1991).
- [16] M. Danek, S. Patnaik, K. F. Jensen, D. C. Gordon, D. W. Brown, and R. U. Kirss, *Chem. Mater.* **1993**, *5*, 1321.
- [17] Foster, D. F.; Bell, W.; Stevenson, J.; Cole-Hamilton, D. J.; Hails, J. E. *J. Cryst. Growth* - in press.
- [18] Benson, S. W *J. Chem. Soc. Faraday Trans. 2* **1987**, *83*, 791.
- [19] Gibson, S. T.; Greene, J. P.; Berkowitz, J. *J. Chem. Phys.* **1986**, *85*, 4815.
- [20] (a) Kamata, A.; Mitsuhashi, H.; Fujita, H. *Appl. Phys. Lett.*, **1993**, *63*, 3353. (b) Wolk, J. A.; Ager, J. W.; Duxstad, K. J.; Haller, E. E.; Taskar, N. R.; Dorman, D.R.; Olego, D.J. *Appl. Phys. Lett.*, **1993**, *63*, 2756.

Chapter 4

OMCVD of ZnSe with Trialkylphosphine Selenides

4. 1. Introduction

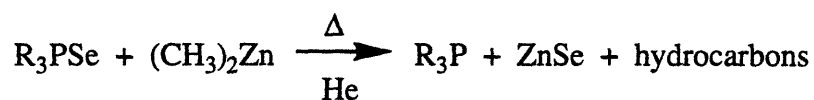
The concept of carrier injection devices operating in the blue and green spectral regions has stimulated extensive research on the deposition and doping of ZnSe epitaxial layers. In particular, the synthesis of low resistivity p-type ZnSe represents a considerable challenge due to the tendency of the material to compensate acceptor states by formation of native donor defects [1]. Although several elements from groups Ia and Va, including Li [2], N [3], P [4], and As [5] were proposed as p-type dopants in ZnSe, only nitrogen doped layers prepared by Molecular Beam Epitaxy (MBE) in combination with nitrogen plasma doping showed properties suitable for construction of diode lasers and light emitting diodes [3,6].

The advances in MBE synthesis of ZnSe:N have not yet been mirrored by OMCVD. Attempts to dope ZnSe with nitrogen in thermal or plasma assisted OMCVD using dopants such as ammonia [7], amines [8], hydrazine [9], and hydrazoic acid and its derivatives [10], resulted in highly compensated layers. Even though nitrogen concentrations in the doped films prepared by OMCVD were quite high ($\sim 10^{18}$ - 10^{19} atoms/cm³), the density of free holes was negligible, typically $< 3 \times 10^{15}$ cm⁻³. Employing FTIR spectroscopy and SIMS, Wolk *et al.* [11] and Kamata *et al.* [12] discovered that the origin of the unsuccessful doping was the formation of electrically inactive N-H complexes. However, growth experiments showed that the solution to this problem is not as simple as selecting hydrogen free dopants and carrier gas. For example, OMCVD growth from MAsE and diethylzinc (DEZn) in a helium carrier gas resulted in heavy contamination of the films with hydrogen ($> 10^{20}$ atoms/cm³), while the films deposited in a hydrogen carrier

showed a significantly lower hydrogen content ($\sim 10^{19}$ atoms/cm³) [13]. Therefore, organometallic precursors themselves can be effective sources of hydrogen contamination.

Precursors containing Se-H bonds, such as hydrogen selenide or alkylselenols, are good hydrogen donors due to the low enthalpy of Se-H bonds [14]. Foster *et al.* found that homolysis of Se-H bonds is the dominant decomposition pathway of aliphatic selenols under gas-phase pyrolysis conditions [15]. However, reactive species containing the Se-H moiety can be generated during deposition from dialkylselenium compounds if β -hydrogen transfer significantly contributes to the conversion of the precursors. Therefore, OMCVD with these precursors may likely result in a heavy hydrogen contamination even at low temperature deposition conditions. Such an explanation would account for the relatively high hydrogen levels ($\sim 10^{19}$ atoms/cm³) in the films grown from *tert*-butyl(allyl)selenium and di-*tert*-butylselenium [13,16]. Activation of C-H bonds and hydrogen gas can be expected at high growth temperatures or under plasma assisted deposition conditions.

In order to circumvent hydrogen incorporation during OMCVD growth of ZnSe, a new precursor chemistry, relying on the use of trialkylphosphine selenides in combination with dimethylzinc (DMZn) and helium carrier gas, is proposed:



Murray *et al.* [17] described similar precursor chemistry, combining dimethylcadmium and trialkylphosphine selenides or tellurides, for liquid phase synthesis of high optical quality CdE (E=Se, Te) nanocrystals. However, application of trialkylphosphine selenides in ZnSe OMCVD introduces several potential problems which are not encountered in the liquid phase synthesis of II-VI semiconductors: (1) The compounds are low melting point

solids with low vapor pressures (in the mTorr range) and standard delivery into an OMCVD system by a carrier gas might be difficult [18]. (2) Decomposition of the parent phosphine under growth conditions, either in the gas-phase or on the ZnSe surface, may result in phosphorus incorporation and unintentional doping of the material. Phosphorus is a shallow acceptor in ZnSe at concentrations below $\sim 10^{16}$ atoms/cm³, however, above this level it forms deep acceptor states whose presence cannot be tolerated in optoelectronic applications [4,19]. (3) The combination of the low vapor pressures and high affinity to metal surfaces raises concerns about maintenance problems and deposition reproducibility.

The purpose of the present study was to test the proposed OMCVD chemistry for synthesis of high optical quality ZnSe layers. To our knowledge there is no report in the literature about the use of phosphine selenides as selenium precursors in OMCVD of II-VI semiconductors. Tripropylphosphine selenide (TPPSe) was selected as the selenium precursor in the initial stage of the research due to its low melting point (~ 32 °C) and availability of the parent phosphine from commercial sources. Growth experiments with TPPSe were carried out under various deposition conditions and the quality of the films was assessed from low temperature photoluminescence (PL) spectra and SIMS analysis. Particular attention was paid to hydrogen, carbon, and phosphorus incorporation. The opportunity to improve the vapor pressure characteristics of the precursors was explored with unsymmetrical trialkylphosphine selenides. Specifically, dimethyl(butyl)phosphine selenide (DMBPSe) proved to be a promising reagent due to its volatility and relatively low melting point (~ 56 °C). Deposition experiments with DMBPSe aimed to probe the stability of the phosphine moiety under growth conditions and assess the feasibility of the precursor for synthesis of high quality ZnSe.

4.2. Experimental

Trialkylphosphine selenides. TPPSe was synthesized by reacting elemental selenium (electronic grade, Aesar) with tripropylphosphine (95%, Aldrich) under nitrogen (UHP, Matheson) according to the procedure described by Zingaro *et al.* [20]. DMBPSe, prepared *via* the same route, was supplied from AT&T Bell Laboratories. The precursors were purified by purging with hydrogen for several hours prior to use to remove volatile impurities. The vapor pressures were measured on a high vacuum system equipped with a MKS Baratron (10 Torr range) and a Leybold-Heraeus turbomolecular pump (model TMP 150). Before the measurement the samples were thoroughly degassed by several thaw-freeze-pump cycles.

OMCVD growth. Growth experiments were carried out in a vertical downflow OMCVD reactor equipped with a laser interferometer for *in-situ* monitoring of growth rate [21]. A schematic of the OMCVD reactor is shown in Fig. 4.1. The substrates were semi-insulating or Zn-doped (100) GaAs (Crystal Specialties). Prior to OMCVD growth, the substrates were degreased in boiling 1,1,2-trichloroethylene (10 min) and acetone (10 min), etched in sulfuric acid (30 sec), thoroughly rinsed in DI water and dried in a stream of nitrogen. The prepared wafers were immediately loaded into the reactor and annealed at ~450 °C for 10 min in a stream of helium carrying vapors of TPPSe or DMBPSe, respectively. The purpose of this pre-treatment step was to remove the residual oxide layer and passivate the GaAs surface. The phosphine selenides and DMZn (electronic grade, Epichem) were delivered into the reactor by a helium or hydrogen carrier gas (UHP, Matheson) at a total flow rate of ~1000 sccm. The films were grown at a reactor pressure of 300 Torr.

Film characterization. The surface morphology was inspected on a Cambridge scanning electron microscope (Model 250 Mk3). The 10 K photoluminescence (PL) spectra were measured on a set-up equipped with a closed-cycle compressed helium cryostat (Janis), 0.50m spectrometer (Jarrell Ash) and PMT detector (Hamamatsu). The 325 nm line of a He-Cd laser with

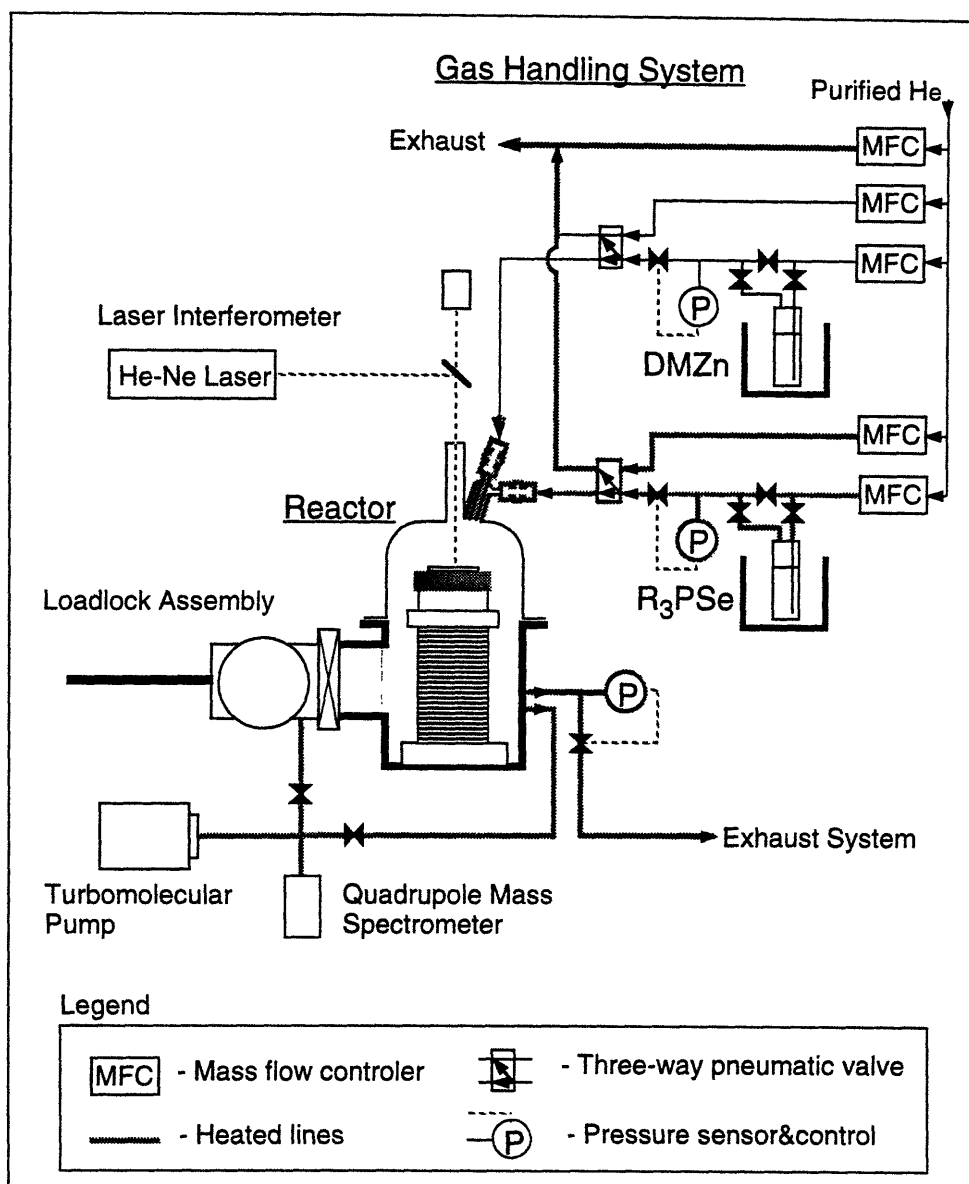


Figure 4.1. Schematic of the OMCVD reactor and gas-handling system used for growth experiments with the phosphine selenides.

an incident power density of ~ 300 mW/cm² was used for the optical pumping of the samples. The 1.9 K PL spectra were recorded on a Spex 1404 spectrometer with a 0.85 m double monochromator. The samples were excited with the 325 nm line of a He-Cd laser at a low incident power density (~ 60 mW/cm²). The SIMS analysis was performed by the Charles Evans & Associates laboratory (Ridwood City, CA) using Cs⁺ ion bombardment (ion current of 53 nA, ion impact energy of 14.5 keV) coupled with a negative secondary ion spectrometry. The beam was rastered over a square area $\sim 150 \times 150$ μm large. An electron flood gun was used to compensate for sample charging. Quantification of H secondary ion counts was based on the relative sensitivity factors derived from ²H implants of a known dose in ZnSe. Quantification of C and P secondary ion counts is based on calculated relative sensitivity factors (Charles Evans & Associates).

4.3. Results and Discussion

4.3.1. OMCVD of ZnSe with Tripropylphosphine Selenide (TPPSe)

Even though TPPSe melts at 32 °C, the vapor pressure of the liquid was too low at this temperature to maintain acceptable growth rates of ZnSe. In order to increase the delivery rates of the precursor, the TPPSe bubbler had to be heated to 90 °C and the temperature of the supply lines maintained at 100-120°C to avoid condensation of the precursor. Despite the elevated temperature of the lines, mixing of TPPSe and DMZn fluxes at the reactor inlet did not result in any severe pre-reaction between the precursors. The reactor nozzle remained without any deposits after many successive growth runs, which allowed reproducible synthesis of ZnSe films. This observation contrasts with the fast pre-reaction between H₂Se and DMZn, resulting in a heavy wall deposit even at room temperature.

Figure 4.2. displays the temperature dependence of the growth rate of ZnSe formed from TPPSe and DMZn in a helium carrier gas. Below ~ 450 °C the

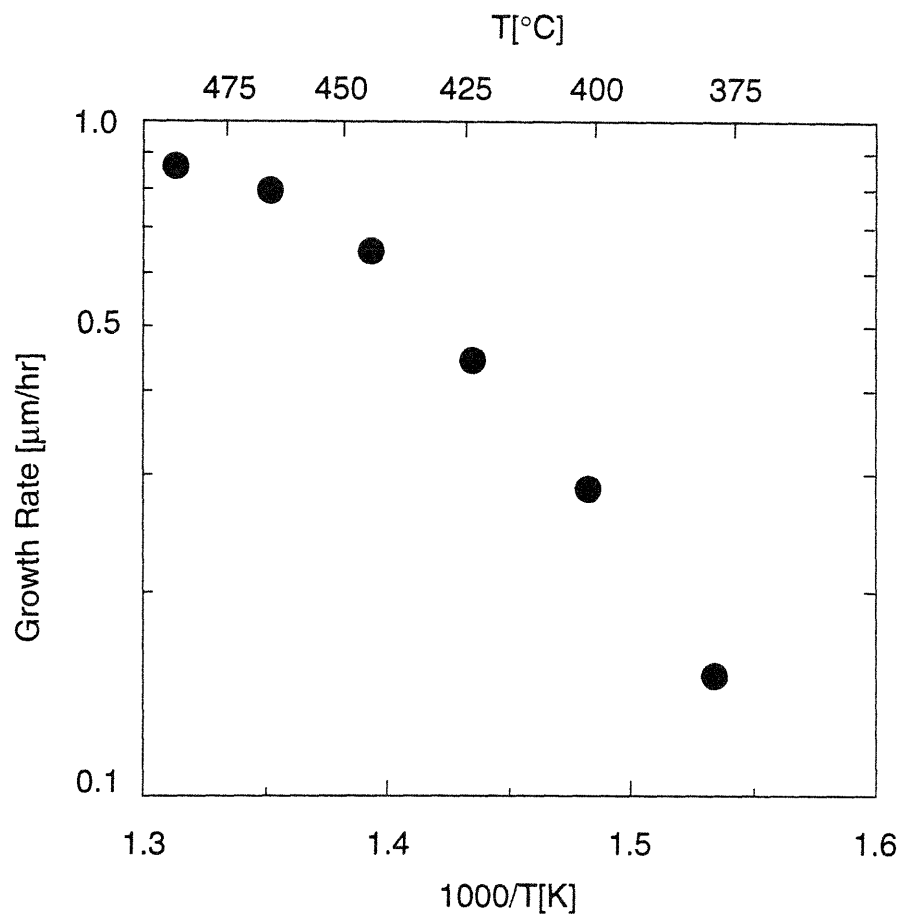


Figure 4.2. Temperature dependence of ZnSe growth rate. The ZnSe film was deposited from TPPSe ($5\mu\text{mol/min}$) and DMZn ($5\mu\text{mol/min}$) in helium at 300Torr.

growth was kinetically controlled with an apparent activation energy of ~ 18 kcal/mol. The growth rate at 425 °C was insensitive to variations in the DMZn delivery rate (range 2.5-10 $\mu\text{m}/\text{min}$), indicating that TPPSe is the rate-limiting reagent. In preliminary experiments we found that an increase in growth rate could be accomplished by using diethylzinc (DEZn) due to its lower thermal stability in comparison to DMZn. However, the possibility of decomposition of the precursor *via* β -hydride elimination renders DEZn less suitable for growth of hydrogen free layers [22].

SEM micrographs of the film surface morphologies for various deposition temperatures are displayed in Fig. 4.3. The surface of the films grown at 375-450 °C had the characteristic "orange peel" texture. The morphology deteriorated with increasing deposition temperature. Nevertheless, the thickness uniformity and surface roughness of the films were superior to those for the films grown from hydrogen selenide and DMZn [23] or DMZnNEt₃ [24]. These results are consistent with a low reactivity of TPPSe under the deposition conditions.

The SIMS depth profiles for hydrogen, phosphorus and carbon concentrations in a film grown from TPPSe and DMZn in helium at 400 °C are shown in Fig. 4.4. The data are compared to the depth profiles for a film grown from tBAsE and DMZnNEt₃ in hydrogen at 350 °C. The hydrogen concentration in the film from TPPSe was low ($\sim 1 \times 10^{18}$ atoms/cm³), comparable to the detection limit of the SIMS analysis, while the hydrogen concentration in the reference sample reached $\sim 10^{19}$ atoms/cm³. However, the hydrogen level increased sharply at the ZnSe/GaAs interface, indicating contamination of the substrate in the initial stage of the growth. The phosphorus level in the film was very low ($\sim 10^{16}$ atoms/cm³), near the detection limit of the SIMS analysis (Fig. 4.4b). The interface with GaAs showed contamination with phosphorus at the level of $\sim 10^{19}$ atoms/cm³. The carbon concentration in the film was also marginal ($< 10^{17}$ atoms/cm³), even lower than in the sample grown from tBAsE (Fig. 4.4c). The increase of the carbon concentration at the interface again points to contamination of the substrate.

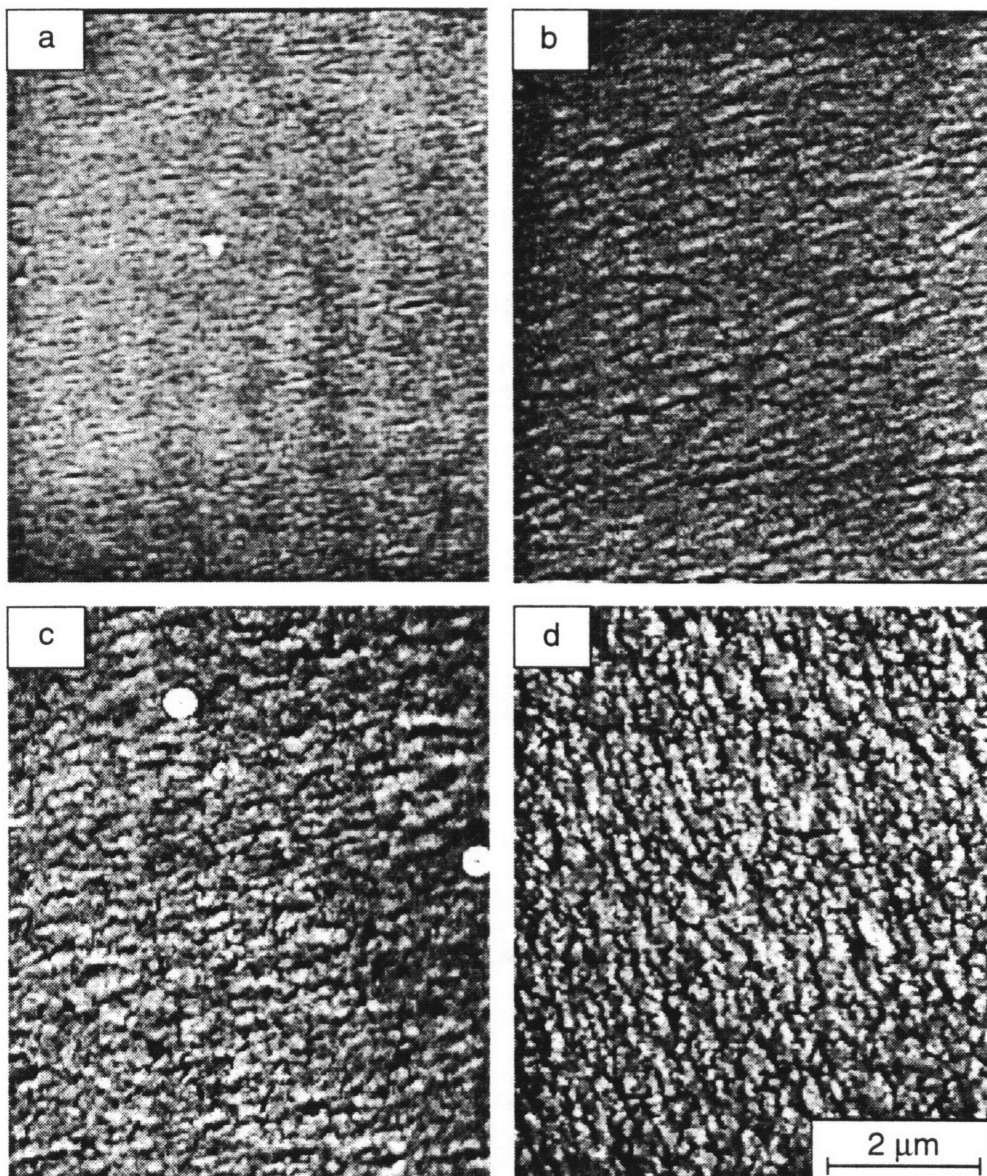


Figure 4.3. SEM images of surface morphology of ZnSe films grown from TPPSe ($5\mu\text{mol}/\text{min}$) and DMZn ($5\mu\text{mol}/\text{min}$) in He at $375\text{ }^\circ\text{C}$ (a), $400\text{ }^\circ\text{C}$ (b), $425\text{ }^\circ\text{C}$ (c), and $450\text{ }^\circ\text{C}$ (d). The layer thicknesses were $\sim 0.5\mu\text{m}$ (a,b) and $\sim 1.0\mu\text{m}$ (c,d).

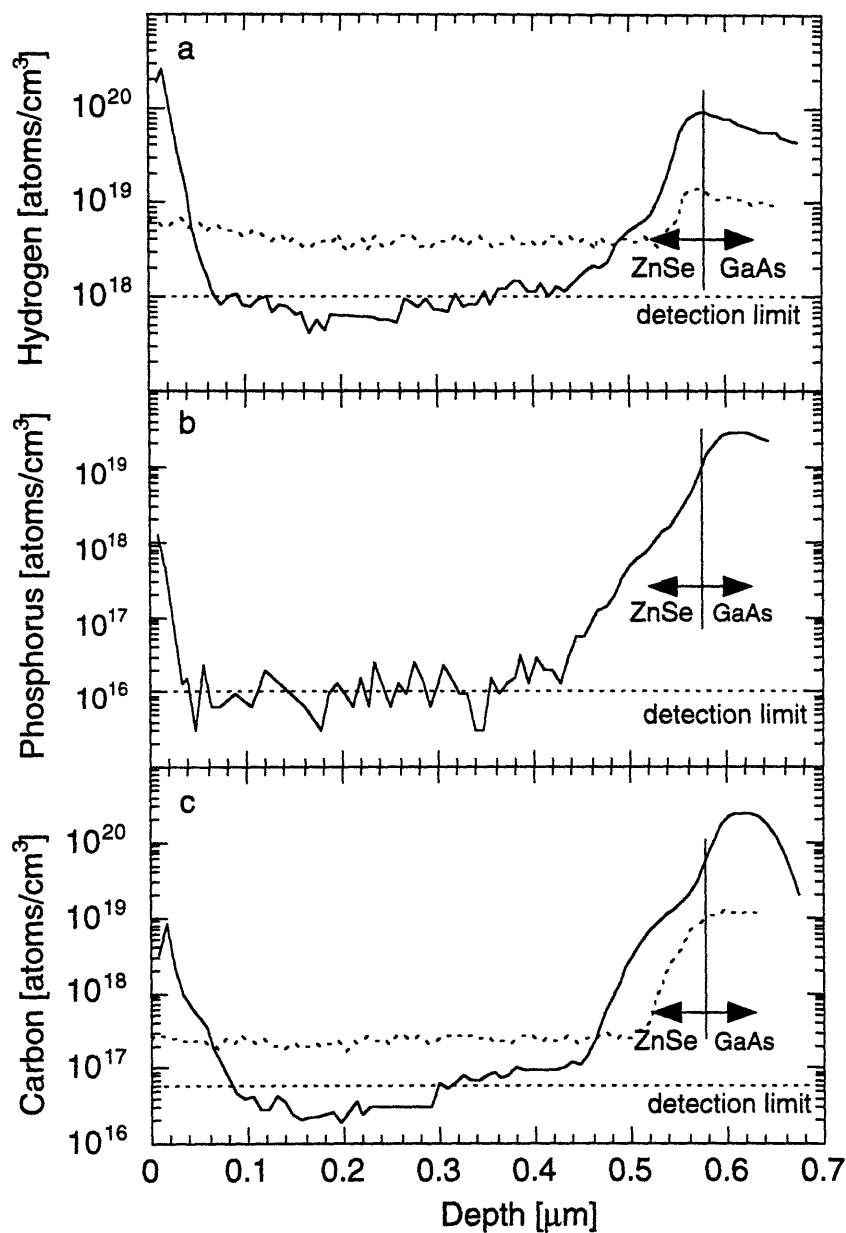


Figure 4.4. SIMS concentration profiles for hydrogen (a), phosphorus (b), and carbon (c) in films grown from TPPSe ($5\mu\text{mol}/\text{min}$) and DMZn ($5\mu\text{mol}/\text{min}$) in He at 400 °C (solid curve), and tBAsSe ($40\mu\text{mol}/\text{min}$) and DMZnNEt₃ ($20\mu\text{mol}/\text{min}$) in H₂ at 350 °C (dashed curve).

The results of the SIMS analysis justify the proposed precursor chemistry for OMCVD of ZnSe with a low hydrogen content. The low contents of phosphorus and carbon are consistent with good stability of the tripropylphosphine moiety under the deposition conditions. This conclusion is not surprising since trialkylphosphines are known to be highly stable in III-V growth systems [25]. The contamination of the ZnSe/GaAs interface is likely related to the high temperature pre-treatment step in vapors of TPPSe.

OMCVD experiments revealed a high reactivity of TPPSe in a hydrogen carrier gas, resulting in a fivefold increase of the growth rate in comparison with growth in helium. Although the films still displayed a good surface morphology (Fig. 4.5), the build-up of the wall deposit in the reactor nozzle indicated the presence of a gas-phase pre-reaction between the precursors. The SIMS data for a film grown at 400 °C in hydrogen are shown in Fig. 4.6. The hydrogen and phosphorus levels reached $\sim 3 \times 10^{18}$ - 1×10^{19} atoms/cm³, while the carbon level remained very low ($< 10^{17}$ atoms/cm³). This result argues for selection of helium or other inert carrier gas for growth of hydrogen free ZnSe.

Low temperature PL spectroscopy was employed to probe optical quality of the layers. Fig. 4.7 displays the 10K PL spectra of nominally undoped films grown at 425 °C for various [TPPSe/DMZn] ratios. The near band-edge emission spectra measured at 1.9K at a low excitation power are shown in Fig. 4.8. The spectra consist of a strong near band-edge emission and weak deep level emission. The band edge emission is composed of partially resolved free exciton lines at ~ 2.804 eV (E_x^{hh}) and 2.7995 eV (E_x^{lh}), and lines of donor-bound excitons at 2.7965 eV (I_2^{hh}) and 2.7942 eV (I_2^{lh}). The splitting of the degenerated valence band into the heavy and light hole components is due to the tensile strain induced by the thermal expansion mismatch between the substrate and ZnSe [26]. The effect of the compressive lattice mismatch induced strain on the shape and position of the excitonic lines is marginal since the film thicknesses are much larger than the critical thickness for ZnSe/GaAs heteroepitaxy (~ 0.15 μm) [27]. The position of the free exciton and

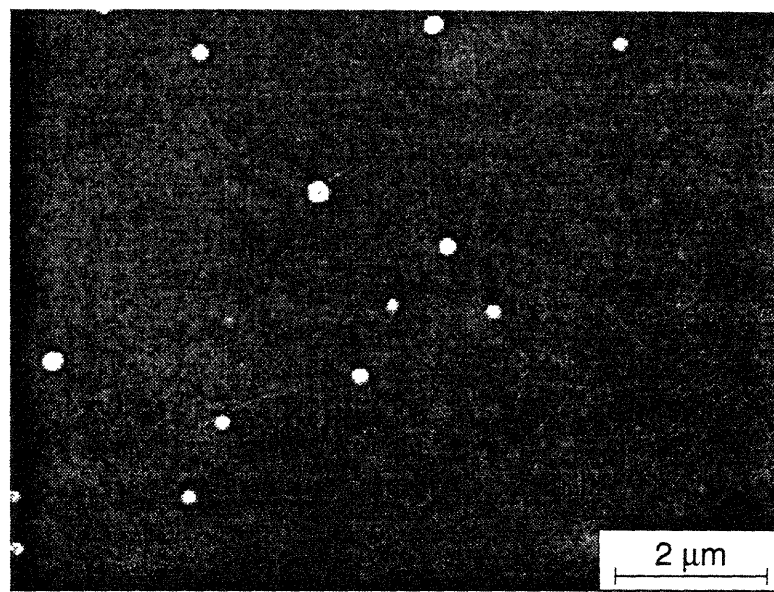


Figure 4.5. SEM image of a ZnSe film grown from TPPSe (5 μmol/min) and DMZn (5 μmol/min) in H₂ at 400 °C. The layer thickness was ~0.5 μm. The white particles were identified by Auger electron spectroscopy as ZnSe.

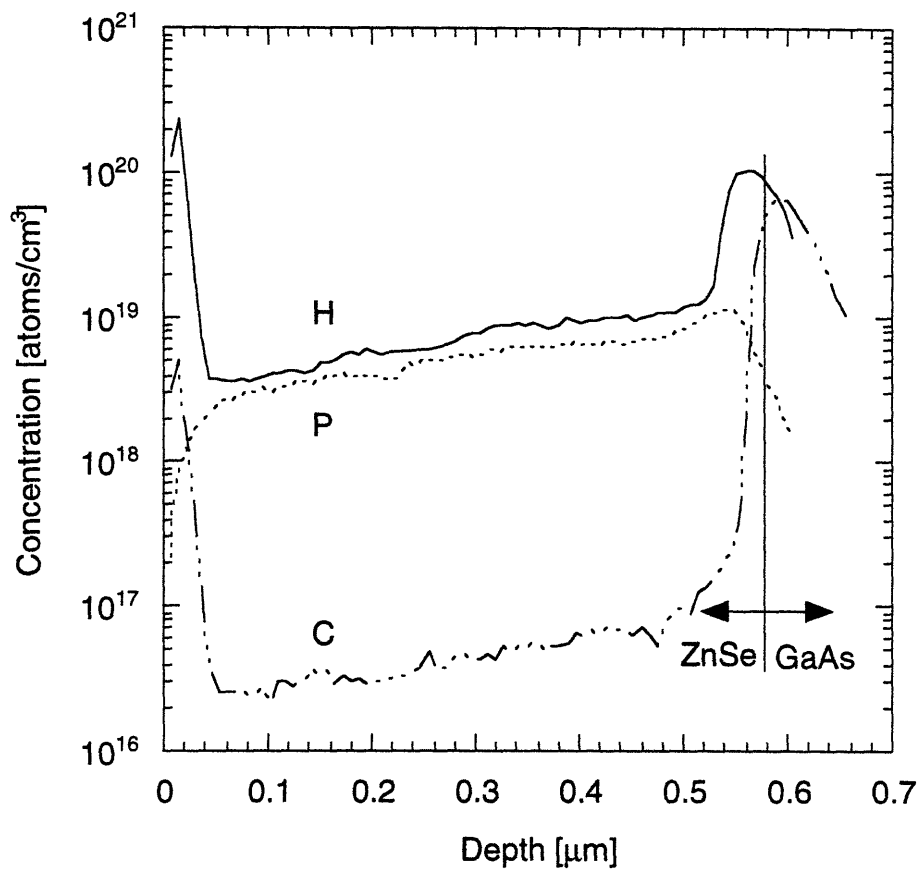


Figure 4.6. SIMS concentration profiles for hydrogen, phosphorus, and carbon in a films grown from TPPSe ($5\mu\text{mol}/\text{min}$) and DMZn ($5\mu\text{mol}/\text{min}$) in H_2 at $425\text{ }^\circ\text{C}$.

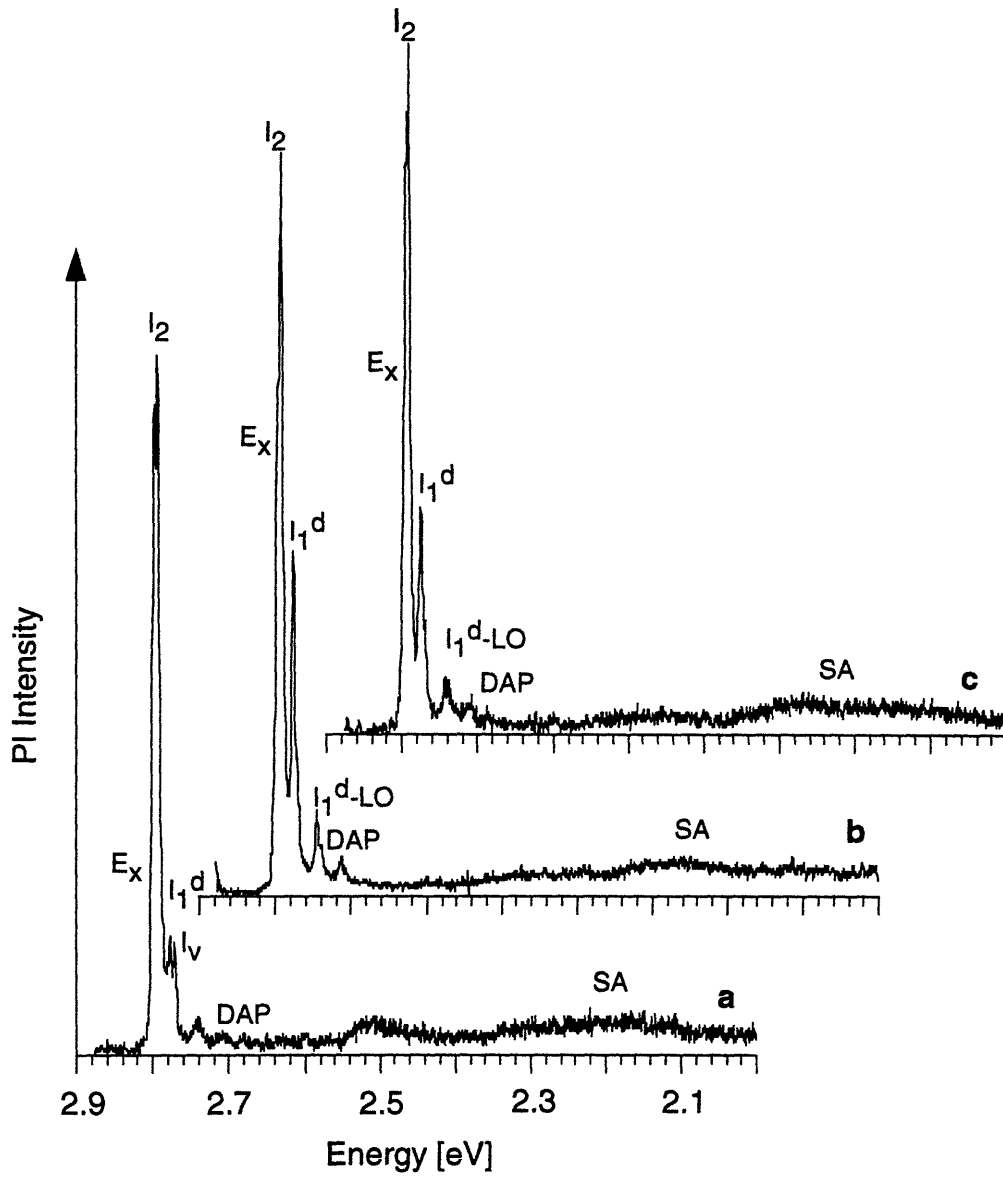


Figure 4.7. 10 K PL spectra of ZnSe grown from TPPSe ($5\mu\text{mol}/\text{min}$) and DMZn in He at $425\text{ }^\circ\text{C}$ at the [VI/II] ratio equals to 0.5 (a), 1 (b) and 2 (c). The film thicknesses were $\sim 1\ \mu\text{m}$.

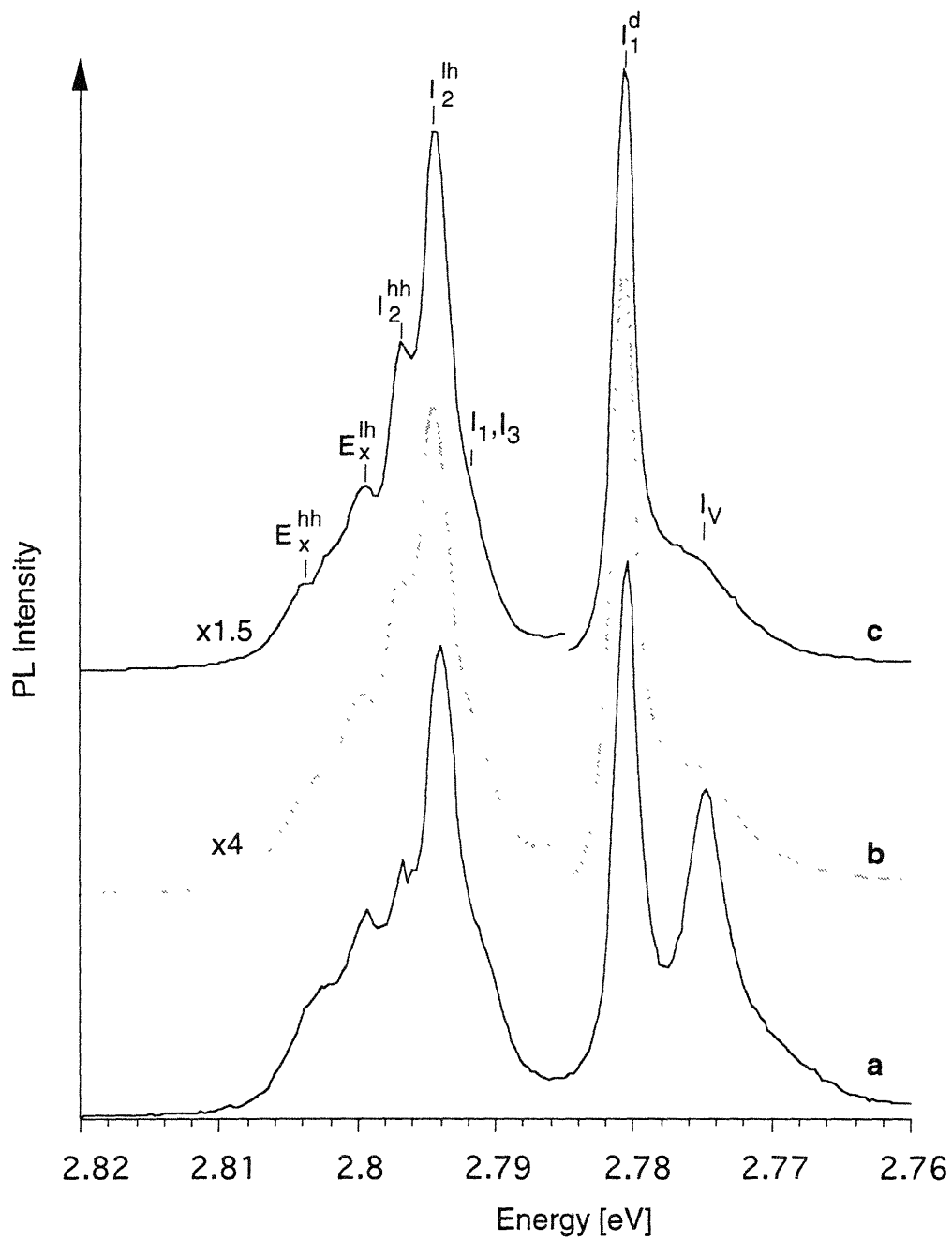


Figure 4.8. 1.9 K near band-edge PL of ZnSe. The films were grown from TPPSe (5 μ mol/min) and DMZn in He at 425 $^{\circ}$ C at the [VI/II] ratio equals to 0.5 (a), 1 (b) and 2 (c). The film thicknesses were \sim 1 μ m.

donor-bound exciton lines is in a good agreement (within 1 meV) with the data reported for fully relaxed films grown from H₂Se and DMZnNEt₃ [24]. The shallow donor state in the films likely originates from chlorine or gallium. Chlorine bearing impurities are expected contaminants in commercial tripropylphosphine, and gallium may interdiffuse from the ZnSe/GaAs interface at the relatively high growth temperatures. Identification of the shallow donor states in ZnSe from PL spectra is difficult due to the narrow range of the donor binding energies (26-29 meV) [28] and the pronounced tendency of the material to incorporate n-type impurities. The variation of the [VI/II] ratio had no significant effect on the position and shape of free and donor bound excitonic lines.

The weak shoulder on the low energy side of the I₂^{lh} line can be assigned either to excitons bound to ionized donors (I₃) or to shallow acceptor-bound excitons (I₁) [29]. The localization energy of 2.791 eV coincides with the I₁ line of shallow phosphorus donors observed on ZnSe:P films prepared by MBE [4]. Identical localization energy can be estimated for a phosphorus acceptor from the known binding energy (88.4 meV) using Hayne's rule [29]. This assignment is also in agreement with the SIMS analysis, revealing only a marginal concentration of phosphorus (<10¹⁶ atoms/cm³).

The strong emission line at 2.7805 eV with the characteristic LO phonon replicas corresponds to a deep acceptor-bound exciton (I₁^d). The origin of this state in ZnSe is controversial and zinc vacancies (V_{Zn}) associated with neutral donors [30] or copper impurities [13] have been proposed. The film grown under zinc-rich conditions showed a significant decrease in the intensity of the I₁^d line. The low energy shoulder of the I₁^d line at 2.775 eV can be attributed to selenium site defects (I_v) [31]. This emission line is particularly pronounced in the spectrum of the film grown at [VI/II]=0.5 because of the decrease in the intensity of the I₁^d line.

At lower energies, the PL spectra display a weak donor-acceptor pair emission (DAP) with the zero LO phonon line at ~2.724 eV. The position of

this line is characteristic of phosphorus in the shallow acceptor state bound to a shallow donor [29]. The spectra show only a marginal Y_0 emission at 2.600 eV, associated with extended structural defects in ZnSe [32]. The optical quality of the layers is further substantiated by the weak deep level emission at energies below ~ 2.5 eV. Such deep level emission is often attributed to zinc vacancies (self-activated centers, SA) [33] or deep copper levels ("copper red") [34].

Figure 4.9 compares PL spectra of ZnSe films grown from TPPSe and DMZn in helium at various substrate temperatures. The structure of the near band-edge PL, measured at 1.9 K and a low excitation power, is shown in Fig. 4.10. The thicknesses of the layers deposited at 425°C and 450 °C were 1 μm , while the films grown at 375 °C and 400 °C were 0.5 μm thick. The excitonic emission of the samples grown at 375 °C and 400 °C displayed only two bands at 2.801-2.802 eV and 2.796-2.798 eV corresponding to free excitons (E_x) and donor-bound excitons (I_2), respectively. The lack of splitting most likely has its origin in a large degree of compensation of the thermal tensile strain by lattice mismatch compressive strain due to the small film thickness [26]. The blue shift of the excitonic transition and the I_1^d line observed on the sample grown at 375 °C clearly indicates the presence of lattice mismatch strain. Splitting of the excitonic emission into the heavy and light hole components can be seen on the samples grown at 425 °C and 450 °C. The partially resolved free exciton components can be localized at ~ 2.804 eV (E_x^{hh}) and 2.7995 eV (E_x^{lh}), while the more pronounced donor-bound exciton lines are at 2.7962 eV (I_2^{hh}) and 2.7942 eV (I_2^{lh}).

At lower energies, all the spectra contain pronounced I_1^d lines and weak DAP emission. The spectrum of the film grown at 450 °C displays a weak Y_0 line and broad deep-level emission bands, indicating deterioration of the optical quality of the material with increasing growth temperature. Similar changes in PL spectra of ZnSe were reported for the growth system combining H_2Se and DMZn, although a pronounced increase in the intensity of Y_0 was observed at 350 °C [35].

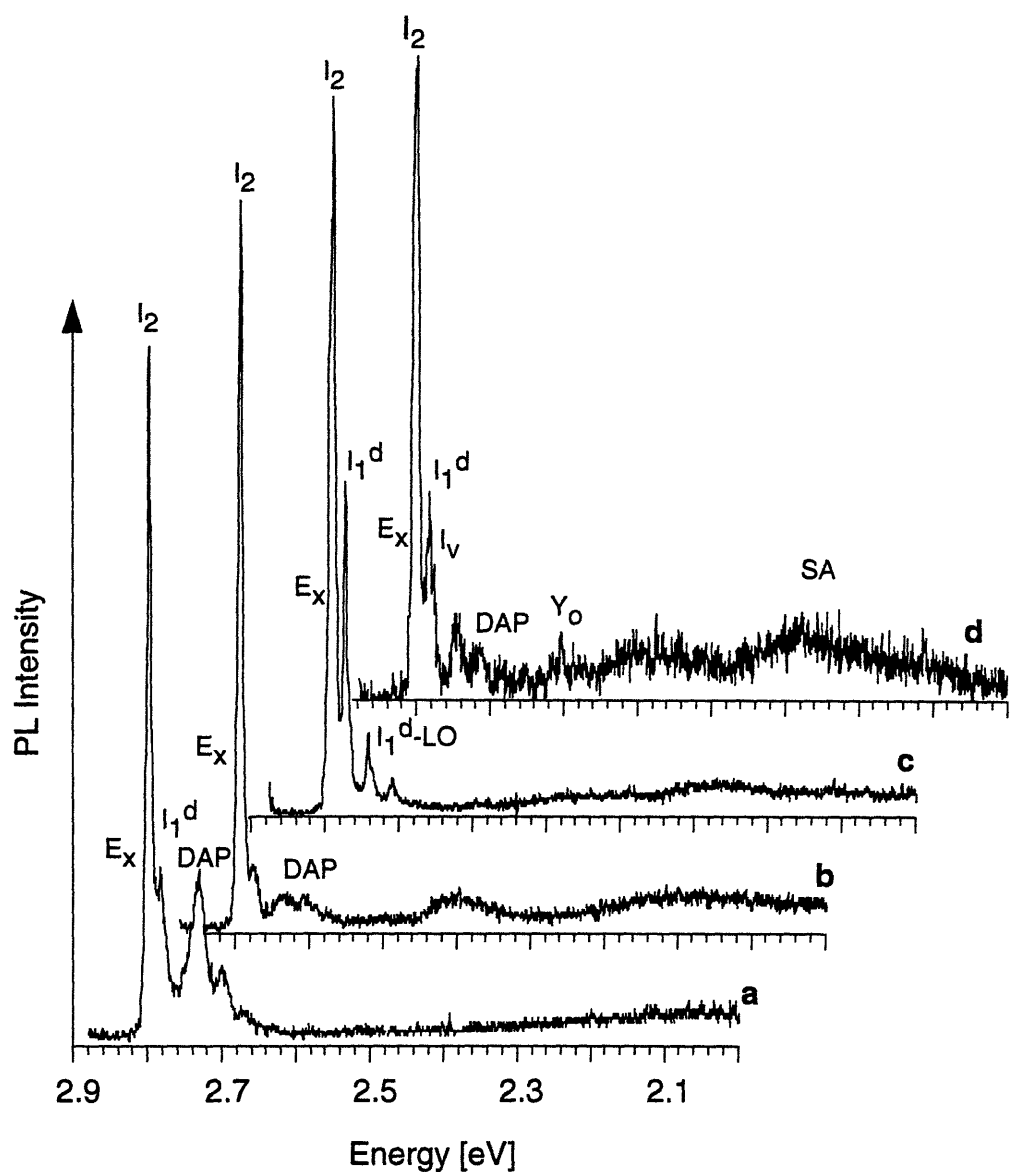


Figure 4.9. 10 K PL spectra of ZnSe grown from TPPSe (5 μ mol/min) and DMZn (5 μ mol/min) in He at various substrate temperatures: 375 °C (a), 400 °C (b), 425 °C (c), and 450 °C (d).

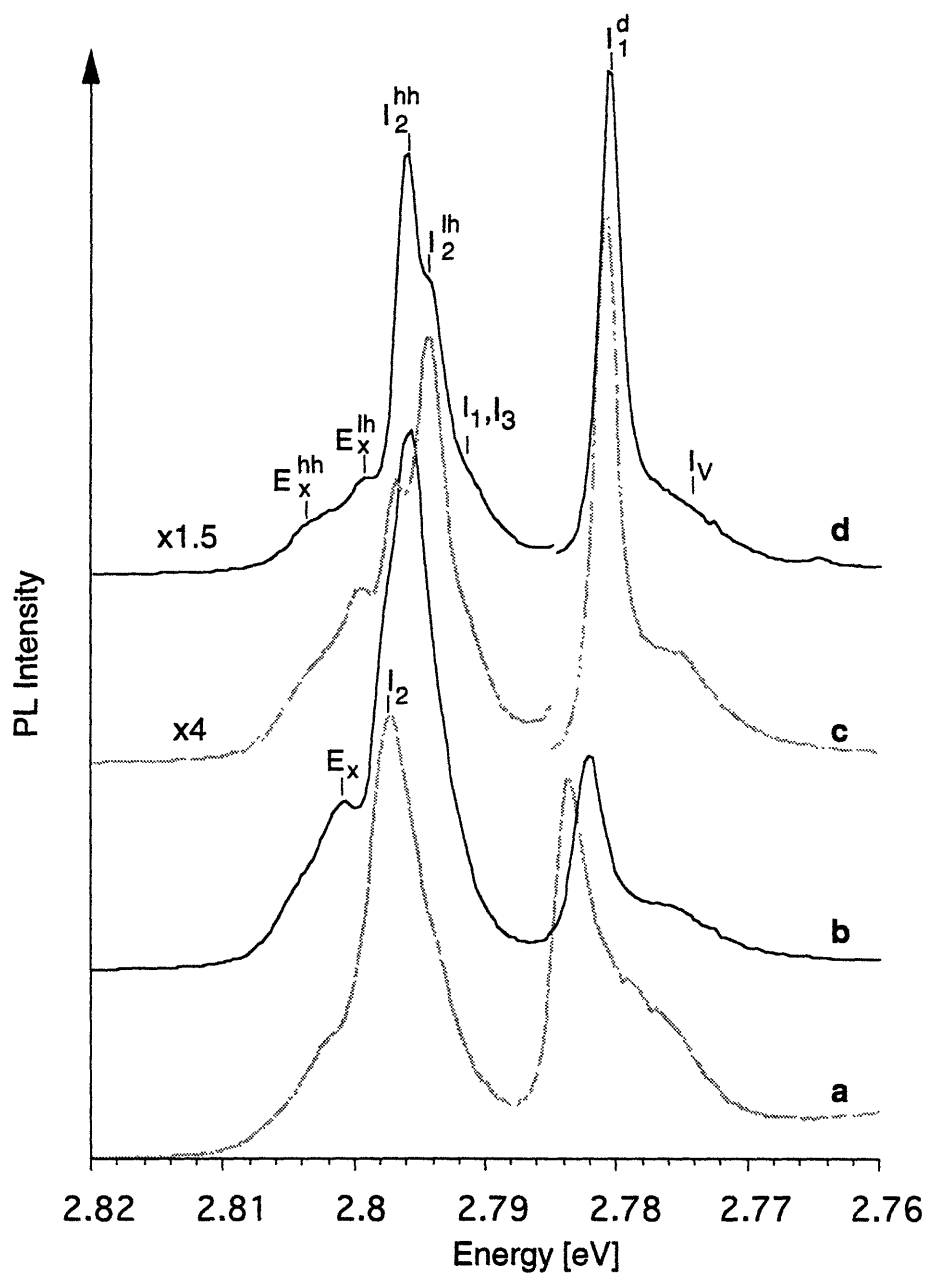


Figure 4.10. 1.9 K near band-edge PL of ZnSe. The films were grown from TPPSe ($5\mu\text{mol}/\text{min}$) and DMZn ($5\mu\text{mol}/\text{min}$) in He at various substrate temperatures: 375 °C (a), 400 °C (b), 425 °C (c), and 450 °C (d).

ZnSe films grown in a hydrogen carrier gas showed very different PL spectra (Fig. 4.11). The near-band edge spectra are composed of the I_1 line at ~ 2.792 eV, I_1^d line at 2.782 eV, and DAP with the zero LO phonon line at 2.73 eV. All the lines were broad. The low energy region was dominated by a wide band with a maximum at 2.0 eV. The I_1 and DAP lines correspond to phosphorus in the shallow acceptor state, while the red emission is consistent with phosphorus in the deep acceptor state [4,19]. Such deep level emission may also originate in zinc vacancies (SA), however, the shape and position of the band differs from the low energy emission typically observed from SA centers (Figs. 4.7 and 4.9). The presence of phosphorus in the deep acceptor states is consistent with the high phosphorus level ($\sim 3 \times 10^{18}$ - 1×10^{19} atoms/cm³) as determined by SIMS.

4.3.2. OMCVD with Dimethyl(butyl)phosphine Selenide (DMBPSe)

Figure 4.12 compares the vapor pressures of DMBPSe and TPPSe. The data verify a significant improvement of precursor volatility with the unsymmetrical phosphine. The OMCVD experiments with DMBPSe, in combination with DMZn and a helium carrier gas, confirmed similar growth characteristics of the new precursors as those of TPPSe. For example, the growth rates of ZnSe in the 400-425°C range were nearly identical for both of the precursors.

The surface morphology of the films grown from DMBPSe appeared smooth with the characteristic "orange peel" texture, analogous to the samples grown from TPPSe (Fig. 4.13). The hydrogen, phosphorus and carbon SIMS profiles in a film grown from DMBPSe at 425 °C are displayed in Fig. 4.14. The profiles show elevated concentrations of the contaminants at the interfaces and low levels in the bulk of the film. The increase of the impurities concentrations at the ZnSe/GaAs interface suggests contamination of the substrate during the high temperature pre-treatment step in the vapor of DMBPSe. Concentrations in the bulk are comparable to those for the films grown from TPPSe under similar conditions.

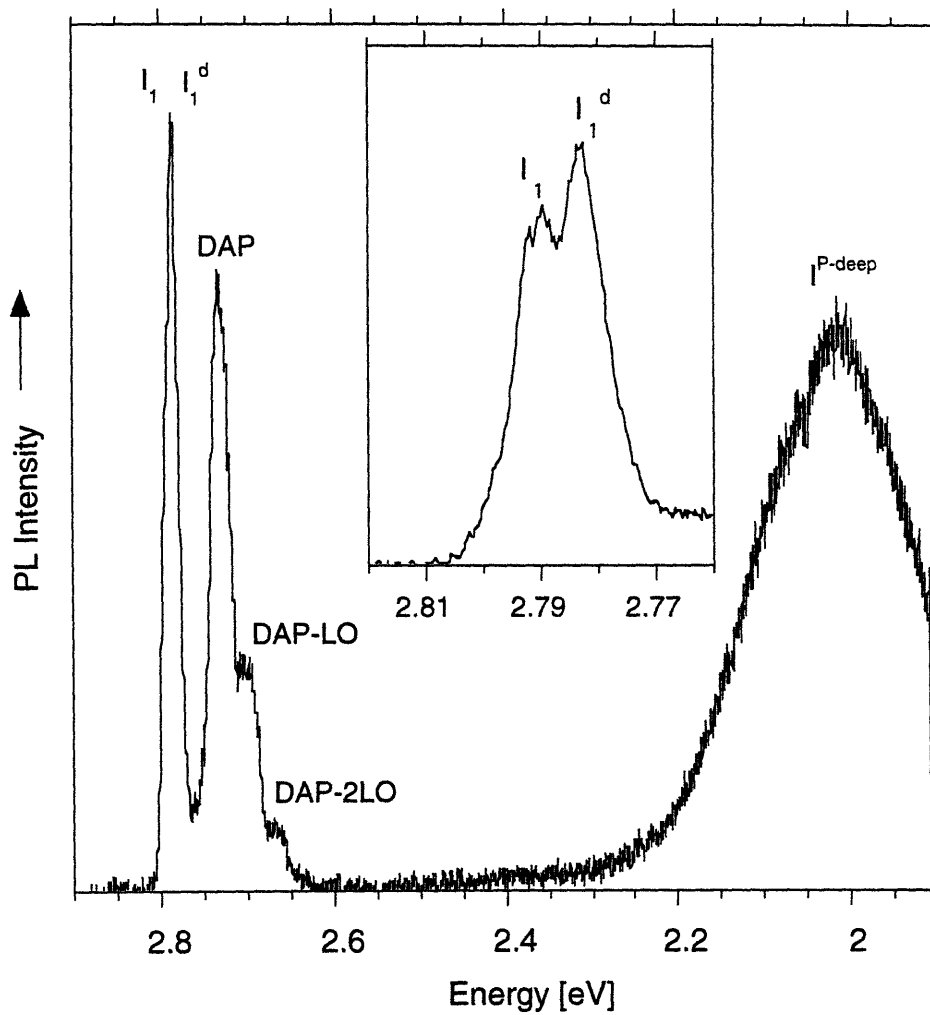


Figure 4.11. 10 K PL spectrum of a ZnSe film grown from TPPSe ($5\mu\text{mol}/\text{min}$) and DMZn ($5\mu\text{mol}/\text{min}$) in H_2 at $400\text{ }^\circ\text{C}$. The inset shows the band-edge emission.

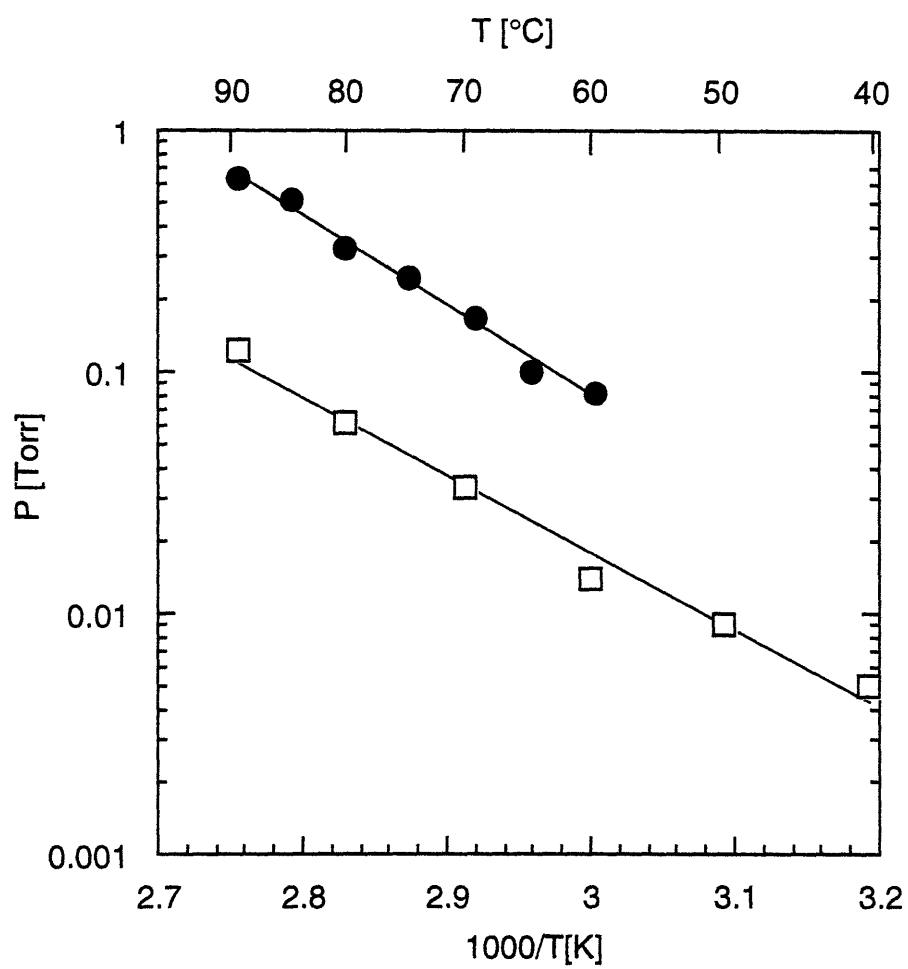


Figure 4.12. Vapor pressure for DMBPSe (●) and TPPSe (□) at various temperatures.

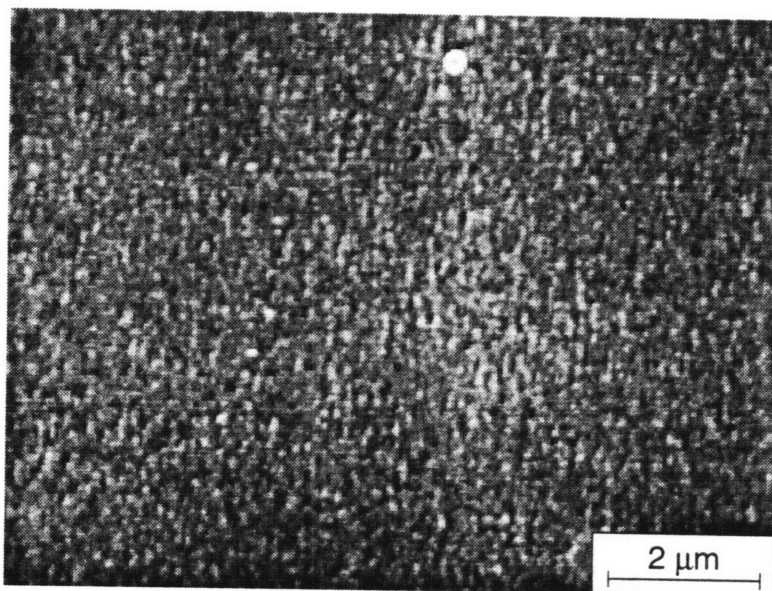


Figure 4.13. SEM image of a ZnSe film grown from DMBPSe ($5\mu\text{mol}/\text{min}$) and DMZn ($5\mu\text{mol}/\text{min}$) in He at $425\text{ }^\circ\text{C}$. The layer thickness was $\sim 1\mu\text{m}$.

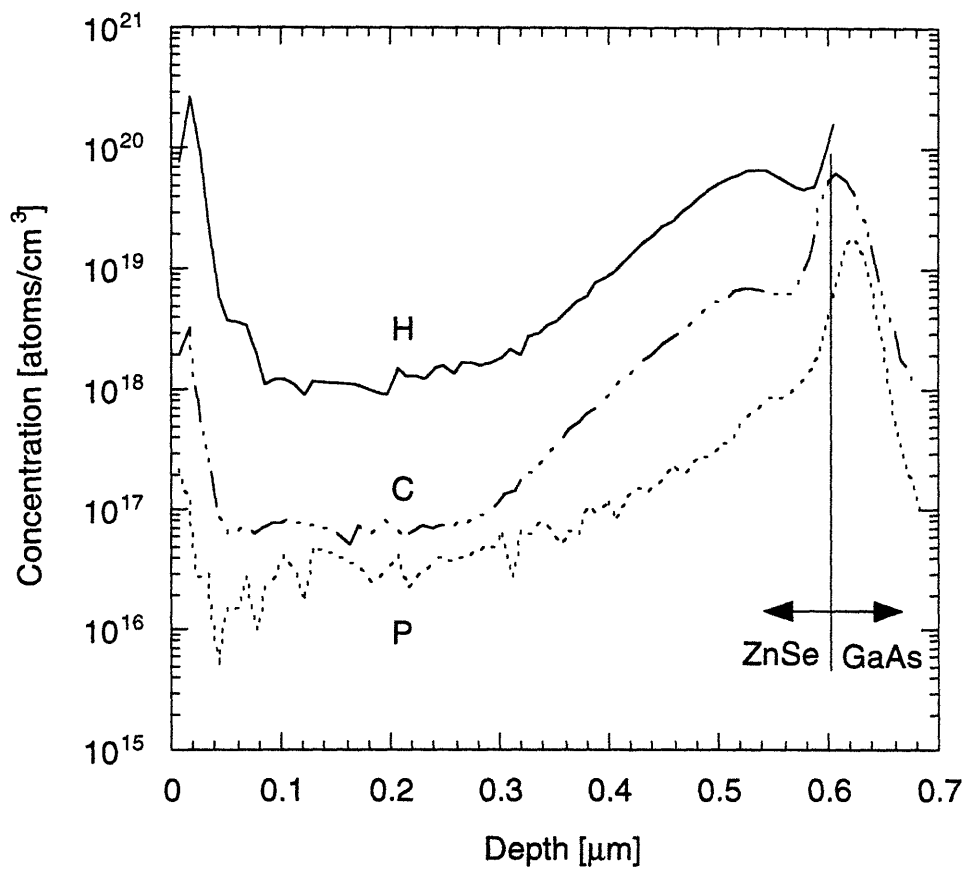


Figure 4.14. SIMS concentration profiles for hydrogen, phosphorus, and carbon in a films grown from DMBPSe (5 μmol/min) and DMZn (5 μmol/min) in He at 425 °C.

The 10 K PL spectrum of a film grown from DMBPSe at 425 °C displays free-exciton emission at ~2.800 eV, donor-bound exciton line at 2.796 eV and deep acceptor emission (I_1^d) with the zero phonon line at 2.782 eV (Fig. 4.15). At lower energies, the PL spectrum contains a weak Y_0 line at 2.600eV and a broad band originating from deep electronic traps. These results indicate that the quality of the layers deposited from DMBPSe is comparable to the quality of the films grown from TPPSe. The appearance of the pronounced I_1^d lines in the spectra of the material indicates the presence of impurities during the growth, most likely originating from the phosphine selenide precursors. Therefore, it is believed that further improvement in the optical quality of the layers can be obtained by purification of the phosphines used for the synthesis of the precursors.

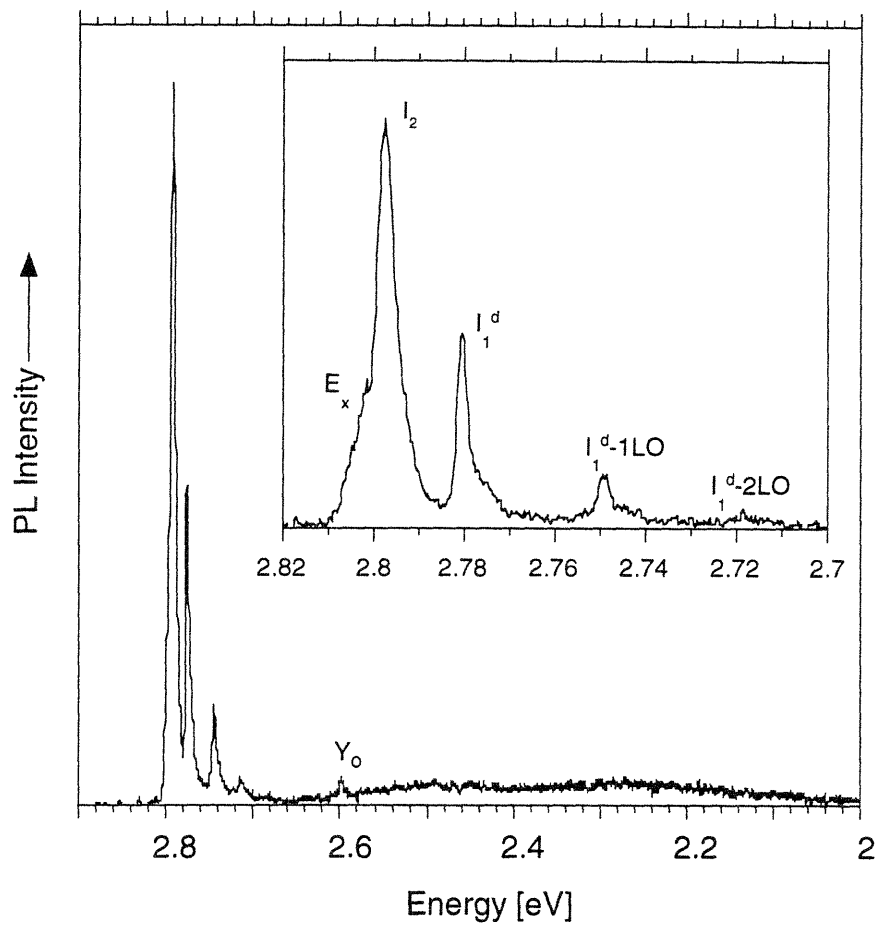


Figure 4.15. 10 K PL spectrum of a ZnSe film grown from DMBPSe ($5\mu\text{mol}/\text{min}$) and DMZn ($5\mu\text{mol}/\text{min}$) in He at $425\text{ }^\circ\text{C}$. The layer thickness was $0.5\ \mu\text{m}$. The insert shows the band-edge emission.

4.4. Conclusion

The OMCVD experiments with TPPSe and DMBPSe demonstrated the feasibility of the proposed precursor chemistry for synthesis of high optical quality ZnSe films. The layers prepared below 425 °C showed good surface morphology and low concentrations of hydrogen, phosphorus and carbon, comparable to the detection limits of SIMS. Low temperature PL spectra displayed a strong excitonic emission dominated by donor-bound excitons. Zinc vacancies associated with shallow donor states are the characteristic optically active defects in the ZnSe layers. Selection of unsymmetrical phosphines provides the opportunity for synthesis of low melting point phosphine selenides with vapor pressures sufficiently high for standard gas-phase delivery. However, purification of the precursor is necessary for further growth and doping experiments.

References

- [1] (a) Jansen, R. W.; Sankey, O. F. *Phys. Rev B* **1989**, *39*, 3192. (b) Laks, D. B.; Van de Walle, C. G. *Mat. Res. Soc. Symp. Proc. Vol. 242*. **1992**, 311.
- [2] Cheng, H.; DePuydt, J. M.; Potts, J. E.; Smith, T. L. *Appl. Phys. Lett.* **1987**, *52*, 147.
- [3] (a) Park, R. M.; Troffer, M. B.; Rouleau, C. M.; DePuydt, J. M.; Haase, M. A. *Appl. Phys. Lett.* **1990**, *57*, 2127. (b) Ohkawa, K.; Tarasawa, T.; Mitsuyu, T. *Jpn. J. Appl. Phys.* **1991**, *30*, L512.
- [4] Yao, T.; Okada, Y. *Jpn. J. Appl. Phys.* **1986**, *25*, 821.
- [5] Shibli, S. M.; Tamargo, M. C.; Skromme, B. J.; Schwartz, S. A.; Schwartz, C. L.; Nahory, R. E.; Martin, R. J. *J. Vac. Sci. Technol. B* **1990**, *8*, 187.
- [6] (a) Haase, M.A.; Qiu, J.; Depuydt, J.M.; Cheng, H. *Appl. Phys. Lett.* **1991**, *59*, 1272. (b) Jeon, H.; Ding, J.; Patterson, W.; Nurmikko, D.V.; Xie, W.; Grillo, D.C.; Kobayashi, M.; Gunshor, R.L. *Appl. Phys. Lett.* **1991**, *59*, 3619. (c) Migata, M.; Taike, A.; Yamamoto, H. *J. Appl. Phys.* **1990**, *68*, 880. (d) Salokatve, A.; Jeon, H.; Ding, J.; Hivinen, M.; Nurmikko, A. V.; Grillo, D. C.; He, L.; Han, J.; Fan, Y.; Ringle, M.; Gunshor, R. L.; Hua, G. C.; Otsuka, N. *Electron. Lett.* **1993**, *25*, 2192.; (e) Nakayama, N.; Itoh, S.; Okuyama, H.; Ozawa, M.; Ohata, T.; Nakano, K.; Ikeda, M.; Ishibashi, A.; Mori, Y. *Electron. Lett.* **1993**, *25*, 2194. (f) Xie, W.; Grillo, D.C.; Gunshor, R.L.; Kobayashi, M.; Jeon, H.; Ding, J.; Nurmikko, D.V.; Hua, G.C.; Otsuka, N. *Appl. Phys. Lett.*, **1992**, *60*, 1999. (g) Rennie, J.; Onomura, M.; Nishikawa, Y.; Saito, S.; Parbrook, P. J.; Nitta, K.; Ishikawa, M.; Hatakoshi, G. *Electron. Lett.* **1994**, *30*, 1090.
- [7] (a) Ohki, A.; Shibata, N.; Ando, K.; Katsui, A. *J. Cryst. Growth* **1988**, *93*, 692. (b) Yoshikawa, A.; Muto, S.; Yamaga, S.; Kasai, H. *J. Cryst. Growth* **1988**, *86*, 279.
- [8] Fujita, S.; Asano, T.; Maehara, K.; Tojyo, Tsuyoshi, Fujita, S. *J. Cryst. Growth* **1994**, *138*, 737.
- [9] (a) Akram, S.; Bhat, I. *J. Cryst. Growth* **1993**, *138*, 105. (b) Akram, S.; Bhat, I.; Melas, A. *J. Electron. Mater.* **1993**, *23*, 259.

- [10] (a) Taskar, N. R., Khan, B. A.; Dorman, D. R.; Shahzad, K. *Appl. Phys. Lett.* **1993**, *62*, 270. (b) Morimoto, K.; Fujino, T. *Appl. Phys. Lett.* **1993**, *63*, 2384.
- [11] Wolk, J. A.; Ager III, J. W.; Duxstad, K. J.; Haller, E. E.; Taskar, N. R.; Dorman, D. R.; Olego, D. J. *Appl. Phys. Lett.* **1993**, *63*, 2756.
- [12] Kamata, A.; Mitsunashi, H.; Fujita, H. *Appl. Phys. Lett.*, **1993**, *63*, 3353.
- [13] Kuhn, W.; Driad, R.; Stanzl, H.; Lusson, A.; Wolf, K.; Qu'Hen, B.; Sahin, H.; Svob, L.; Grattepain, C.; Quesada, X.; Gebhardt, W.; Gorochoy, O. *J. Cryst. Growth* **1994**, *138*, 448.
- [14] Gibson, S. T.; Greene, J. P.; Berkowitz, J. *J. Chem. Phys.* **1986**, *85*, 4815
- [15] Foster, D. F.; Bell, W.; Stevenson, J.; Cole-Hamilton, D. J.; Hails, J. E. *J. Cryst. Growth* - in press.
- [16] Kuhn, W.; Naumov, A.; Stanzl, H.; Bauer, S.; Wolf, K.; Wagner, H. P.; Gebhardt, W.; Pohl, U. W.; Krost, A.; Richter, W.; Dumichen, U.; Thiele, K. H. *J. Cryst. Growth* **1992**, *123*, 605.
- [17] Murray, C. B.; Norris, D. J.; Bawendi, M. G. *J. Amer. Chem. Soc.* **1993**, *115*, 8706.
- [18] *Dictionary of Organophosphorus Compounds*. (R. S. Edmundson, Ed.). Chapman and Hall, 1988.
- [19] Strachan, D. J.; Ming-Li, M.; Tamargo, M. C.; Weinstein, B. A. *J. Cryst. Growth* **1994**, *138*, 318.
- [20] Zingaro, R. A.; Steeves, B. H. Igorlic, K. *J. Organomet. Chem.* **1965**, *4*, 320.
- [21] (a) Giapis, K. P.; Jensen, K. F.; Potts, J. E.; Pachuta, S. J. *J. Electron. Mater.* **1990**, *19*, 453. (b) Patnaik, S.; Jensen, K. F.; Giapis, K. P. *J. Cryst. Growth* **1991**, *107*, 390.
- [22] O'Brien, P. *Chemtronics*, **1991**, *5*, 61.
- [23] Giapis, K. P.; Lu, D. C.; Jensen, K. F., *Appl. Phys. Lett.* **1989**, *54*, 353.
- [24] Huh, J.-S.; Parnaik, S.; Jensen, K. F. *J. Electron. Mater.* **1993**, *22*, 509.
- [25] Stringfellow, G. B. *J. Electron. Mater.* **1988**, *17*, 327.
- [26] Kudlek, G.; Gutowski, J. *J. Lumin.* **1992**, *52*, 55.
- [27] (a) Mitsunashi, H.; Mitsuishi, I.; Mizuta, M.; Kukimoto, H. *Jpn. J. Appl. Phys.* **1985**, *24*, L578. (b) Kleiman, J.; Park, R. M.; Quadri, S. B. *J. Appl. Phys.* **1987**, *61*, 2067.

- [28] Dean, P. J.; Herbert, D. C.; Werkhoven, C. J.; Fitzpatrick, B. J.; Bhargava, R. N. *Phys. Rev. B* **1981**, *23*, 4888.
- [29] Zhang, Y.; Liu, W.; Skromme, B. J.; Cheng, H.; Shibli, S. M.; Tamargo, M. C. *J. Cryst. Growth* **1994**, *138*, 310.
- [30] Pohl, U. W.; Kudlek, G. H.; Klimakow, A.; Hoffman, A. *J. Cryst. Growth* **1994**, *138*, 385.
- [31] Shahzad, K.; Olego, D. J.; Cammack, D. A. *Phys. Rev. B*, **1989**, *39*, 13016.
- [32] Myhajlenko, S.; Batsone, J. L.; Hutchinson, H. J.; Steeds, J. W. *J. Phys. C: Sol. State Phys.* **1984**, *17*, 6477.
- [33] Bouley, J. C.; Blanconnier, P.; Herman, A.; Ged, P.; Henoc, P.; Noblanc, J. P. *J. Appl. Phys.* **1976**, *46*, 3549.
- [34] Grimmeiss, H. G.; Ovren, C. Mach, R. *J. Appl. Phys.* **1979**, *50*, 6328.
- [35] Giapis, K. P.; Lu, D-Ch.; Jensen, K. F.; Potts, J. E. *J. Cryst. Growth* **1990**, *104*, 291.

Chapter 5

Electrospray OMCVD Synthesis of CdSe/ZnSe Quantum Dot Composites

5. 1. Introduction

Composites incorporating semiconductor nanocrystals (quantum dots) in a wide band-gap semiconductor matrix are attractive materials for a variety of optoelectronic applications including flat panel displays and optical switches. In principle, the optical properties of these composites, such as absorption and emission wavelengths, can be tailored by selecting the composition and size of the quantum dots [1]. Techniques based on co-deposition of *in-situ* formed nanocrystals and semiconductor matrices have already been explored for preparation of quantum dot composites [2]. However, the methods available for *in-situ* synthesis of nanocrystals, *e.g.*, laser ablation, exploding wire technique, and gas-phase pyrolysis, suffer from difficult control of the size distribution, stoichiometry and crystallinity of the particles. Consequently, the materials display a severe inhomogeneous broadening of the optical transitions and lack luminescence.

On the other hand, remarkable progress has been made recently in solution synthesis of semiconductor nanocrystals [1,3-5]. In particular, high yield procedures relying on controlled growth of nanoparticles in coordinating solvents are available for synthesis of nearly monodisperse nanocrystals of II-VI compound semiconductors [5]. These particles can be stabilized in liquid or polymer matrices by capping their surface with coordinating compounds, such as phosphine oxides, pyridine derivatives and thiols. This chapter describes a novel technique which allows incorporation of these nanocrystals into a II-VI semiconductor matrix. The technique relies on transfer of the nanocrystals from a liquid dispersion into the gas phase using electrospray (ES). The transferred nanocrystals are co-deposited with a

matrix grown by OMCVD. The impetus for development of the ES-OMCVD technique was the recent breakthrough of the ES ionization source in mass spectrometry [6]. This ES source is remarkably efficient in transfer of extremely heavy ($\sim 5 \times 10^6$ amu) and non-volatile molecules from solution into the gas phase. We expected similar performance of the ES source in transferring the capped semiconductor nanocrystals (with a typical molecular weight of $\sim 10^5$ amu). However, the implementation of ES into the classical OMCVD process brought new conceptual questions regarding chemical compatibility of the techniques which this study also aimed to address.

The ES-OMCVD technique was used for synthesis of novel quantum dot composites consisting of a ZnSe matrix and CdSe nanocrystals. The choice of the nanocrystals provides opportunity for adjustment of the emission wavelength of the composites in a broad region of the visible spectrum by selecting the nanocrystal size [5a]. The ZnSe matrix, with a band gap of 2.7 eV at room temperature, provides a wide spectral window for exploitation of this quantum size effect. In addition, the ZnSe matrix is chemically well suited to passivate the deep electronic states on the CdSe surface. Such electronic passivation is indispensable for preserving the attractive luminescence properties of the quantum dots. The matrix should also stabilize the incorporated nanocrystals chemically, in particular, prevent oxidation of the nanocrystal surface. In principle, the electrical conductivity of the composites could be controlled by doping the matrix. This new approach to II-VI quantum dot composite synthesis possesses the processing capability of classical OMCVD and allows, therefore, integration of these materials into microelectronics device structures.

5.2. Experimental

General procedures and materials. Synthesis and solution manipulations were carried out under an atmosphere of argon or nitrogen using standard Schlenk techniques, vacuum lines, and a glovebox. Hexane (HPLC grade, Mallincrodt), methanol (electronic grade, Mallincrodt), butanol

(Mallincrodt), pyridine (anhydrous, Aldrich), acetonitrile (anhydrous, Aldrich), trioctylphosphine (Fluka), trioctylphosphine oxide, nonane (anhydrous, Aldrich), selenium (electronic grade, Aesar) were used as received. Dimethylcadmium (Organometallics, Inc.) was vacuum transferred prior to use. A 1.0 M stock solution of trioctylphosphine selenide was prepared according to the literature [5a]. Hydrogen carrier gas (ultra-high purity, Matheson) was purified in a palladium cell. The OMCVD precursors, hydrogen selenide (electronic grade, Solkatrionic) and diethylzinc (electronic grade, Texas Alkyls) were used as received.

Synthesis of CdSe nanocrystals. Nearly monodisperse CdSe nanocrystals were synthesized by a described procedure [5a]. Two sizes of nanocrystals, ~3.5 nm and ~5.0 nm, were prepared for the ES-OMCVD experiments. In hexane, these nanocrystal samples showed narrow absorption bands at 560 nm and 608 nm, respectively. The phosphine/phosphine oxide cap was exchanged for pyridine by repeated dispersion of the nanocrystals in pyridine and precipitation by hexane [5a]. The pyridine capped nanocrystals were dispersed in a mixture of anhydrous pyridine and acetonitrile under nitrogen prior to synthesis of the composites.

The deposition of the composite films was carried out at 600 Torr in a tubular, up-flow OMCVD reactor equipped with a custom build ES head (Fig. 5.1). The design of the ES head was essentially identical with that described by Henion *et al.* [7] and further improved by Kaberle *et al.* [8]. In our system, the head consisted of two concentric stainless steel capillaries (diameters: 100/200 μ m and 300/560 μ m) and a ring counterelectrode (diameters: 4.8/6.4mm) mounted on a PTFE nozzle connecting the head with the inlet of the reactor. The gap between the tip of the inner capillary and the counterelectrode was typically 15 mm. During the deposition experiments, the dispersion of CdSe nanocrystals in pyridine/acetonitrile mixtures (CdSe concentration typically ~1mg/ml) was delivered with a syringe pump into the inner stainless steel capillary maintained at a DC voltage of 4.0-4.5 kV (positive polarity). A stream of hydrogen gas (1000 sccm) from the outer stainless steel capillary carried the aerosol through the grounded

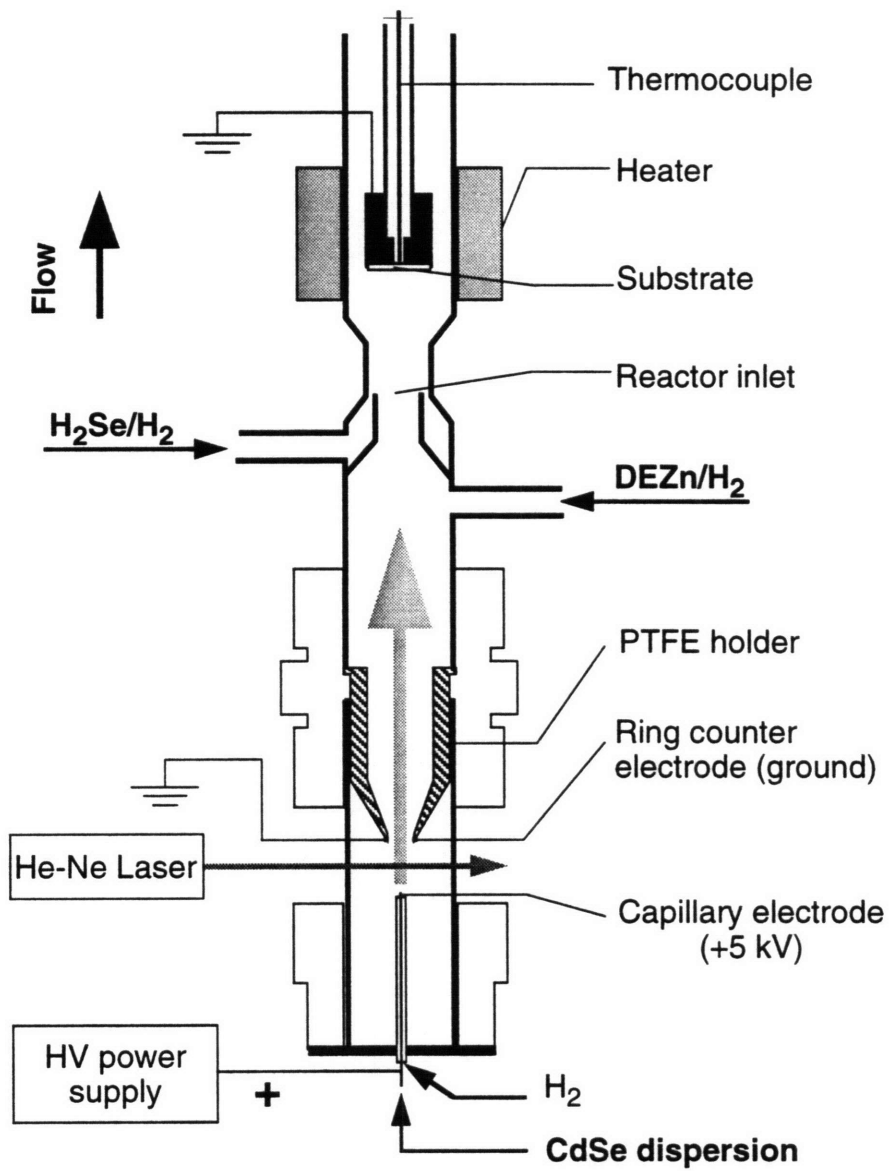


Figure 5.1. Schematic of the Electro spray OMCVD reactor.

counterelectrode and the nozzle into the growth zone of the OMCVD reactor. The ES pattern was visualized by scattering the light from a low power He-Ne laser.

The transferred nanocrystals were combined with the matrix forming precursors, hydrogen selenide (110 $\mu\text{mol}/\text{min}$) and diethylzinc (10 $\mu\text{mol}/\text{min}$), in the mixing zone at the reactor inlet. Films of the CdSe/ZnSe composites were deposited on glass substrates at temperatures of 150-250°C. Prior to the deposition, a thin film of polycrystalline ZnSe (~0.1-0.2 μm) was grown on the substrate to allow nucleation of the matrix. At the end of the deposition procedure, delivery of the dispersion into the ES head was discontinued and the composite film was covered with a 0.1-0.3 μm overlayer of ZnSe. The overall thickness of the composite layer structure was typically ~1 μm as determined with a profilometer. The amount of incorporated CdSe nanocrystals could be adjusted by selecting the delivery rate of the nanocrystal dispersion into the ES head and delivery rates of the ZnSe precursors.

Composition analysis. The overall composition of the films was determined with a x-ray fluorescence spectrometer using a Diano V generator (Cr anode) and a HNU Si:Li detector. ZnSe films grown by OMCVD in our laboratory and CdSe powder (99.99%, Alfa) were used as the standards. Depth composition profiles were determined by Auger electron spectroscopy on a Perkin-Elmer Auger electron microprobe (model 660). The energy of the incident electron beam was 5 keV. In order to minimize charging interference, the samples were covered with aluminum foil and the analysis was carried out through a pinhole in the foil.

Electron Microscopy. Surface morphology of the films was inspected with a Cambridge (Model 250 Mk3) scanning electron microscope (SEM). High resolution transmission electron microscopy (HRTEM) images were obtained on a Topcon EM002B microscope operating at 200 kV. Composition maps of selected areas on the composite films were determined by x-ray fluorescence analysis using a VG HB5 scanning transmission electron microscope (STEM).

Samples of composite films for electron microscopy were deposited by ES-OMCVD on C/Ni TEM grids.

X-ray Diffraction. X-ray diffraction patterns were measured on a Rigaku 300 rotating anode diffractometer operating in the Bragg configuration using monochromatized CuK α radiation.

5.3. Results and Discussion

The nanocrystals prepared according to the procedure described by Murray *et al.* [5a] are terminated with a trioctylphosphine-trioctylphosphine oxide functionality. This surface functionality (cap) is not suitable for OMCVD synthesis of a contaminant-free ZnSe matrix. Therefore, we selected a pyridine cap since this compound is tolerated by the ZnSe growth chemistry [9]. Moreover, the presence of pyridine in the growth system should enhance the growth rate of ZnSe due to the inhibition of the parasitic gas-phase reactions between diethylzinc and hydrogen selenide [9]. However, all attempts to atomize pyridine by electrospray were unsuccessful due to the unfavorable combination of electrical conductivity, dielectric constant and surface tension of the liquid [8,10]. A substantial improvement of the solvent properties for electrospray atomization was accomplished by mixing pyridine with acetonitrile since the latter liquid can be easily electrosprayed in a highly pure form [8]. The acetonitrile *vs.* pyridine ratio was optimized at 2:1 to allow a steady operation of electrospray under OMCVD conditions (hydrogen ambient, sub-atmospheric pressure) and yet stabilize the pyridine capped nanocrystals in the dispersion. Experiments without nanocrystals confirmed no detrimental effect from the electrosprayed solvent on the properties of the ZnSe layers grown on (100) GaAs.

The CdSe/ZnSe composites were deposited on glass. In order to ensure that all the co-deposited nanocrystals are imbedded in the matrix, the composite layer was deposited on a thin film of ZnSe (~0.1-0.2 μm thick) and capped with a thin overlayer of ZnSe (~0.1-0.2 μm thick). Glass was chosen as

a substrate material because of its advantage in optical characterization and its technological importance for electroluminescent flat panel displays. The films were synthesized at relatively low temperatures, 150-250°C, to avoid interdiffusion at the CdSe/ZnSe interface, a problem commonly encountered in the synthesis of CdSe/ZnSe superlattices by Molecular Beam Epitaxy (MBE) [11]. In this temperature range, the matrix underwent a broad transition from amorphous to polycrystalline form. The matrix grains were highly oriented in the <111> cubic or <001> hexagonal direction. This effect is documented in Fig. 5.2 by x-ray diffraction patterns of composites incorporating ~5.0 nm CdSe nanocrystals. The diffraction pattern from the nanocrystals is obscured by the stronger diffraction background of the matrix.

The color of the deposited films was characteristic of the color of the parent CdSe nanocrystals. The films were translucent and their surface appeared dull to the naked eye due to the surface roughness, typical for the ZnSe films grown from hydrogen selenide [9,12]. However, SEM revealed that the surface morphology is also deteriorated by the formation of micron-sized particles (Fig. 5.3). These particles are likely generated from the droplets which did not undergo a successive disintegration due to a lack of charge. After evaporation of the solvent, the agglomerated CdSe particles would be effective seeds for nucleation of ZnSe, resulting in a further increase of the particle size. Smaller particles were observed under the "multijet" mode operation of ES, which can be accomplished by increasing potential at the capillary tip [13]. For our experimental conditions the local electrostatic field at the ES tip for the "multijet" mode was estimated to be $\sim 1.5 \times 10^7$ V/m^{*}. Such operation of ES also improved the uniformity of the films with respect to the CdSe coverage.

The zinc and cadmium depth profiles, as determined by Auger electron spectroscopy (AES), in a layer incorporating ~3.5 nm CdSe nanocrystals, are displayed in Figure 5.4. The top layer did not contain any detectable cadmium, while the underlying composite film contained both of the metals. The cadmium and zinc concentration levels within the composite layer were

*) Using formula 4.2 in ref. 10a

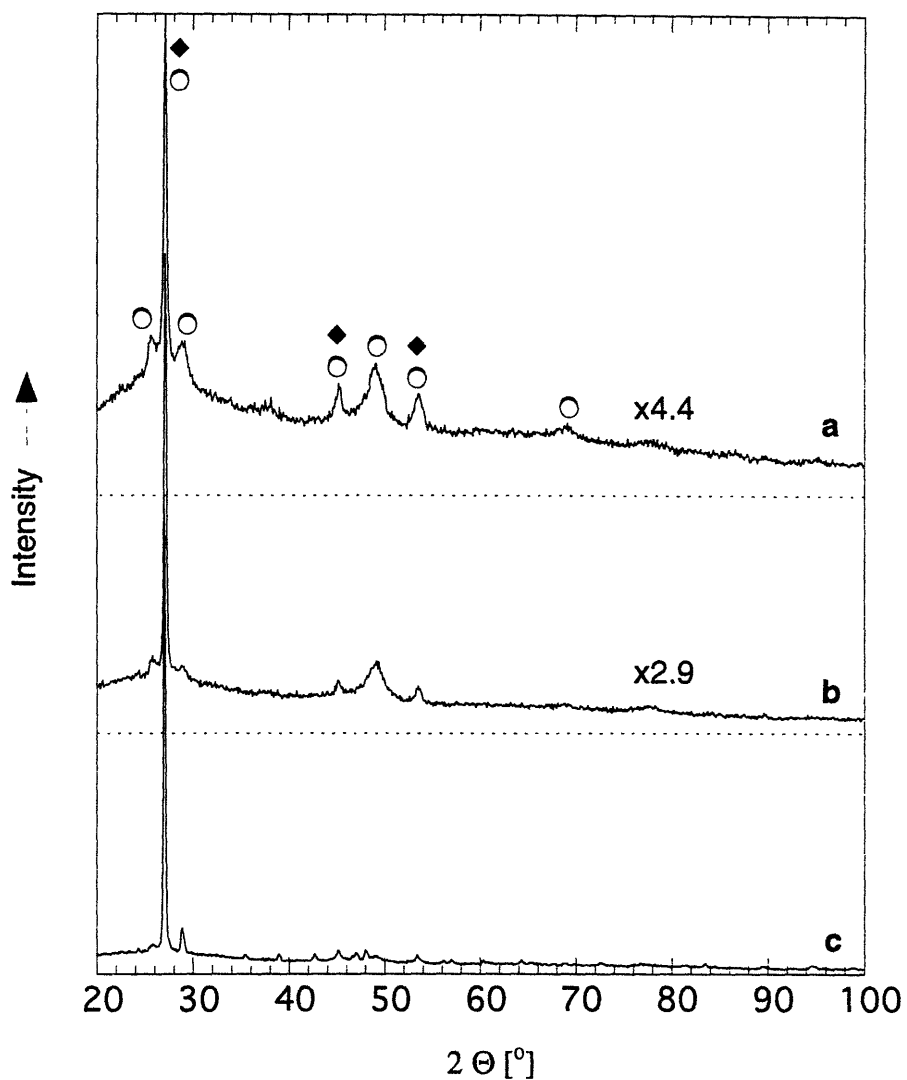


Figure 5.2. X-ray diffraction patterns of CdSe/ZnSe composites deposited by ES-OMCVD at 150 °C (a), 200 °C (b), and 250 °C (c). The size of the CdSe nanocrystals was ~5.0 nm. The zinc blende and wurtzite diffractions of ZnSe are labeled with ◆ and ○, respectively.

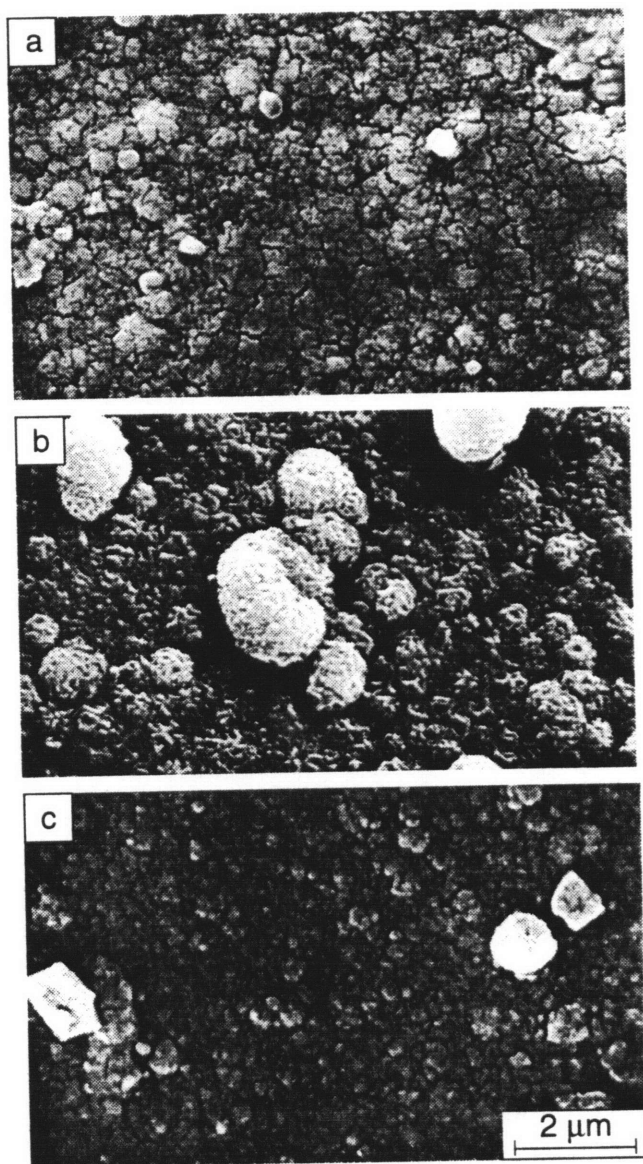


Figure 5.3. SEM images of CdSe/ZnSe composites deposited by ES-OMCVD at 150 °C (a), 200 °C (b), and 250 °C (c).

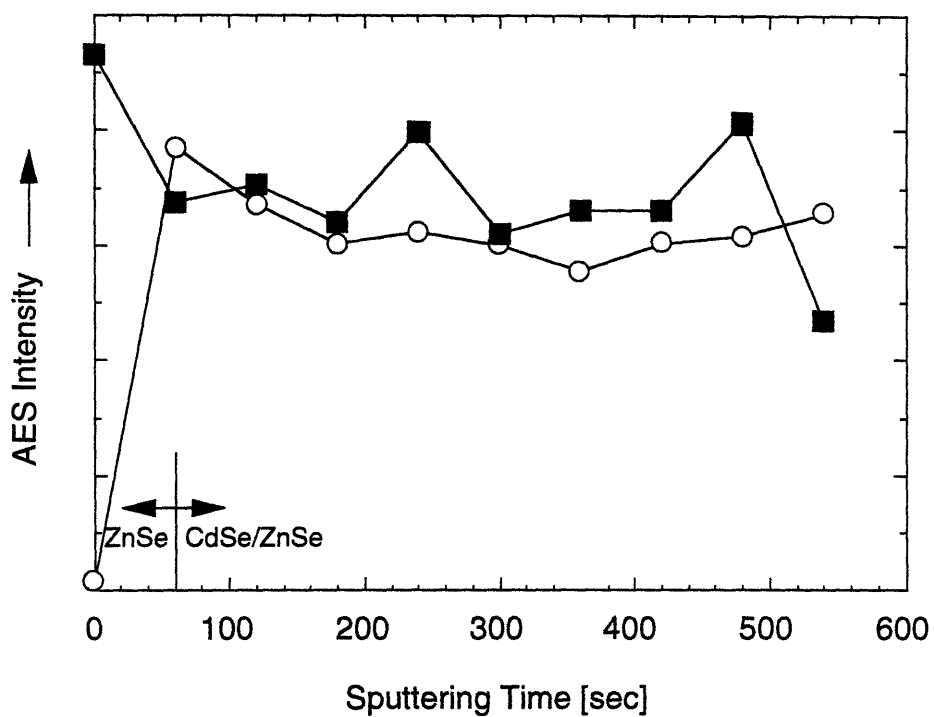


Figure 5.4. AES depth profiles of Zn (■) and Cd (○) concentrations in a CdSe/ZnSe composite with ~3.5 nm CdSe nanocrystals. The film was deposited at 240°C.

flat, demonstrating an uniform composition of the material. The overall composition of the films was determined with x-ray fluorescence analysis. The samples used for optical characterization contained typically ~5% Cd, however, composites with various stoichiometries could be prepared by adjusting the matrix growth rate and the concentration of the electrospayed dispersion. No detectable N or P were observed in the composite layers, and the signals from O and C reached noise levels after 1-2 minutes of sputtering with Ar⁺. This observation substantiates the compatibility of the ES technique with the matrix OMCVD synthesis.

The optical absorption and photoluminescence spectra of CdSe/ZnSe composite incorporating ~3.5 nm CdSe nanocrystals are shown in Fig. 5.5. The absorption spectra show the 1s-1s absorption band of CdSe nanocrystals with a maximum at ~560 nm. The position of the absorption maximum corresponds to that of the initial CdSe nanocrystals in solution. The PL maximum of the composites was slightly red shifted (6-10 nm) from the measured absorption bands. A similar Stokes shift was observed with nanocrystal in solution [5a]. The bandwidths of the emission indicate that the nanocrystals preserve their size distribution after the ES transfer and OMCVD co-deposition. This results provides evidence that the ES-OMCVD technique does not damage the nanocrystals during transfer and the optical properties of the composites are similar to those of the parent nanocrystals in solution.

In separate experiments, when the nanocrystals capped with pyridine were electrospayed on glass substrates at 200 °C without co-deposition of the matrix, the deposits showed no photoluminescence at room temperature. Thus, a ZnSe matrix appears to provide electronic passivation of the nanocrystal surface to some extent.

Figure 5.6 further demonstrates that the emission wavelength can be tuned by selecting the size of the nanocrystals. The composite incorporating ~3.5 nm nanocrystals emitted at 568 nm, while the composite with ~5.0 nm nanocrystals had its emission maximum at 616 nm. The PL intensity varied only slightly when the excitation wavelength was tuned from the blue side of

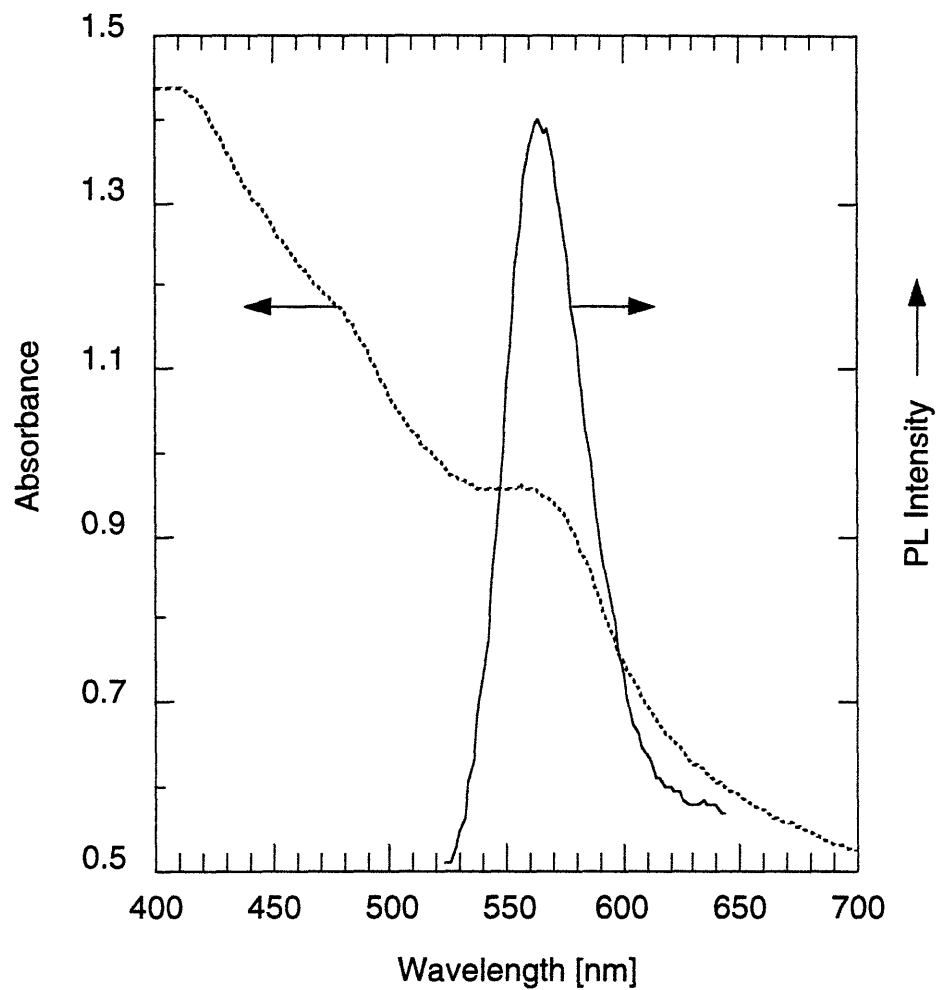


Figure 5.5. Optical absorption (dashed line) and PL (solid line) spectra of a CdSe/ZnSe composite incorporating ~ 3.5 nm CdSe nanocrystals. The excitation wavelength for the PL spectrum was 470 nm.

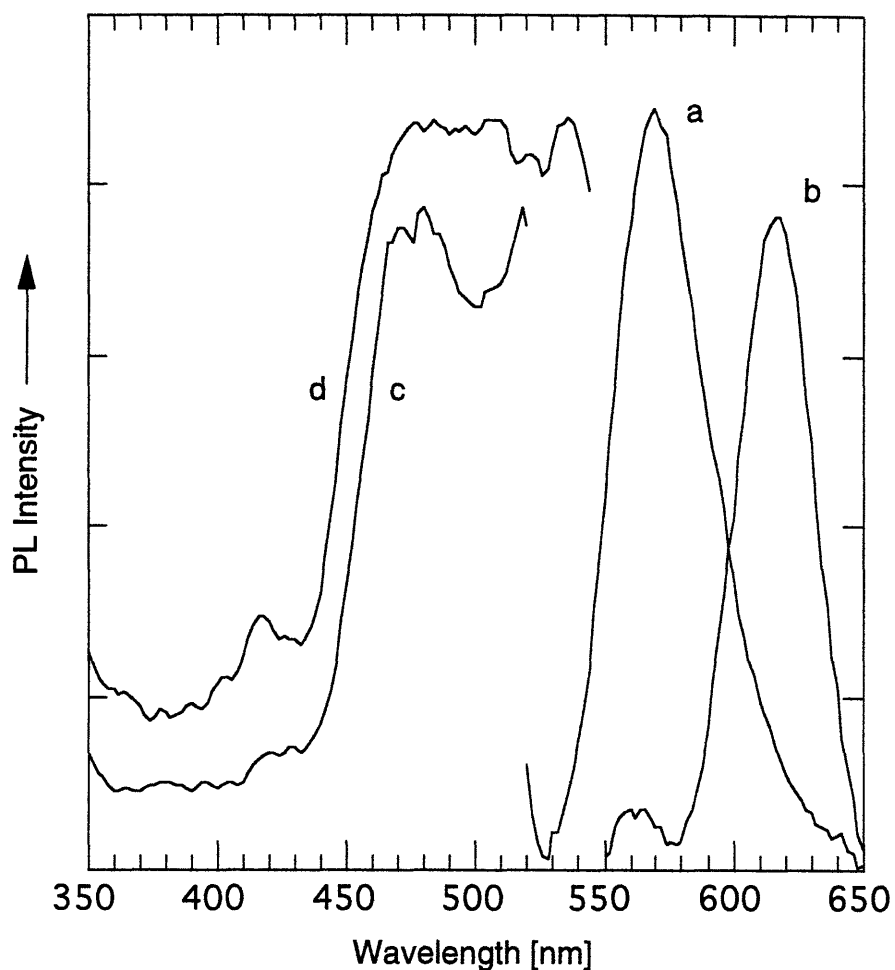


Figure 5.6. Room temperature PL (a,b) and PL excitation (c,d) spectra of CdSe/ZnSe quantum dot composites with ~ 3.5 nm nanocrystals (a,c) and ~ 5.0 nm nanocrystals (b,d), respectively. The films were deposited at 150°C . The excitation wavelength for the PL spectra was 470 nm. The detection wavelengths for the PL excitation spectra were 570 nm (c) and 616 nm (d), respectively.

the 1s-1s band to ~470nm. In this range, the excitation light is only partially absorbed in the films and the excitation spectrum should follow the absorption spectrum of the nanocrystals. However, below ~470 nm the PL intensity drops sharply due to absorption of the excitation light by the ZnSe matrix. Thus, the excitation spectra provide additional evidence that the observed emission originates from the buried nanocrystals and not the matrix.

ES-OMCVD experiments revealed that an increase in the deposition temperature above 200°C leads to degradation of the photoluminescence. This effect is documented in Fig. 5.7 in the composite incorporating ~5.0 nm nanocrystals. The decay of the band-edge photoluminescence intensity with increasing deposition temperature was accompanied by a red shift of the photoluminescence maximum. This shift may indicate an increase of the nanocrystal size at elevated temperature.

The microstructure of the composites was probed by high resolution transmission electron microscopy (HRTEM) on samples deposited on a C/Ni TEM grid at 150°C and 250°C (thickness ~0.05 μm). HRTEM images revealed that both individual and agglomerated nanocrystals were present in the composites. The films deposited at 150°C show nanocrystals surrounded by an amorphous matrix. HRTEM images and selected area electron diffraction show both zinc blende and wurtzite grains of ZnSe in the film prepared at 250°C. Images of the (100) wurtzite lattice planes with the characteristic 6-fold symmetry were used for calibrating the lateral scale of the HRTEM pictures. The CdSe nanocrystals were identified on the basis of the characteristic spacing of the (002) CdSe planes (Figure 5.8). Images of the interface between the CdSe nanocrystals and ZnSe matrix displayed regions of matrix overgrowth with a large density of structural defects. Such interface defects are probably responsible for the low PL efficiency observed for films deposited above 200°C, the temperature at which the matrix becomes predominantly polycrystalline.

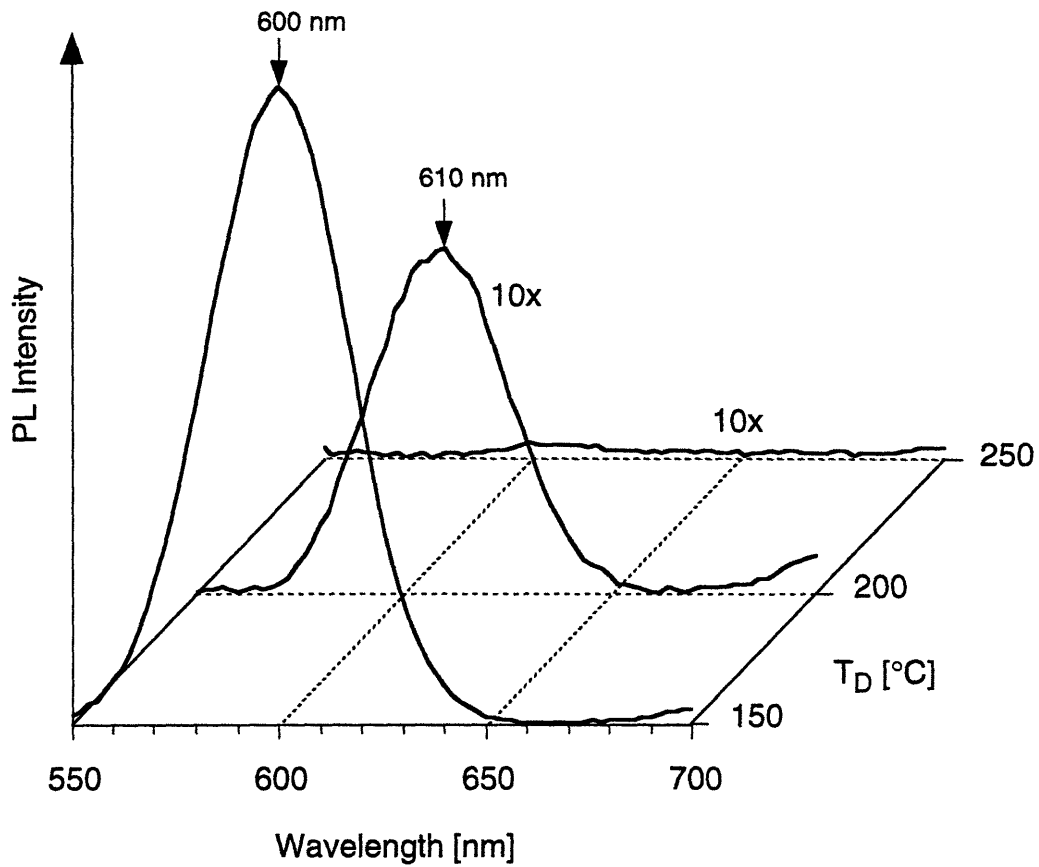


Figure 5.7. Room temperature PL of CdSe/ZnSe quantum dot composites deposited at various substrate temperatures. The size of the imbedded nanocrystals was ~ 5.0 nm. The excitation wavelength was 470 nm.

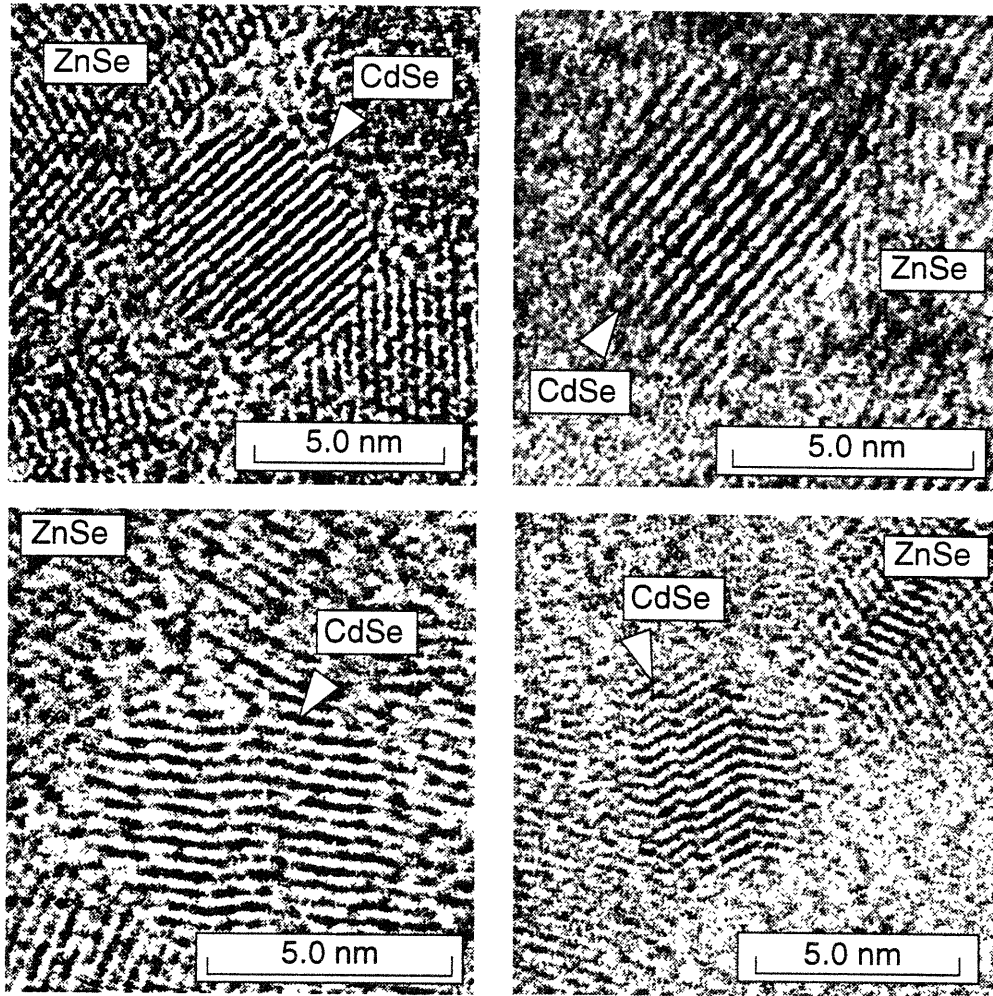


Figure 5.8. Bright field TEM images of a CdSe/ZnSe quantum dot composite film with ~ 5.0 nm nanocrystals deposited on a C/Ni TEM grid at 250°C . The view shows individual CdSe nanocrystals surrounded by grains of a ZnSe matrix. The (002) wurtzite planes of the nanocrystals are resolved ($d_{002}=0.35$ nm).

The composition of thin films grown on C/Ni TEM grids was analyzed by scanning transmission electron microscopy (STEM). At relatively low magnifications the images of the films showed particles ~20-100 nm large. Energy dispersion x-ray analysis revealed a high level of Cd in some of these particles, while the surrounding film contained Zn, Se and only a low concentration of Cd (Fig. 5.9). This is consistent with the TEM observations of a large number of the nanocrystals in agglomerates overgrown with the ZnSe matrix. It was not possible to analyze areas with individual CdSe nanocrystals because of poor stability of the films in the focused electron beam under high magnifications.

The possible agglomeration of the nanocrystals during the ES transfer process was further explored by deposition of the nanocrystals on C/Ni TEM grids at room temperature. At low coverages, individual as well as agglomerated nanocrystals were observed by TEM. The size of the agglomerates varied broadly from a few nanometers to ~100 nm (Fig. 5.10). Considering the coverage and size of the agglomerates, the majority of the incorporated nanocrystals was most likely in the agglomerated form. There are two possible explanations for the agglomeration process. First, the agglomerates are formed after evaporation of the remaining solvent from the droplets after the Coulombic breakup of the charged aerosol [6,14]. Based on the typical agglomerate size of ~50 nm, the final droplet dimensions should be well below 1 μm , depending on the actual concentration of the dispersion. Secondly, the limited solubility of the nanocrystals in the pyridine/acetonitrile mixture may result in agglomeration in the dispersion even before the ES atomization, and/or during the droplet evaporation when the concentration of the nanocrystals increases and droplet temperature decreases. Dilution of the nanocrystal dispersion and use of a better co-solvent than acetonitrile will afford some control of agglomeration and further optimization of the ES-OMCVD process.

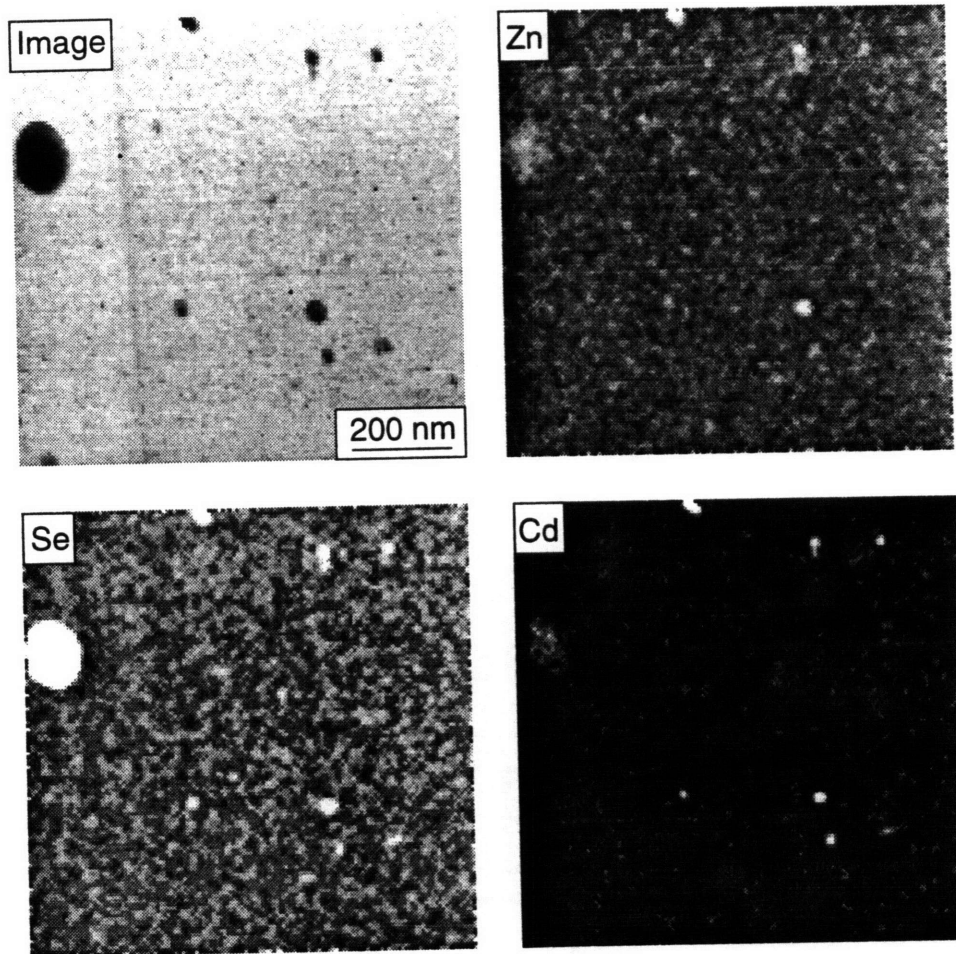


Figure 5.9. STEM image of a CdSe/ZnSe quantum dot composite film with ~ 5.0 nm nanocrystals deposited on a C/Ni TEM grid at 250°C (a), and the corresponding Zn, Se and Cd elemental maps (white color represents regions of high concentration levels, black color shows areas with low concentrations).

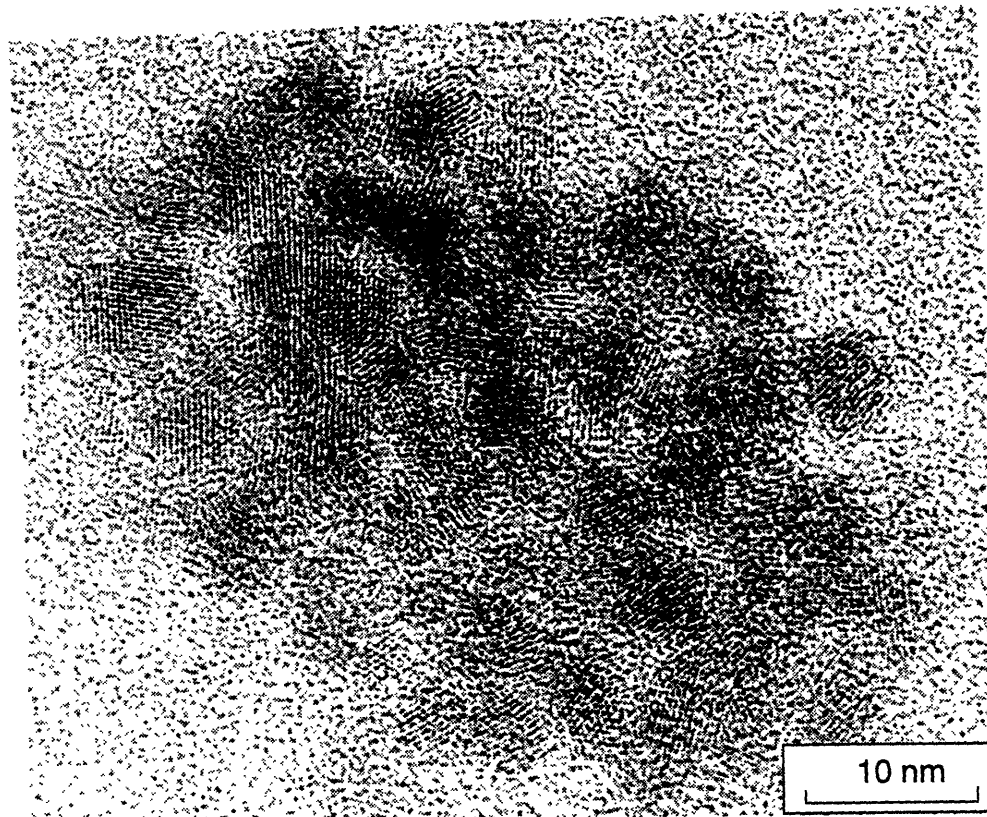


Figure 5.10. HRTEM image of an agglomerate of ~5.0 nm CdSe nanocrystals formed in electrospray. The agglomerate was collected on a C/Ni TEM.

5.4. Conclusion

The ES-OMCVD technique allows preparation of new II-VI quantum dot composites incorporating highly monodisperse CdSe nanocrystals in a ZnSe matrix. The absorption and emission properties of the composites can be finely adjusted in a broad spectral region by selecting the size of the nanocrystals. The emission properties of the composites are likely determined by the small fraction of the individual nanocrystals which are accessible for effective passivation by the matrix. The growth temperature strongly affects the PL intensity, probably due to the formation of grain boundaries and structural defects at the nanocrystal/matrix interfaces. Therefore, electronic and chemical passivation of the nanocrystals prior to the ES-OMCVD co-deposition is required to improve the luminescence properties and thermal stability of the composites. This approach is described in Chapter 6.

References:

- [1] (a) Brus, L. *Appl. Phys.* **A53**, 465 (1991). (b) Wang, Y.; Herron, N. *J. Phys. Chem.* **1991**, *95*, 525. (c) Weller, H. *Angew. Chem. Int. Ed. Engl.* **1993**, *32*, 41.
- [2] (a) Liu, X.; Wu, X.; Bao, X.; He, Y. *Appl. Phys. Lett.* **1994**, *64*, 220. (b) Flagan, R. C.; Atwater, H. A.; Vahala, K. J. *J. Aerosol Sci.* **1991**, *22*, S31. (c) Saunders, W. A.; Sercel, P. C.; Atwater, H. A.; Vahala, K. J.; Flagan, R. C. *Appl. Phys. Lett.* **1992**, *60*, 950. (d) Sercel, P. C.; Saunders, W. A.; Atwater, H. A.; Vahala, K. J.; Flagan, R. C. *Appl. Phys. Lett.* **1992**, *61*, 696. (e) Koyama, T.; Ohtsuka, S.; Nagata, H.; Tanaka, S. *J. Crystal Growth* **1992**, *117*, 156.
- [3] (a) Heath, J. R. *Science*, **1992**, *258*, 1131. (b) Heath, J. R.; Seidler, P. F. *Mat. Res. Soc. Symp. Proc. Vol. 298*, **1993**, 91.
- [4] (a) Uchida, H.; Curtis, C. J.; Nozik, A. J. *J. Phys. Chem.*, **1991**, *95*, 5382. (b) Buhro, W. E. *Polyhedron*, **1994**, *13*, 1131.
- [5] (a) Murray, C. B.; Norris, D. J.; Bawendi, M. G. *J. Amer. Chem. Soc.* **1993**, *115*, 8706. (b) Vossmeier, T.; Katsikas, L.; Giersing, M.; Popovic, I. G.; Diesner, K. Chemseddine, A.; Eychmuller, A.; Weller, H. *J. Phys. Chem.* **1994**, *98*, 7665.
- [6] for reviews see (a) Fenn, J. B.; Mann, M.; Meng, C. K.; Wong, S. T.; Whitehouse, C. M. *Science* **1989**, *246*, 64. (b) Fenn, J. B. *J. Am. Soc. Mass Spectrom.* **1993**, *4*, 524.
- [7] (a) Bruins, A. P.; Covey, T. R. Henion, J. D. *Anal. Chem.*, **1987**, *59*, 2642. (b) Huang, E. C.; Henion, J. D. *J. Am. Soc. Mass Spectrom.* **1990**, *1*, 158.
- [8] Ikonomou, M. G.; Blades, A. T.; Kaberle, P. *Anal. Chem.*, **1991**, *63*, 1989.
- [9] Wright, P. J.; Cockayne, B.; Oliver, P. E.; Jones, A. C. *J. Crystal Growth* **1991**, *108*, 525.
- [10] (a) Michelson, D. "Electrostatic Atomization". Adam Hilger: 1990. (b) Bailey, A. G. "Electrostatic Spraying of Liquids". Research Studies Press, Ltd.: 1988.
- [11] (a) Zhu, Z.; Yoshihara, H.; Takebayashi, K.; Yao, T. *J. Appl. Phys. Lett.* **1993**, *63*, 1678. (b) Zhu, Z.; Yoshihara, H.; Takebayashi, K.; Yao, T. *J. Cryst. Growth* **1994**, *138*, 619.

- [12] (a) Giapis, K. P.; Lu, D. C.; Jensen, K. F., *Appl. Phys. Lett.* **1989**, *54*, 353. (b)
Huh, J.-S.; Parnaik, S.; Jensen, K. F. *J. Electron. Mater.* **1993**, *22*, 509.
- [13] Cloupeau, M.; Prunet-Foch, B. *J. Electrostatics* **1990**, *25*, 165.
- [14] Gomez, A.; Tang, T. *Phys. Fluids* **1994**, *6*, 404.

Chapter 6

Synthesis and Characterization of CdSe/ZnSe Composites with Passivated CdSe Nanocrystals

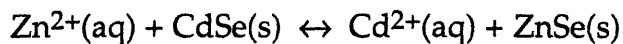
6.1. Introduction

Electrospray Organometallic Chemical Vapor Deposition (ES-OMCVD) was introduced in the previous chapter as a new technique for the synthesis of thin films of semiconductor quantum dot composites. Novel luminescent composites incorporating CdSe nanocrystals of selected size in ZnSe matrices were prepared by this method [1]. Even though the composite films displayed room temperature photoluminescence (PL) characteristic of the quantum dots, the emission was weak and deteriorated with increasing deposition temperature of the matrix. High resolution transmission electron microscopy (HRTEM) and scanning transmission electron microscopy (STEM) revealed extensive agglomeration of the nanocrystals in the films and the presence of matrix grain boundaries at the CdSe-ZnSe interface. The low PL yield and poor thermal stability of the materials are likely related to these defects.

This chapter describes a new approach to ES-OMCVD synthesis of luminescent CdSe/ZnSe quantum dot composites relying on the passivation of CdSe nanocrystals prior to the co-deposition. The passivation was accomplished with a thin layer of ZnSe grown on the surface of the nanocrystals. Precedent for electronic passivation of nanocrystals with an overlayer of wide band gap material appeared in reports on layered semiconductor particles, *e.g.*, ZnS on CdS [2], ZnS on CdSe [3], CdS on HgS [4], and SiO₂ on Si [5].

Crystalline overlayers of a compound semiconductor can be formed on semiconductor nanocrystals either by heterogeneous nucleation

(precipitation) or by ion displacement reactions [3-4,6]. The selection of a CdSe core and a ZnSe shell makes the nucleation technique more suitable since the displacement reaction:



is thermodynamically unfavorable ($\Delta G^\circ = 56.0 \text{ kJ/mol}$). Hoener *et al.* [7] prepared CdSe/ZnSe particles by overgrowth of CdSe seeds with ZnSe using an inverse micelle technique, and demonstrated a shell-core structure of the particles by x-ray photoemission and Auger electron spectroscopies. However, the reported absorption spectra indicate poor optical quality and a broad size distribution of the initial CdSe particles. In this study, the CdSe nanocrystals were prepared by an organometallic procedure described by Murray *et al.* [8]. This technique provided high optical quality nanocrystals which could be easily purified and size-selected for the synthesis of CdSe/ZnSe particles.

The new solution procedure for overgrowth of CdSe nanocrystals with ZnSe using organometallic precursors, presented here, yields high quality CdSe/ZnSe particles which can be easily purified and derivatized with pyridine to provide for compatibility with the OMCVD chemistry of the ZnSe matrix [9]. The structure and optical properties of the passivated particles in solution are probed to assess the effect of the ZnSe overlayer on the luminescent properties of the CdSe nanocrystals. The overcoated CdSe nanocrystals are subsequently used for synthesis of CdSe/ZnSe composites by ES-OMCVD. The PL characteristics of the composites with the passivated nanocrystals are compared to those for composites containing bare nanocrystals.

6.2 Experimental

Materials. Hexane (HPLC grade, Mallincrodt), methanol (electronic grade, Mallincrodt), butanol (Mallincrodt), pyridine (anhydrous, Aldrich),

acetonitrile (anhydrous, Aldrich), trioctylphosphine (Fluka), nonane (anhydrous, Aldrich), selenium (electronic grade, Aesar) were used as received. Diethylzinc (Aldrich) was filtered through a 0.2 μm PTFE filter and dimethylcadmium (Organometallics, Inc.) was vacuum transferred prior to use. A 1.0 M stock solution of trioctylphosphine selenide was prepared according to the literature [8]. Hydrogen carrier gas (ultra-high purity, Matheson) was purified in a palladium cell. The OMCVD precursors, hydrogen selenide (electronic grade, Solkatrionic) and diethylzinc (electronic grade, Texas Alkyls) were used as received.

Synthesis of CdSe/ZnSe nanocrystals. CdSe nanocrystals of selected size were prepared by controlled growth of CdSe nuclei in a trioctylphosphine-trioctylphosphine oxide (TOP/TOPO) mixture according to a described procedure [8]. The nanocrystals were purified by repeated precipitation with methanol and re-dispersion in hexane. The initial size distribution width of the purified sample was narrowed by size-selective precipitation from hexane/methanol mixtures [8].

Overgrowth of the CdSe nanocrystals with a ZnSe layer was carried out in TOP under Ar using the Schlenk line technique. In a standard procedure, a sample containing ~100 mg of purified and size-selected CdSe nanocrystals was precipitated with methanol, separated on a centrifuge and transferred into a glove box. The nanocrystals were re-dispersed in 10 ml of TOP containing 0.5 mmol of trioctylphosphine selenide (TOPSe). If necessary, a small amount of anhydrous nonane (2-5 ml) was added to the slurry to accelerate re-dispersion of the nanocrystals. The dispersion was filtered with a 0.2 μm PTFE filter, transferred into a flask backfilled with Ar and heated to 150 °C. In a glove box, equimolar amounts of diethylzinc (DEZn) and TOPSe were mixed in 10 ml of TOP and filtered with a 0.2 μm PTFE syringe filter (CAUTION: DEZn is highly pyrophoric!). The solution of the ZnSe precursors was continuously dosed at a flow rate of ~0.3 ml/min to the heated and stirred dispersion using a syringe pump. The overgrowth of ZnSe was followed by UV/Vis absorption spectroscopy. After addition of the desired amount of the precursors, the reaction mixture was cooled to room

temperature. A small amount of butanol (~5 ml) was added to the reaction mixture to hydrolyze unreacted DEZn. The overcoated nanocrystals were precipitated from the mixture with hexane and separated by centrifugation. Repeated re-dispersion of the sample in pyridine and precipitation with hexane was used to purify the CdSe/ZnSe particles and derivatize the surface with pyridine [8]. The nanocrystals were stored dispersed in anhydrous pyridine under nitrogen.

Preparation of the nanocrystal dispersions for ES-OMCVD. Pyridine capped CdSe [8] or CdSe/ZnSe nanocrystals were precipitated with hexane, separated on a centrifuge and transferred into a glove-box. The nanocrystals were re-dispersed in anhydrous pyridine and filtered with a 0.2 μm PTFE filter. The concentration of CdSe was adjusted to ~3 mg/ml. Before the ES-OMCVD synthesis, the dispersion was diluted with two fold excess of anhydrous acetonitrile, the mixture was degassed by several thaw-pump-freeze cycles on a high vacuum line. The ratio of pyridine *vs.* acetonitrile was optimized previously for steady operation of the electrospray [1]. The manipulation of the nanocrystal dispersions was carried out on a custom-made liquid handling system attached to the ES-OMCVD reactor.

ES-OMCVD synthesis. The ES-OMCVD system used for the synthesis of the composites is described elsewhere [1a]. The composite films were deposited on degreased glass substrates (microscope slides, Fisher) at temperatures ranging from 150 °C to 270 °C. Hydrogen selenide (20 $\mu\text{mol}/\text{min}$) and diethylzinc (1 $\mu\text{mol}/\text{min}$), carried in a hydrogen gas, were used as the matrix precursors. The electrospray atomization of the nanocrystal dispersions was carried out at 4.5 kV DC, imposed between a capillary electrode (positive polarity) and ring counter electrode (ground). The capillary electrode was fed with the nanocrystal dispersion at a flow rate of 17 $\mu\text{l}/\text{min}$ using a syringe pump. The aerosol was carried into the growth zone of the ES-OMCVD reactor in a stream of 1000 standard cm^3/min (sccm) of hydrogen gas. The reactor and electrospray pressures were maintained at 600 Torr. The deposition was initiated by growth of a ZnSe film (thickness ~ 0.1 μm), followed by deposition of the composite (thickness ~ 1 μm), and

finally terminated by growth of a ZnSe capping layer (thickness $\sim 0.1 \mu\text{m}$). This sandwiched structure ensured that all the deposited nanocrystals were buried within the ZnSe matrix.

Optical Characterization. UV/Vis absorption spectra were measured on a Hewlett-Packard 8452 diode array spectrometer. Photoluminescence and photoexcitation spectra were obtained on a Spex Fluorolog-2 spectrometer with front face collection of the emission. The spectra were corrected for the response of the spectrometer using experimentally determined correction factors. The absolute PL yields were estimated by comparing the integrated emission intensities of the particles in pyridine dispersion with the integrated intensity for Rhodamine 590 in methanol ($\Phi \approx 1$). The low temperature PL measurements on the composites films were carried out in a Janis cryostat cooled with liquid helium. The relative photoluminescence yields for the composite films were determined from the band-edge emission intensities. Absorption of the excitation light was estimated from the intensity of the transmitted light measured on the back-side of the samples with an Oriel silicon photodiode.

Chemical Composition. The Zn/Cd ratios in the ZnSe/CdSe nanocrystals and composite films were determined with a x-ray fluorescence spectrometer using a Diano V generator (Cr anode) and a HNU Si:Li detector. Samples of nanocrystals were prepared by evaporation of a few droplets of pyridine dispersion on a silicon wafer. ZnSe films grown by OMCVD in our laboratory and CdSe powder (99.99%, Alfa) were used as standards. Auger electron spectra of the nanocrystals were measured on a Perkin-Elmer AES microprobe Model 660 at a primary beam energy of 5 keV.

Electron Microscopy. High resolution transmission electron microscopy (HRTEM) images were obtained on a Topcon EM002B microscope operating at 200 kV. The nanocrystal specimens were prepared by placing a drop of a diluted pyridine dispersion on C/Ni TEM grids and rinsing off the excess dispersion with solvent after a short contact time. Overcoating of the

samples with a carbon film was used to improve the stability of the specimen in the electron beam of the microscope.

X-ray Diffraction. X-ray diffraction spectra of the nanocrystals were obtained on a Rigaku 300 rotating anode diffractometer operating in the Bragg configuration using $\text{CuK}\alpha$ radiation. The specimens were prepared by spreading a thin layer of precipitated nanocrystals on (100) or (111) silicon wafers.

6.3. Results and Discussion

6.3.1. Synthesis and Characterization of CdSe/ZnSe Nanoparticles

Synthesis

The CdSe/ZnSe particles were prepared by overgrowth of size-selected CdSe nanocrystals with ZnSe in trioctylphosphine (TOP) at 150-160°C. The overgrowth was controlled by the delivery of trioctylphosphine selenide (TOPSe) and diethylzinc (DEZn), the ZnSe precursors, into the reaction mixture. The feasibility of the precursor chemistry for synthesis of high quality ZnSe epilayers was recently demonstrated [10]. In order to avoid separate nucleation of ZnSe, a slow steady dosing of the precursors was maintained during the overgrowth.

The UV/Vis absorption spectra of the reaction mixture at various stages of the overgrowth are shown in Fig. 6.1. The formation of ZnSe was accompanied by a dramatic increase of the absorption in UV. This increase is consistent with the formation of ZnSe either on the CdSe nuclei or separately in the solution. In a comparative experiment without the presence of CdSe nuclei, the precursors reacted slowly, yielding a white precipitate soluble in hexane. The UV/Vis absorption spectrum of the product showed a sharp intense band at 320 nm. Similar absorption spectra were reported for small (molecular) clusters of CdS [11] and CdSe [8], indicating that the product might be a ZnSe analog of these species.

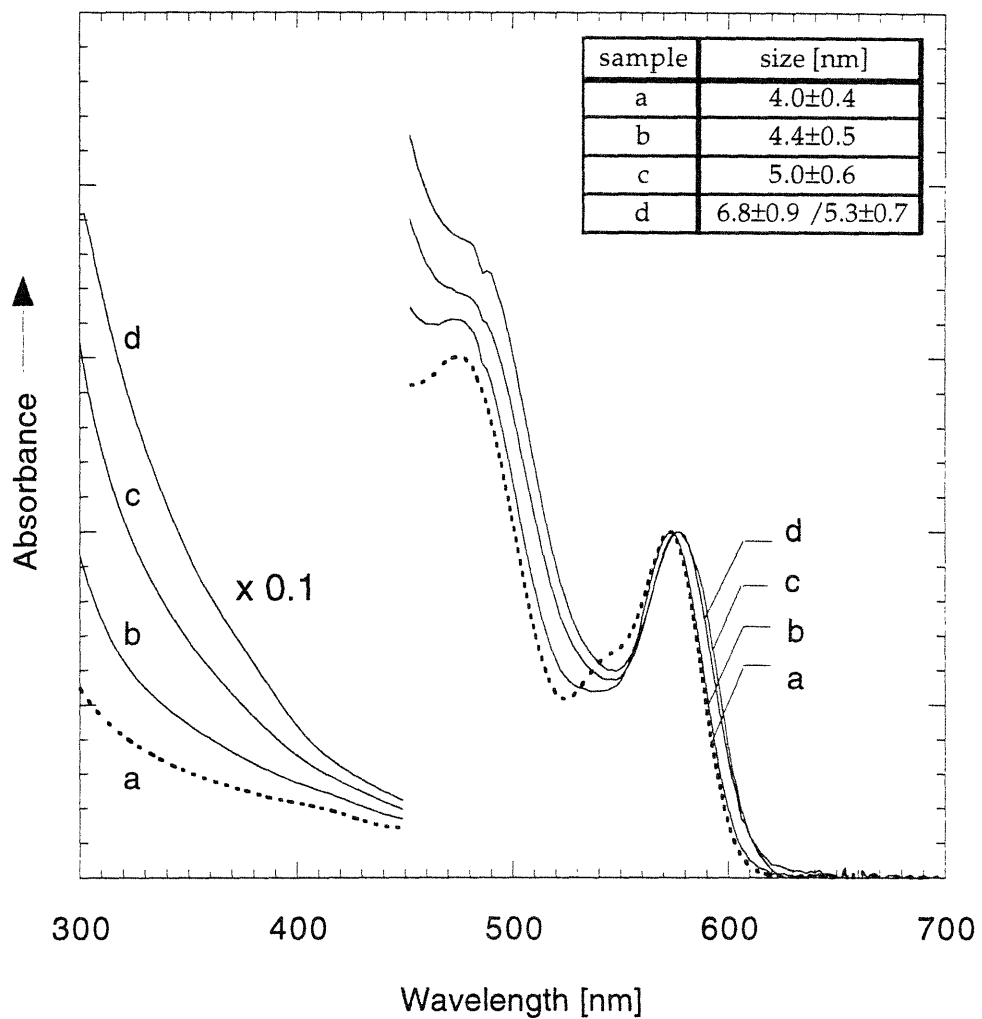


Figure 6.1. Evolution of the UV/Vis absorption spectra of the reaction mixture during overgrowth of ~ 4.0 nm CdSe nanocrystals with ZnSe. The inset shows the corresponding particle sizes as determined with HRTEM.

However, in the presence of CdSe nanocrystals, the formation of this side-product is not observed, supporting the heterogeneous nucleation mechanism.

The band-edge absorption of the initial CdSe nanocrystals remained almost unaffected during ZnSe growth. Only a small red shift (~2 nm) of the 1s-1s absorption maximum could be observed after a short reaction period. A comparative experiment without dosing DEZn into the reaction mixture showed that this shift is not caused by growth of the CdSe particles *via* an Ostwald ripening mechanism. At higher reaction temperatures (~200°C), a small blue shift (~2 nm) of the 1s-1s absorption maximum could be observed in the initial stage of the overgrowth, followed by a small red shift. This effect is consistent with alloying at the CdSe/ZnSe interface at elevated temperatures. Thus, the 1s-1s absorption band provides a sensitive probe for monitoring the integrity of the CdSe nuclei during the overgrowth.

The evolution of particle sizes in the reaction mixture during overgrowth was determined by HRTEM (inset of Fig. 6.1). As expected for a heterogeneous growth mechanism, the increase of the UV absorption was accompanied by an increase of the average particle sizes from ~4.0 nm to ~6.8 nm. The size distribution width (σ) increased from the initial ~10% to ~13% for the largest particles. At the same time the particle morphology changed from a nearly spherical shape to slightly irregular shapes with an aspect ratio of ~1.3 for the largest particles (Fig. 6.2). The increase of the particle sizes was consistent with the changes in the ZnSe/CdSe stoichiometry as determined by x-ray fluorescence analysis. For example, the [ZnSe/CdSe] ratio for particles with average dimensions of 6.8/5.3 nm was 2.5 ± 0.2 . These observations further support a heterogeneous growth mechanism over formation of separate ZnSe particles.

The described technique allows synthesis of composite particles as large as ~7 nm. Above this size the TOP dispersion is not stable and the particles precipitate out of the reaction mixture preventing a uniform overgrowth. The solubility properties of the overgrown particles vary with the particle

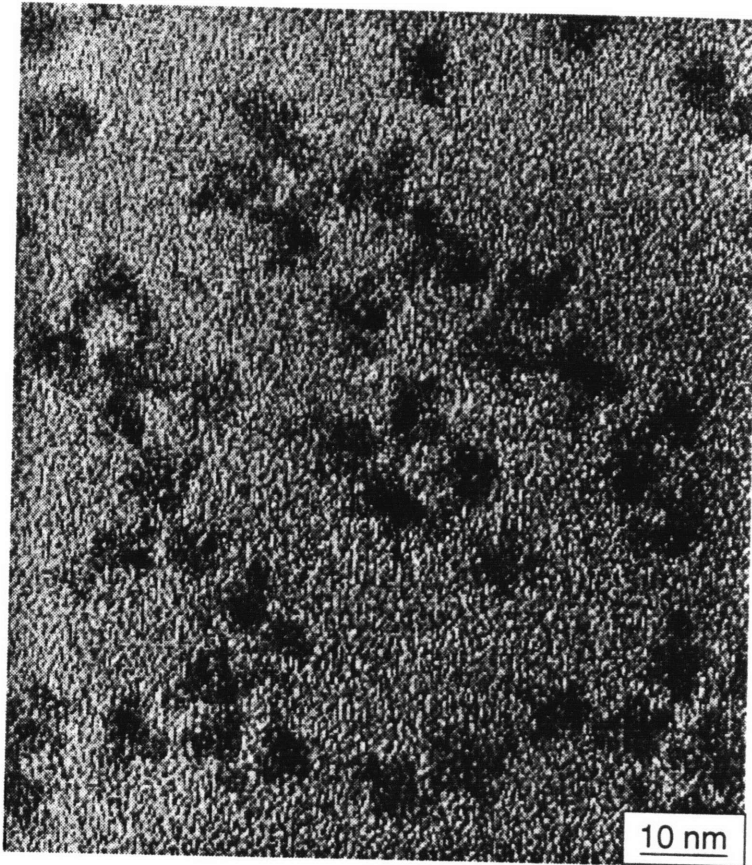


Figure 6.2. Low magnification TEM image of CdSe/ZnSe particles with $[\text{ZnSe}/\text{CdSe}]=2.5$. The initial size of the CdSe nanocrystals was ~ 4.0 nm.

size. For example, small particles (~4-5 nm) are fairly soluble in hexane while large particles (>5 nm) precipitate almost quantitatively after addition of hexane to the dispersion in TOP. However, the precipitated particles can be re-dispersed readily in pyridine. This different solubility in hexane and pyridine allow isolation and purification of large composite particles from the reaction side-products and unreacted TOPSe by a dissolution and precipitation sequence. During this purification the TOP surface functionality (cap) is quantitatively exchanged for a pyridine cap since the purified particles contain phosphorus below the detection limit of Auger electron spectroscopy (AES). The solubility properties of the composite particles exposed to air change over time, indicating susceptibility of the ZnSe surface to oxidation. Nevertheless, dispersions in anhydrous pyridine could be stored under an inert gas for several weeks without any precipitation or changes in the UV/Vis absorption.

Structural Characterization

High-magnification TEM images of derivatized particles with [Zn/Cd]=2.5 are shown in Fig. 6.3. The images show well resolved diffraction fringes of the particle lattice. The coherence of the fringes, as seen on a large fraction of the particles, is consistent with epitaxial overgrowth of ZnSe on the CdSe surface. However, the images do not provide any direct evidence about the location of the CdSe/ZnSe interface. Some of the particles display a lack of diffraction contrast on the periphery, which might indicate the presence of an amorphous or disordered ZnSe overlayer on the CdSe nuclei.

The crystallinity of the derivatized particles was further probed by x-ray diffraction. Fig. 6.4 displays diffraction spectra of ~6.8 nm composite particles ([ZnSe/CdSe]=2.5) and ~4.0 nm CdSe nanocrystals. The spectrum of the composite particles consist of rather broad features which do not overlap with the diffraction lines of wurtzite ZnSe or wurtzite CdSe. Such a diffraction pattern could be expected for largely alloyed particles. However, the alloying effect can be ruled out on the basis of an annealing experiment with a thin film of the overcoated particles. The absorption spectrum of the film as deposited from solution on a glass slide is shown in Fig. 6.5. After

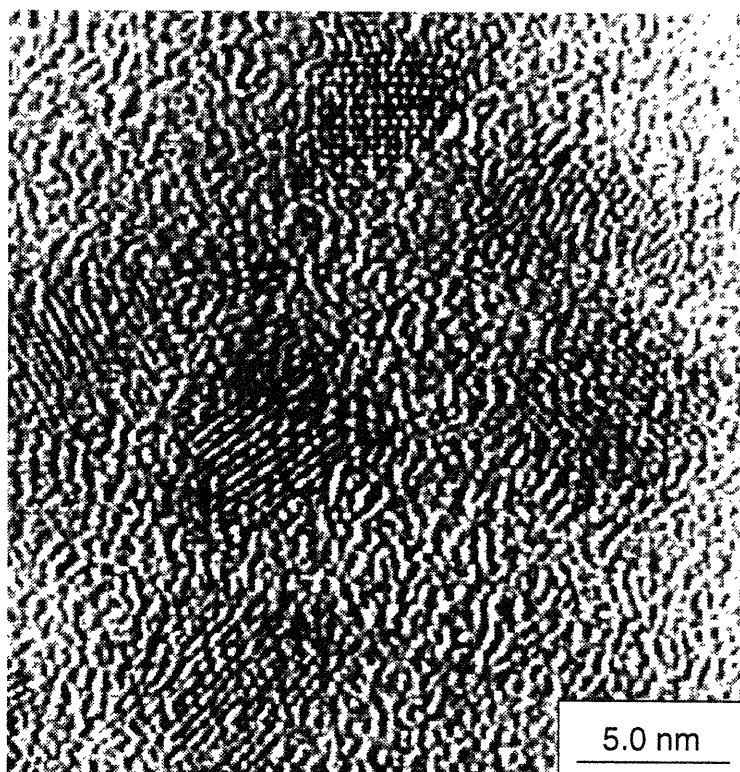


Figure 6.3. HRTEM image of CdSe/ZnSe particles with $[\text{ZnSe}/\text{CdSe}]=2.5$. The initial size of the CdSe nanocrystals was ~ 4.0 nm.

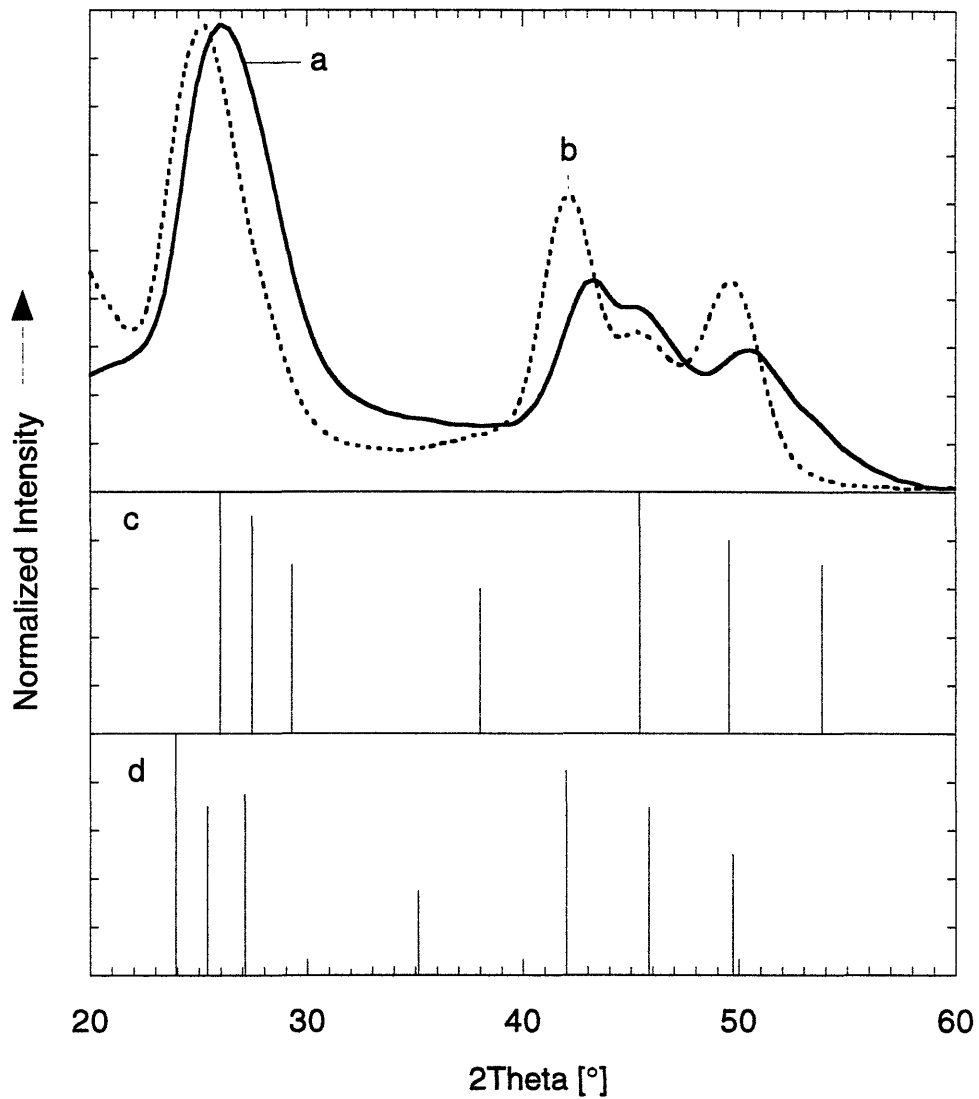


Figure 6.4. X-ray diffraction spectra of ~6.8 nm CdSe/ZnSe particles (a), ~4.0 nm CdSe nanocrystals (b), and powder diffraction lines of wurtzite ZnSe (c) and wurtzite CdSe (d). The [ZnSe/CdSe] ratio for the overcoated particles was ~2.5.

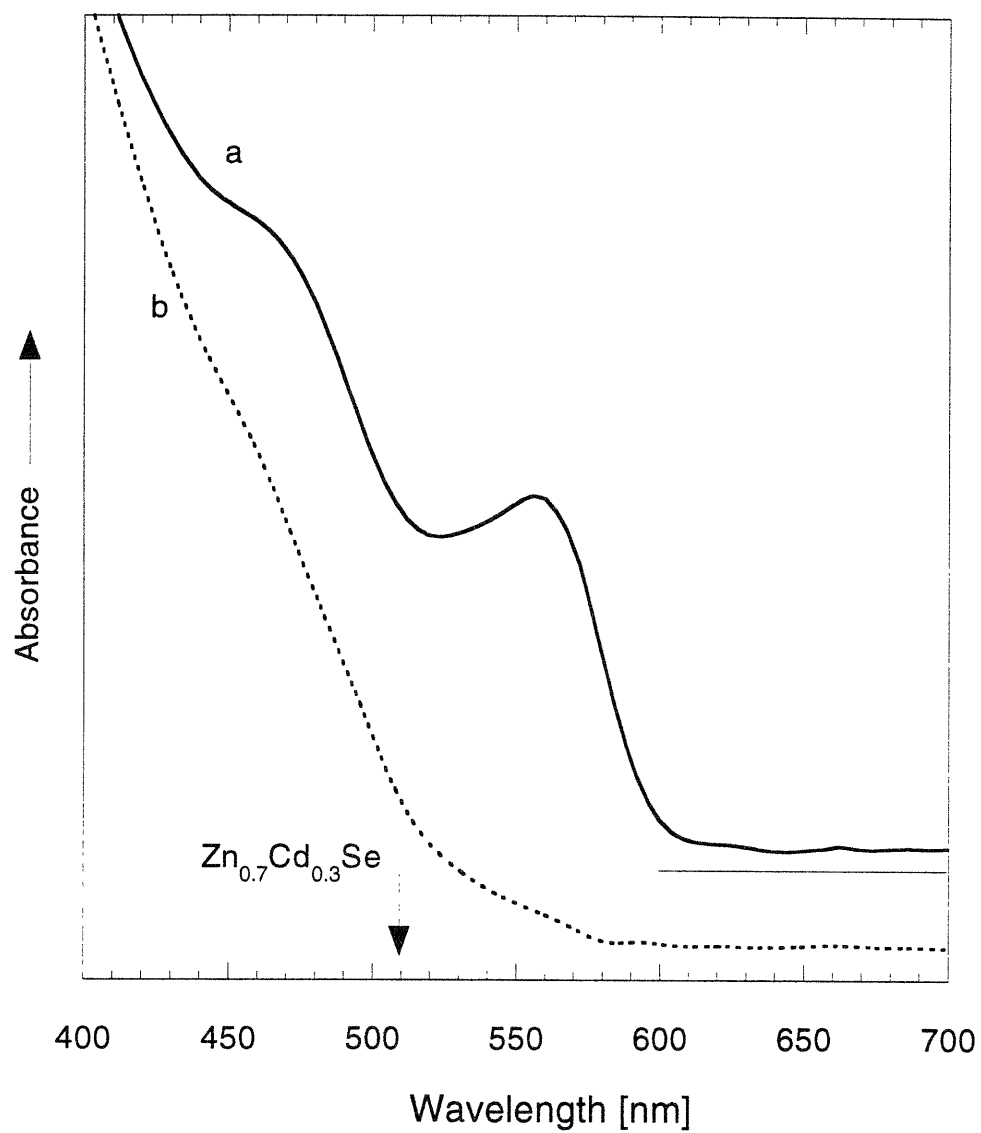


Figure 6.5. Optical absorption spectra of a film of CdSe/ZnSe particles with $[ZnSe/CdSe]=2.5$ before (a) and after (b) annealing in hydrogen at ~ 450 °C. The band-gap energy for $Zn_{0.7}Cd_{0.3}Se$ bulk is shown.

~10 min of annealing at ~450 °C in hydrogen flow, the absorption edge of the film moved into a short wavelength region as expected for the ternary alloy with a [Zn/Cd] stoichiometry of the original particles.

The broad diffraction features of the overcoated particles suggest a poor crystallinity of the ZnSe overlayer. This explanation is consistent with the observation of structural disorder in the periphery region of some of the particles. However, such a broadening of the diffraction spectra could also be caused by strain in the overlayer and core induced by the lattice mismatch [6b].

The shell-core structure of the passivated particles was probed qualitatively by a combination of AES and x-ray fluorescence analysis [3,7]. While AES is sensitive to the surface composition due to a short escape depth for Auger electrons (~1.0 nm), x-ray fluorescence allows analysis of the overall composition of the particles. X-ray fluorescence analysis of ~6.5 nm particles with a ~3.5 nm core yielded [ZnSe/CdSe] = 4.8 ± 0.3 , while AES gave [ZnSe/CdSe] = 7.0 ± 0.7 . This AES ratio is rather low for a symmetrical shell-core structure with ~1.3 nm thick overlayer since the escape depth for the Auger electrons in ZnSe is roughly 1 nm [7]. Therefore, we assume that the overlayer is not uniform around the CdSe core.

Optical Characterization

The effect of ZnSe overcoating on the optical properties of the CdSe quantum dots was explored with a set of samples isolated from a single preparation at various stages of the overgrowth. The samples were purified and derivatized with pyridine in parallel. Such a set of samples with identical CdSe cores allowed observation of the evolution of the particle properties with increasing thickness of the overlayer. The absorption spectra of the bare CdSe nanocrystals and CdSe/ZnSe particles with [ZnSe/CdSe] ratio ranging from 3.6 to 4.8 are shown in Fig. 6.6. All the spectra display a similar shape and width of the first absorption band. The 1s-1s absorption maximum underwent a slight red shift (~4 nm) after deposition of a ZnSe

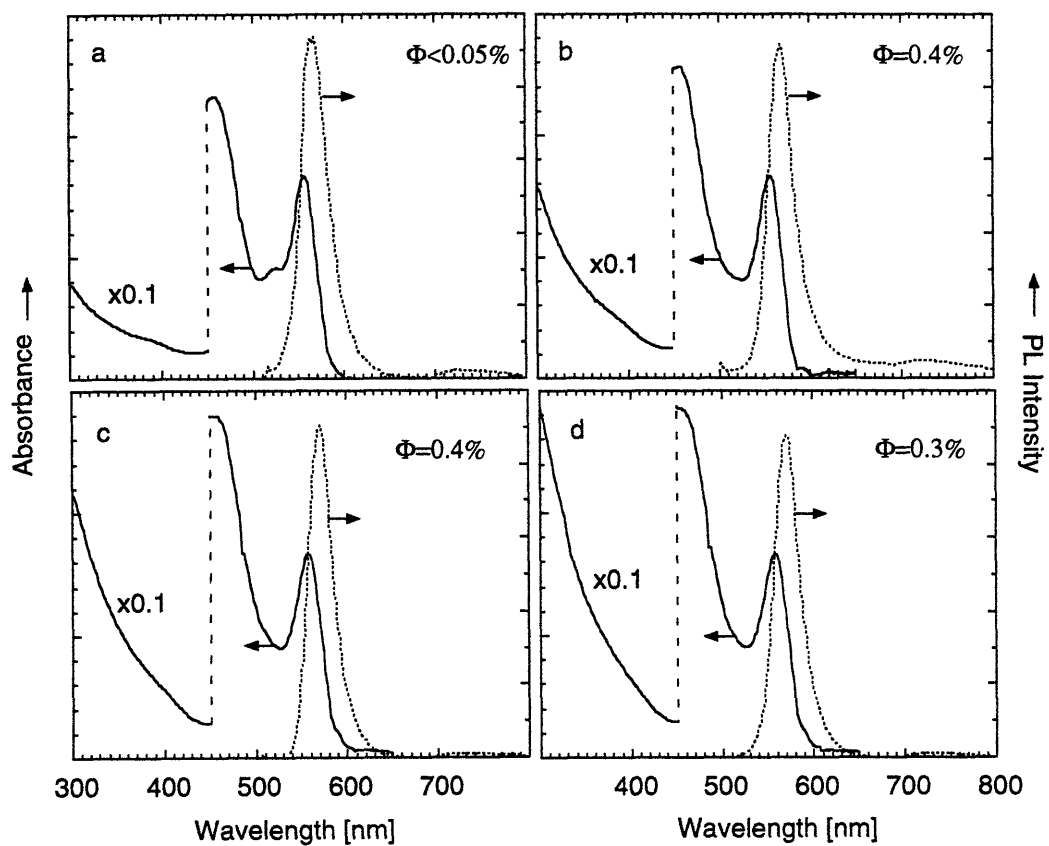


Figure 6.6. Optical absorption and PL spectra of CdSe (a) and CdSe/ZnSe particles with various [ZnSe/CdSe] ratios: 3.6 (b), 4.3 (c) and 4.8 (d). The samples were dispersed in pyridine. The excitation wavelength for the PL was 480 nm.

layer on the CdSe surface. The decrease of the exciton energy is consistent with a slight relaxation of the quantum confinement in the CdSe dots due to the presence of ZnSe on the CdSe surface. Interestingly, the surface derivatization was also accompanied by the disappearance of the second absorption band in the valley of the 1s-1s absorption band. The dramatic increase of the absorption in the short wavelength region with increasing [ZnSe/CdSe] ratio suggests that the high energy optical transitions are largely localized in the ZnSe layer.

The PL spectra of the bare and passivated particles are shown in Fig. 6.6. The spectra consist of a sharp band-edge emission and weaker, broad luminescence originating from deep electronic traps. The presence of the passivating layer resulted in a small red shift (~2-4 nm) of the band-edge emission of CdSe nanocrystals, consistent with the shift of the band-edge absorption. Thus, the same Stokes shift (~10 nm) of the band-edge emission was observed for both bare and overcoated particles. The width of the emission band is identical for all the particles, providing further evidence that the CdSe dots preserved their initial size distribution during the passivation. However, there was a significant difference in the PL yield between the bare and passivated nanocrystals. The yield of band-edge emission for the bare particles capped with pyridine was very low ($\Phi \sim 0-0.05\%$) while the yield for the overcoated particles was $\sim 0.3-0.4\%$. This result is consistent with the observation of enhanced band-edge emission from CdSe(core)-ZnS(shell) particles [3]. The absolute photoemission yield for the overcoated particles is, however, low in comparison to $\Phi \sim 10\%$ for CdSe nanocrystals capped with TOP/TOPO [8]. This result is not surprising since characterization of the particles revealed some degree of structural imperfection in the overlayer. Based on the assumption that one optically active defect may be sufficient for quenching the band-edge luminescence of the particle, it is likely that the observed yield corresponds to a small fraction of particles with a defect free overlayer.

The effect of passivation on the emission properties of the nanocrystals was further probed by PL excitation spectroscopy. The excitation spectra of

the bare and overcoated particles are displayed in Fig. 6.7. The spectra were normalized to the excitation efficiency at 550 nm, a wavelength predominantly absorbed by the CdSe core. The spectra show an increase of the excitation efficiency in the short-wavelength region for the overcoated particles where the absorption in the ZnSe layer is significant (Fig. 6.6.). This result provides additional evidence for the presence of ZnSe on the CdSe surface since energy transfer between separated particles in such a diluted dispersion is unlikely. If the ZnSe and CdSe particles were separated, the ZnSe phase would be an “internal” filter for the short-wavelength excitation light and the photoexcitation efficiency would drop dramatically. Moreover, the spectra indicate a high quality ZnSe-CdSe interface as the capture of the photogenerated carriers by CdSe can compete with the nonradiative recombination within the ZnSe overlayer. However, the excitation efficiency in the short wavelength region did not increase monotonically with an increase of the [ZnSe/CdSe] ratio. The spectrum for the particles with [ZnSe/CdSe]=4.8 indicates that the efficiency might even drop for thick overlayers. This peculiar dependence on the [ZnSe/CdSe] ratio can be explained by relaxation of the lattice mismatch strain in ZnSe as the thickness of the overlayer increases. Such a relaxation would be analogous to the relaxation of strained CdSe/ZnSe superlattices *via* formation of misfit dislocations, resulting in a significant deterioration of PL efficiency [12]. In the superlattices, the critical thickness for defect formation in CdSe quantum wells is ~4 monolayers.

6.3.2. Synthesis of CdSe/ZnSe Composites with Passivated CdSe Nanocrystals

Thin film composites incorporating bare and overcoated nanocrystals in ZnSe matrices were prepared by ES-OMCVD [1]. The effect of the pre-formed ZnSe overlayer on the luminescent properties of the composites was probed by PL spectroscopy at 300K and 10K. The 300K spectra of the composites prepared from bare CdSe nanocrystals at various substrate temperatures are shown in Fig. 6.8. The spectra consist of a weak band-edge emission and a

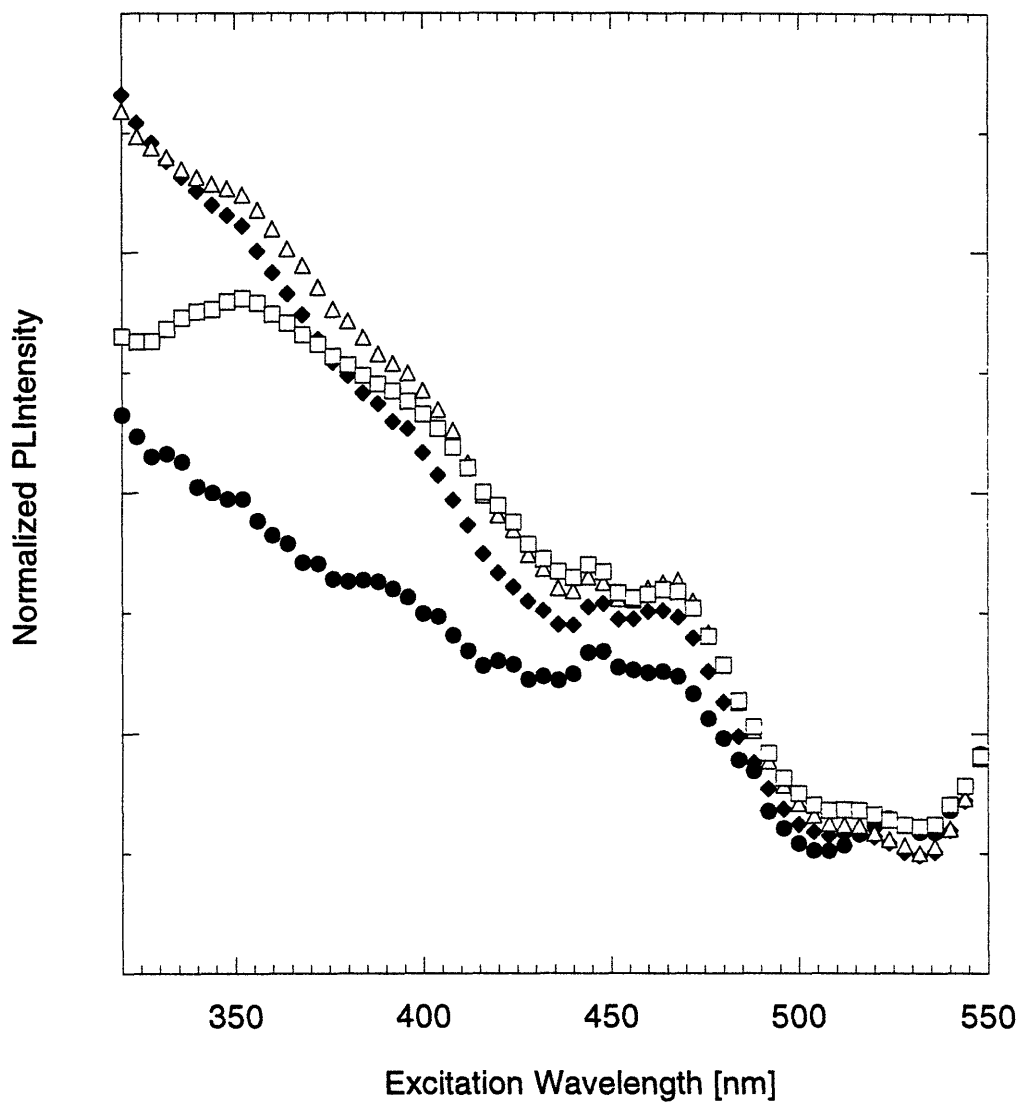


Figure 6.7. PL excitation spectra of CdSe (●) and CdSe/ZnSe particles with [ZnSe/CdSe] ratio of 3.6 (◆), 4.3 (Δ) and 4.8 (□). The samples were dispersed in pyridine. The PL was detected at 570 nm and the spectra were normalized to the PL intensity at 550 nm.

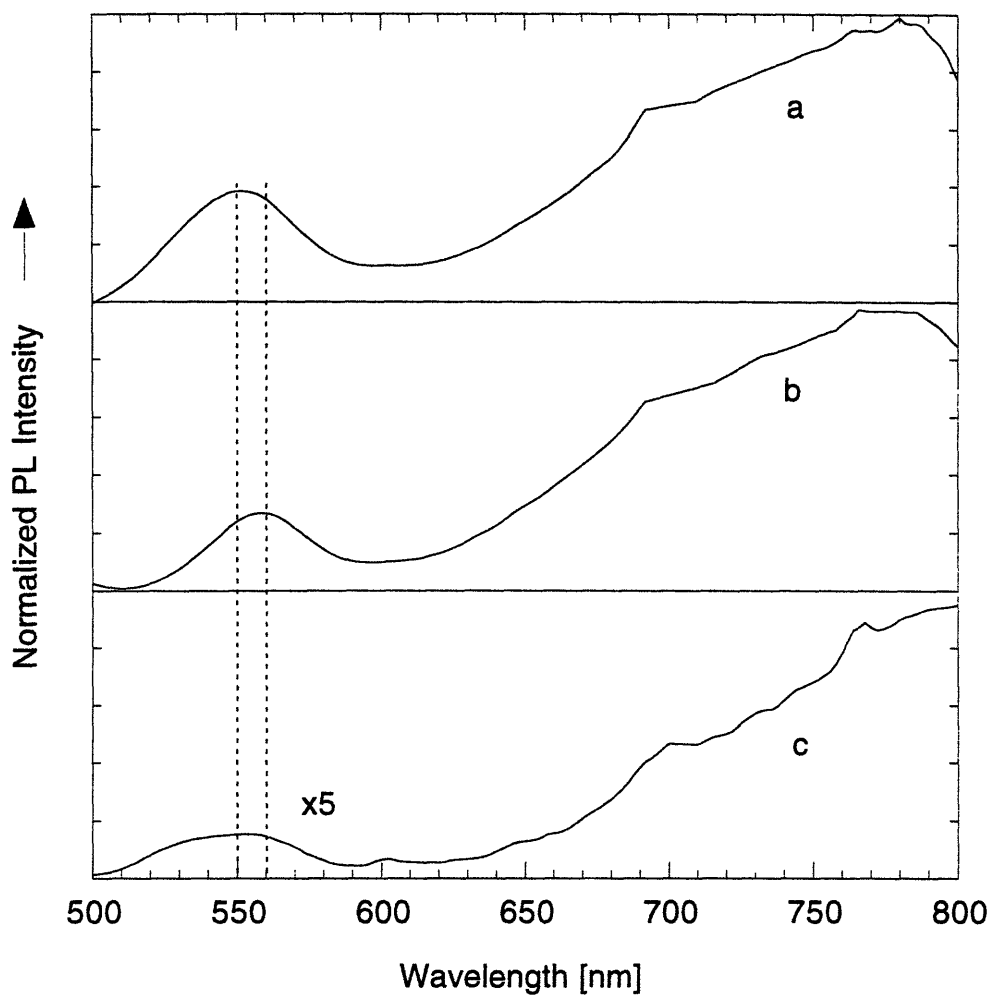


Figure 6.8. 300K PL spectra of CdSe/ZnSe composite films with bare CdSe nanocrystals (~3.5 nm). The films were synthesized by ES-OMCVD at substrate temperatures of 150 °C (a), 200 °C (b) and 250 °C (c). The excitation wavelength was 480 nm.

dominant deep-level emission. The wavelength of the band-edge emission is characteristic of the size of the initial CdSe nanocrystals [1]. The maximum of the band-edge emission underwent a ~ 10 nm red shift with increasing deposition temperature from 150 °C to 200 °C. Further increase of the temperature to 250 °C moved the emission wavelength back to ~ 550 nm. Similar changes in the emission wavelengths with deposition temperature were also observed in PL spectra of composites incorporating nanocrystals of a different size. Since a large fraction of the incorporated nanocrystals is in agglomerates [1a], the red shift for a deposition temperature of ~ 200 °C might indicate ripening or coalescence of the agglomerated particles. The blue shift at higher temperatures (~ 250 °C) is consistent with alloying at the CdSe-ZnSe interface. At the same time the relative yield of the band-edge emission drops by one order of magnitude. The predominance of deep-level emission is consistent with the presence of defects at the CdSe-ZnSe interface as observed with HRTEM [1].

The 10 K spectra further accentuate the presence of deep electronic traps on the surface of the CdSe nanocrystals (Fig. 6.9). The spectra are dominated by an intense and broad deep-level emission. The enhancement of the deep-level emission is consistent with a decrease in the rate of nonradiative exciton recombinations at the low temperature. The band-edge emission remains very weak, indicating that only a marginal fraction of the nanocrystals is electronically passivated by the matrix.

PL excitation spectra recorded at 300 K and 10 K confirm the assignment of the PL spectra and provide additional insight into the optical characteristics of the composites (Fig. 6.10). In the range of 460-520 nm, the excitation spectra for the band-edge emission display the absorption spectrum of the initial nanocrystals. At shorter wavelengths the excitation efficiency drops dramatically due to absorption of the excitation light in the matrix. The absorption edge of the matrix at 300 K and 10 K is clearly visible in the spectra. The 10 K excitation spectrum for the deep-level emission displays a maximum corresponding to the 1s-1s absorption band of the nanocrystals. Thus, the spectrum provides clear evidence that the deep-level

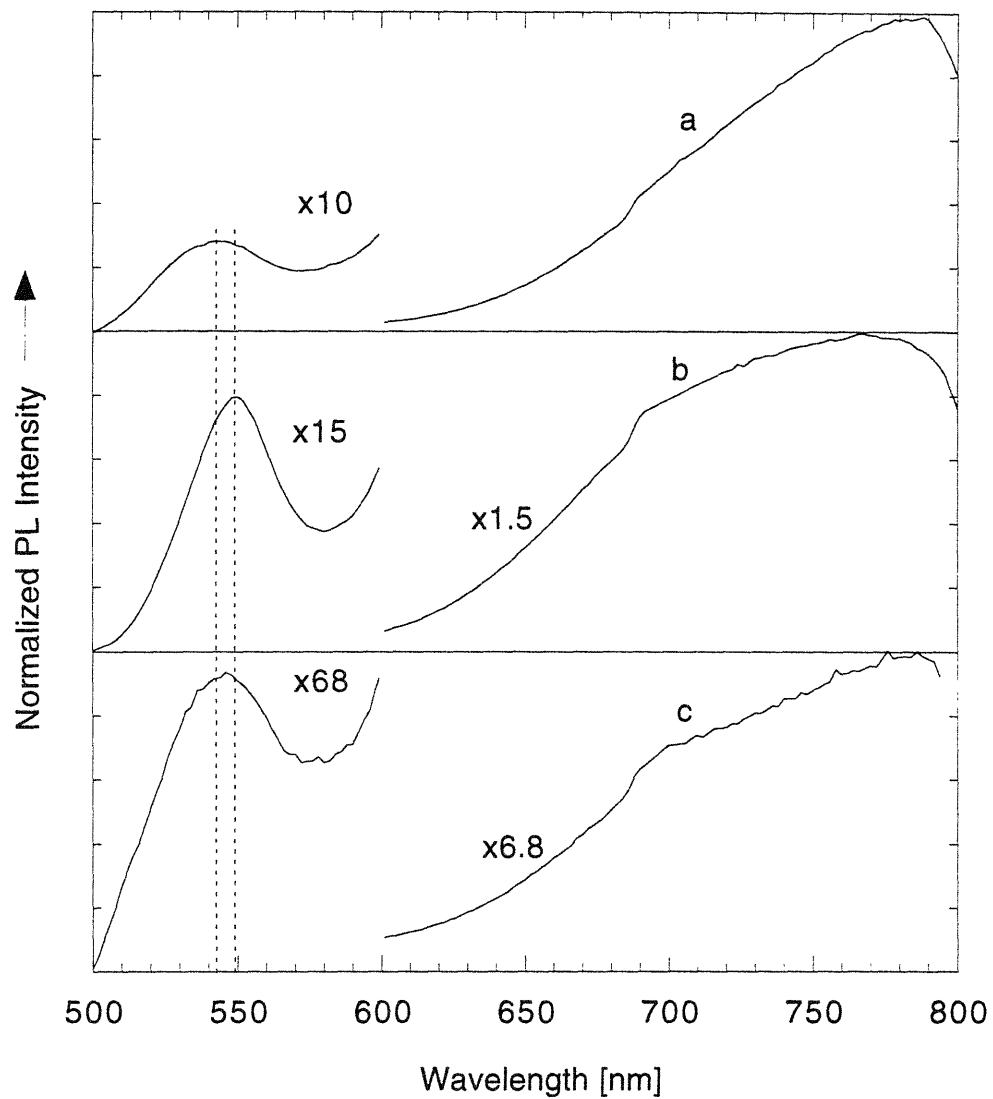


Figure 6.9. 10K PL spectra of CdSe/ZnSe composite films with bare CdSe nanocrystals (~3.5 nm). The films were synthesized by ES-OMCVD at substrate temperatures of 150 °C (a), 200 °C (b) and 250 °C (c). The excitation wavelength was 480 nm.

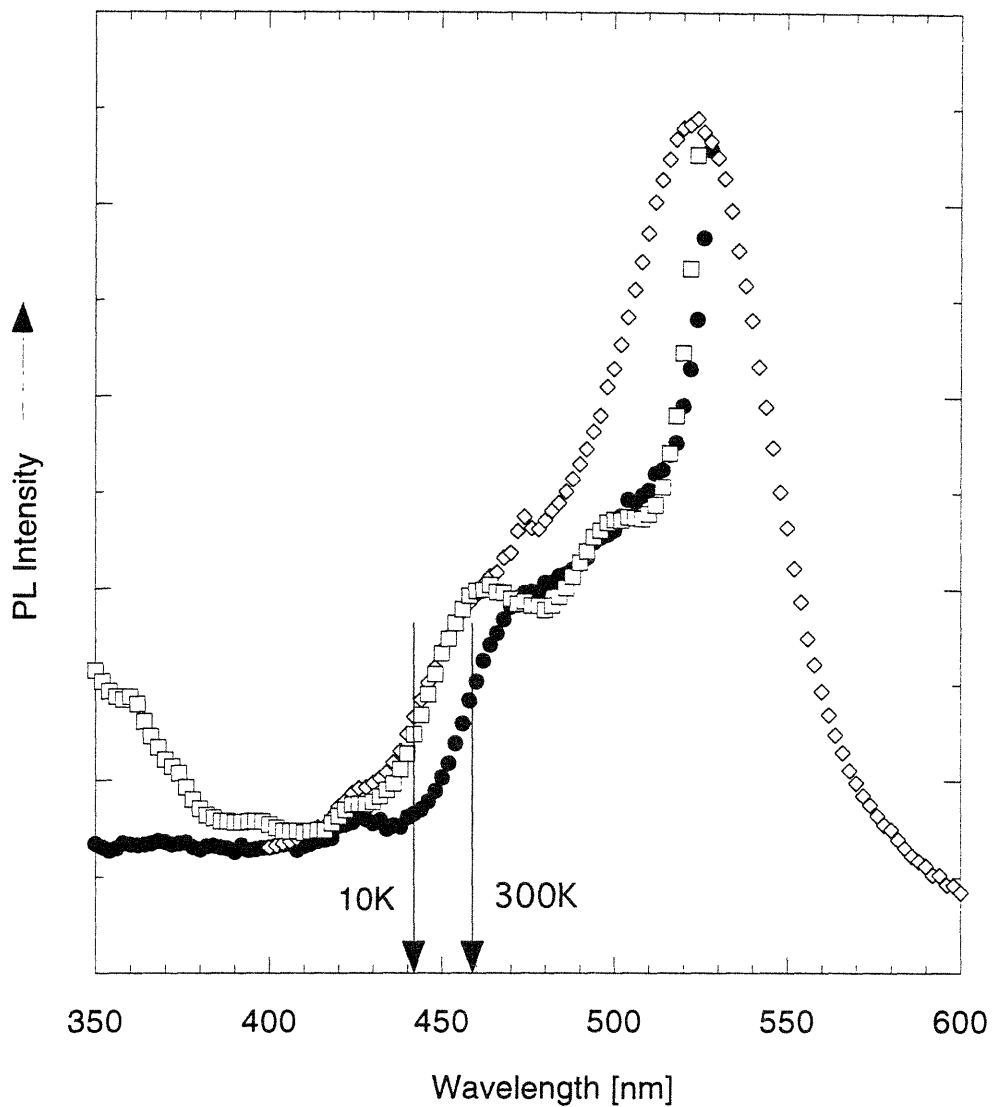


Figure 6.10. 300 K and 10K PL excitation spectra of CdSe/ZnSe composite films with bare CdSe nanocrystals (~3.5nm) synthesized by ES-OMCVD at 200 °C. The 300 K PL was detected at 554 nm (●), the 10 K PL detection wavelengths were 546 nm (◻) and 710 nm (◊). The band-gap energies of zinc blende ZnSe at 300 K and 10K are shown with the arrows.

emission in Fig. 6.9 originates from the buried CdSe nanocrystals and not from the matrix.

Incorporation of the overcoated nanocrystals resulted in a remarkable enhancement of the PL properties of the materials. The 300 K spectra (Fig. 6.11) are dominated by an intense band-edge emission. The widths of the emission bands are similar for all the samples deposited in the range of 150-270°C. However, increasing deposition temperature resulted in a small blue shift (~4 nm) of the emission maximum. This result is consistent with alloying at the CdSe/ZnSe interface. The deep-level emission remains weak even for composites deposited at ~270 °C.

The band-edge emission also dominated 10 K PL (Fig. 6.12), although the relative intensity of the deep-level emission increased slightly. A small blue shift of band-edge PL (~8 nm) was observed as an effect of increasing deposition temperature, although the FWHM of the bands remained identical. This result is rather surprising, since the imbedded particles experienced various exposure times to elevated temperatures during the synthesis depending on their depth in the composite layer (the overall deposition time was ~60 minutes). Intuitively, the composites grown at a high temperature should display a broadening of the emission bandwidth. However, this effect might be compensated by a narrowing of the emission bands due to alloying of the CdSe/ZnSe interface. Such a narrowing of emission bandwidths due to interfacial alloying was reported for ZnSe/CdSe superlattices [12b,c].

The 300 K and 10 K PL excitation spectra for the band-edge emission show the absorption bands of the overcoated nanocrystals in the range of 480-550 nm, and the absorption edge of the matrix at shorter wavelengths (Fig. 6.13). The excitation spectra indicate that the emitting state of the dots is populated by absorption of the excitation light in the nanocrystals. A high density of recombination centers in the polycrystalline matrix, associated with structural defects and grain boundaries, does not allow an efficient population of the CdSe excited state by optical pumping of the matrix.

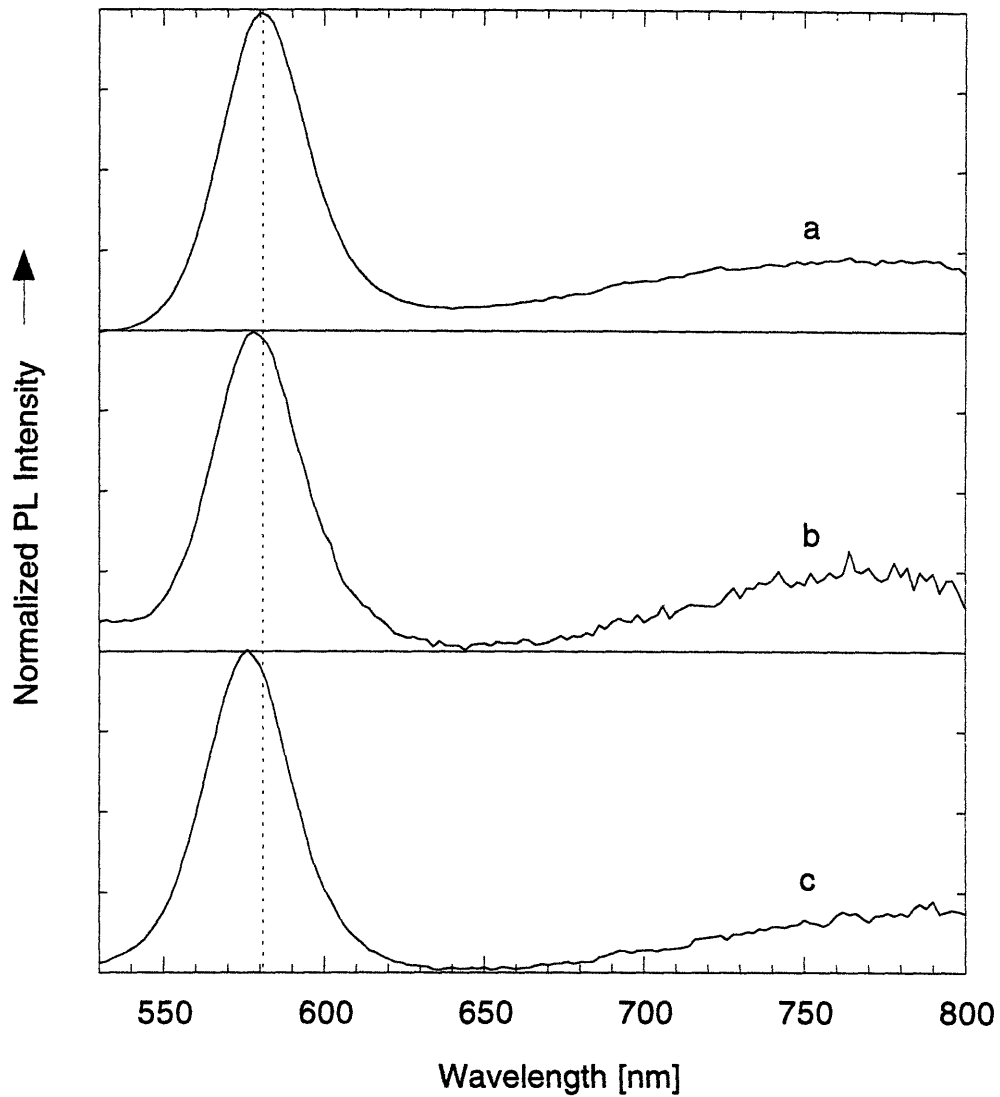


Figure 6.11. 300 K PL spectra of CdSe/ZnSe composite films with overcoated CdSe nanocrystals. The size of the initial CdSe dots was ~ 3.7 nm; $[\text{ZnSe}/\text{CdSe}] = 4.0$. The films were synthesized by ES-OMCVD at substrate temperatures of 150 °C (a), 200 °C (b) and 270 °C (c). The excitation wavelength was 480 nm.

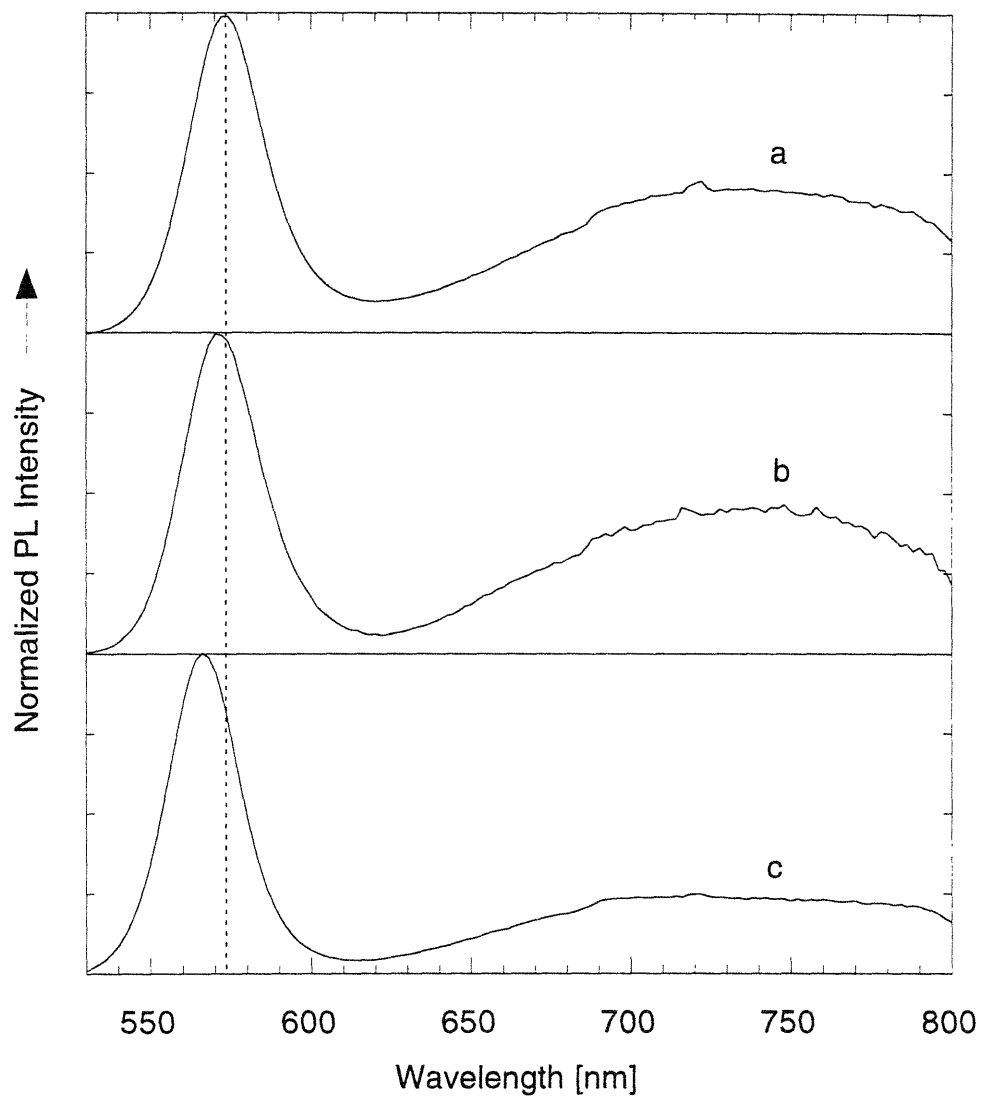


Figure 6.12. 10 K PL spectra of CdSe/ZnSe composite films with overcoated CdSe nanocrystals. The size of the initial CdSe dots was ~ 3.7 nm; $[\text{ZnSe}/\text{CdSe}] = 4.0$. The films were synthesized at substrate temperatures of 150 °C (a), 200 °C (b) and 270 °C (c). The excitation wavelength was 480 nm.

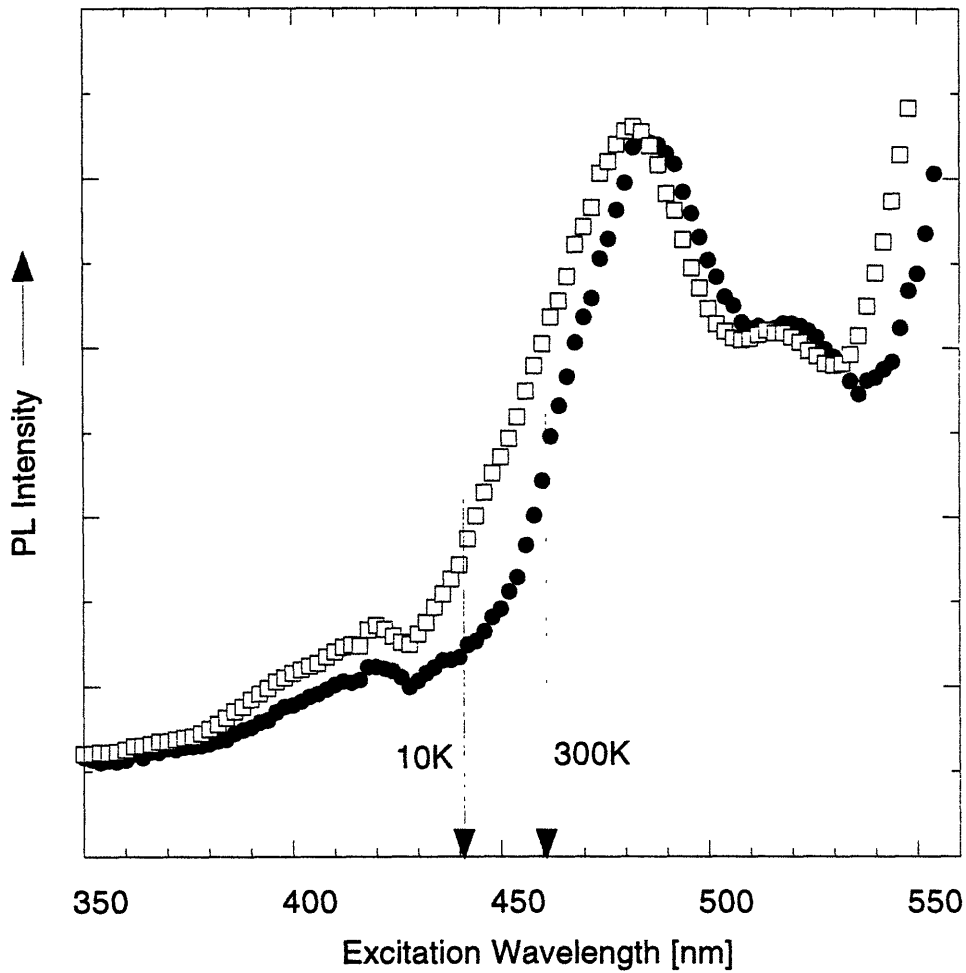


Figure 6.13. 300 K and 10K PL excitation spectra of a CdSe/ZnSe composite film with overcoated CdSe nanocrystals. The film was synthesized by ES-OMCVD at 200 °C. The size of the initial CdSe dots was ~3.7nm; [ZnSe/CdSe]=4.0. The 300 K PL was detected at 576 nm (●), the 10 K PL was monitored at 570 nm (□). The band-gaps of zinc blende ZnSe at 300 K and 10K are shown with the arrows.

The effect of the passivation on the luminescent properties of the composites was further explored with films containing nanocrystals with various thicknesses of the ZnSe overlayer (as calculated from the [ZnSe/CdSe] stoichiometry and the known size of the initial particles assuming a symmetrical shell-core structure). The dependence of the band-edge emission yield on the thickness of the ZnSe overlayer is shown in Fig. 6.14 for two deposition temperatures. A significant enhancement of the emission yield, by more than one order of magnitude as compared to composite films containing bare CdSe dots, was observed for the films incorporating particles passivated with ~ 0.6 monolayer of ZnSe. Deposition of ~ 3 monolayers of ZnSe resulted in an increase of the yield by a factor of ~ 100 . This enhancement of the PL yield, accompanied by conversion of deep-level emission into band-edge emission, demonstrates an effective electronic passivation of the CdSe dots with the ZnSe overlayer. Moreover, the relative PL yield for the passivated nanocrystals was insensitive to the deposition temperature. Therefore, the ZnSe overlayer provides for both electronic and chemical passivation of CdSe nanocrystals in the composite films.

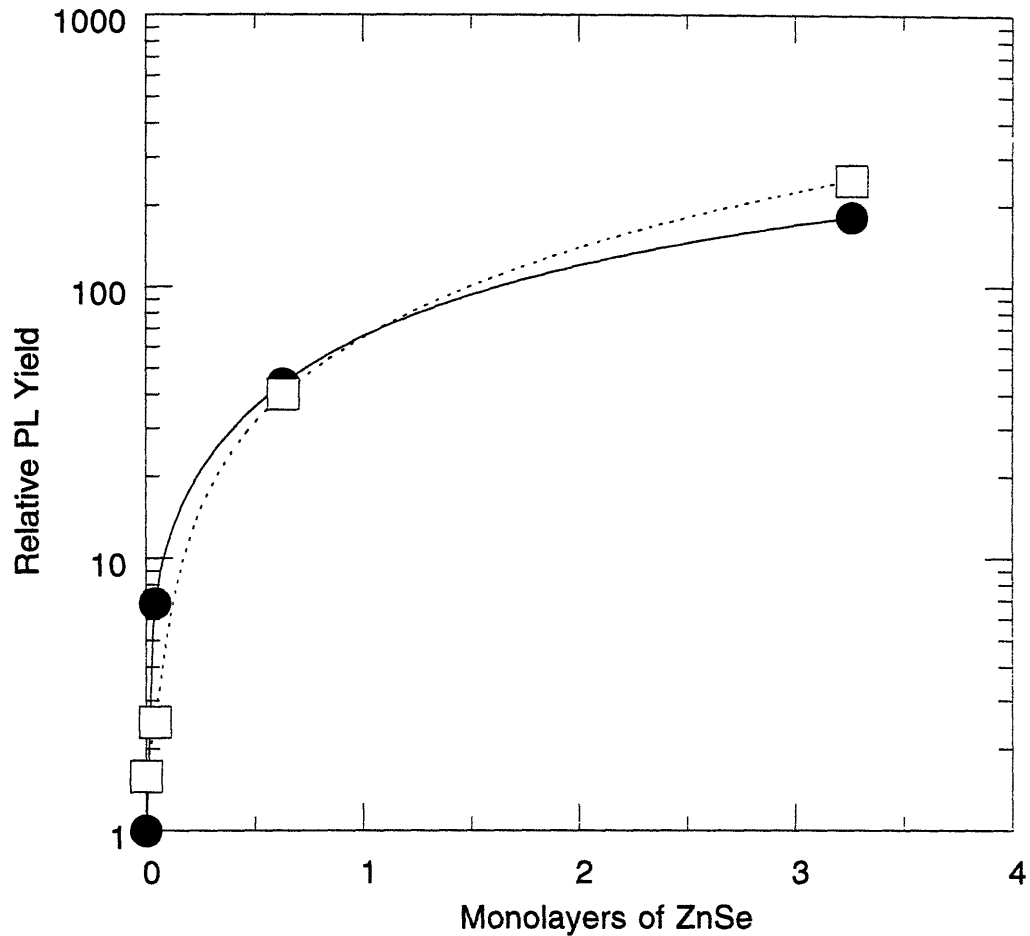


Figure 6.14. Relative band-edge PL yields for CdSe/ZnSe composite films with bare and passivated CdSe dots. The samples were synthesized by ES-OMCVD at substrate temperatures of 200°C (●) and 260 °C (□). The number of ZnSe monolayers in the passivating layer was estimated from the know size of the initial CdSe nanocrystals and [ZnSe/CdSe] stoichiometry of the composite particles assuming a symmetrical core-shell structure. The excitation wavelength was 500 nm.

6.4. Conclusions

Electronic and chemical passivation of CdSe nanocrystals is indispensable for the synthesis of luminescent CdSe/ZnSe quantum dot composites by ES-OMCVD. Such passivation can be obtained by overcoating CdSe nanocrystals with a layer of ZnSe. The described solution procedure, relying on heterogeneous nucleation of the passivating layer on the surface of the nanocrystals, allows controlled growth of a highly crystalline overlayer of ZnSe on CdSe nanoparticles. The PL spectra of the CdSe/ZnSe composites incorporating the passivated particles display a pronounced band-edge emission. The relative PL yields for the composites with the passivated particles are higher by two orders of magnitude than the yields for the composites with bare CdSe. The combination of solution synthesis, passivation of semiconductor nanocrystals, and ES-OMCVD presents a versatile route to novel quantum dot materials with attractive optical properties.

References

- [1] (a) Danek, M.; Jensen, K. F.; Murray, C. B.; Bawendi, M. G. *Appl. Phys. Lett.* **1994**, *65*, 2795. (b) Danek, M.; Jensen, K. F.; Murray, C. B.; Bawendi, M. G. *J. Cryst. Growth* - in press.
- [2] Youn, H. C.; Baral, S.; Fendler, J. H. *J. Phys. Chem.* **1988**, *92*, 6320.
- [3] Kortan, A. R.; Hull, R.; Opila, R. L.; Bawendi, M. G.; Steigerwald, M. L.; Carroll, P. J.; Brus, L. E. *J. Amer. Chem. Soc.* **1990**, *112*, 1327.
- [4] (a) Hässelbarth, A.; Eychmüller, A.; Eichberger, R.; Giersig, M.; Mews, A.; Weller, H. *J. Phys. Chem.* **1993**, *97*, 5333. (b) Mews, A.; Eychmüller, R.; Giersig, M.; Schooss, D.; Weller, H. *J. Phys. Chem.* **1994**, *98*, 934.
- [5] (a) Littau, K. A.; Szajowski, P. J.; Muller, A. J.; Kortan, A. R.; Brus, L. E. *J. Phys. Chem.* **1993**, *97*, 1224. (b) Wilson, W. L.; Szajowski, P. J.; Brus, L. E. *Science* **1993**, *262*, 1242. (c) Warwa, E.; Seraphin, A. A.; Chiu, L. A.; Zhou C.; Kolenbrander K. D. *Appl. Phys. Lett.* **1994**, *64*, 1821. (d) Chiu, L. A.; Seraphin, A. A.; Kolenbrander K. D. *J. Electron. Mater.* **1994**, *23*, 347.
- [6] (a) Henglein, A. *Chem. Rev.* **1989**, *89*, 1861. (b) Zhou, H. S.; Honma, I.; Koimiyama, H.; Haus, J. W. *J. Phys. Chem.* **1993**, *97*, 895. (c) Zhou, H. S.; Sasahara, H.; Honma, I.; Komiyama, H.; Haus, J. W. *Chem. Mater.* **1994**, *6*, 1534.
- [7] Hoener, C. F.; Allan, K. A.; Bard, A. J.; Champion, A. Fox, M. A.; Mallouk, T. E.; Webber, S. E.; White, J. M. *J. Phys. Chem.* **1992**, *96*, 3812.
- [8] Murray, C. B.; Norris, D. J.; Bawendi, M. G. *J. Amer. Chem. Soc.* **1993**, *115*, 8706.
- [9] Wright, P. J.; Cockayne, B.; Oliver, P. E.; Jones, A. C. *J. Crystal Growth* **1991**, *108*, 525.
- [10] Danek, M.; Foley, L.; Jensen, K. F. *J. Cryst. Growth* - in press.
- [11] Herron, N.; Calabrese, J. C.; Farneth, W. E.; Wang, Y. *Science*, **1993**, *259*, 1426.
- [12] (a) Zajicek, H.; Juza, P.; Abramof, E.; Pankratov, O.; Sitter, H.; Helm, M. Brunthaler, G.; Faschinger, W.; Lischka, K. *Appl. Phys. Lett.* **1993**, *62*, 717. (b) Zhu, Z.; Yoshihara, H.; Takebayashi, K.; Yao, T. *Appl. Phys. Lett.* **1993**, *63*, 1678. (c) Zhu, Z.; Yoshihara, H.; Takebayashi, K.; Yao, T. *J. Cryst.*

Growth, **1994**, *138*, 619. (d)Matsumoto, T.; Iwashita, T.; Sasamoto, K.; Kato, T. J. *Cryst. Growth*, **1994**, *138*, 63.

Chapter 7

Conclusions and Future Work

Wide band-gap II-VI semiconductors are promising materials for optoelectronic applications, including flat panel displays and carrier injection emitters. The thesis research was focused on chemical approaches to OMCVD of II-VI materials, specifically ZnSe, ZnTe and CdSe/ZnSe quantum dot composites.

Highly volatile (trifluoromethyl)tellurium compounds, such as *tert*-butyl(trifluoromethyl)tellurium, were previously suggested as novel precursors for low temperature OMCVD of IIb group tellurides. OMCVD experiments with *tert*-butyl(trifluoromethyl)tellurium showed that the new precursor produced ZnTe films heavily contaminated with ZnF₂ crystallites at growth temperatures below 400 °C. Even though the films grown at higher temperatures did not contain a ZnF₂ phase, islands of high fluorine contamination of ZnTe films were detected by SIMS. A gas-phase pyrolysis study under OMCVD conditions pointed to β -hydrogen elimination as the major low temperature decomposition pathway of *tert*-butyl(trifluoromethyl)tellurium. At higher temperatures this pathway competes with homolysis of the Te-C(*tert*-butyl) bond and difluorocarbene extrusion. Hydrogen fluoride, likely formed from (trifluoromethyl)tellurol (the primary product of β -hydrogen elimination), is the suspected source of the fluorine contamination. The study concludes that (trifluoromethyl)tellurium moiety, in the combination with an alkyl group facilitating decomposition *via* β -hydrogen elimination, is unstable under the growth conditions and should be avoided in future precursor design.

OMCVD experiments with *tert*-butyl(allyl)selenium, a new selenium precursor proposed for low temperature growth, confirmed that the *tert*-butyl group effectively blocks the carbon contamination reaction encountered with other allylselenium precursors, *e.g.* methyl(allyl)selenium and

diallylselenium. The precursor allowed growth of epitaxial ZnSe at low temperatures (~350 °C) and the films displayed good crystallinity and photoluminescence spectra. However, the decomposition mechanism of the heteroleptic precursor is complicated, involving β -hydrogen elimination and homolysis of the Se-C bonds as the primary decomposition steps. The β -hydrogen elimination pathway prevails at low pyrolysis temperatures and diallylselenium was observed as a minor decomposition by-product. Pyrolysis in the presence of dimethylzinc yielded methyl(allyl)selenium, diallylselenium and dimethylselenium. These side-reactions of the precursor are undesirable since the presence of the allylselenium by-products may result in carbon contamination of the films. The results of the pyrolysis study suggest that the side-reactions could be controlled by depositing ZnSe at low partial pressures of the precursors, short reactor residence times, and low [VI/II] ratios. Since the allylselenium by-products are thermally more stable than *tert*-butyl(allyl)selenium, their contribution to the growth should be marginal at low growth temperatures (~350 °C). Further work is necessary to optimize the growth conditions to obtain films with low resistivity.

In order to circumvent hydrogen contamination of ZnSe films, a new precursor chemistry utilizing trialkylphosphine selenides, dimethylzinc and a helium carrier gas was proposed. OMCVD with tripropylphosphine selenide yielded ZnSe films with good photoluminescence spectra and very low hydrogen, carbon and phosphorus concentration levels (comparable to the detection limits of SIMS). The possibility to improve the volatility of the phosphine selenide precursor was explored with dimethyl(butyl)phosphine. Growth experiments with dimethyl(butyl)phosphine selenide, a selected compound with a low melting point and high volatility, provided films of quality comparable to those grown from tripropylphosphine selenide. The phosphine selenide precursor chemistry opens new opportunity for OMCVD synthesis of hydrogen free ZnSe and p-type doping. Purification of the phosphine selenide precursors is necessary to realize the potential of the precursor system.

A novel technique, implementing electrospray into the classical OMCVD process, was developed for synthesis of II-VI quantum dot composites. The technique relies on electrospray transfer of semiconductor nanocrystals (quantum dots) from a liquid dispersion into gas-phase and co-deposition with a II-VI matrix synthesized by OMCVD. New composites incorporating CdSe nanocrystals in a ZnSe matrix were prepared and characterized. The CdSe/ZnSe composites displayed room temperature photoluminescence characteristic of the incorporated nanocrystals and the emission wavelength of the materials could be adjusted by selecting the size of the initial nanocrystals. A large variety of new materials may be prepared by electrospray OMCVD selecting other semiconductor nanocrystals and matrices. Such investigations could bring new insights into OMCVD growth and open new routes to high performance light emitting materials. Construction of electroluminescent devices with electrospray OMCVD is also a future prospect.

A new solution procedure was described for controlled overgrowth of size-selected CdSe particles with a thin layer of ZnSe. The overcoated particles displayed absorption and emission properties characteristic of the initial CdSe nanocrystals. The passivated particles were used in electrospray OMCVD synthesis of CdSe/ZnSe composites. The films with the passivated nanocrystals displayed a remarkable enhancement of the photoluminescence yield (by one to two orders of magnitude) in comparison with the films incorporating bare CdSe nanocrystals. The passivation also allowed processing of the nanocrystals at elevated temperatures without any degradation of the luminescence properties. The passivation technique may be extended to other II-VI nanocrystals and such experiments would open new opportunity for exploration of quantum size effects in layered quantum dots, and synthesis of novel materials for light emitting devices.

Acknowledgments

This thesis would not be possible without contribution of many people. First of all, it was my research advisor, Prof. Klavs F. Jensen, who provided me intellectual guidance and financial support throughout my stay at MIT.

I would like to thank to Prof. Mounqi G. Bawendi for his support and many helpful suggestions during my work on quantum dot composites. I am grateful to Chris Murray for introducing me to synthesis of CdSe quantum dots, and for many stimulating discussions.

I also would like to acknowledge my colleagues who worked together with me on OMCVD of II-VIs: Sanjay Patnaik, Jeung-Soo Huh and Larry Foley.

Much of appreciation belongs to the members of the KFJ group for the friendly and inspiring environment where research was always a great fun.

Mike Frongillo helped me with HRTEM and Libby Shaw assisted with AES. Dough Gordon and Walter Kosar of Advanced Technology Materials, Inc. prepared the precursors described in Chapters 2 and 3. Mike Steigerwald of AT&T Bell Laboratories kindly supplied dimethyl(butyl)phosphine selenide for the growth experiments described in Chapter 4.

Finally, I thank to my wife, Katerina, for her love, patience and understanding. To her, I dedicate this thesis.

List of Publications

The following is a list of publications presenting some of the results of the thesis research:

- M. Danek, S. Patnaik, K. F. Jensen, D. C. Gordon, D. W. Brown, R. U. Kirss, "*tert*-Butyl(trifluoromethyl)tellurium : A Novel Organometallic Chemical Vapor Deposition Source for ZnTe." *Chem. Mater.* **1993**, *5*, 1321.
- M. Danek, J.-S. Huh, K. F. Jensen, D. C. Gordon, W. P. Kosar, "New Organometallic Selenium Reagents for Low Temperature OMCVD of ZnSe." in "Gas-Phase and Surface Chemistry in Electronic Materials Processing", *Mater. Res. Soc. Symp. Proc.* **1994**, *334*, 231.
- M. Danek, K. F. Jensen, C. B. Murray, M. G. Bawendi, "Preparation of II-VI Quantum Dot Composites by Electrospray OMCVD." in "Growth, Processing, and Characterization of Semiconductor Heterostructures", *Mater. Res. Soc. Symp. Proc. Vol. 326* - in press.
- M. Danek, K. F. Jensen, C. B. Murray, M. G. Bawendi, "Electrospray OMCVD - A Novel Technique for Preparation of II-VI Quantum Dot Composites." *Appl. Phys. Lett.* **1994**, *65*, 2795.
- M. Danek, J.-S. Huh, K. F. Jensen, D. C. Gordon, W. P. Kosar, "Gas-Phase Pyrolysis Study of *tert*-Butyl(allyl)selenium : A New Precursor for Low Temperature OMCVD of ZnSe." *Chem. Mater.* - in press.
- M. Danek, J.-S. Huh, L. Foley, K. F. Jensen, "New Allyl Selenide and Trialkyl Phosphine Selenide Precursors for MOVPE of ZnSe." *J. Cryst. Growth.* - in press.
- M. Danek, K. F. Jensen, C. B. Murray, M. G. Bawendi, "Preparation of II-VI Quantum Dot Composites by Electrospray OMCVD." *J. Cryst. Growth.* - in press.